

THE UNIVERSITY OF HULL

**INVESTIGATION OF A NOVEL SOLAR  
PHOTOVOLTAIC/MICRO-CHANNEL LOOP-  
HEAT-PIPE HEAT AND POWER SYSTEM**

being a Thesis submitted for the Degree of Doctor of Philosophy

at the University of Hull

by

**Min Yu**

*MSc Taiyuan University of Technology, China*

*BEng Taiyuan University of Technology, China*

January 2021



# CONTENTS INDEX

<b>CONTENTS INDEX</b> .....	<b>I</b>
<b>ABBREVIATIONS</b> .....	<b>VI</b>
<b>ABSTRACT</b> .....	<b>VII</b>
<b>PUBLICATIONS</b> .....	<b>IX</b>
<b>ACKNOWLEDGEMENTS</b> .....	<b>XII</b>
<b>LIST OF FIGURES</b> .....	<b>XIV</b>
<b>LIST OF TABLES</b> .....	<b>XX</b>
<b>NOMENCLATURE</b> .....	<b>XXII</b>
<b>CHAPTER 1: INTRODUCTION</b> .....	<b>1</b>
1.1 Background .....	1
1.2 Research aim and objectives .....	6
1.3 Research concept .....	7
1.4 Research methodology.....	9
1.5 Novelty and added value.....	11
1.6 Thesis Structure .....	12
<b>CHAPTER 2: LITERATURE REVIEW</b> .....	<b>15</b>
2.1 Chapter introduction .....	15
2.2 Basic concept and relevant theory of PV/T and LHP technologies .....	16
2.2.1 Concept and primary theory of PV/T.....	16
2.2.2 Research achievement and findings in PV/T subject.....	22
2.2.3 LHP and PV/LHP technologies .....	30
2.3 PCM and its applications .....	38
2.4 Fractal theory for porous media fluid flow and heat/mass transfer.....	41
2.5 Chapter summary .....	45

## CONTENTS INDEX

---

<b>CHAPTER 3 PRELIMINARY DESIGN OF THE NOVEL PV/ MCLHP HEAT AND POWER SYSTEM.....</b>	<b>47</b>
3.1 Chapter introduction .....	47
3.2 System description and working principle .....	47
3.3 Unique features (innovations) of the system.....	50
3.4 System components and their characteristic parameters .....	51
3.4.1 PV/micro-channel evaporator with upper and lower end headers .....	51
3.4.2 Co-axial tubular triple-pipe heat exchanger with PCM (as the condenser)....	55
3.4.3 Vapour and liquid transportation lines .....	56
3.4.4 Micro-channel Loop Heat Pipe (MCLHP) .....	56
3.4.5 Working fluid.....	57
3.4.6 PV power system.....	58
3.5 Chapter summary.....	59
<b>CHAPTER 4. THEORETICAL ANALYSIS AND COMPUTING MODELS DEVELOPMENT .....</b>	<b>61</b>
4.1 Chapter introduction .....	61
4.2 Analytical model for the assessment of the heat transfer limits of the MC-LHP based on the Fractal Theory .....	61
4.2.1 Fractal characters of the sintered powder wick in the evaporator of MC-LHP .....	64
4.2.2 Mathematical model for the MCLHP heat transfer limits .....	69
4.2.3 Algorithm of the Computer Model Set-up .....	76
4.2.4 Case study - results and discussion .....	80
4.3 Steady state analytical model for the PV/MCLHP system .....	94
4.3.1 Theoretical and governing equations .....	94
4.3.3 Modelling results and case studies .....	115
4.3.4 Comparison of the novel system with the conventional system .....	132
4.3.5 Conclusion .....	135

## CONTENTS INDEX

---

4.4 Chapter summary .....	137
<b>CHAPTER 5: PROTOTYPE CONSTRUCTION AND EXPERIMENTAL TESTING, AND MODEL VALIDATION .....</b>	<b>139</b>
5.1 Chapter introduction .....	139
5.2 Fabrication of the prototype system .....	139
5.2.1 PV/micro-channel evaporator with headers .....	139
5.2.2 Co-axial tubular triple-pipe heat exchanger with PCM (as the condenser) .	142
5.2.3 The integrated PV/MCLHP Module .....	145
5.3 Experimentation set-up .....	147
5.3.1 Experimental system .....	147
5.3.2 Experimental procedure .....	151
5.3.3 Performance evaluation indicators.....	151
5.3.4 Uncertainties analysis.....	152
5.4 Results and discussion .....	153
5.4.1 Solar electrical efficiency of the novel PV/MCLHP system.....	154
5.4.2 Impact of the solar radiation .....	156
5.4.3 Impact of the coolant water inlet temperature .....	158
5.4.4 Impact of the coolant water flow rate .....	159
5.4.5 Impact of the ambient temperature .....	161
5.4.6 Impact of the height difference between the condenser and the evaporator	162
5.4.7 Overall efficiency of the PV/MCLHP system .....	163
5.4.8 Comparison between the PV/MCLHP system and the existing PV/T system and BIPV/T system.....	166
5.5 Comparison between the experimental and modelling results - model validation .....	167
5.5.1 Influence of the ambient air temperature .....	168
5.5.2 Influence of solar radiation.....	169
5.5.3 Influence of different height difference between evaporator and condenser	171

## CONTENTS INDEX

---

5.5.4 Error analysis .....	173
5.6 Chapter summary .....	173
<b>CHAPTER 6: ENERGY SAVING, ECONOMIC, ENVIRONMENTAL AND REGIONAL ACCEPTANCE ANALYSIS .....</b>	<b>176</b>
6.1 Chapter introduction .....	176
6.2 Annual operational performance .....	176
6.2.1 Weather conditions as the input parameters .....	176
6.2.2 Monthly performance predictions of the PV/MCLHP system in London and Hong Kong .....	178
6.3 Life-cycle economic analysis .....	181
6.3.1 Capital cost of the PV/MCLHP systems .....	181
6.3.2 Annual operational cost and saving of the PV/MCLHP systems .....	183
6.3.3 Annual maintenance cost.....	185
6.3.4 Cost payback time and life-cycle net cost savings.....	185
6.4 Life-cycle environmental benefits based on CO <sub>2</sub> emission .....	187
6.5 Chapter summary.....	188
<b>CHAPTER 7: CONCLUSIONS AND FUTURE WORKS .....</b>	<b>191</b>
7.1 Conclusions .....	191
7.1.1 Micro-channel loop heat pipe with a unique upper liquid feeding header ...	191
7.1.2 An integrated PV/MCLHP heat and power system .....	192
7.1.3 A prototype PV/MCLHP system for testing and model validation .....	194
7.1.4 Energy saving and socio-economic analysis .....	194
7.2 Further opportunities and Challenges .....	195
7.2.1 System demonstration .....	195
7.2.2 PV/MCLHP stakeholders .....	195
7.2.3 Research Development.....	196
7.2.4 Evaluation Standards.....	196
7.2.5 Market analysis .....	197

CONTENTS INDEX

---

REFERENCE..... 199

## ABBREVIATIONS

BIPV	Building integrated photovoltaic
CC	Capital cost
CNY	Chinese Yuan
COP	Coefficient of performance
CR	Cost reduction
EPBT	Energy payback time
EVA	Ethylene-vinyl acetate
GBP	Great Britain Pound
GHG	Greenhouse gases
GPBT	Greenhouse gas payback time
HVAC	Heating, ventilation and air conditioning
IPVTS	Integrated photovoltaic/thermal system
LCA	Life-cycle assessment
LHP	Loop heat pipe
MC	Micro-channel
MC-LHP	Micro-channel Loop heat pipe
MCT	Micro-channel Tube
PCM	Phase change material
PP	Payback period
PV	Photovoltaic
PV/e	Photovoltaic/evaporator
PV/LHP	Photovoltaic/loop heat pipe
PV/MC-LHP	Photovoltaic/Micro-channel-loop heat pipe
PV/T	Photovoltaic/Thermal
RHI	Renewable heat incentive
TPT	Tedlar-Polyster-Tedlar

## ABSTRACT

To tackle the crisis of climate change, increasing the use of renewable energy and enhancing the efficiency of the energy systems are crucial to creating more sustainable and inclusive communities and resilience. This research aims to develop a novel, high efficiency, low cost, and building integrate-able PV/micro-channel loop heat pipe system which can make effective use of solar energy for space heating, hot water and power generation and thus remove certain barriers remaining within the existing Photovoltaic/Thermal (PV/T) technologies. The new PV/T system has a number of unique features (1) a novel loop-heat-pipe (LHP) with micro-channel evaporator and co-axial triple-pipe heat exchanger as the condenser enabling a higher heat transport capacity compared to the latest existing LHP; (2) upper liquid header creating the continuous liquid film on the inner wall of the LHP evaporator which prevents the liquid ‘dry-out’ phenomena occurring; (3) liquid/vapour separator assembled on the liquid header making clear separation of the vapour and liquid which prevents the entrainment effect of the LHP and enhances the heat transfer capacity of the LHP; (4) combination of a micro-channel LHP evaporator with the PV module using a special lamination approach creating a reliable, building integrate-able PV/T panel with a higher overall solar efficiency than existing PV/T panels.

This study investigated the proposed novel solar PV/MCLHP heat and power system through a critical literature review, preliminary design, theoretical analysis using fractal theory, computation modelling, prototype design and construction, indoor (laboratory-controlled) and outdoor (real weather conditions) testing, simulation models validation, and energy saving and socio-economic performance analysis.

For the proposed system, firstly the impact of the fractal geometrical parameters of the wick on the heat transport capacity of the MCLHP was investigated, finding that the

## ABSTRACT

---

capillary limit is the governing limit and the fractal theory is thought to be an ideal method to address the impact of an irregular porous wick on the heat transfer performance of a MC-LHP. A lower inlet water temperature, a higher water flow rate, a higher ambient temperature, and a larger height difference between the condenser and the evaporator can help increase the solar thermal efficiency of the system. Under a range of testing conditions with the refrigerant charge ratio of 30%, a peak solar thermal efficiency (i.e., 71.7%) happened at solar radiation of  $561\text{W/m}^2$ , inlet water temperature of  $18^\circ\text{C}$ , water flow rate of  $0.17\text{m}^3/\text{h}$ , ambient temperature of  $30^\circ\text{C}$ , and height difference of 1.3m. This set of parametrical data is therefore regarded as the optimal operational condition of the PV/MCLHP system. Under these specific operational conditions and the real weather solar radiation, the solar thermal efficiency of the system was in the range 25.2% to 62.2%, while the solar electrical efficiency of the PV panel varied from 15.6% to 18.3%. Compared to the existing PV/T and BIPV/T systems, the new PV/MCLHP system achieved 17.2% and 33.3% higher overall solar efficiency. The prototype PV/MCLHP heat and power system would be best suited for the use in a subtropical climatic region, such as Hong Kong. This system has a cost payback period of around 5 years and the life-cycle net cost saving of nearly £3970 in China compared to a conventional gas boiler, while compared to a conventional electric water heater, the cost payback period and the life-cycle net cost saving of this proposed system are 5.6 years and £2220 respectively. Further, the relevant  $\text{CO}_2$  emissions reduction are 456.7kg and 1751.3kg in Hong Kong.

The research results are expected to configure feasible solutions for future solar PV/T technologies and develop a new solar-driven heating and power system. The main technologies may significantly lead to a wider deployment of the renewable solar systems in buildings and contributing to significant fossil fuel energy saving and carbon emission reduction on the global scale

## PUBLICATIONS

### Book Chapter

1. Thierno Diallo, **Min Yu**, Jinzhi Zhou, Yi Fan, Xudong Zhao, Micro (Mini)-Channels and Their Applications in Solar Systems (Chapter 6), Advanced Energy Efficiency Technologies for Solar Heating, Cooling and Power Generation. Green Energy and Technology. DOI: [https://doi.org/10.1007/978-3-030-17283-1\\_6](https://doi.org/10.1007/978-3-030-17283-1_6), Springer, Cham 2019, 165-209.

### Journal Publications

1. **Yu M**, Diallo T, Zhao X\*, Zhou J, Du Z, Ji J, et al. Analytical study of impact of the wick's fractal parameters on the heat transfer capacity of a novel micro-channel loop heat pipe. Energy 2018(158):746-759. <https://doi.org/10.1016/j.energy.2018.06.075>.
2. **Yu M**, Chen F, Zheng S, Zhou J, Zhao X\*, et al. Experimental Investigation of a Novel Solar Micro-Channel Loop-Heat-Pipe Photovoltaic/Thermal (MC-LHP-PV/T) System for Heat and Power Generation. Applied Energy 2019 (256): 113929. <https://doi.org/10.1016/j.apenergy.2019.113929>.
3. Diallo T, **Yu M**, Zhou J, Zhao X\*, Shittu S, Li G, et al. Energy performance analysis of a novel solar PVT loop heat pipe employing a microchannel heat pipe evaporator and a PCM triple heat exchanger. Energy 2019(167):866–88. <https://doi.org/10.1016/j.energy.2018.10.192>.
4. Ren X, **Yu M**, Zhao X\*, Li J, Zheng S, Chen F, et al. Assessment of the cost reduction potential of a novel loop-heat-pipe solar photovoltaic/thermal system

- by employing the distributed parameter model. Energy 2020(190):116338.  
<https://doi.org/10.1016/j.energy.2019.116338>.
5. Diallo T, **Yu M**, Zhou J, Zhao X\*, Ji J, Hardy D. Analytical investigation of the heat-transfer limits of a novel solar loop-heat pipe employing a mini-channel evaporator. Energies 2018;11. <https://doi.org/10.3390/en11010148>.
  6. Li G, Shittu S, Diallo T, **Yu M**, Zhao X, Ji J. A review of solar photovoltaic-thermoelectric hybrid system for electricity generation. Energy 2018;158. <https://doi.org/10.1016/j.energy.2018.06.021>.
  7. Chen FC, Hu ML, Badiei A, **Yu M**, et al., Experimental and numerical investigation of a novel photovoltaic/thermal system using micro-channel flat loop heat pipe (PV/T-MCFLHP), International Journal of Low-Carbon Technologies, 2020 (15): 513–527, <https://doi.org/10.1093/ijlct/ctaa019>
  8. Weng CB, Wang ZY, Xiang JW, Zhao XD, Chen FC, Zheng SM, **Yu M**, Numerical and experimental investigations of the micro-channel flat loop heat pipe (MCFLHP) heat recovery system for data centre cooling and heat recovery, Journal of Building Engineering, Volume 35, 2021,102088,ISSN 2352-7102, <https://doi.org/10.1016/j.jobe.2020.102088>.

### Conference Papers

9. **Yu M**, Zhao X, Diallo T.M.O., et.al. Fractal analysis of the heat and mass transfer limit of a novel PV/micro-channels-loop heat pipe. SET2017, Bologna, Italy, 2017.
10. Diallo T, **Yu M**, Zhao XD, Numerical investigation of the heat transfer capacity of a loop heat pipe with mini channel evaporator applied to solar collector. 10th

## PUBLICATIONS

---

International Symposium on Heating, Ventilation and Air Conditioning (ISHVAC 2017), Proceedings of a meeting held 19-22 October 2017, Jinan, China.

11. **Yu M**, Zhou J, Zhao X, Yi Fan Y, Impact study of height difference on solar thermal performance of a novel solar micro-channel loop heat pipe-PV/T heating system, pp. 11–14. International Conference on Applied Energy 2019, Aug 12-15, 2019, Västerås, Sweden.

## ACKNOWLEDGEMENTS

I would like to express my sincere and heartfelt gratitude and appreciation to my respectable PhD supervisor, Professor Xudong Zhao, who I have had the pleasure of studying and working with for more than 4 years now. Since the days of supervising my CSC-UOH scholarship project application to the conclusion of my PhD, he has provided me with continuous support and guidance needed to successfully complete my PhD. I am forever grateful to him for his patience, motivation, enthusiasm, immense knowledge and enthusiastic involvement throughout the whole process of my PhD research, as well as for believing in me and adding me to his world-class research centre.

I would like to extend my gratitude to my pre-second supervisor, Dr Theirno Diallo and to my brother in research Dr. Jinzhi Zhou. It has been a pleasure working and learning closely from Dr. Diallo and Dr. Zhou throughout the first two years of the PhD period and I am grateful for all their help especially regarding paper publications and the experiment setup. I would also like to thank Dr. Jing Li, Dr. Guiqiang Li, Dr. Xiaoli Ma and Dr. Xin Xiao for their help regarding on paper writing skills and thank Dr.Zishang Zhu for his support.

I wish to thank to Professor Zhangyuan Wang for her kindness help on experimentation and paper viewing, and her research group especially Mr. Fucheng Chen, Mr. Siming Zheng and Mr.Zicong Hong for their support on the experiment stage set up. I'd like to thank professor Xingxing Zhang for his help on building computation model and professor Boming Yu for his comments on using fractal theory. Thanks to Five-star Solar Energy Ltd especially Mr. Wenxue Tang, Mr. Lancong Yang and all the workers who had helped me on manufacturing the prototype system and the experiment setup.

## ACKNOWLEDGEMENTS

---

Furthermore, I would like to thank the China scholarship Council (CSC) and the University of Hull for the support of international maintenance fee and tuition fee bursary for the duration of my PhD. Thank you to all my research centre colleagues especially, Yi Fan, Yuanda Cheng, Samson Shittu, Yousef Golizadeh Akhlaghi, Zishang Zhu, David Hardy who I have had the pleasure of going through this PhD journey with. Thank you for all the wonderful memories. In addition, thank you to professor Xudong Zhao, Dr Yi Fan, Dr. Huanan Yu, Ms. Li Wang, Mr. Di Wu, Mr. Shuangyu Liu, professor Kai Chen , Dr. Hui Yang for their help and care within the difficult time in COVID-19 lockdown period. I would also like to thank all my friends and teachers from high school to university in my life, especially, Mr. Guoqiang Li, Mr. Hao Xu, Ms Jing Tang, Ms Hong Yao, Mr. Keyuan Yu, Ms Boya Wang, Ms Yi Qin, Mr. Lei Yan, Mr. Kai Wang, Ms Yingying Wu for their support and encouragement. I would love to present my appreciation to Mr. Ruichen Chou for his help and encouragement during the thesis writing-up period. Thank you to special friends from all over the world in the Divine Metaphysics Wechat group and all my Douyin (Tiktok) friends and fans for their encouragement, support, positive energy and happy memories.

Sincerely, I'd love to present my heartfelt gratitude and appreciation to my Msc Master, Professor Zhenyu Du for his continuous support and encouragement throughout my PhD period.

Finally, I would like to express my sincere appreciation to my dear parents for giving me life and strength to complete my study carrier. Thank you to my old sister, brother in law and my dear niece for their great love and encouragement always. Thank you all my family members and relatives especially my youngest aunt and my grandma for always favouring and supporting me, I love you all forever.

# LIST OF FIGURES

## Chapter 1

Fig. 1- 1 The energy performance of building directive in the EU [6] .....	2
Fig. 1-2 Solar energy installation capacity in the world[14] .....	4
Fig. 1- 3 Schematic of the PV/MCLHP heating and power system .....	7

## Chapter 2

Fig.2-1 Schematic of a typical PV/T module [28] .....	18
Fig.2-2 Cross-section view of the Photovoltaic/Thermal system[29] .....	18
Fig.2-3 Sample of glass wool for thermal insulation .....	18
Fig.2-4 Solar energy distribution diagram of PV/T panel.....	20
Fig.2-5 Cross sections of typical air-based PV/T module designs[26].....	23
Fig.2-6 A function of the electrical efficiency and the PV temperature .....	25
Fig.2-7 Cross sections of typical water-based PV/T module designs[26] .....	26
Fig.2-8 Schematic of a conventional heat pipe.....	28
Fig.2-9 The Heat pipe based PV/T solar collector.....	29
Fig.2-10 Schematic of the traditional LHP[68] .....	31
Fig.2-11 Commercially available PCM solutions[104] .....	39
Fig.2- 12 Examples of natural fractal phenomena .....	41

## Chapter 3

Fig. 3-1 Schematic of the novel solar PV/ MCLHP system.....	48
Fig. 3- 2. Cycle loop of the novel solar PV/T-MCLHP heating system.....	49
Fig. 3- 3. PV/micro-channel-evaporator module .....	52
Fig. 3-4. Solar collector with PV/micro-channel evaporator and condensate liquid pathway (units in mm). .....	54

## LIST OF FIGURES

---

Fig. 3-5. The structure of the triple-pipe heat exchanger .....	55
Fig. 3-6. Schematic of the novel Micro-channel loop-heat pipe, the refrigerant flow and evaporation in the micro-channel .....	58
Fig. 3-7. Solar power process from the PVs to the User (Coils and Fan) .....	59
 <b>Chapter 4</b>	
Fig.4- 1. The SEM image within the porous stack sintered on .....	65
Fig.4-2. A simplified model for the cross section of a capillary tube partially .....	68
Fig.4-3. Schematic of the novel solar loop-heat pipe, the refrigerant flow and evaporation in the micro-channel with porous wick.....	71
Fig.4- 4: Computation program flow chart .....	79
Fig.4- 5: Fractal dimension $D_f$ vs. Effective porosity $\epsilon$ ( $d=2$ , $d=3$ ) .....	81
Fig.4-6: Fractal dimensions $D_t$ vs. effective porosity $\epsilon$ ( $d=2$ , $d=3$ ).....	81
Fig.4-7. Permeability of different pores diameter vs. effective porosity $\epsilon$ ( $d=3$ ).....	82
Fig.4- 8. Effective thermal conductivity of different pores diameter vs. effective porosity $\epsilon$ ( $d=3$ ).....	83
Fig.4-9. Boiling limit (QBL) vs. Effective porosity ( $\epsilon$ ) (Euclidean dimension $d=3$ ) .....	85
Fig.4-10. Boiling limit (QBL) vs. Pore distribution fractal dimension ( $D_f$ ) (Euclidean dimension $d=3$ ).....	86
Fig.4- 11. Boiling limit (QBL) vs. the tortuosity fractal dimension $D_t$ , $d=3$ .....	86
Fig.4-12. Boiling limit for evaporator $Q_{BL,e}$ vs. effective porosity $\epsilon$ (a) and fractal dimension $D_f$ (b) ( $d=3$ ) .....	87
Fig.4-13. Capillary limit ( $Q_{cl}$ ) vs. Effective porosity $\epsilon$ (a) and fractal dimension $D_f$ (b), ( $d=3$ ).....	89
Fig.4-14. Fractal dimension $D_f$ vs. Porosity of skeleton (Effective porosity $\epsilon=0.8$ , $d=3$ ) .....	90
Fig.4-15. Capillary limit vs. Porosity at different hight differences ( $d=3$ ) .....	91

## LIST OF FIGURES

---

Fig.4-16. Impact of evaporator inclination angle on the maximum heat transfer capacity .....	92
Fig.4-17. Impact of quantity of MC-flat tube on max-heat transfer capacity .....	93
Fig.4-18. Impact of evaporator length on max-heat transfer capacity .....	93
Fig.4-19. Solar energy process model from the ambient air to the PV/MC-evaporator.	95
Fig.4-20 Thermal circuit model.....	97
Fig.4-21 Schematic of heat transfer resistances along the PV/MC-LHP .....	102
Fig.4-22 Heat flow pattern at the elemental length 'dx' on the Al plate[89] .....	103
Fig.4-23. The design of the heat exchanger .....	109
Fig.4-24. PV/MCLHP system model simulation flow chart .....	113
Fig.4-25. Influence of solar radiation on: a) the thermal, electrical, overall efficiencies; b) PV cell temperature.....	116
Fig.4-26. Influence of solar radiation on: a) the heat outputs, and b) the water outlet temperature .....	117
Fig.4-27. Influence of solar radiation on the COP .....	117
Fig.4-28. Influence of the ambient air temperature on: a) the thermal, electrical, overall efficiencies, b) PV cell temperature.....	118
Fig.4-29. Influence of the ambient temperature on a) the heat outputs and b) the water outlet temperature .....	119
Fig.4-30. Influence of ambient temperature on the COP .....	120
Fig.4-31. Influence of the wind velocity on the a) the thermal, electrical, overall efficiencies, b) PV cell temperature.....	121
Fig.4-32. Influence of wind velocity on: a) the heat outputs and b) the water outlet temperature .....	121
Fig.4-33. Influence of wind velocity on the COP .....	122
Fig.4-34. Influence of the cover number on the efficiency .....	123

## LIST OF FIGURES

---

Fig.4-35. Influence of the cover number on heat transfer rates and the outlet water temperature .....	124
Fig.4-36. Influence of the cover on the COP .....	124
Fig.4-37. Influence of the packing on the efficiency .....	125
Fig.4-38. Influence of the packing factor on heat transfer rates and the outlet water ..	126
Fig.4-39. Influence of the packing factor on the COP .....	126
Fig.4-40 Influence of the microchannel heat pipe number on the efficiency .....	127
Fig.4-41. Influence of microchannel the heat pipe number on the PV cell temperature and the outlet water temperature .....	127
Fig.4-42. Influence of microchannel heat pipe number on the COP .....	128
Fig.4-43. Influence of the water inlet temperature on the efficiency .....	129
Fig.4-44. Influence of the water inlet temperature on heat transfer rates and the outlet water.....	129
Fig.4-45 Influence of the water inlet temperature on the COP .....	130
Fig.4-46. Influence of the water mass flow rate on heat transfer rates and the outlet water .....	131
Fig.4-47. Influence of the water mass flow rate on the efficiency .....	131
Fig.4-48. Influence of the water mass flow rate on the COP .....	132
Fig.4-49 Comparison between, a) the novel PVT system b) the conventional PVT system .....	133
Fig.4-50. Comparison between the new PVT system and the conventional PVT system a) evolution of thermal, electrical, overall efficiencies b) overall efficiency increase .....	134
Fig.4-51. Comparison between the new PVT system and the conventional PVT system a) evolution of the COPPVT and b) the ration of COP novel by COP conventional.....	135
<b>Chapter 5</b>	
Fig.5-1. PV/micro-channel-evaporator module.....	140

## LIST OF FIGURES

---

Fig.5-2. The photographic image of Micro-channel evaporator.....	141
Fig.5-3. A photograph of such a co-axial condensation heat exchanger .....	143
Fig.5-4. Co-axial condensation heat exchanger.....	143
Fig.5-5 DSC of A44 .....	144
Fig.5-6. MC-LHP evaporator pre-assembling testing.....	146
Fig.5-7. The photographic image of the PV/MCLHP module .....	146
Fig.5-8. Solar power process from the PVs to the User (Coils and Fan) .....	148
Fig.5-9. Outdoor experimental system.....	149
Fig.5-10 Experimental PV/MCLHP heating system view in the lab.....	150
Fig.5-11. Schematic of the experimental set up and instrumentation .....	150
Fig.5-12. (a) Solar radiation, (b) electrical efficiency, and power output.....	155
Fig.5-13. Solar electrical efficiency against PV cells temperature.....	155
Fig.5-14 Temperature distribution on different parts the PV/T panel under three solar radiation levels.....	157
Fig.5-15. Variation of the average solar thermal efficiency against solar radiation.....	158
Fig.5-16. Solar thermal efficiency against the coolant water inlet temperature.....	159
Fig.5-17. Solar thermal efficiency against coolant water flow rate.....	160
Fig.5-18. Average heat efficiency vs ambient air temperature.....	161
Fig.5-19. Solar thermal efficiency changing with height difference between heat exchanger (condenser) and evaporator.....	163
Fig.5-20. Water tank temperature under real weather .....	164
Fig.5-21. Solar thermal and electrical performance under real weather .....	164
Fig.5- 22. Correlations between the efficiencies and the indicative parameter, $(t_{in}-t_a)/G$ .....	166
Fig.5-23. Experimental and simulation results of outlet water temperature under different ambient air temperature.....	169

## LIST OF FIGURES

---

Fig.5-24. Experimental and simulation results of the solar thermal efficiency with different ambient air temperature .....	169
Fig.5-25. Influence of the solar radiation on the outlet water temperature of the PV/MCLHP system (exp. vs sim.) .....	170
Fig.5-26. Influence of the solar radiation on the solar thermal efficiency of the PV/MCLHP system (exp. vs sim.) .....	171
Fig.5-27 Influence of height difference on the outlet water temperature (exp. vs sim.) .....	172
Fig.5-28 Influence of height difference on solar thermal efficiency (exp. vs sim.) .....	172
<b>Chapter 6</b>	
Fig.6-1. Monthly average solar radiation in London and Honking .....	177
Fig.6-2. Monthly average ambient air temp London and Hong Kong .....	177
Fig.6-3. Monthly average PV temperature and air temperature in London and Hong Kong .....	178
Fig.6-4. Solar energy efficiencies of the PV/MCLHP system in London and Hong Kong .....	179
Fig.6-5. Overall energy output of the PV/MCLHP system in London and Hong Kong .....	180

# LIST OF TABLES

## Chapter 2

Table 2-1: Heat pipe working fluids[76].....	32
Table 2-4 Comparison of different LHPs in terms of FR and parameters .....	34

## Chapter 3

Table 3-1. Parameters of the solar glazing cover .....	53
Table 3-2. Parameters of the PV panels .....	53
Table 3-3. Parameters of the PV/MCLHP system.....	57

## Chapter 4

Table 4-1. Different heat transfer limits ( $d=3$ , $\lambda_{\max}=100 \mu\text{m}$ ) .....	84
--	----

## Chapter 5

Table 5-1. Parametrical data of the PV panels .....	141
Table 5-2. Item description of the heat exchanger configuration .....	143
Table 5-3. Thermal physical properties of PCM (A44) .....	144
Table 5-4. List of the testing and monitoring components .....	147
Table 5-5. The experimental RMEs of the variables .....	153
Table 5-6: The test data of the PV/MCLHP system under real weather condition .....	165
Table 5-7: The novel PV/MCLHP system vs. other PV/T systems.....	167

## Chapter 6

Table 6-1 Monthly average wind speed in London and Hong Kong (m/s).....	177
Table 6-2 Total annual energy output of the prototype system in Hong Kong and London .....	181
Table 6-3: 1.2kW related PV/MCLHP capital cost summary .....	182

## LIST OF TABLES

---

Table 6-4: Renewables tariffs for the installation of a solar system in London and Hong Kong.....	183
Table 6-5 Annual operational costs of different systems.....	184
Table 6-6 Cost payback period and life-cycle net cost saving .....	186
Table 6-7 Annual CO <sub>2</sub> emission reduction of the proposed PV/MCLHP system.....	188

## NOMENCLATURE

<i>Parameters</i>		<i>Subscripts</i>	
a	micro-channel port width, m	an	annular
A	area, m <sup>2</sup>	av	average
A <sub>p</sub>	the total pore area for the representative cell, m <sup>2</sup>	b	bubble
b	micro-channel port height, m	BL	boiling limit
B	temperature attenuation coefficient, 1/°C	c	cold, charge, cover
Bo	bond number ,m	CH	conventional heater
C	heat capacity, W/K	ch	channel
C,d	discharge coefficient	ch	micro-channel ports
d	hole diameter, m	cond	condensation
D	diameter, m	CL	capillary limit
D <sub>hp</sub>	hydraulic diameter of a single mini- channel tube, m	d	Discharge, days
D <sub>f</sub>	fractal dimension of porous media	e	Electrical, effective, evaporator
D <sub>f,g</sub>	the fractal dimension of gas/vapor in porous media	eq	equivalent
D <sub>t</sub>	fractal dimension for tortuous stream tubes in porous media	ei	electrical insulation
D <sub>v,e</sub>	equivalent diameter of the vapour section, m	EL	entrainment limit
D <sub>w</sub>	the condensed liquid film hydraulic diameter	EVA	ethylene-vinyl acetate
e	thickness, m	f	Fin, fluid, fractal
f	liquid fraction, friction factor	F	efficiency factor
g	gravitational acceleration 9.81, m/s <sup>2</sup>	g	gas, vapour
G	solar radiation, W/m <sup>2</sup>	g	gravity
G	mass velocity, kg/m <sup>2</sup> /s	h	hole, header
H	solar radiation per day, MJ/day	he	heat exchanger
H	hight difference, m	hp	heat pipe
h <sub>fg</sub>	latent heat of evaporation, J/kg	Hp-he	heat pipe to heat exchanger
		i	inner

## NOMENCLATURE

---

h	heat transfer coefficient, $W/(m^2 \cdot K)$	l	liquid
$h_{fg}$	latent heat of vaporisation, $J/(kg \cdot K)$		liquid header
I	current, A	lh	
		lf	liquid film
		ltl	liquid transportation line
k	thermal conductivity, $W/(m \cdot K)$	L	loss
$k_l$	effective thermal conductivity of liquid, $W/(m \cdot K)$	LO	liquid only
$k_s$	the effective thermal conductivity of solid, $W/(m \cdot K)$	vtl	vapour transportation line
K	proportional constant for bubble diameter ( 2 or 1.8 )	m	maximum
$K_e$	effective thermal conductivity, $W/(m \cdot K)$	max	maximum
$K_p$	permeability of a porous medium, $m^2$		mixed chains of particles/skeletons
L	length scale ,m	mc	with fluid
$L_e$	length of micro-channel evaporator, m	min	minimum
$L_0$	representative length ,m	mt	middle tube
L	length, m	n	nontouching particles or skeletons
m	variable, $m^{-1}$	o	outer
M	molecular weight of the refrigerant R134a, kg/mol	out	outlet
$M(L)$	length of a line or area of a surface or the volume of a cube or the mass of an object	oc	open-circuit
N	Number	p	port, pore, pv cell
$N_{ch}$	the number of micro-channels of one solar panel		phase change material
Nt	the total number of pores	PCM	
$N_{ch}$	number channel ports	Pr	pranlt
Nu	nusselt number	p-fin	pv-fin
		pm	at maximum output power
		PV	photovoltaic

## NOMENCLATURE

---

P	power, W	PVT	photovoltaic/thermal
P <sub>c</sub>	capillary pressure ,Pa	s	solid (wick skeleton)
P <sub>v</sub>	corresponding saturated vapor pressure,Pa	SL	sonic limit
P	pressure drop	sc	short-circuit
P	pressure	t	thermal
q	heat density, W/m <sup>2</sup>	th	thermal
Q	heat transfer rate ,W	tp	two-phase
r <sub>b</sub>	radius of the boiling bubble departure (2.54 × 10 <sup>-7</sup> m),W	u	utile
R	radius,m	v	vapour
R <sub>0</sub>	universal gas constant,J/(kmol·K)	vh	vapour header
R <sub>v</sub>	vapor constant of R134a ,J/(kmol·K)	VL	viscosity Limit
R <sub>o</sub>	specific gas constant ,J/(kg K)	vtl	vapour transportation line
R	thermal resistance ,W/K	w	water, wick
Re	reynolds number		
S	saturation		
T	temperature, °C	$\beta$	temperature coefficient
T <sub>w</sub>	wall temperature , °C	$\rho$	density, kg/m <sup>3</sup>
t	temperature ,°C	$\lambda$	thermal conductivity, W/(m*K)
u	velocity,m/s	$\eta$	efficiency
U	heat loss,W/K	$\eta_{rc}$	electrical Efficiency under standard condition
V	voltage, V	$\lambda$	pore diameter or pore size
W	collector width,m	$\epsilon$	porosity of porous media
x	vapour quality	$\epsilon$	efficiency ; difference
		$\mu$	dynamic viscosity ,Pa·s
		$\delta$	thickness
		$\sigma$	surface tension,N/m
		$\nu$	specific volume,m <sup>3</sup> /kg
		$\tau$	tortuosity of porous media
			thermal boundary layer
		$\delta$	thickness,m
		$\gamma$	vapour-specific heat ratio

### Greek Symbols

## NOMENCLATURE

---

$\gamma_{al}$	the ratio of geometrical length scale for a particle
$\gamma_{cl}$	the ratio of contact length scale for a particle



# CHAPTER 1: INTRODUCTION

## 1.1 Background

Climate change is now affecting every aspect of the world, causing huge number of environment and social challenges at today and even more tomorrow [1]. It is reported by the Intergovernmental Panel on Climate Change (2018) that the world is found to be already witnessing the consequences of 1°C global warming [2]. Every bit of additional warming brings greater risks, such as extreme weather, rising of sea levels and diminishing of the Arctic sea ice. Therefore, governments address serious concerns on climate change and are taking urgent actions on reducing emissions of greenhouse gases, in order to reflect the impacts of climate change. The major reason of the global warming is the continuous emissions of greenhouse gases resulted from extensive fossil fuel consumption by human activities, whilst greenhouse gas emissions are reported to be now at their highest levels in history.

Fossil fuel energy is central to nearly every major challenge and opportunity the world faces today, and is also the dominant contributor to climate change, accounting for around 60% of total global greenhouse gas emissions [3]. Focusing on universal access to energy, increasing the use of renewable energy and enhancing the efficiency of the energy systems are crucial to creating more sustainable and inclusive communities and resilience to the above environmental issues.

United Nations set out the ambitious Sustainable Development Goals [3], which are to (1) Enhance international cooperation to facilitate access to clean energy research and technology, including renewable energy, energy efficiency and advanced and cleaner fossil-fuel technology, and promote investment in energy infrastructure and clean energy technology; (2) Double the global rate of improvement in energy efficiency; and (3)

Achieve absolute per capita greenhouse gas emission reductions of 25% by 2025 and 45% by 2030, which are realised through per capita reductions in electricity consumption of 20% by 2025 and 35% by 2030, and sourcing 40% of its electricity from renewable energy before 2025 and 80% by 2030 [4]. European Union (EU) committed to reducing greenhouse gas emissions by at least 40 % by 2030 as compared with the levels of 1990 [5], which can be realised through the development of sustainable, competitive, secure and decarbonised energy technologies and systems.

In the EU, buildings are responsible for approximately 40% of energy consumption and 36% of CO<sub>2</sub> emissions, making them the single largest energy consumer. At present, around 35% of the EU's buildings are over 50 years old and almost 75% of the EU buildings are energy inefficient. Furthermore, around 80% of energy inputs to buildings is used for heating, cooling and power generation. To enhance the energy performance of the EU buildings, the integration of renewable energy technologies and improvement of the energy efficiency of the building energy systems are in priority action list. Fig. 1- 1 shows the energy profile of the EU buildings.

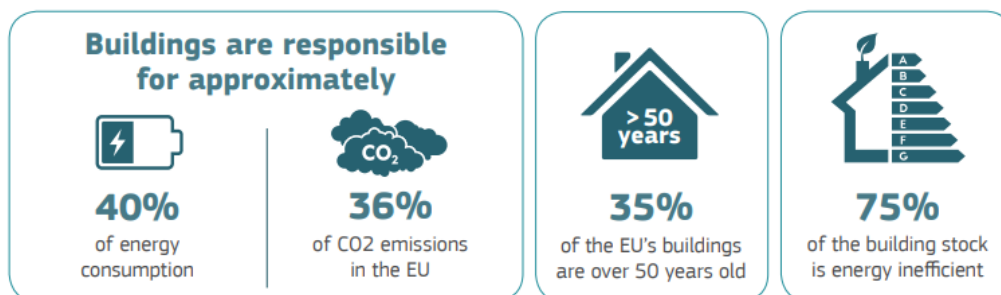


**Fig. 1- 1 The energy performance of building directive in the EU [6]**

In China, the buildings account for around 37% of energy consumption and about 42% of China's CO<sub>2</sub> emissions in 2018[7]. And the building operation contribute 23% of energy consumption and 20% of China's CO<sub>2</sub> emissions.

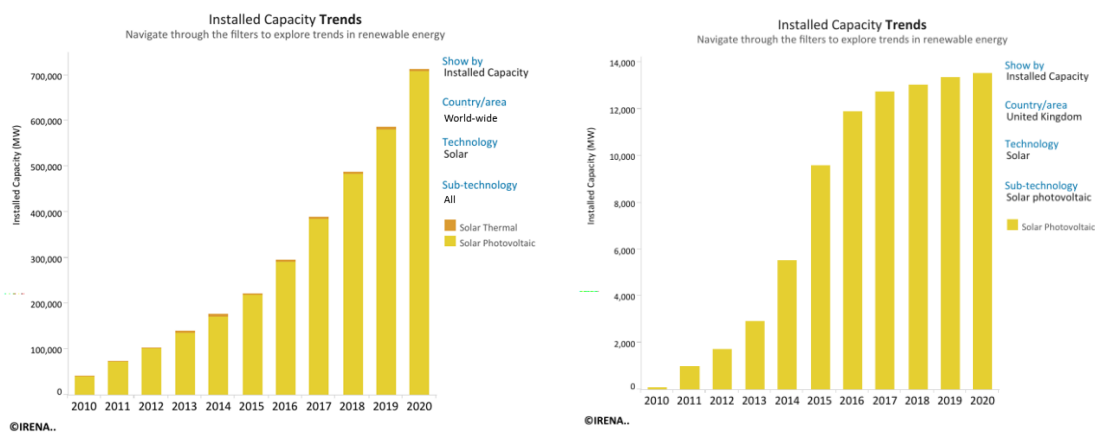
Renewable energy applications represent a third of the world growth, making a growth rate of 14.5% by 2017 [8]. However, the challenges are still in place and there are urgent needs to be more access to clean fuels and innovative technologies. In particular, advanced technologies are highly required to enable integrating renewable energy into end-user applications, e.g. in buildings, transport and industry.

There is a variety of renewable energy sources, e.g. sun, earth, wind, sea waves, biomasses etc. Among these renewable sources, sun is the most abundant and free renewable energy source that is available globally. Energy is emitted from the sun at a rate of  $3.8 \times 10^{23} kW$  and approximately  $1.8 \times 10^{14} kW$  of this energy is intercepted by the earth. Furthermore, the earth's surface receives about 60% of this energy while the remaining is reflected back to space and absorbed by the atmosphere. Converting only 0.1% of this energy at an efficiency of 10% will provide four times the total global generating capacity. In addition, the total annular solar radiation incident on the earth is 7,500 times greater than the global total annular primary energy consumption [9]. Therefore, it is obvious that the global energy demand can be met by the use of solar energy as a result of its vast energy capacity.

Solar energy application can date back to 212BC, when the scientist, Archimedes from Greek, used a mirror made of metal to burn a Roman fleet [10]. Until 19<sup>th</sup> century, solar energy was used to convert electrical energy. With the development of the economy, science and technologies, solar energy is more and more popular for generating power or heating and desalinating water. Nowadays, growing demand of power generation in both developed and developing countries create rapid raising in solar power systems. As a result, the solar power systems are expected to provide up to 25% global electricity by 2050 [11]. **Fig. 1-2** shows the solar installation capacity across the world and in the UK.

Solar power is generated in two major methods: (1) by Photovoltaicss (PV) which are kind of electronic devices to convert solar energy directly into electricity, and (2) by

concentrated solar power (CSP) which applies mirror to concentrate sun rays to heat working fluid to create steam thus driving a turbine to generate electricity. To date, PV is one of the fastest-growing renewable energy technologies, which is ready to play a major role in the future global electricity generation mix. Apart from the solar PV technology, solar thermal collection is also one of the most commonly used solar technologies [12]. Solar thermal collectors convert solar radiation into the usable heat, with a typical thermal efficiency of around 60-70% [12] , while some specific solar collectors can achieve the thermal efficiency of up to 80% [13].



World wide

UK

**Fig. 1-2 Solar energy installation capacity in the world[14]**

Compared to solar thermal collectors, PV panels have less energy conversion rate, which is usually in a range 4% to 20% [13], and PV panels normally have a linear efficiency drop-off as the surface temperature rises, which typically lose efficiency of up to 0.4% per degree centigrade rise in the PV-cells' temperature [15][16]. Furthermore, the life span of the PV cells could be shorten when the PVs are continuously operated at a higher temperature. To make effective use of solar energy, and keep PV in a safe and efficient operational condition, the Photovoltaic/Thermal (PV/T) technology was recently developed. The PV/T, by collecting the heat trapped behind of the PV modules, can cool

down the PV cells by a certain degrees, thus enabling PVs to improve the electrical efficiency and maintain its life span to the expected level. The heat collected from the PVs can be used for providing space heating or hot water for buildings, thus creating the combined heat and power generation and improving the overall efficiency of the PV/T.

The PV/T development can date back to 1970s and recent progress in PV/T technologies is fairly fast. A simple version of PV/T is to have air passed across the backside of the PV module, thus removing certain amount of heat away from the PVs and generating the warm air for the use of building ventilation. This technology has a feature of simple structure and easy implementation. However, its heat removal effectiveness is poor owing to the air's small thermal mass and significant heat loss to surrounding.

Currently, the most popular PV/T systems use water as a working fluid. Compared to the air-based PV/T, the water-based PV/T can achieve the improved heat removal effectiveness and thus increased overall solar efficiency. However, this type of system have a few critical disadvantages: (1) water gives a higher pressure drop and thus needs a greater pump power; (2) PV and thermal panels have poor binding effect owing to the different thermal & physical properties; and (3) limited heat removal capacity owing to the sensible heat transfer and limited temperature rise level.

To advance the PV/T technologies and enhance their energy performance, heat pipes were recently brought into use. A heat pipe is a passive heat transportation device that, making use of the evaporation of the working fluid on one side and condensation of the working fluid on the other side, can effectively removes heat away from the PV back surface and transfer it to the working fluid on its other side. This approach creates a high efficient, safe and passive way of PV cooling and thus enables an improved overall solar efficiency. Compared to the water-based PV/T which involves sensible heat transfer only, the HP-based PV/T can achieve much higher heat removal effectiveness owing to the latent heat transfer involved. Despite of

these distinguished advantages, the existing HP-PV/T has a few disadvantages: (1) high cost, (2) relies on the gravity of the working fluid owing to relatively smaller wick capillary effect; and (3) liquid film ‘dry-out’ occurring in the upper part of the evaporator[17] leading to significantly reduced heat transport capacity [18].

### **1.2 Research aim and objectives**

To overcome the above addressed problems remaining with the PV/T technologies and systems, the research aims to develop a novel, high efficiency, low cost, and building integrate-able PV/T system which can make effective use of solar energy for space heating, hot water and power supply. The new PV/T system has a number of unique features (1) a novel loop-heat-pipe (LHP) with micro-channel evaporator and co-axial triple-pipe heat exchanger as the condenser enabling a higher heat transport capacity compared to the latest existing LHP; (2) upper liquid header creating the continuous liquid film on the inner wall of the LHP evaporator which prevents the liquid ‘dry-out’ phenomena occurring; (3) liquid/vapour separator assembled on the liquid header making clear separation of the vapour and liquid which prevents the entrainment effect of the LHP and enhances the heat transfer capacity of the LHP; (4) combination of a micro-channel LHP evaporator with the PV module using a special lamination approach creating a reliable, building integrate-able PV/T panel with a higher overall solar efficiency than existing PV/T panels; As a result, the new PV/T system is expected to achieve significant higher overall solar efficiency and cost saving compared to the existing PV/T systems. To achieve this challenging target, the research sets out the following specific objectives:

- ❖ To carry out an extensive literature review of PV/T and heat pipe technologies, thus identifying the existing challenges and giving relevant suggestions about the potential solutions;

- ❖ To develop a preliminary design of a novel PV/T system combined with micro-channel loop heat pipe technology aiming to increase the overall solar efficiency and decrease the cost;
- ❖ To develop a computer model for the proposed PV/T system to optimise the system configurations and predict the system operation performance;
- ❖ To design, construct and test a prototype micro-channel loop heat pipe PV/T (PV/MC-LHP) system, and validate/refine the established computer models.
- ❖ To evaluate the economic & environmental performance of the novel PV/T system.

### 1.3 Research concept

The proposed micro-channel loop heat pipe PV/T (i.e. PV/MCLHP) heating and power supply system is shown schematically in **Figure 1-2**. This system, making use of R-134a as the working fluid, comprises a co-axial tubular heat exchanger as the condenser, PV-bound multiple micro-channel tubes array as the PV/evaporator, the upper end liquid header with tiny holes as the liquid header and liquid/vapour separator, and the upper end vapour header as the vapour collector and distributor. This will create the improved condensation and evaporation effects within the loop-heat-pipe (LHP) and thus, achieve significantly enhanced solar thermal and electrical efficiencies compared to traditional PV/T systems.

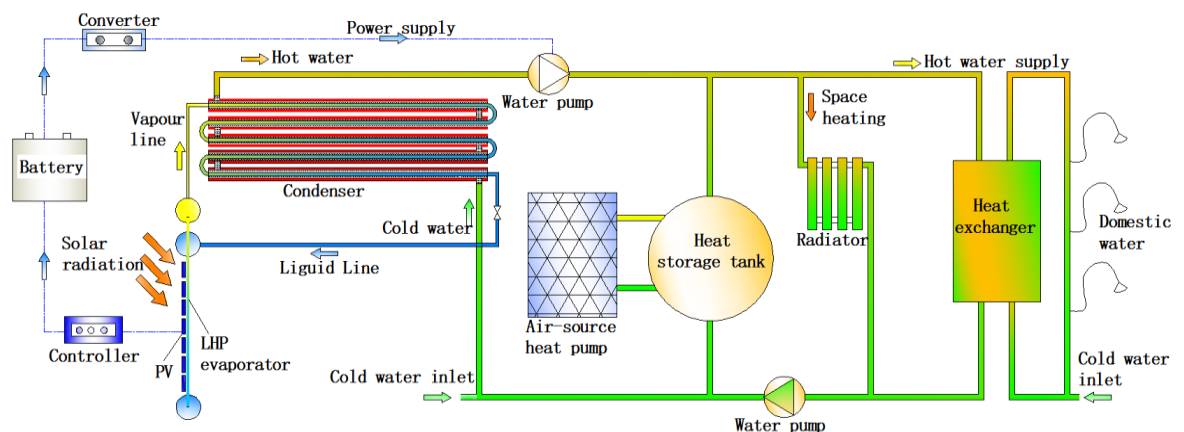


**Fig. 1- 3 Schematic of the PV/MCLHP heating and power system**

When the PV/evaporator receives the solar radiation striking on its upper surface, part of which is converted into electricity owing to the photo-electron effect of the PV cells, its second part is converted into heat which is absorbed by the working fluid flowing across the microchannel evaporator, and the remainder is dissipated into the surrounding. As a result, the fluid within the micro-channel evaporator is converted into vapour and this amount of vapour gathers at the upper end vapour header, and then is uplifted to the condenser by the buoyancy effect of the vapour. Within the condenser, the vapour in the interior channel transfers heat to the coolant water at the mid-channel, leading to the gradual condensation of the vapour. At the end of the channel, the vapour is completely condensed and the condensed liquid falls into the liquid header by gravity. In the meantime, the water within the mid-channel is heated to a temperature of around 40-50°C at the end of the channel and this is delivered to a building for the purposes of space heating or hot water supply. The PCM particles at the outside channel are functioned to absorb additional heat when the interior channel fluid carries more heat than the actual need of the water in the mid channel, and discharge some of the heat into the mid-channel when the interior channel fluid carries less heat than the actual need. The condensed liquid gathers at the liquid header to a certain height level. This amount of water is then distributed to the inner wall of the micro-channel evaporator, through the holes fixed to the surface of the liquid header. A conventional LHP, which returns the condensed liquid refrigerant to the bottom of the evaporator and draws the liquid refrigerant from the evaporation section of the heat pipe using the capillary force of the heat pipe inner wall, suffers from the 'dry out' problem in the upper part of the evaporating section of the heat pipe and therefore has a lower heat transport capacity. Unlike the conventional LHPs, the novel LHP returns the condensed liquid refrigerant from the upper feeding liquid header. The upper feeding liquid header, with numerous tiny holes on the side wall of the micro-channels pipes that allow the liquid refrigerant to penetrate through under the effect of the pressure difference between the

liquid on the condensation pipe and the vapour within the micro-channel pipes, can effectively distribute the liquid throughout the evaporation section wall, by using the gravity of the refrigerant, thus preventing the ‘dry-out’ problem inhibited with the conventional LHPs and significantly increasing the heat transport capacity of the LHP.

The combination of these specific components concepts is expected to produce a novel low carbon (nearly to zero) space heating, hot water supply and power generation system applying solar PV/T technology.

However, in this research, owing to the limited time and project budget, the proposed system would be designed for hot water supply with water tank and power generation, while in the near future study, the other function would be investigated.

### **1.4 Research methodology**

This research aims to take advantages of LHP, micro-channels, PCM integrated into PV/T to overcome the current barriers remaining with the existing PV/T modules, i.e., high cost, low efficiency, short life span, and non-fit to buildings, and therefore develop a novel, high efficiency, low cost, and building integrate-able PV/T system that can make effective use of solar energy for space heating, hot water and power supply. This research work is expected to gain a superior performance of the system relative to existing PV/Ts, represented by 30% higher overall solar efficiency and 10% cost saving. To achieve this ambitious goal, the research sets out a number of specific objectives as addressed in 1.2, the methodologies related to objectives are briefly described as below:

**Approach to objective 1: Studying the existing PV/T and heat pipe technologies to identify the current existing challenges and giving relevant suggestions about the potential solutions**

This approach will contribute to (1) an extensive literature review on energy consumption distribution and renewable energy application and technologies relevant to solar energy and solar PV/T technologies; (2) reviewing on the research and development (R&D) and the application of the existing PV/T and relevant LHP, PCM technologies; (3) identifying the typical features and critical highlights and barriers of the existing PV/T technologies; (4) providing potential solutions for tackling the current related challenges.

### **Approach to objective 2: Establishing a conceptual design of a novel PV/T system combined with micro-channel loop heat pipe technology**

This approach will (1) develop a conceptual design for the PV/MCLHP system; (2) complete the sketch drawings of the proposed system components and generate the plan of the integrated unit. A list of components will be proposed, each of which will be preliminarily evaluated in terms of its likely geometrical sizes and material types, as well as the potential performance data likely to be achieved. Furthermore, the research questions relating to fluid evaporation & condensation, heat & mass transfer and solar-to-power conversion (e.g. flow pattern, liquid-vapour distribution, boiling and condensation mechanism, flow resistance, heat transfer criteria, simulation method, macroscopic heat transfer, solar electrical efficiency, solar thermal efficiency, environmental parameters etc.) will be identified and these will form the foundation for the follow-on approaches.

### **Approach to objective 3: Theoretical analysis and computation models development for the proposed PV/T system**

This approach will (1) carry out theoretical analysis of the PV/T system using the fundamental mathematical theory and associated equations, addressing the heat and mass transfer occurring at the PV/T system; (2) develop a series of computation models to

simulate the performance of the system and optimise the system configurations, addressing the PV/micro-channel panel, loop heat pipe, heat storage/exchanger, and internet-based intelligent monitoring & control.

### **Approach to objective 4: Construction of a prototype micro-channel loop heat pipe PV/T (MC-LHP-PV/T) system**

This approach will (1) design a prototype PV/micro-channel loop heat pipe (PV/MC-LHP) system based on the simulation results; (2) construct and test this system in an indoor (laboratory-controlled) space, where the relatively steady state operational conditions can be maintained; and (3) test the prototype system at real climate condition to evaluate its real life performance.

### **Approach to objective 5: Economical & environmental performance**

This approach will (1) briefly develop a computation model based on the experimentation and simulation results to predict the annual operational performance of the proposed novel PV/T system; and (2) analysis the system life cycle, carbon dioxide emission saving, power and heat output to evaluate the relevant socio-economic and environmental impacts.

## **1.5 Novelty and added value**

The proposed research has the following innovative aspects:

- ❖ **Concept:** First kind of effort in developing a unique loop heat pipe and integrating it with PV panels to achieve enhanced heat and power harvest from the solar radiation and making it building-integrate-able;
- ❖ **System structure:** (1) Applying microchannel loop heat pipe as the solar thermal absorber and carrier; (2) Combination of a micro-channel LHP evaporator with

the PV module using a special lamination approach; (3) co-axial triple-pipe heat exchanger as the condenser using phase change materials to store excess heat and release it as needed; (4) upper liquid header creating the continuous liquid film on the inner wall of the LHP evaporator which prevents the liquid ‘dry-out’ phenomena occurring; (5) liquid/vapour separator assembled on the liquid header making clear separation of the vapour and liquid which prevents the entrainment effect of the LHP and enhances the heat transfer capacity of the LHP; and (6) a heat storage/exchanger, using phase change material, had the reduced size and increased heat transfer efficiency;

- ❖ **Methodology:** (1) By treating the wick of the micro-channel evaporator of the MCLHP as a thin porous layer, first time to bring the fractal theory into the heat and mass transfer analysis of the heat pipe wicks from micro to macro scales; (2) Combination of the analytical model and numerical model of the PV/T system to enable optimal design of the PV/T system and its performance prediction; (3) Both the steady state and dynamic performance tests of the PV/T system were carried out to validate and refine the computer models and investigate its operational performance; and (4) social economic performance model is integrated into the technical performance model to develop a full range of performance assessment of the novel PV/T system.
- ❖ **Fabrication:** Use of the aluminium welding and thermal assisted pressing technologies to binding the micro-channel LHP panel into PV module.

### 1.6 Thesis Structure

**Chapter 1 – Introduction:** This chapter gives a brief introduction of the research background, objectives, significance, research concept, methodology and innovations related to the novel PV/T research.

**Chapter 2 – Literature review:** This chapter provides an extensive literature review on worldwide energy consumption, renewable energy application, and solar PV/T, LHP, PCM technologies, identify the typical features and critical barriers of the existing PV/T technologies, and thus develop the potential solutions for tackling these identified challenges.

**Chapter 3 – Conceptual design:** This chapter presents the conceptual design of the proposed PV/T system and shows its basic working principle. In the meantime, this chapter also provides the drawings and characteristic data of the individual system components.

**Chapter 4 – Theoretical analysis and computer modelling:** This chapter develops a series of computation models for the MCLHP components and the system by applying fractal theory, energy balance method, and associated heat and mass transfer equations. Through the simulation, appropriate MCLHP design/operational parameters are recommended, and the optimum geometry/capacity of the relevant system components is determined. These results will then be applied to the prototype design, construction and experiment testing.

**Chapter 5 – Prototype design, construction, and lab-testing:** This chapter presents the specific procedure of the PV/T system prototype design, fabrication and experimentation. A series of experimental tests under the controlled laboratory condition and real weather condition were carried out to evaluate the performance of the novel PV/T system, and then for.

**Chapter 6 – Energy saving, economic, environmental analysis:** This chapter (1) develops a computation model based on the experimentation and simulation results to predict the annual operational performance of the proposed novel PV/T system; (2) analyses the system life cycle, carbon dioxide emission saving, power and heat output to evaluate the relevant socio-economic and environmental impacts.

**Chapter 7 – Conclusion and further works:** this chapter concludes the main observations of this research and addressed the further opportunities and challenges

## CHAPTER 2: LITERATURE REVIEW

### 2.1 Chapter introduction

This chapter aims to provide a literature review on research and engineering application of the PV/T based heat and power system, as well as associated system components including LHP, PCM heat exchanger, and PV/T combination. These are detailed as below:

- ❖ Introduce the concept of PV/T technologies and performance indicators
- ❖ Present the concept of HP/LHP and MC technologies applicable to solar PV/T systems
- ❖ Review on heat exchangers and PCM that can be integrated into PV/T systems
- ❖ Introduce the fractal theory and its application in simulation of porous media heat and mass transfer
- ❖ Present a comprehensive literature review on the research, development, combination and practical applications of PV/T integrated with LHP technologies and the relevant theories
- ❖ Clarify the main characterizations, current research and development status, research highlights and potential breakthroughs of various PV/T technologies.
- ❖ Instruct the existing barriers, challenges and opportunities for further research and development of PV/T technology.

Overall, this chapter will provide a relatively comprehensive background and foundation for the research that is dedicated to (1) indicate the technical barriers and challenges existing in current PV/T and LHP technologies; (2) develop scientific approaches for PV/T and LHP studies; (3) build up the research plan for this study; and (5) consequently clarify the direction for the research works.

## **2.2 Basic concept and relevant theory of PV/T and LHP technologies**

### **2.2.1 Concept and primary theory of PV/T**

Solar photovoltaic energy conversion is well known as a conversion process generating electrical energy from light energy. The solar cell is a basic module of solar photovoltaics. In 1839, Edmund Bequerel firstly reported the photovoltaic (PV) effect when he observed an electric current produced by the action of light on a silver coated platinum electrode immersed in electrolyte[19]. After more than 100 years research and development in photovoltaic effect from selenium to crystalline silicon, it was until 1954, the first silicon solar cell converting sunlight with an efficiency of 6% was introduced by Chapin, et.al.[20]. However short solar cell histories are reported elsewhere [21] [22] then, until 1990s, a range of interest in photovoltaics were explored and expanded, as with the growing interest in alternative electrical energy source instead of only relying on fossil fuels. In recent decades, with the development of economic and renewable energy demand and application, photovoltaic (PV) technology has made significantly progress in both scientific studies and practical applications, and it is still on the putting foot forward for lower cost and higher conversion efficiency [23].

The conversion efficiency from light energy to electricity, called solar electrical efficiency, is a key indicator for evaluating the performance of solar PV panels. The solar electrical efficiency is well known that it mainly relies on the cells' material and temperature, which is measured under the standard test conditions (STC) [24][25] (i.e. Solar irradiance at 1,000 W/m<sup>2</sup>, temperature of the solar cell itself at 25 °C, mass of the air at 1.5 spectrum) and is usually in a range 4% to 20% [15] [16]. It is found that PV panels normally have a linear drop-off in efficiency as the surface temperature rises,

which typically lose efficiency of up to 0.4% per degree centigrade rise in the PV-cells' temperature [26][27]. The Photovoltaic/Thermal (PV/T) technology was therefore brought forward to cool down the PV cells to maintain/improve the electrical efficiency of the PV, to keep its expected life span, and thus to make full use of solar light energy striking on the surface of PV as well as making advanced utilisation of the absorbed superfluous heat simultaneously.

A solar PV/T system is a combination of photovoltaic and solar thermal components/systems, which represents a new breakthrough for the solar energy applied in heating and power cogeneration. *Fig.2-1* and *Fig.2-2* gives the conventional structure schematic of a typical PV/T module which normally comprises several main layers filled with thermal silica gel and through lamination approaches. These include: (1) a flat-plate transparent glazing cover as the top layer to protect the PV cells from damaging and also to prevent the dust; (2) arrayed PV cells layer sandwiched with two adhesive Ethylene-vinyl acetate (EVA) layers and an electrical isolation Tedlar-polyester-Tedlar (TPT) layer, from which there may be (or not) an air gap to the glazing cover; (3) a layer of thermal absorbing plate is closely attached to the PV layer; (4) arrayed tubes layer working as the condenser to cool down the absorbing plate by circulating the coolant fluid in the tubes; (5) a layer of thermal insulation which, as shown in *Fig.2-3*, is normally comprised of glass wool made from glass fibres arranged applying a binder into a wool-like texture, thus characterizing with many small air pockets to present high thermal insulation properties to prevent heat loss. All these layers are grouped into a holding aluminium-alloy frame.

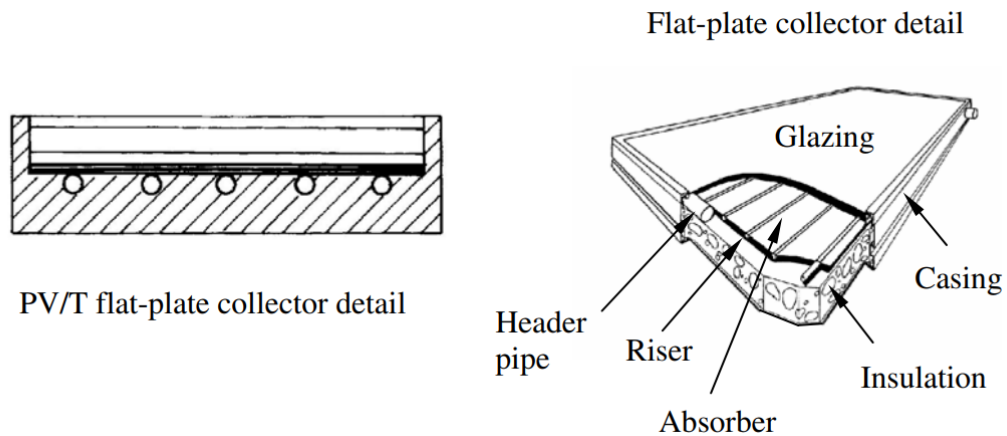


**Fig.2-1 Schematic of a typical PV/T module [28]**

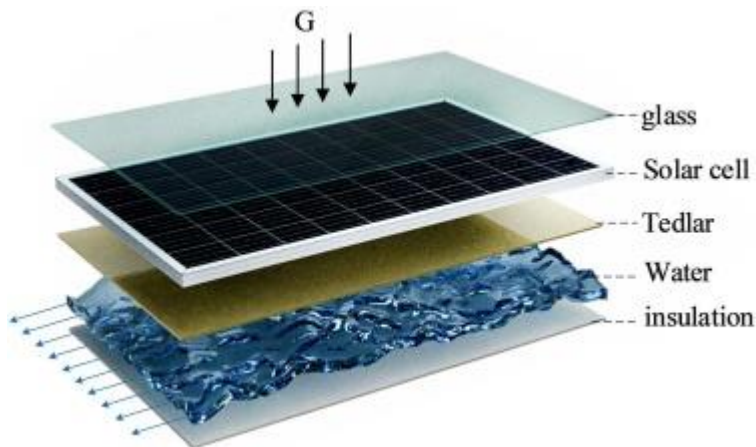


**Fig.2-2 Cross-section view of the Photovoltaic/Thermal system[29]**



**Fig.2-3 Sample of glass wool for thermal insulation**

With the growing attention in conceptual design of PV systems, investigation of PV/T module were carried out as early as in 1970s [30]. Kern and Russell [31] firstly reacted to the hybrid collector concept on different occasions with the application of either air or water

as the back flow coolant fluid and tested hybrid PV/T collectors in 1978, showing that the hybrid PV/T collectors can produce more useful energy per unit area than either individual type alone (single PV or single thermal collector). This creates the potential to develop a highly effective and low-cost heat and electricity co-generation system [26].

PV/T module as known as hybrid solar-energy collector converts striking solar radiation into a balance of low-grade heat and direct-current electricity at the same time. As presented in **Fig.2-4**, ideally, the solar energy absorbed by the hybrid PV/T module ( $Q_{abs}$ ) can be divided and converted into four parts, which are (1) the useful energy collected by the panel ( $Q_U$ ); (2) the lost energy in the form of heat to the surroundings ( $Q_L$ ); (3) the converted electrical energy ( $Q_E$ ), and (4) the energy absorbed and stored by the absorber  $Q_{so}$ , whose relationships can be described as following equations [32]:

$$Q_{abs} = Q_U + Q_E + Q_L + Q_{so} \quad (2-1)$$

$$Q_{abs} = A_{cl}G(\gamma_\lambda) \quad (2-2)$$

$$Q_E = A_{cl}G\eta_e \quad (2-3)$$

$$Q_U = A_{cl}G\eta_t \quad (2-4)$$

$$Q_L = A_{cl}G(T_{pv} - T_{am}) \quad (2-5)$$

$$Q_{so} = C_p M_{cl} \frac{dT}{d\tau} \quad (2-6)$$

Where,  $A_{cl}$  is the collecting area of the PV/T panel (m<sup>2</sup>);  $G$  is the solar irradiation (W/m<sup>2</sup>);  $(\gamma_\lambda)$  is the transmittance – absorption coefficient of the glazing cover;  $\eta_e$  is the solar electrical efficiency;  $\eta_t$  is the solar thermal efficiency;  $T_{pv}$  is the temperature of the PV cell layer (K);  $T_{am}$  is the ambient air temperature (K);  $C_p$  is the specific heat capacity of the absorber (kJ/kg·K);  $M_{cl}$  is the absorber quality (kg),  $\tau$  is the time.

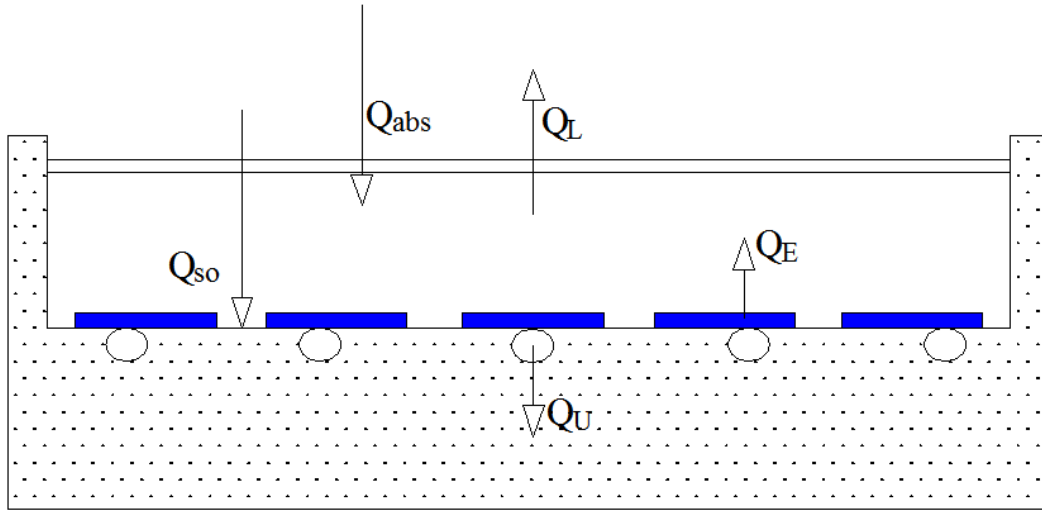


**Fig.2-4 Solar energy distribution diagram of PV/T panel**

Therefore, the overall solar efficiency of the hybrid PV/T collector is the sum of the above solar thermal efficiency and the electrical efficiency, which can be presented as:

$$\eta_o = \eta_t + \eta_e \quad (2-7)$$

Where,  $\eta_o$  is the overall solar efficiency of the hybrid PV/T module.

(1) The electricity energy

The electricity energy known as the output power of the hybrid PV/T module can be expressed as:

$$Q_E = P_{PVT} = U_{PVT} I_{PVT} \quad (2-8)$$

Where;  $U_{PVT}$  is the output voltage of the PV/T panel and  $I_{PVT}$  is the current of the PV/T panel.

(2) Solar thermal efficiency

The solar thermal efficiency ( $\eta_t$ ), which is defined as the ratio of the useful system thermal energy gain to the overall incident solar irradiation, can be expressed as:

$$\eta_t = \frac{Q_u}{G \cdot A_c} = \frac{c_{pw} m_w (T_{wout} - T_{win})}{G \cdot A_c} \quad (2-9)$$

Where,  $A_c$  is the collector area of base panel.  $c_{pw}$  is the specific heat at constant pressure of working fluid (e.g. water, 4186W/kg/°C),  $m_w$  is the mass flow rate of working fluid flow in the back channel of the panel ( $m^3/s$ ),  $T_{wout}$  and  $T_{win}$  is the outlet and inlet coolant working fluid temperature.

(3) Solar electrical efficiency

The electrical efficiency of the PV/MCLHP panel is the ratio of the electrical power output of the panel to the solar radiation striking on it, as given by:

$$\eta_e = \frac{P_{PVT}}{G \cdot A_{PV}} = \frac{U_{PVT} I_{PVT}}{G \cdot A_{PV}} \quad (2-10)$$

Where  $\eta_e$  is the electrical efficiency of PV/T panel,  $P_{PVT}$  is the output power of PV/T panel,  $U_{PVT}$  is the output voltage of PV/T panel,  $I_{PVT}$  is the current of the PV/T panel, and  $G$  is the solar radiation,  $A_{PV}$  is the PV area of base panel.

$$\eta_e = \eta_{rc} [1 - \beta_{PV} (T_{PV} - T_{rc})] \quad (2-11)$$

Where,  $\eta_{rc}$  is the initial electrical efficiency at reference temperature (298.15K);  $\beta_{PV}$  is temperature coefficient;  $T_{PV}$  is PV cells temperature at operation;  $T_{rc}$  is reference temperature.

In a summary, as the Photovoltaic/Thermal (PV/T) technology enables the dual solar collecting functions in one module for generation of the both electricity and heat. The output power, solar electrical and thermal efficiencies, and overall solar efficiency, are key indicators applied to evaluation of the performance of a hybrid PV/T module. Such synergetic integration of the PV and thermal collector not only results in the improved PV efficiency, but also generates more energy per unit area compared to the standard-alone PV panels or solar collectors[33]. Additional characteristics of the PV/T technology lie in the potential saving in material use, reduction in installation cost and homogeneous

facade appearance. It is becoming an effective solution to yield more electricity and offset heating load freely in contemporary built environment.

### **2.2.2 Research achievement and findings in PV/T subject**

In recent years, solar energy are widely utilized in commercial, residential, and industrial applications such as power generation, hot water supply, daylighting, industrial processes, space heating and cooling [34]. At the same time, growing demand of thermal and electrical energy in developed and developing countries results in rapid development in solar heat and power generation technologies. Consequently, with the rapid development of the solar power technologies, solar systems are expected to provide 12% to 25% of global electricity by 2050 [11]. However, to date, a technical argument of traditional PV systems is the relative lower efficiency that is in the range 10 to 20% [13], and the PV panels normally have a linear efficiency drop-off as the surface temperature rises, which typically lose efficiency of up to 0.4% per degree centigrade rise in the PV-cells' temperature [26][35]. The PV/T technology was therefore brought forward to cool down the PV cells and make advanced utilisation of the absorbed superfluous heat simultaneously. Technologies for this purpose can be normally classified into different categories in terms of cooling medium, configuration, operation temperature level as well as function. From the cooling medium perspective, there are several types of PV/T, including air-based, water-based, refrigerant-based and heat pipe-based collectors.

#### *(a) Air-based PV/T*

The common way to cool the PV panels is by naturally/mechanically ventilated air [9,10]. As shown in **Fig.2-5**, the air-based PV/T technologies utilize a naturally/mechanically air channel to cool the PV layer, which can derive the air from above, below or double sides of the PV layer. A number of studies have been reported on air-based PV/T systems

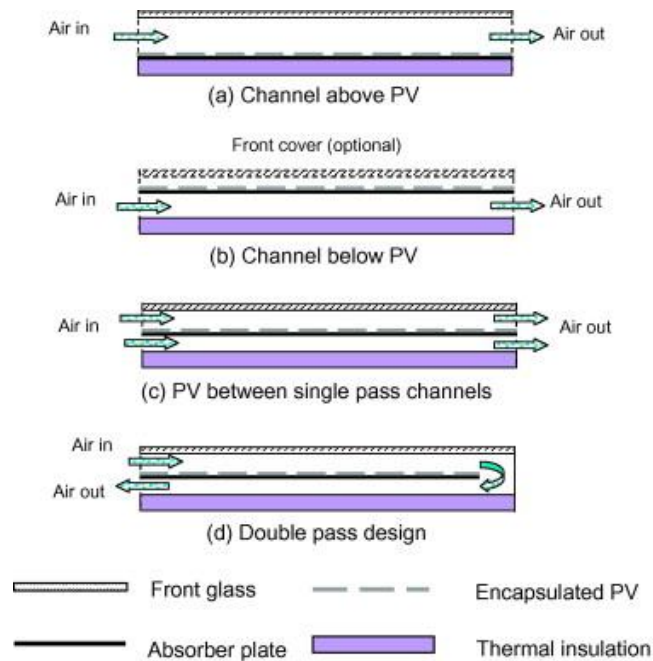


**Fig.2-5 Cross sections of typical air-based PV/T module designs[26]**

Garg et al.(1997)[36] developed a simulation model to analyse the performance of a conventional hybrid air-based PV/T heating collector in terms of single-glass and double-glass configurations and various operational parameters. They found that the selection of single-glass or double-glass is determined by the temperature range of the system, and increasing collector length, mass flow rate as well as PV cell density can improve the system efficiencies.

Aste et al. (2008) [37] presented the experimental and theoretical study of an air-based PV/T collector based on a R&D program led by the Politecnico di Milano. This led to development of a simulation model able to predict the solar thermal and electrical performance of an air-based PVT collector.

Sarhaddi[38] developed a numerical model to simulate and predict the thermal and electrical performance of a solar PV/T air collector, indicating that the solar thermal, electrical and overall efficiency of this PV/T air collector were 17.18%, 10.01% and 45% respectively.

Solanki et al.[39] developed an indoor standard testing procedure and a computation model based on energy balance equations to study the solar electrical and thermal performance of an air-based PV/T solar heater. The results showed that the solar electrical and thermal efficiencies of this air-based PVT module are 8.4% and 42% respectively.

Sukamongkol, et.al. [40] reported an experimental work aiming to validate the established simulation model for a PV/T air heating collector. It is found that the solar efficiencies of the air-based PV/T collector is quite lower compared to water-based ones, owing to the lower thermal mass of the air [41]

Fan et al. (2018) [42] designed a novel air-based PV/T with fins to optimize the utilization of thermal energy and gain more electrical energy. Several parameters in terms of geometry, construction materials and operation were studied, showing that the useful thermal efficiency vary from 48.8% to 56.9%.

Tonui [43] presented a modified air-based PV/T solar collector which makes use of the suspended thin flat metallic sheet at the middle or fins fitted into the backside convective duct to improve the heat transfer performance of the collector. They compared the modified system with the typical air based PV/T system in terms of the steady-state thermal efficiencies and found that the application of fins addressed an efficiency at 30% and the thin metallic sheet at 28% while the typical at 25%. This indicates that the suggested modification led to the increased thermal efficiency and better electrical performance compared to the normal one.

Fudholi et al. (2019)[44] presented a theoretical and experimental study of the exergy and sustainability index of an air-based PV/T system using a  $\nabla$ -corrugated absorber. The results showed that the sustainability index of the new air-based PV/T system, which is

in the range 1.147 to 1.68, normally decreased with the mass flow rate, while the exergy efficiency varied from 12.81% to 14.41%.

Barone et al. (2019a)[45] designed, constructed and tested an innovative low cost air-based PV/T prototype coupled with a heat pump for heating with different operation parameters (including air flow rate, tilt angle and weather conditions), as well as developed a dynamic simulation model to evaluated its energy performance and economic feasibility. The results showed that the solar electrical efficiency decreases with the increasing PV temperature, which is featured by the equation of  $\eta_{el} = -0.0005 \cdot T_{PV} + 0.1765$  ( $R^2 = 0.92$ ) as shown in **Fig.2-6**. The power generation rate of the system was in the ranges 11.0 to 19.8 MWh/year.

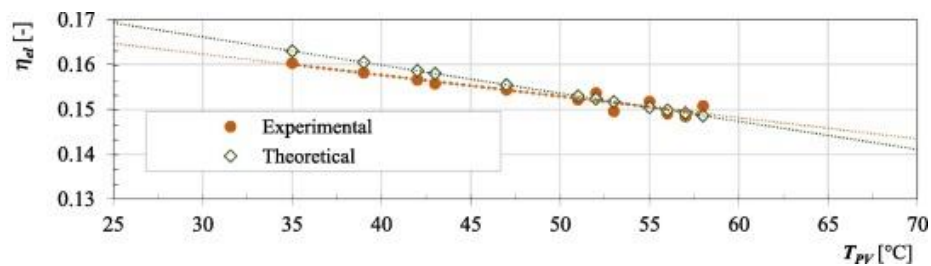


**Fig.2-6 A function of the electrical efficiency and the PV temperature**

It is found that the solar efficiencies of the air-based PV/T collector is lower compared to water-based ones, owing to the lower thermal mass of the air.

*(b) Water-based PV/T*

The structure of a water-based PV/T collector, as shown in **Fig.2-7**, is similar to a traditional flat-plate PV/T module. Water is forced to flow through the tube or channel to cool the PV plate. Due to the higher thermal properties of water compared to air, using water as working fluid to cool the PV plate is more efficient[46].

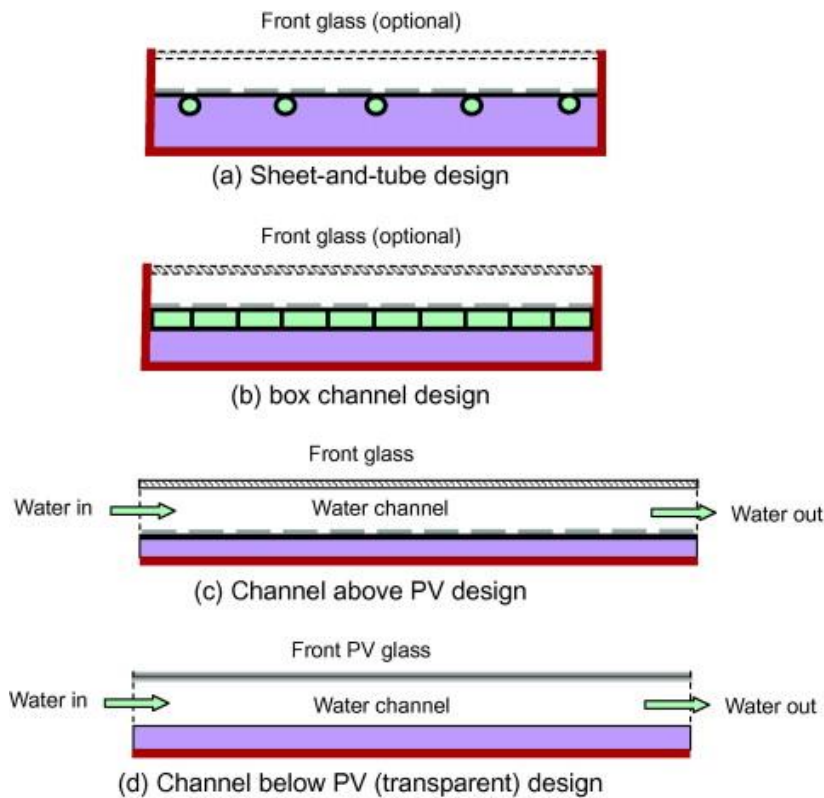


**Fig.2-7 Cross sections of typical water-based PV/T module designs[26]**

Hung et al. (2001) [47] investigated the performance of an integrated solar water-based PVT system, and compared it with traditional solar water heater. It was found that the primary-energy saving efficiency of this system exceeds 0.60; the thermal efficiency decreases with the rising hot water temperature; and the maximum solar thermal and electrical efficiencies of this water-based PVT module achieved 44.5% and 9.1% respectively.

Fraisse [48] investigated the energy performance of the water-based PV/T collectors based on a dedicated numerical simulation model, showing that the inlet fluid temperature plays an important role in cooling the PV plate.

Alternatively, PV panels could be cooled by using the circulating water across the back-side coils [49]. Herrando [50] developed an analytical model to predict the performance of the hybrid PVT systems which are designed to generate hot water and electrical power.

Yazdanpanahi et al. (2015)[51] carried out a numerical and experimental study of exergy efficiency of a water-based PV/T collector in terms of different parameters including the wind velocity, solar radiation, open circuit voltage, solar short circuit current, maximum power point voltage and maximum power point current, ambient temperature, fluid inlet and outlet temperature. The both numerical and experimental results show a good agreement.

Aste et al. (2015)[52] designed an innovative glazed water-based PV/T collector and developed a mathematical simulation model for evaluating its solar efficiencies. The investigation indicated that the daily mean solar electrical efficiency of this water-based PV/T is 6.0% while the PV module has a daily average solar electrical efficiency of 6.2%. The daily average solar thermal efficiency of this PV/T collector was 25.8%.

Senthilraja et al. (2020)[53] assessed and compared the performance of air and water based PV/T collector for hydrogen production application. Experimental testing was undertaken in which a PVM was considered as a reference in comparing the two systems. At noon and for 0.011 kg/s mass flow rate, the electrical and thermal efficiencies were 8% and 31.1% for air based PVT collector and 8.5% and 33.8% for water based PVT collector respectively.

Compared to the air-based PV/Ts, the water-based one has a very limited improvement in solar efficiency [54] and also faces the challenges of fluid freezing under the cold climatic condition [55]. The heat pipe was applied to cool the PV panel by exchanging the absorbed heat to the coolant fluid in heat-pipe condenser [56].

### *(c) Heat pipe based PV/T*

A heat pipe (HP), as illustrated in **Fig.2-8**, comprises three sections including an evaporator section, an adiabatic section, and a condenser section, which can effectively

conducting heat through phase change. Typically, the evaporator is attached to the heat source to absorb heat as the working fluid evaporating in this section, and the condenser is attached to the heat sink to release heat as the working fluid condensing in this section. The adiabatic section is insulated. In the operation cycle, as working fluid (liquid) absorbs heat and is vaporized in the evaporator, the vapour pressure rises up and forces working fluid (vapour) to flow axially along the centre core to the condenser; Vapour condenses in the condenser to liquid and then flow back along the inside wall to the evaporator driven by the capillary force. Owing to involving the phase change latent heat transfer during the operation, HP has a heat transfer coefficient that is several orders of magnitude larger than that of the currently available thermal conductors. This kind of heat transfer device can be effectively used in PV cooling with a much smaller heat transfer area. Thus the heat pipe based PV/T has recently been utilized and studied.

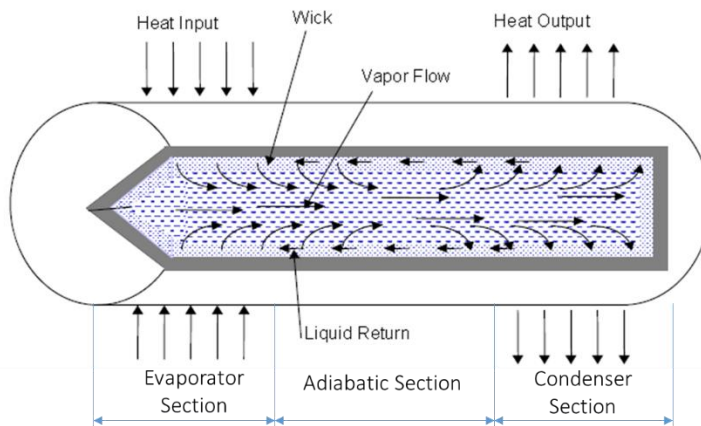


**Fig.2-8 Schematic of a conventional heat pipe**

In 2011, Pei et al. [57] have firstly introduced a novel heat-pipe based PV/T system as shown in **Fig.2-9** which can be applied in cold regions without being frozen. They investigated the performance of this system on both experimentation and simulation stage, finding that the daily solar thermal and electrical efficiencies were 41.9% and 9.4%, respectively. Wu et al.[58] theoretically investigated a wick heat pipe based PV/T system,

finding that the solar thermal and electrical of the heat pipe based PV/T hybrid system corresponding to 63.65% and 8.45% respectively can be achieved under certain operating conditions. Pei et al.[59] also proposed a simulation model to predict and analyse the annual solar thermal and electrical performance of this HP-PV/T system when applied in Hongkong, Lhasa, and Beijing which are three typical climate regions of China.

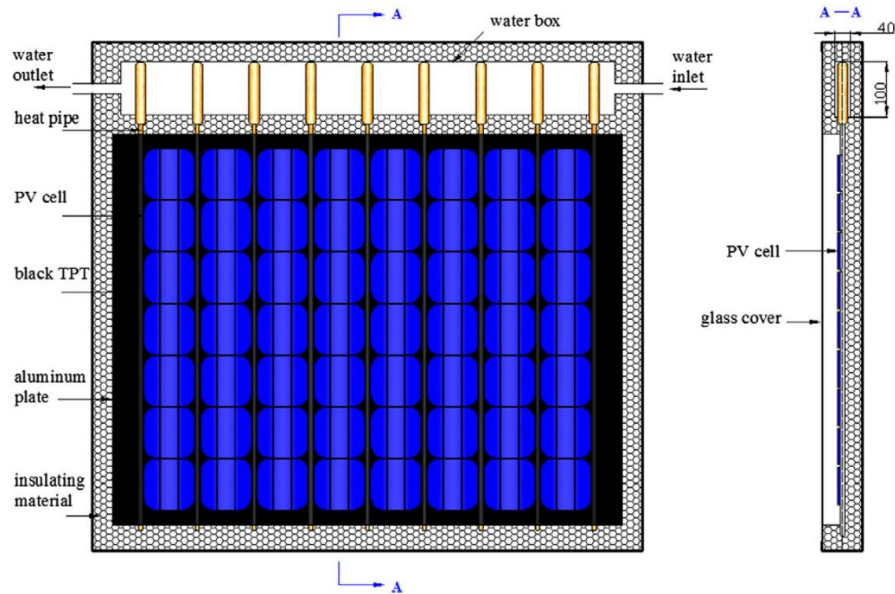


**Fig.2-9 The Heat pipe based PV/T solar collector**

Pei et al. [60] developed a dynamic model of a novel heat pipe PV/T system, which was also validated by experimentation, to study the performance of the system under different parametric conditions including flow rates, PV cell covering factor of the collector, tube space of heat pipes, and kinds of solar absorptive coating of the absorber plate. They found that reducing the tube space of heat pipes can improve the solar thermal and electrical efficiencies of the HP-PV/T system. But this reduction would cause high costs with increasing number of heat pipes of each solar collector.

However, heat transport distance of the traditional heat pipe is very short and thus is unsuitable for real site application[61]. In recent years, micro-channels or micro-channel heat pipes(MCHPs) [62] and loop heat pipes [63][64] were integrated into PV/T systems

to cool the PV modules. MCHPs are highly efficient heat transfer devices that rely on the phase transition of the working fluid to transport heat with the advantages of good heat transfer capacity, excellent thermal respond speed, low-pressure difference, isothermal ability, and compact structure[65]. In particular, the micro-channel tubes could be well applied to the PV integrated evaporator. Owing to the flat surfacing structure, the micro-channel tubes could be perfectly combined with PV modules, thus removing the difficulties remaining with the fin-tubing structure, and leading to the increase in heat transfer rate by 30% [66]. Zhou et al. [66] first-time proposed the concept of a PV/micro-channels-evaporator module. And they assessed the performance of this innovation, by designing, construction and testing of a PV/micro-channels-evaporator-modules-based heat pump heating system under real-time operational condition, finding that the average thermal, electrical and overall efficiency can be achieved to 56.6%, 15.4% and 69.7% respectively at specified operational conditions.

### **2.2.3 LHP and PV/LHP technologies**

Loop heat pipes (LHPs) are efficient two-phase heat transfer equipment which can transfer heat over a relative long distance with a small temperature gradient using the characteristic of the latent heat of vaporisation. The LHP, as shown in **Fig.2-10**, typically consists of an evaporator and a condenser like the conventional heat pipes, but differs in having separate liquid and vapour transportation lines and also compensation chamber for the traditional LHPs[64][67]. In the evaporator, the working fluid absorbs the heat and is vaporized. This amount of vapour is transported to the condenser in which the vapour is condensed into a liquid of the same temperature and returned to the evaporator through the liquid line for replenishment[63] [64].

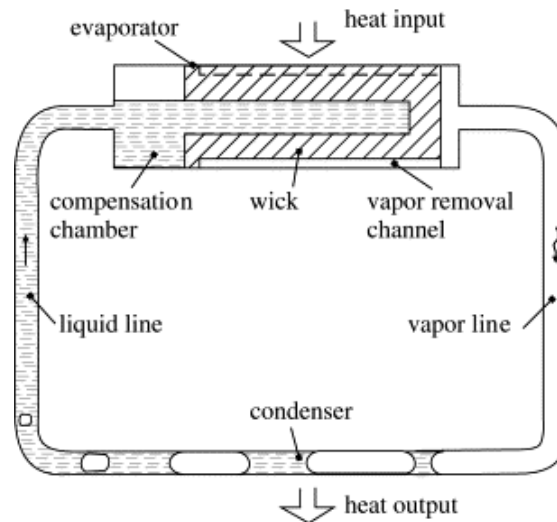


**Fig.2-10 Schematic of the traditional LHP[68]**

The distinct feature of a LHP over a conventional straight heat-pipe (HP) is the separated vapour and liquid transportation lines which can minimize the entrainment between vapour and liquid flows and thus reduce the pressure loss across the flow path[69][70]. Such a particular heat pipe configuration makes it possible to transport a larger heat flux through a long distance.

In general, closed loop heat pipes have the advantage to drive passively with natural circulation of the working fluid changing within liquid and vapour phases without any additional energy input. For this regular phase changing cycle, i.e. evaporation and condensation, of refrigerant, the operation is sensitive to the working fluid category and fill volume[71], as well as the system performance is directly relative to parametrical configuration. Several parameters including filling ratio, working fluid, inclination angle, structure parameter and etc., have important impact to the thermal performance of a LHP[72]. Considerable studies have been undertaken to improve their thermal performance by applying different approaches such as using nano-fluids [73] and changes in structure[74]. This part will focus on the review of working fluids and filling ratios.

***(1) The working fluids***

## CHAPTER 2: LITERATURE REVIEW

As with decades development and research of heat pipes, the working fluids application have been developed ranging from cryogenic liquids to liquid metals[75].

The selection of working fluids for LHPs based on the same criteria as for conventional heat pipes[68]. The first factor that should be considered is the operation vapour temperature range of the fluid, which is shown in **Table 2-1**. Secondly, a series of properties must be valued as the main requirements. These include (1) Compatibility with the wall and wick materials[18]; (2) Good thermal stability; (3) Wettability of the wall and wick materials; (4) Appropriate vapour pressures at the operational temperatures; (5) High latent heat; (6) High thermal conductivity; (7) Low liquid and vapour viscosities; (8) High surface tension; and (9) Acceptable freezing or pour point.

**Table 2-1: Heat pipe working fluids[76]**

Medium	Melting Point(°C)	Boiling Point at Atmospheric Pressure(°C)	Useful Range(°C)
Helium	-271	-261	-271 to -269
Nitrogen	-210	-196	-203 to -160
Ammonia	-78	-33	-60 to 100
Pentane	-130	28	-20 to 120
Acetone	-95	57	0 to 120
Methanol	-98	64	10 to 130
Flutec PP2 <sup>1</sup>	-50	76	10 to 160
Ethanol	-112	78	0 to 130
Heptane	-90	98	0 to 150
Water	0	100	30 to 200
Toluene	-95	110	50 to 200
Flutec PP9 <sup>1</sup>	-70	160	0 to 225
Thermex <sup>2</sup>	12	257	150 to 350
Mercury	-39	361	250 to 650
Caesium	29	670	450 to 900
Potassium	62	774	500 to 1000
Sodium	98	892	600 to 1200
Lithium	179	1340	1000 to 1800
Silver	960	2212	1800 to 2300

Note: The useful operating temperature range is indicative only. Full properties of most of the above are given in ref. [77] Appendix 1.

<sup>1</sup>Included for cases where electrical insulation is a requirement.

<sup>2</sup>Also known as Dowtherm A, a eutectic mixture of diphenyl ether and diphenyl.

In that case, however, to ensure the device start-up at a minimum temperature difference between the evaporation zone and the compensation chamber, the value of  $dP/dT$  should be taken into account. With allowance made for it, the most efficient working fluid for LHPs in the temperature range from  $-20\text{ }^{\circ}\text{C}$  to  $+80\text{ }^{\circ}\text{C}$  is ammonia. The advantages of water manifest themselves at higher temperatures and reach the maximum at  $100\text{--}150\text{ }^{\circ}\text{C}$ . When the working fluid is water, one should bear in mind that freezing is impermissible because of the risk of disturbing the device tightness. Neon, oxygen, nitrogen, ethane, propane, propylene, freon 152A, freon 11, n-pentane, acetone and toluene were also successfully used as working fluids for LHPs [68].

The working fluid selection should also take into account the heat transfer limitations including sonic, capillary viscous, entrainment and boiling limit occurring within the LHPs. According to D. Reay [78], the convenient criteria to choose an acceptable working fluid in most of the cases is to compare the figure of merit number (M) which is defined as a function of surface tension  $\sigma_l$ , latent heat L, liquid density  $\rho_l$  and viscosity  $\mu_l$  as :

$$M = \frac{\sigma_l L \rho_l}{\mu_l} \quad (2-12)$$

A larger M value leads to a higher heat transfer capacity. However, a large merit number is not the only criteria in selecting a working fluid. Instead, the cost, availability and other factors are also the important criteria in determination of a work fluid.

## **(2) Filling ratio**

Normally, a closed loop heat pipes have the advantage to drive passively with natural circulation of the working fluid changing within liquid and vapour phases without any additional energy input. For this regular phase changing cycle, i.e. evaporation and condensation, of refrigerant, the operation is sensitive to the working fluid fill volume[79],

thus the thermal performance of a LHP system can be highly affected by the refrigerant filling ratio (defined as the ratio between the working fluid volume and the evaporator volume, FR). Lower FR results in dry-out phenomenon of the evaporation part, while too high FR leads to excess working fluid resulting in the whole evaporator full of liquid when bubbles easily form due to boiling[80]. The recommended (experience) filling ratio of a heat pipe system should be at least 50% of the volume of the evaporator[80]. **Table 2-2** presents the comparison among different LHPs in terms of the working fluid and filling ratio.

**Table 2-2 Comparison of different LHPs in terms of FR and parameters**

References	Material/working fluid	Filling ratio
Ling et al. [81]	/R22	88%-101%
Babu et al. [82]	copper tube/ acetone	60%
Molan et al. [83]	stainless steel/helium	48.8%- 66.1%
Ding et al. [84]	copper tube/ R134a	71%
Ling et al. [85]	copper/Deionized water	30%
Chang et al. [86]	R22	68-100%
Li et al. [87]	refrigerant	30-40%
Samba et al. [88]	n-pentane	9.20%
Zhang et al. [89]	copper/water and glycol (95%/5%)	0.1kg
He et al. [17]	R134a	35%

Ling et al. [81] experimentally studied the impact of filling ratio on a closed loop heat pipe system with separate evaporator and condenser consisting of micro-channels which was defined as micro-channel separate heat pipe (MCSHP) as a cooling device for telecommunication stations (TSs), showing that the optimal filling ratio was in the range of 88%-101%. Babu et al. [82] studied the thermal performance of a pulsating heat pipe

with CFD simulation and experiment under different filling ratios at the range 50% to 90% of its volume, showing that the FR of 60% conducted a smaller thermal resistance. Molan et al. [83] experimentally investigated the effect of the filling ratio on the thermal performance of a multi-turn Pulsating Heat Pipe (PHP), indicating that the optimal filling ratio may be in the range of 48.8%- 66.1% and related to the heat input level. Ding et al.[84] mainly studied the filling ratio and Feron types as influence factors of the LHP system used in data centre cooling, which was defined as separate heat pipe system in their study, analysing the relationship, varying from Feron types, between heat transfer capacity and filling ratio. Ling et al. [85] first time applied smooth and rough porous copper fiber sintered sheets into a LHP system. They tested the capillary pumping performance and investigated the influence of filling ratio, highlighting that a filling ratio at 30% of the deionized water is the optimal combination for their designed LHP. Chang et al. [86] established a CFD model to simulate the evaporator of a MCSHP . The simulation results showed that the optimal refrigerant filling ratio was in the range 68% to 100%, which were validated by relevant experiment results. Hong Li et al. [87] experimentally investigated the thermal and electrical performance of a solar photovoltaic/loop-heat-pipe water heating system with different refrigerant FRs in similar ambient environment, showing that FR at 30% was conducive to improve solar thermal and overall energy efficiencies of this system and FR at 40% was conducive to improve electrical efficiency and overall exergy efficiency of this system. Samba et al. [88] experimentally found the optimal filling ratio (defined as the ratio between the working fluid volume and the thermosyphon loop volume) is about 9.2%, which corresponds to the minimum operating temperature and also the minimum of system thermal resistance. Liu et al. [90] carried out the theoretical and experimental study of a loop separated heat pipe with the working fluid filling ratio, but not give the optimal FR value. Zhang et al. [89] simulated the impact of liquid filling mass on the heat transfer limits of a novel solar

photovoltaic/ loop-heat-pipe (PV/LHP) heat pump system, indicating that the minimum liquid filling mass should be more than 0.01 kg for the screen-mesh wicked LHP system. He et al.[17] theoretically and experimentally analysed the operational performance of a novel heat pump assisted solar façade loop-heat-pipe (LHP) water heating system, which is charged with R600a as working fluid at the FR of 35%. However the effect of the filling ratio on the operational performance was not investigated for the system. Zhang et al. [91] [61] carried out the theoretical and experimental investigation of the performance of a novel solar photovoltaic/ loop-heat-pipe (PV/LHP) heat pump system. However they didn't address the impact of filling ratio on this PV/LHP system, instead, gave a figure of liquid filling level which is 75ml. Zhou et al [92] presented a miniature loop heat pipe (mLHP) employing a 1.2 mm thick flat evaporator with deionized water as the working fluid. The filling ratio of 37% was selected owing to consideration the start-up characteristics.

From a systematic literature review, we conclude that (1) the most LHPs are constructed with round tubes which are attached with flat-plate fins (RTPF), while the researches on micro-channel LHP (MC-LHP) were less reported. Owing to the distinguished advantages of the MC-LHP relative to RTPF-LHP, i.e. increased heat transfer coefficient between the pipe wall and transporting fluid owing to the increased fluid speed, enhanced shear force and reduced boundary laminar flow film thickness. (2) The FR varies significantly with the structure of the LHP, as well as the type of the working fluid. Further, the FR is difficult to determine by using a pure theoretical method. Instead, it is determined by experiment. For a designated LHP system, it seems to be critically important to develop the correlation between the heat transport capacity and the FR using a dedicated experimental method, which is subsequently applied to assess the

performance of the system and determine its optimal operational condition, in particular, the most favourite FR value.

To date, the LHP [93] has been widely applied in thermal controls of satellites [94], spacecraft, electronics [95][96], and semi-conductor devices [97][98], while its utilization in solar thermal collecting and PV/T systems is limited. Recent researches carried out by the authors showed that the LHP could possibly be used in the solar thermal collecting and (or) PV/T devices [63][99]. This kind of new application led to a number of advantages, e.g., removing use of the water pump, enabling an effective heat transfer using the least pipe run, use of the anti-freezing medium within the loop, and hermetically sealed loop and homogeneous capillary force[99]. Meanwhile, the applicants also found that the conventional LHPs have two shortfalls that have impeded their wider application: (1) a complicated/high-cost wick structure, e.g., fine pores, is needed to enable generating a high capillary pressure to drive the work fluid across the loop [100]; (2) liquid film ‘dry-out’ phenomenon always occurs at the upper part of the evaporator [17] that would cause the significantly reduced heat transport capacity [18].

To overcome the above addressed difficulties, the author recently developed a novel liquid upper-feeding LHP with a dedicated vapour-liquid separator [61][99]. This kind of new LHP structure can simplify the wick structure, eliminate the ‘dry-out’ phenomenon, and thus create a high-efficient and cost-effective heat transport solution to solar thermal collecting and PV/T systems. The liquid-vapour separator is fitted above the evaporator and structured as the combination of the T-junction and an expander [101]. This structure, by controlling the liquid reserve level in the T-junction tube, can create a uniformly distributed downward liquid flow stream across the inner surface of the LHP evaporator while it is continuously evaporating from the surface, thus keeping the inner surface constantly wet, and separating the generated vapour clearly from the downward liquid

films [61]. It is found that the heat transport capacity of the new LHP was 6.75 and 1.55 times that of the existing straight HP and LHP [101][102].

## 2.3 PCM and its applications

Thermal Energy Storage (TES) is the temporary storage of high or low temperature energy for later use, which bridges the time gap between energy requirement and energy use. For HVAC and refrigeration application, water and water ice [103] constitute the principal storage media. Water has the advantage of universal availability, low cost and high latent heat capacity, but it can only be produced using inefficient low temperature refrigeration units if one wishes to use the latent heat capacity. If it is applied purely for sensible energy storage capacity it requires large storage tanks. Phase Change Materials (PCM) between +4°C and +90°C range overcomes the disadvantages of water by combining the latent and sensible energy storage capacities into a single storage unit and therefore offer designers new horizons and practical application options [104].

In simple terms, Phase Change Materials (PCMs)[105] can be described as mixtures of chemicals having freezing and melting points above or below the water freezing temperature of 0°C. They are ideal products for thermal management solutions as they store and release thermal energy during the process of melting & freezing (changing from one phase to another). To be a useful PCM, a material has to meet several criteria[106]:

- ❖ Release and absorb large amounts of energy when freezing and melting.
- ❖ Have a fixed and clearly determined phase change temperature (freeze/melt point).
- ❖ Avoid excessive super cooling and remain stable and unchanged over many freeze/melt cycles.
- ❖ Non-hazardous.
- ❖ Economic.

PCMs can broadly be classified into five categories [107]: eutectics, salt hydrates, organic, solid-solid and molten salt materials, which are detailed below.

- ❖ **Eutectics** tend to be solutions of salts dissolved in water that have a phase change temperature **below 0°C (32°F)**.
- ❖ **Salt hydrates** are specific salts that are able to incorporate water of crystallisation during their freezing process and tend to change phase **above 0°C (32°F)**.
- ❖ **Organic materials** used as PCMs tend to be polymers with long chain molecules composed primarily of carbon and hydrogen like alcohols, waxes, oils, fatty acids and polyglycols.
- ❖ **Solid-Solid PCMs** are used to avoid the problems associated with handling liquid. They offers additional flexibility for applying PCM solutions. The phase change that these solid-solid PCM undergo is in its crystalline matrix.
- ❖ **Molten Salts** are naturally solid salt materials which turn to liquid when they are heated to above their transition temperatures and act as a PCM energy storage material.

The summary of the commercially available and widely applied PCM solutions are presented in **Fig.2-11**.

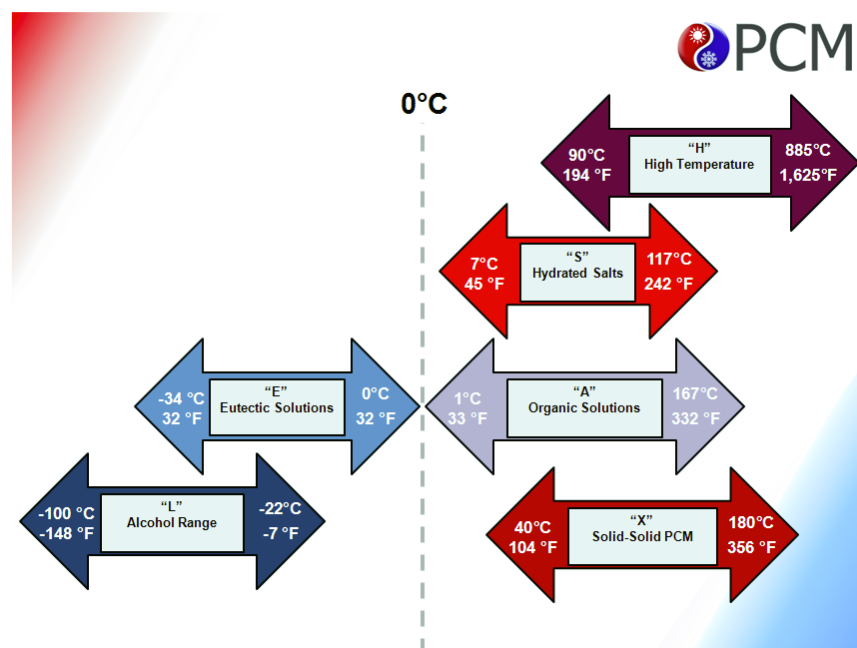


**Fig.2-11 Commercially available PCM solutions[104]**

Phase change material based thermal energy storage (TES) have been widely used in solar energy systems and waste heat recovery[108]. A tank filled with a storage medium is commonly used to store the energy for both sensible and latent heat. As mentioned before, sensible thermal energy storage (STES) collects thermal energy by increasing the temperature of single-phase storage medium whilst latent thermal energy storage (LTES) uses the phase change of a PCM from solid to liquid. Currently water is the most popular material for heat storage, especially when using solar power (solar collector and PV/T panel) due to low cost and convenience [109].

One technique to overcome the above problem is to introduce PCM into the solar heated storage tank with latent heat replacing purely sensible heat. Qin et al. [110] used the PCM as the inside wall of the tank. The testing result showed that the length of time for the water to cool from 65 °C to 40 °C in the tank with PCM is over 8.5% longer compared to the tank without PCM. Both Ibanez [111] and Cabeza [112] placed the PCM on the top of the water tank, replacing some water to strength thermal energy collecting capacity. These experimental and numerical studies showed that owing to the large heat capacity, PCM not only can provides hot water continually by itself, but also can reduce the volume of the tank for the same heating needs. Dzikevics et al. [113] examined the effects of PCMs on a hot water storage tank under various flow rates. It was shown that the flow rate of working fluid has little effect on the heat transfer rates, which is in agreement with the findings of other authors that heat transfer is proportional to power rather than flow rates.

A further technique has been studied, where the tank is entirely filled with PCM. López-Navarro [114] analysed the performance of a tank filled with paraffin, with a phase-change temperature between 3 °C and 8 °C. The results show that up to 78% of the maximum capacity is reached within 4 hours. Castell [115] focused on the impact of flow

rate and investigated two different configurations for cold storage applications. It was shown that the heat exchange effectiveness of the system has the same variation trend as the heat transfer area and the opposite variation trend as the flow rate. Furthermore, it keeps steady during the testing time.

Many studies on the PCM storage tank addressed adding small amounts of PCM into water, which does not provide a sufficient latent heat capacity to store energy from the system[116]. The pure PCM tanks, while having a huge heat storage capacity, also have smaller heat transfer area between the PCM and passing fluid. In this case, the low thermal conductivity of the PCM [117] prevents its timely energy absorption from the working fluid, leading to the reduced energy efficiency of the system.

### **2.4 Fractal theory for porous media fluid flow and heat/mass transfer**

Fractal theory is a mathematical branch established by Mandelbrot [118], a famous mathematician, to research the disordered and irregular structures in nature, such as rough surfaces, cost lines, mountains, rivers, lakes and a fern leaf, etc., as shown in **Fig.2-12**.

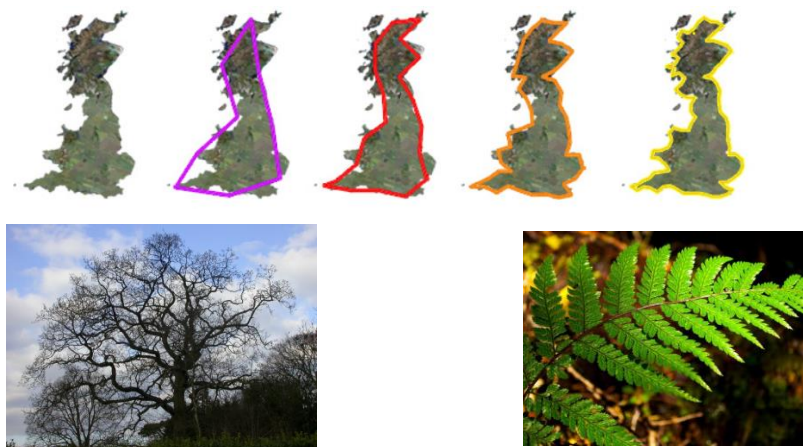


**Fig.2-12** Examples of natural fractal phenomena

Fractals always have two important properties, including self-similarity and non-integer dimension [118]. These are detailed below:

### **(1) Self-similarity**

As the tree and the leaf presented in the **Fig.2-12**, it is obvious that every little part of the bigger one has the same shape as the whole, which can be regarded as self-similar. The same is with fractals, which can be magnified many times and after every step the same shape will be easily found. This is characteristic of that particular fractal.

### **(2) Non-integer dimension**

The property of non-integer dimension is much more difficult to explain. It is normal to describe the classical geometry objects by integer dimensions, such as squares and circles by 2-dimension (2d), cubes and spheres by 3d. However, many natural phenomena cannot be described with simple integer dimensions, e.g. the coastline of the UK shown in Figure 2, which is better to using a dimension between two whole numbers. Alternatively, this is that while a straight line has a dimension of one, a fractal curve will have a dimension between one and two, depending on how much space it takes up as it twists and curves. The more the flat fractal fills a plane, the closer it approaches two dimensions. Likewise, a "hilly fractal scene" will reach a dimension somewhere between two and three. So a fractal landscape made up of a large hill covered with tiny mounds would be close to the second dimension, while a rough surface composed of many medium-sized hills would be close to the third dimension.

This theory creates an effective tool to describe this complex geometrical problem and associated thermal-fluid mechanisms [119]. Research on fractal theory and its application has progressed steadily in recent years and has made the important conclusion [119][120] [121] that materials with random pores can be appropriately characterised using fractal theory to give analytical description of the interior porous structure and associated fluid flow and heat/mass transfer.

Yu et al. (2002) [122] developed a fractal permeability model for bi-porous media according to the pores fractal features in the media finding that the fractal permeability is a function of fractal dimensions including the tortuosity fractal dimension and pore area fractal dimension, particles and clusters sizes, micro and the effective porosity of a medium. They (2004) [123][124] also investigated a complete fractal model of permeabilities for porous media in terms of saturated and unsaturated situation and found that the tortuosity fractal dimension from the present relative permeability models are independent of porosity/pore-area fractal dimension, and it depend only on saturation in the porosity below 0.9.

Huai et al. (2007) [125] generated a number types of fractal models to describe porous media structures and utilized finite volume method (FVM) to simulate the heat conduction feature in these porous structures. They found that the porosity is the main factor determining the effective thermal conductivity of the fractal porous media.

Spagnol et al. (2007) [126] found that in terms of the heat conduction characterization, periodic patterns established with elementary Von Koch snowflake are good structural type of nano-porous media which can apply fractal theory. They developed a numerical model based on fractal theory to build a determination function for the effective thermal conductivity of density and tortuosity.

Based on porous media's fractal characters and pore-throat model of capillary, Wu et al.(2007) [127] established a fractal resistance model of flow across porous media, which is a function of several parameters including porosity, pore-throat ratio, property of fluid, particle sizes and pore/capillary, fluid speed and fractal dimensions of porous media.

Zhu et al.(2013) [128] developed a fractal series-parallel model for predicting the effective thermal conductivity of fibrous porous media and compared this model with

other theoretical models and experimental data finding that the fractal models are more applicable for predicting effective thermal conductivity of two-phase systems.

Li et al. (2013)[129] derived a fractal effective thermal conductivity model of biological tissue based on assuming that the mother channel diameters of vascular trees obey the fractal scaling law and found that in the fractal model, the effective thermal conductivity of biological media has a linear relation with the ratio of the thermal conductivity of blood and the effective thermal conductivity of the biological media

Miao et al. (2017) [130] extended the methodology to study the slug flow's seepage characteristics in fractal porous media and found that the relative permeability for slug flow is a function of micro-structural parameters of porous media including slugs, bubbles and fluid properties.

Complex pore geometries within porous media make it impossible to derive accurate analytical expressions for the interior voids using conventional methods. Fractal theory, emerged at the end of the 20th century, creates an effective tool to describe this complex geometrical problem and associated thermal-fluid mechanisms.

Based on the above background analysis, the authors made the first kind of attempt to combine a number of innovations into a single MC-LHP-PV/T system. This involves the use of a co-axial tubular heat exchanger as the condenser, PV bound micro-channel tubes array as the PV/evaporator, the upper end liquid header with tiny holes as the liquid feeder and liquid/vapour separator, and the upper end vapour header as the vapour collector and distributor. The innovative aspects of the system lie in: (1) a co-axial tubular heat exchanger as the condenser can have sufficient length enabling full condensation of the work fluid and be coupled with the multiple evaporators. This can also create the one point connection that can minimise the risk of leakage and facilitate the pressure maintain

with the LHP; (2) the PV-bound micro-channel tubes array as the evaporator, owing to the reduced interior cross-sectional area, can create a very high vapour speed within the channels which will generate a higher shear stress force against the liquid film on the inner wall of the micro-channel tube. This will lead to the increased heat transfer coefficient and the higher solar thermal and electrical efficiencies; (3) an upper end liquid header with numerous tiny holes can create a uniformly distributed liquid film across the surface of the micro-channel inner wall and prevent the dry-out effect inhibited with the traditional loop heat pipe, thus significantly enhancing the heat transport capacity of the LHP.

This kind of MC-LHP-PV/T system would be theoretically studied by developing an analytical model, which is expected to gain a range of useful results that can help optimisation of the system configuration and prediction of its performance. However, a dedicated experimental study of such a MC-LHP-PV/T system seems to be necessary in order to evaluate its operational performance, especially the solar thermal and electrical efficiencies and their relevant impact factors. This research therefore would make its first go ahead to carry out experimental study of such a novel MC-LHP-PV/T system. The results of the research can help develop a high performance, commercially viable and low cost solar PV/T system for the use of building heat and power generation, thus leading to a wider deployment of the renewable solar systems in buildings and contributing to significant fossil fuel energy saving and carbon emission reduction on the global scale.

### **2.5 Chapter summary**

This chapter presents a comprehensive review on R&D of solar PV/T technology, LHP, PCM, and fractal theory for porous media application. Consequently, the results of the work presents a general information of the current development status, existing barriers and

## CHAPTER 2: LITERATURE REVIEW

---

development potential in PV/T technology, the potential application of LHP technology and phase change materials in PV/T, as well as the new investigation methods based on fractal theory to study the heat and mass transfer mechanism from micro scale to macro scale.

In brief, the current PV/T systems, using water or refrigerant as a working fluid, have a few critical difficulties: (1) water gives a higher pressure drop and thus needs a greater pump power; (2) a refrigerant has problems of liquid boiling and imbalanced distribution; (3) PV and thermal panels have poor binding effect owing to the different thermal & physical properties. This kind of system is therefore high cost, low efficient, short life span and unfit to buildings, and thus, has limited application. Based on the above background analysis, this thesis made the first kind of attempt to combine a number of innovations into a single PV/MCLHP system which will be detailed in following chapters.

# CHAPTER 3 PRELIMINARY DESIGN OF THE NOVEL PV/ MCLHP HEAT AND POWER SYSTEM

## 3.1 Chapter introduction

This chapter proposes a novel conceptual PV/T system for heating and power supply by applying a new PV/micro-channel evaporator concept, loop heat pipe technology, co-axial triple pipe heat exchanger with phase change material (PCM) and a PCM heat storage tank. It is designed to accomplish the following assignments:

- ❖ Present the design sketch drawings of the novel system with key points.
- ❖ Describe the working principle of the novel PV/T system.
- ❖ Introduce the unique features and key innovations of the system.
- ❖ Provide the parametric design and the roles of different system components respectively for following theoretical analysis, prototype fabrication and experimental testing.

## 3.2 System description and working principle

This novel PV/MCLHP system is designed to make effective use of solar energy for space heating, hot water and power supply, thus achieving significant fossil fuel consumption, carbon emission reduction and renewable solar energy application. The schematic of the system is shown in **Fig. 3-1**. This system comprises (1) a PV integrated micro-channel tubes array as the PV/evaporator, (2) a co-axial tubular heat exchanger as the condenser, (3) an upper end liquid header, within which numerous tiny holes opened on the upper side wall of micro-channels, as the liquid distributor and liquid/vapour separator, (4) upper end vapour header as the vapour collector and conveyor, (5) liquid transport line, and (6) vapour transport line. The system was charged with R-134a with a certain filling

## CHAPTER 3: PRELIMINARY DESIGN OF THE NOVEL PV/ MCLHP HEAT AND POWER SYSTEM

ratio [131], a refrigerant compatible with the micro-channel aluminium, and conducts the heat transfer with the coolant water passing across the condenser's mid-channel.

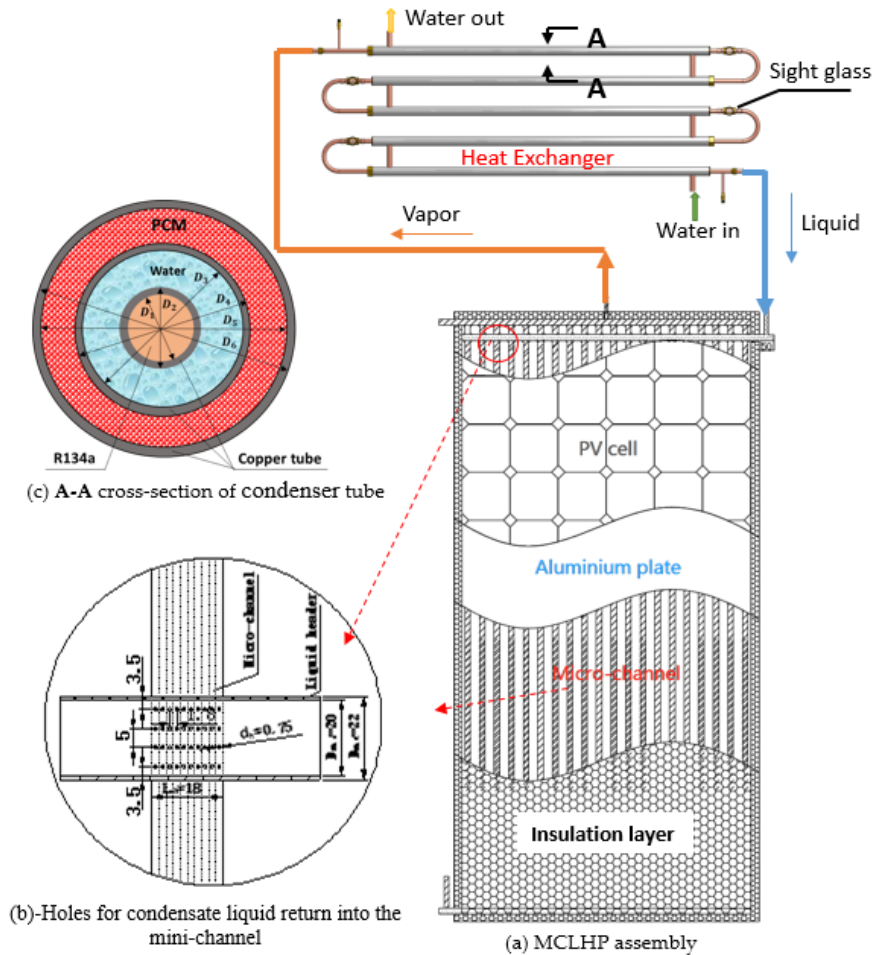


**Fig. 3-1 Schematic of the novel solar PV/ MCLHP system**

When the PV/evaporator receives the solar radiation striking on its upper surface, part of which is converted into electricity owing the photo-electron effect of the PV cells, its second part is converted into heat which is absorbed by the working fluid flowing across the micro-channel evaporator, and the remainder is dissipated into surrounding as shown in **Fig. 3-2**. As a result, the fluid within the micro-channel evaporator is converted into vapour and this amount of vapour gathers at the upper end vapour header, and then uplifted to the condenser by the buoyancy effect of the vapour. Within the condenser, the vapour in the interior channel transfers heat to the coolant water at the mid-channel, leading to the gradual condensation of the vapour. At the end of the channel, the vapour is completely condensed and the condensed liquid falls into the liquid header by gravity.

## CHAPTER 3: PRELIMINARY DESIGN OF THE NOVEL PV/ MCLHP HEAT AND POWER SYSTEM

In the meantime, the water within the mid-channel is heated to a temperature of around 40-50°C at the end of the channel and this is delivered to a building for the purposes of space heating or hot water supply. The PCM particles at the outside channel is functioned to absorb additional heat when the interior channel fluid carries more heat than the actual need of the water in the mid channel, and discharge some of heat into the mid-channel when the interior channel fluid carries less heat than the actual need. The condensed liquid gathers at the liquid header to a certain height level. This amount of water is then distributed to the inner wall of the micro-channel evaporator, through the holes fixed to the surface of the liquid header.

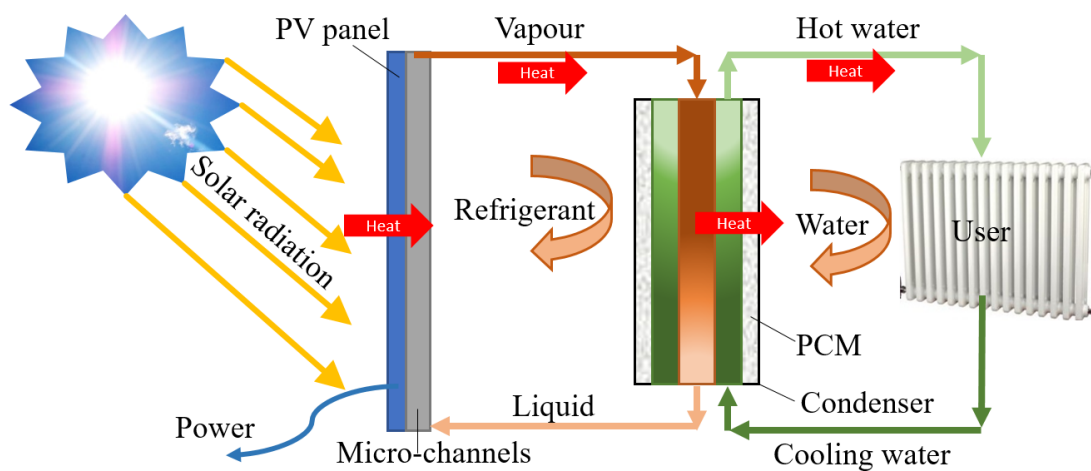


**Fig. 3-2. Cycle loop of the novel solar PV/T-MCLHP heating system**

A conventional LHP, which returns the condensed liquid refrigerant to the bottom of the evaporator and draws the liquid refrigerant from the evaporation section of the heat pipe using the capillary force of the heat pipe inner wall, suffers from the ‘dry out’ problem in the upper part of the evaporating section of the heat pipe and therefore has a lower heat transport capacity. Unlike the conventional LHPs, this novel LHP returns the condensed liquid refrigerant from the upper feeding liquid header. The upper feeding liquid header, with numerous tiny holes on the side wall of the micro-channels pipes that allow the liquid refrigerant to penetrate through under the effect of the pressure difference between the liquid on the condensation pipe and the vapour within the micro-channel pipes, can effectively distribute the liquid throughout the evaporation section wall, by using the

gravity of the refrigerant, thus preventing the 'dry-out' problem inhibited with the conventional LHPs and significantly increasing the heat transport capacity of the LHP[18].

### **3.3 Unique features (innovations) of the system**

Unlike a traditional LHP which employs the fin-attached round tubes as the evaporator, the PV/ MCLHP system employs the micro-channel tube array as the evaporator. The micro-channels, owing to the reduced interior cross-sectional area compared to traditional round tubes, lead to the increased vapour flow speed, larger shear force between the upward vapour flow and downward liquid flow, thinner liquid film thickness, and larger heat transfer coefficient between the film fluid and vapour. This will consequently result in the increased heat transport capacity of the LHP. Further, the micro-channel tubes arrays, having a larger flat surface compared to the fin-attached round tubes, can enable a better contact between the evaporator and PV cells with the larger and closer contact area. This will lead to an enhanced heat transfer and increased cooling effectiveness to the PV. As a result, the overall thermal and electrical efficiencies of the LHP PV/T system will be significantly higher than that of the traditional LHPs. Besides, there are three main innovations of the proposed system including, (1) a novel loop-heat-pipe (LHP), employing a co-axial tubular heat exchanger as the condenser, micro-channel-panels-array as the evaporator, the upper end liquid header with tiny holes as the liquid header and liquid/vapour separator, enables higher heat transport capacity compared to the latest LHPs; (2) combination of a micro-channel LHP evaporator with the PV module using a unique heat-assisted-pressing approach creates a reliable, building integrate-able PV/T panel (3) applying PCM in a heat exchanger creates a compact and highly efficient heat storage/exchanger. Such technological advances are supposed to tackle the critical

challenges remaining with existing PV/T systems, i.e., high cost, low efficiency, short life span, and non-fit to buildings.

### **3.4 System components and their characteristic parameters**

In this section, the comprehensive description and parametric design of all the components will be presented in detail. All these figures are applied as the initial input parameters of the computer simulation programs.

#### **3.4.1 PV/micro-channel evaporator with upper and lower end headers**

Structure of the PV/micro-channel evaporator is shown schematically in **Fig. 3-3**, where the micro-channel tubes, with the size of 2mm x 18mm as shown in **Fig. 3-1(c)**, comprising numerous mini holes with equivalent hydraulic diameter of around 0.75mm, were used to make the evaporator of the loop heat pipe. These tubes were then adhered to an aluminium plate and grouped by the lower end liquid header and upper end vapour and liquid headers. This formed a fully integrated micro-channel tubes array which acted as the evaporator of the LHP. This evaporator was then combined with a PV module by including: (1) back tedlar polyester tedlar (TPT) to be used as the backsheet of PV panel to enhance the longevity of the panel and to keep power isolation, (2) ethylene-vinyl-acetate (EVA) as an essential sealant of the PV module for ensuring the reliability and performance, (3) PV cells layer to convert part of solar energy into electricity by exciting electrons in silicon cells using the photons of light from the solar irradiance, (4) ethylene-vinyl acetate (EVA), and (5) glazing cover which is directly pressed on without air gap to protect the PV cells and reduce the convective heat loss directly from PV cell to the air, thus formulating an integrated PV/micro-channel evaporator. This PV/micro-channel evaporator is then accommodated into an insulated house with insulation layer to prevent the heat loss and thus becomes a modular PV/evaporator unit.

## CHAPTER 3: PRELIMINARY DESIGN OF THE NOVEL PV/ MCLHP HEAT AND POWER SYSTEM

As shown in **Fig. 3-3**, both the upper end vapour header and lower end liquid header were simply the aluminium cylinders with diameter of 22 mm each. These, being weld with the micro-channel tubes, served as the containers to collect liquid and vapour from the micro-channel tubes. Unlike in the upper end vapour header and lower end liquid header, the micro-channel in the upper end liquid header was drilled with numerous tiny holes which are dedicated to deliver liquid across the inner wall of the micro-channel evaporator, thus creating a uniformly distributed liquid film across the inner surface of the evaporator. It should be noted that pressure difference of the liquid prior and after the holes was controllable by adjusting the height of the liquid level within the header, thus matching the heat input through the micro-channel surface and keeping a balance between the liquid supply and evaporation.

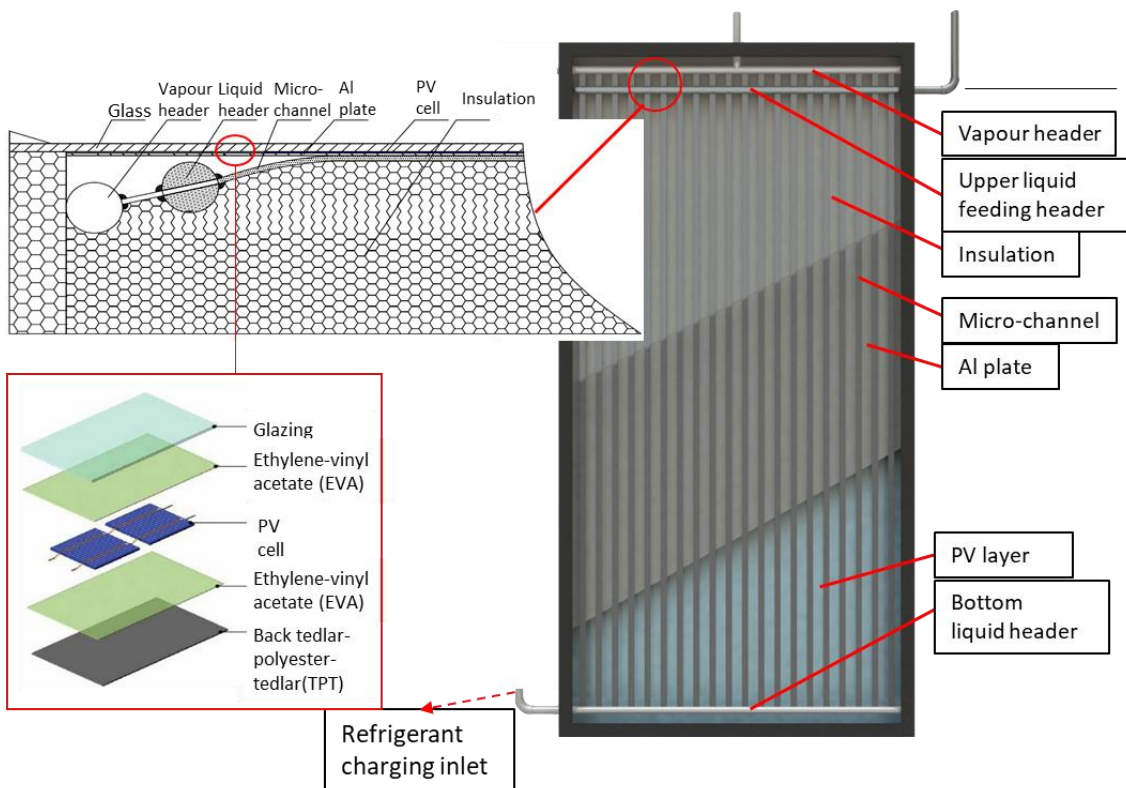


**Fig. 3-3. PV/micro-channel-evaporator module**

## CHAPTER 3: PRELIMINARY DESIGN OF THE NOVEL PV/ MCLHP HEAT AND POWER SYSTEM

---

### 3.4.1.1 Glazing cover

In order to reduce the excessive convective heat loss to the ambient air and protect the PV layer from external damage such as rain, dust and hail, a glazing cover is applied into this PV module without air gap. However, its characteristic parameters can affect the amount of solar energy transferred to the PV layer thus influence the solar performance of the PV or PV/T module. Therefore, it is essential to select proper glazing cover, which has detailed technical specifications shown in **Table 3-1**.

**Table 3-1. Parameters of the solar glazing cover**

Glazing	Emissivity	Transmittance	Size (W*L*T mm)	Thermal conductivity (W/m/K)
Single	0.89	0.912	1980*980*3.2	2.4

**Table 3-2. Parameters of the PV panels**

Item	Parameter
Technology (PV cell)	Multi-c-Si
Packing factor (%)	85.4
PV area $A_{pv}$ (m <sup>2</sup> )	1.769
Electrical Efficiency under standard condition $\eta_{rc}$ (%)	18.6
Temperature attenuation coefficient $B_{pv}$ (1/°C)	-0.45
Isc (A)	7.637
Voc (V)	44.894
Pm (W)	292.792
Ipm (A)	7.534
Vpm (V)	38.869

### 3.4.1.2 PV layer

In this proposed PV module, there are 6\*12 pieces of PV cells being arrayed on the glass with the single size of 156.75\*156.75\*0.3 mm and the total area of 1.769 m<sup>2</sup>, which covers around 95% of the baseboard surface. The performance of this kind of PV/T panel

**CHAPTER 3: PRELIMINARY DESIGN OF THE NOVEL PV/ MCLHP  
HEAT AND POWER SYSTEM**

was estimated under standard testing condition, i.e. solar radiation at 1000W/m<sup>2</sup> and ambient air temperature at 25 °C, and the relevant technical parameters of the PV/T panel are presented in **Table 3-2**.

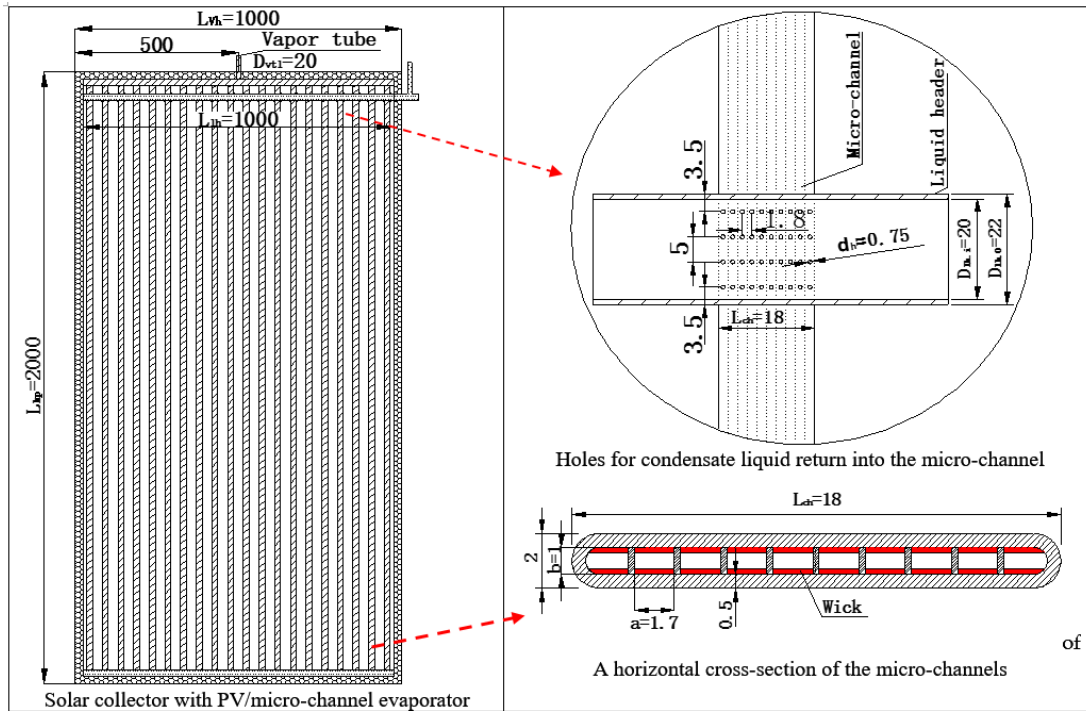


**Fig. 3-4. Solar collector with PV/micro-channel evaporator and condensate liquid pathway (units in mm).**

**3.4.1.3 Micro-channel layer**

As shown in **Fig. 3-4**, 20 micro-channel rectangular flat tubes (2mm x 18mm x 10), with the both ends welded into the end headers, are adhered onto the back of the Al plate by thermal silica gel with relatively high thermal conductivity. The structure and parametric design of the micro-channel layer is also illustrated in **Fig. 3-4**. Within the upper end liquid header, four tiny holes are opened on the side wall of the micro-channel tubes, which allows the condensate liquid to penetrate the pipe wall, and thus formulate the downward liquid films. It should be noted that the micro-channel tubes are arranged side by side; the top sides of the tubes are integrated into the vapour and liquid headers which

are arranged one another on the vapour transport line, while the bottom sides of the tubes are integrated into the liquid reservation header.

### 3.4.2 Co-axial tubular triple-pipe heat exchanger with PCM (as the condenser)

Structure of the co-axial tubular heat exchanger is shown schematically in **Fig. 3-5**, while the relevant parameters are presented in **Table 3-3**. This heat exchanger is a triple-channels structure which allowed the heat pipe working fluid to travel across the interior channel, water fluid to travel through the mid-channel, and PCM particles capped into the outside channel. During the operation, the heat pipe working fluid within the interior channel transferred heat to the water at the mid-channel, leading to the gradual condensation of the vapour within the interior channel. At the end of the channel, the vapour was completely condensed and the condensed liquid fell into the liquid header by gravity. In the meantime, the water within the mid-channel was heated to a temperature of around 40°C at the end of the channel and this was delivered to a building for the purposes of space heating or hot water supply. The PCM particles at the outside was functioned to absorb additional heat when the interior channel fluid carried more heat than the actual need of the water in the mid-channel, and discharge some of heat into the mid-channel when the interior channel fluid carries less heat than the actual need.

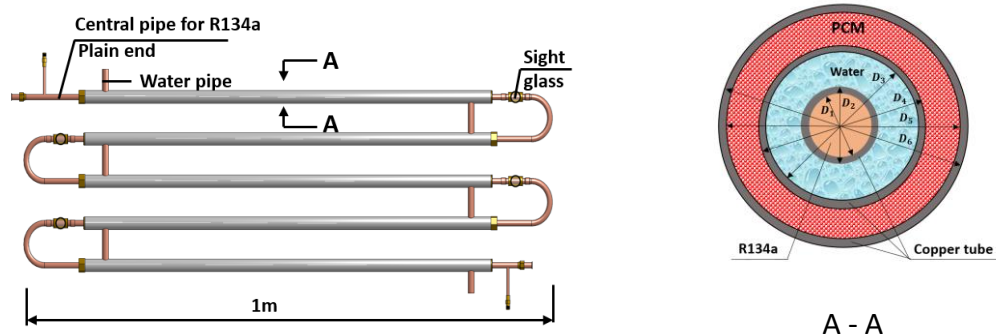


**Fig. 3-5. The structure of the triple-pipe heat exchanger**

### 3.4.3 Vapour and liquid transportation lines

Vapour and liquid transportation lines are designed to convey the vapour from the evaporator to condenser and deliver the condensed liquid from the condenser to evaporator as shown in **Fig. 3-1**. The technical specifications of the lines are presented in **Table 3-3**.

### 3.4.4 Micro-channel Loop Heat Pipe (MCLHP)

Combining the above parts, a novel preliminary Micro-channel Loop Heat Pipe (MCLHP) in this research is established and presented in **Fig. 3-6**. Within this novel MCLHP, a new design for the condensate liquid return path comprising the liquid transportation line and liquid upper feed header is proposed. It should be stressed that this kind of MCLHP has a unique structure which, positioning the liquid and vapour headers on the top of the micro-channels array, can effectively collect the vapour from the array, and more importantly, make an even distribution of the liquid across the inner walls of the micro-channel pipes, via numerous tiny holes drilled on side walls of the pipes. This structure, originating from our previous award-winning innovation titled ‘liquid upper-fed loop heat pipe’ [101], can achieve constant wetting condition of the heat pipes’ wall, thus increasing its heat transport capacity which is justified by the limits of heat transfer. Compared to our previous innovation, the MCLHP has implemented several innovative concepts into the loop that makes it unique and distinctive: (1) micro-channel pipes array comprising numerous rectangular pipes that enables a better holes’ set-up and increased heat transfer; (2) separated vapour and liquid headers; and (3) tiny holes designed based on the pressure difference between the header water and the micro-channel pipe vapour.

### 3.4.5 Working fluid

The novel MCLHP is filled with refrigerant R134a instead of water, which is chemically incompatible with the aluminium mini-channel. In fact, the water interaction with the aluminium can lead to a corrosion reaction without natural inhibition. This corrosion can generate non-condensable gas and then causes the breakage of the internal vacuum, which causes the non-functioning of the heat pipe [132].

**Table 3-3. Parameters of the PV/MCLHP system**

Parameters	Nomenclature	Value	Unit
Micro-channel port width	a	0.0017	m
Micro-channel port height	b	0.001	m
Evaporator length	$L_{hp}$	1.9	m
Number of micro-channel heat pipes	$N_{hp}$	20	-
Number of micro-channel ports	$N_p$	10	-
Total number of micro-channel ports	$N_{ch}$	200	-
Operating temperature range	$T_v$	20-60	°C
Evaporator to condenser height difference	$H_{hp-he}$	0.6	m
Transportation line outer diameter	$D_{tl,o}/D_{vtl,o}$	0.015	m
Transportation line inner diameter	$D_{tl,i}/D_{vtl,i}$	0.0174	m
Liquid head length	$L_{lh}$	1	m
Liquid Head diameter	$D_{lh}$	0.022	m
Vapour header length	$L_{vh}$	1	m
Hole diameter	$d_h$	0.00075	m
Transportation line length	$L_{tl}/L_{vtl}$	1.5/1.5	m
Heat exchanger central tube total length	$L_{he}$	5	m
Heat exchanger central tube diameters	$D_1/D_2$	0.016/ 0.017	m
Heat exchanger middle tube diameters	$D_2/D_4$	0.019/ 0.021	m
PCM tube diameters	$D_5/D_6$	0.027/ 0.029	m
PCM melting temperature	$T_{pcm}$	44	°C
PCM density	$\rho_{pcm}$	800	kg/m <sup>3</sup>
PCM Latent Heat	$L_h$	242	kJ/kg
PCM thermal conductivity	$\lambda_{pcm}$	0.18	W/mK
PCM Maximum operating temperature	$T_{pcm-max}$	300	°C

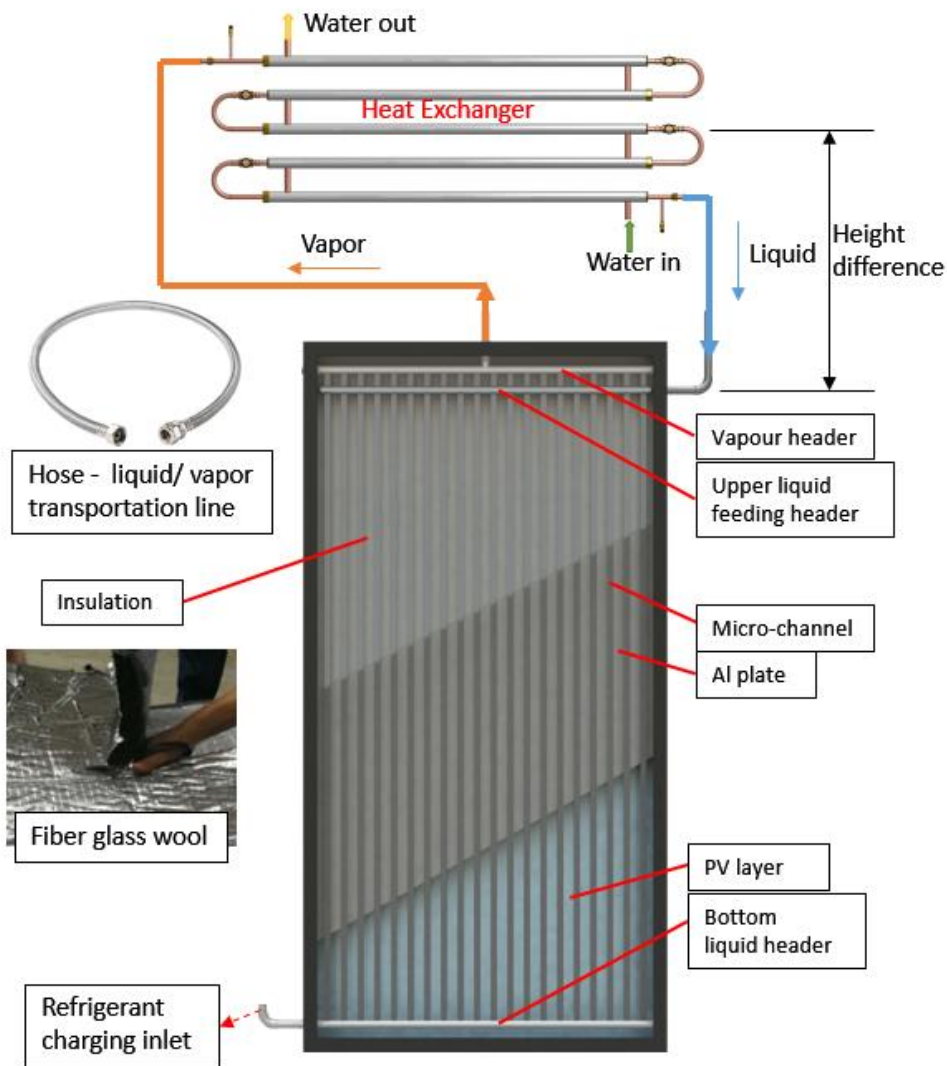


**Fig. 3-6. Schematic of the novel Micro-channel loop-heat pipe, the refrigerant flow and evaporation in the micro-channel**

### 3.4.6 PV power system

As shown in **Fig. 3-7**, a MPPT solar power controller, installed with Maximum Power Point Tracking (MPPT) algorithm, can maximize the amount of current charged into the battery. This controller acts as both an electrical recorder and a converter, which accepts the DC input from the PV/T module, converts it into AC, and then deliver the AC into the battery bank to reserve. A separate DC/AC inverter was used to convert DC from the battery bank into AC which is used to driven the fan and pump in this system. The electrical supply of such a system is expected to meet with itself demand.

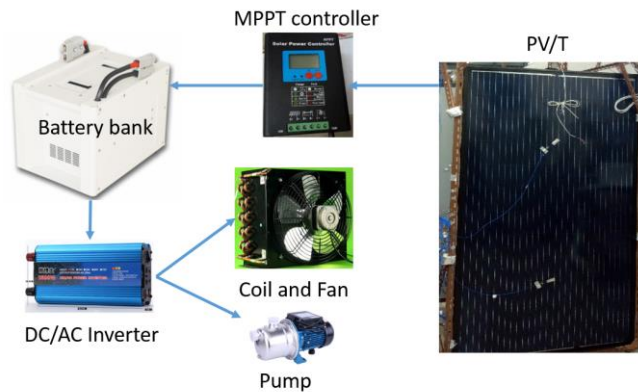


**Fig. 3-7. Solar power process from the PVs to the User (Coils and Fan)**

### 3.5 Chapter summary

This chapter presents a novel conceptual PV/T system for heat and power generation by applying a new PV/micro-channel evaporator concept, loop heat pipe technology, co-axial triple pipe heat exchanger with phase change material (PCM) and its operating principles from the perspectives of PV/micro-channel evaporator, the LHP loop, and the heat exchanger. The main features of the proposed PV/MCLHP heating and power generation system lie in : (1) a novel loop-heat-pipe (LHP), employing a co-axial tubular heat exchanger as the condenser, micro-channel-panels-array as the evaporator, the upper end liquid header with tiny holes as the liquid header and liquid/vapour separator, enables higher heat transport capacity compared to the latest LHPs; (2) combination of a micro-channel LHP evaporator with the PV module using a unique heat-assisted-pressing approach creates a reliable, building integrate-able PV/T panel; (3) applying PCM in a heat exchanger creates a compact and highly efficient heat storage/exchanger.

This chapter also summarised a series of parameters for further characterising the proposed system performance, including structure, geometry and material design of different system components and the operational parameters.

## CHAPTER 3: PRELIMINARY DESIGN OF THE NOVEL PV/ MCLHP HEAT AND POWER SYSTEM

---

The chapter provides a foundation for development of the follow-on chapters. Based on the proposed PV/T system, the heat transport capacity of the LHP will be investigated and the optimum geometrical sizes (e.g. diameter, length, and number) of the LHP will be determined using the HP characterisation model developed in Chapter 3. Further, the operational performance of the LHP-based PV/T system will be investigated using its dedicated analytical model, thus giving the predicted heat and power outputs of the system and the correlations of the heat and power outputs and associated impact factors, which will be addressed in Chapter 4. The simulation results obtained from Chapter 4 will be validated by the controlled lab and site tests, which will be addressed in Chapters 5 and 6. Consequently, the socio-economic performance of the PV/T system will be investigated in Chapter 7.

# CHAPTER 4. THEORETICAL ANALYSIS AND COMPUTING

## MODELS DEVELOPMENT

### **4.1 Chapter introduction**

On the basis of the preliminary design, this chapter will address the theoretical analysis and computer model development of the MC-LHP and PV/MCLHP systems. These involve the use of fractal theory and energy balance equations among different parts of the systems, taking into account transient solar energy conversion, heat transfer, fluid flow and electricity generation. The major outcomes of the chapter include:

- (1) Theoretical equations and algorithms established for the MC-LHP heat transfer limits calculation and the PV/MCLHP operational performance analysis;
- (2) One MATLAB based computer analytic model to calculate the heat transport capacity of the MC-LHP system;
- (3) One MATLAB based analytic model for simulating the heat transfer performance of the MC-LHP system and integrated PV/ MCLHP heat and power system;
- (4) Models validation and accuracy analysis;
- (5) The models operation and results discussion.

This part of work establishes the foundation of design and construction of the prototype PV/MCLHP system and enable the parallel comparison between the experimental and modelling results.

### **4.2 Analytical model for the assessment of the heat transfer limits of the MC-LHP based on the Fractal Theory**

As described in Chapter 3, the MC-LHP part plays a critical role in conveying heat transportation from the PV rear surface to the heat collection point. Its performance

## CHAPTER 4: THEORETICAL ANALYSIS AND COMPUTING MODEL DEVELOPMENT

---

dominates the solar thermal efficiency of this system and will also directly affect the solar electrical efficiency of the PV/MCLHP panel, thus impacting on the total amount of the useful energy absorbed from the striking solar energy. In this sense, investigation of the heat transfer limits of the MC-LHP is the precedence action for design and performance assessment of the the integrated PV/MCLHP system. With the determination of the heat transfer limit from the analytical analysis, the maximum heat transfer capacity of the PV/MCLHP system can thus be understood, and associated geometrical and operational parameters can then be determined.

A Loop Heat Pipe (LHP), comprising a heat pipe evaporator (wicked or wickless type), a condenser, a liquid transportation line, a vapour transportation line and a compensation chamber, is a two phase (condensation/evaporation) device that can transport heat throughout a long distance [133] [134]. The LHP is usually fitted with some kind of wick, e.g., meshes, sintered powder, or grooves, on the inner surface of the evaporator and condenser that can help distribute liquid streams uniformly across the surface and thus create an enhanced heat transfer performance. Over the past decades, sintered powder wick has been widely used in the evaporator of loop heat pipes [134], which can be treated as a layer of porous material comprising the metal skeletons and random/tortuous pores. The characteristic parameters of the wick, including the effective thermal conductivity, pores' maximum diameter and permeability, impose significant impacts on the performance of the MC-LHP [135]. Complex pore geometries within porous wicks make it impossible to derive accurate analytical expressions for the interior voids using conventional methods. Fractal theory, emerging at the end of the 20th century, creates an effective tool to describe this complex geometrical problem and associated thermal-fluid mechanisms [118]. Research on fractal theory and its application has progressed steadily in recent years and has made the important conclusion [136][137], i.e., materials with

## CHAPTER 4: THEORETICAL ANALYSIS AND COMPUTING MODEL DEVELOPMENT

---

random pores can be appropriately characterised using fractal theory to give analytical description of the interior porous structure and associated fluid flow and heat/mass transfer. In terms of a wick, as its structure can be considered as a porous media, fractal theory [138] can therefore be applied to investigate the impact of the wick structure on the performance of a LHP.

Consequently, this section presents an analytical study of the heat transfer capacity of the proposed novel micro-channel loop heat pipe (MC-LHP) considering the impact of a wick's fractal geometrical parameters inside the micro-channels. By treating the wick of the micro-channel evaporator of the MCLHP as a thin porous layer, i.e. a combination of random/tortuous pores and water-containing skeletons, the impact of the fractal geometrical parameters of the wick on the heat transport capacity of the MCLHP was investigated. Based on the classical heat transfer limits and fractal equations, a dedicated computerised analytical model was developed by using the Newton-Raphson method; this model was then applied to analyse a few macro parameters of the wick (i.e., effective thermal conductivity and permeability) and heat transfer limits of the MCLHP, including capillary, viscous, entrainment, sonic and boiling ones. Comparison among these five limits was made using the minimum value searching approach, leading to the determination of the final heat transfer constraint of the MCLHP. To the best of our knowledge, this is the first kind of effort in bringing fractal theory into the study of the heat transfer problem in the loop heat pipe, which can generate more realistic and accurate outcomes.

### 4.2.1 Fractal characters of the sintered powder wick in the evaporator of MC-LHP

#### (1) Fractal parameters

The wick structure has a significant impact on the performance of the MCLHP. Sintered powder, which is one of the widely used bi-dispersed porous media [139], can be viewed by electron microscope scanner (SEM) [140] as shown in **Fig.4-1**. Its sintered particles form the skeletons and the void spaces between the skeletons form numerous pores which, acting as the vapour vent paths, can significantly increase the surface area of liquid evaporation. Small pores, accommodated within the skeletons, can increase the liquid pumping capability owing to the pores' capillary effect. Individual metal projections, when linked together, can be easily identified as the skeletons and pores. However, the small pores within the skeletons are difficult to identify [140]. The diameter of the pores in the bi-dispersed porous media varies from 2 $\mu\text{m}$  to 200 $\mu\text{m}$  [140] [141]. The disordered nature of the pore structure in the sintered powder, especially the pore size distributions, plays an important role in conducting heat and mass transfer within a porous media, and thus can be well described using fractal theory.

A number of studies [138][142] have been carried out to address the highly disordered pore distribution with a porous media through a scaling law [120], as below:

$$M(L) \sim L^{D_f} \quad (4-1)$$

Based on the fractal laws, the relationship between the pores' number and pores' maximum diameter [122] can be expressed as:

$$N(L \geq \lambda) = \left(\frac{\lambda_{\max}}{\lambda}\right)^{D_f} \quad (4-2)$$

The total number of the pores, ranging from the minimum pore diameter  $\lambda_{\min}$  to the maximum pore diameter  $\lambda_{\max}$ , can be expressed as:

$$N_t(L \geq \lambda_{\min}) = \left(\frac{\lambda_{\max}}{\lambda_{\min}}\right)^{D_f} \quad (4-3)$$

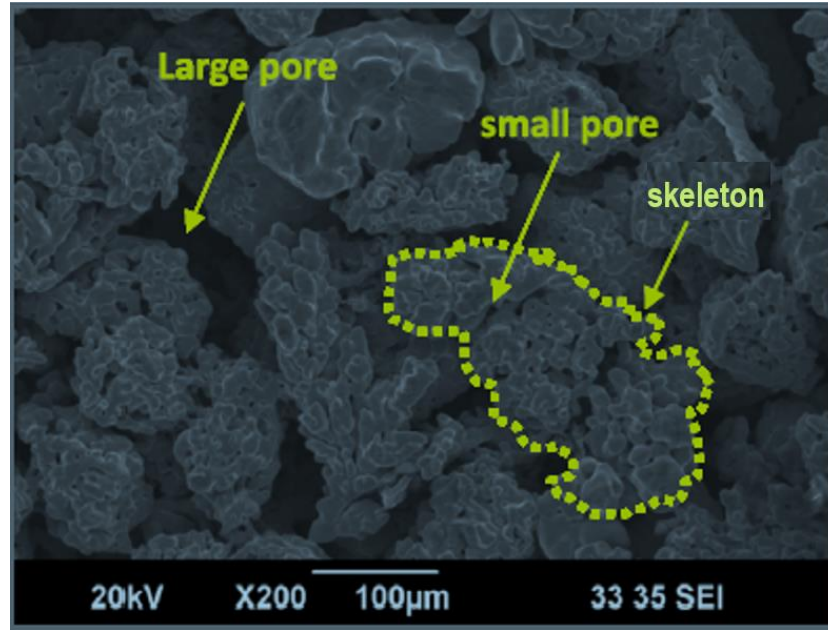


**Fig.4-1. The SEM image within the porous stack sintered on the evaporator wall [140]**

Eq. (4-1) can be further derived as:

$$-dN = D_f \lambda_{max}^{D_f} \lambda^{-(D_f+1)} d\lambda \quad (4-4)$$

Eq. (4-4) presents the number of pores from the diameter  $\lambda$  to the radius  $\lambda + d\lambda$ .

Combination between Eq. (4-4) and Eq. (4-3) yields:

$$-\frac{dN}{N_t} = D_f \lambda_{min}^{D_f} \lambda^{-(D_f+1)} d\lambda = f(\lambda) d\lambda \quad (4-5)$$

Where  $f(\lambda) = D_f \lambda_{min}^{D_f} \lambda^{-(D_f+1)}$  is the probability density function of the pore distribution. If  $f(\lambda) \geq 0$ , Eq. (4-5) can be written as:

$$\int_{-\infty}^{\infty} f(\lambda) d\lambda = \int_{\lambda_{min}}^{\lambda_{max}} D_f \lambda_{min}^{D_f} \lambda^{-(D_f+1)} d\lambda = 1 - \left(\frac{\lambda_{max}}{\lambda_{min}}\right)^{D_f} \quad (4-6)$$

According to the probability theory, the probability density function should abide by the following correlation:

CHAPTER 4: THEORETICAL ANALYSIS AND COMPUTING MODEL  
DEVELOPMENT

---

$$\int_{-\infty}^{\infty} f(\lambda) d\lambda = \int_{\lambda_{min}}^{\lambda_{max}} f(\lambda) d\lambda = 1 \quad (4-7)$$

Eq. (4-7) implies that if  $(\frac{\lambda_{min}}{\lambda_{max}})^{D_f} = 0$ , Eq. (4-6) stands [130].

This item is considered as a criterion for justifying whether or not a porous fibrous media can be characterized by fractal theory and method. In principle, if  $\lambda_{min}/\lambda_{max} \leq 10^{-2}$ , Eq. (4-7) stands. The cumulative probability in the range  $\lambda_{min}$  to  $\lambda$  can be expressed as:

$$P(\lambda) = \int_{\lambda_{min}}^{\lambda} f(\lambda) d\lambda = \int_{\lambda_{min}}^{\lambda} D_f \lambda_{min}^{D_f} \lambda^{-(D_f+1)} d\lambda = 1 - (\frac{\lambda_{min}}{\lambda})^{D_f} \quad (4-8)$$

Eq. (4-8) indicates that if  $\lambda_{min} = \lambda_{max}$ ,  $P(\lambda) = 0$ ; and if  $\lambda = \lambda_{max}$ ,  $P(\lambda) \approx 1$ . A correlation between the fractal dimension and effective porosity of the porous media is given by [143]:

$$D_f = d - \frac{\ln \varepsilon}{\ln \frac{\lambda_{min}}{\lambda_{max}}} \quad (4-9)$$

Where  $d$  is the Euclidean dimension; while  $d$  values of 2 and 3 refer to the two- and three-dimension spaces, respectively.

The fractal dimension,  $D_t$ , for tortuous stream tubes in a porous media can be expressed as [144]:

$$D_t = 1 + \frac{\ln \tau_{av}}{\ln \frac{L}{\lambda_{av}}} \quad (4-10)$$

The averaged tortuosity  $\tau_{av}$  can be calculated by Eq. (4-11a)

$$\tau_{av} = \frac{1}{2} \left[ 1 + \frac{1}{2} \sqrt{1 - \varepsilon} + \sqrt{1 - \varepsilon} \frac{\sqrt{\left(\frac{1}{\sqrt{1-\varepsilon}} - 1\right)^2 + \frac{1}{4}}}{1 - \sqrt{1-\varepsilon}} \right] \quad (4-11a)$$

The average pore/capillary diameter or size  $\lambda_{av}$ , can be calculated by Eq. (4-11b)

$$\lambda_{av} = \int_{\lambda_{min}}^{\lambda_{max}} \lambda f(\lambda) d\lambda = \frac{D_f}{D_f-1} \lambda_{min} \left[ 1 - \left( \frac{\lambda_{min}}{\lambda_{max}} \right)^{D_f-1} \right] \quad (4-11b)$$

Derived from Eq. (4-11), the total pore area for the representative cell is expressed as [130][145]:

$$A_p = - \int_{\lambda_{min}}^{\lambda_{max}} \frac{\pi \lambda^2}{4} dN = \frac{\pi D_f \lambda_{max}^2 (1-\varepsilon)}{4(2-D_f)} \quad (4-12)$$

The total cross-sectional area  $A$  of the representative cell of the porous surface can be calculated by Eq. 4-13:

$$A = \frac{A_p}{\varepsilon} = \frac{\pi D_f \lambda_{max}^2 (1-\varepsilon)}{4(2-D_f) \varepsilon} \quad (4-13)$$

Furthermore, the representative length ( $L_0$ ) can be calculated by Eq. 14:

$$L_0 = \sqrt{A} \quad (4-14)$$

### **(2) Fractal permeability model**

The porous wick of the evaporator in a MCLHP is a mixture of numerous metal skeletons and water-containing pores. A fractal model established by Yu et al [122], based on Darcy's law, can be applied to calculate the absolute permeability of the saturated porous media. This can be expressed as:

$$K = \frac{\mu L_0 Q}{\Delta P A} = \frac{\pi}{128} \frac{L_0^{1-D_t}}{A} \frac{D_f}{3+D_t-D_f} \lambda_{max}^{3+D_t} \quad (4-15)$$

## CHAPTER 4: THEORETICAL ANALYSIS AND COMPUTING MODEL DEVELOPMENT

---

If  $D_t = 1$ , Eq. (4-15) can be simplified as:

$$K = \frac{\pi}{128} \frac{1}{A} \frac{D_f}{4-D_f} \lambda_{max}^4 \quad (4-16)$$

For an unsaturated porous media shown in **Fig.4-2**, a simplified model, which refers to a capillary tube filled with water and gas (in this proposed model, substitute water by R134a), was developed by Yu et all [146]. This model could be applied to calculate the fractal permeability of the unsaturated porous media, given by:

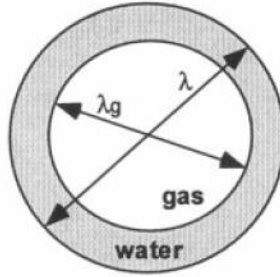


**Fig.4-2. A simplified model for the cross section of a capillary tube partially filled with fluid and gas [146]**

$$K_w = \frac{\pi}{128} \frac{L_0^{1-D_t}}{A} \frac{D_{f,w}}{3+D_t-D_{f,w}} (\lambda_{max} \sqrt{S_w})^{3+D_t} \quad (4-17a)$$

$$K_g = \frac{\pi}{128} \frac{L_0^{1-D_t}}{A} \frac{D_{f,g}}{3+D_t-D_{f,g}} (\lambda_{max} \sqrt{1-S_w})^{3+D_t} \quad (4-17b)$$

Where:

$$D_{f,w} = d - \frac{\ln(S_w \epsilon)}{\ln \frac{\lambda_{min}}{\lambda_{max}}} ; \quad D_{f,g} = d - \frac{\ln[(1-S_w) \epsilon]}{\ln \frac{\lambda_{min}}{\lambda_{max}}} \quad (4-18)$$

$S_w$  is saturation degree of the wick [147].

### **(3) Effective thermal conductivity**

## CHAPTER 4: THEORETICAL ANALYSIS AND COMPUTING MODEL DEVELOPMENT

---

Based on the Fourier's law and thermal-electrical analogy principle, Yu et al. [148] established a fractal model to predict the effective thermal conductivity.

$$K_e = \frac{A_n}{A} k_{e,n} + \left(1 - \frac{A_n}{A}\right) k_{e,mc} \quad (4-19)$$

Where

$$k_{e,n} = k_l (1 - \sqrt{1 - \varepsilon}) + \frac{k_l (1 - \sqrt{1 - \varepsilon})}{1 + \left(\frac{1}{\beta} - 1\right) \sqrt{1 - \varepsilon}} ;$$

$$k_{e,mc} = \frac{\lambda_{max}^2}{A} \left(\frac{\lambda_{max}}{L_0}\right)^{D_t - 1} \cdot \frac{D_f}{D_t - D_f + 1} \cdot \left[ \frac{\frac{\gamma_{a1}}{\sqrt{1 - \varepsilon_c}}}{\beta \sqrt{1 - \varepsilon_c} + 2(1 - \sqrt{1 - \varepsilon_c})} + \frac{1 - \gamma_{a1}}{\gamma_{c1}^2 (1 - \varepsilon_c) (\beta - 1) / \gamma_{a1}^2 + 1} \right]^{-1}$$

$\gamma_{a1} = l/a$ , assumed as 0.7, is the ratio of geometrical length scale for a particle; and  $\gamma_{c1} = c/l$ , assumed as 0.13, is the ratio of contact length scale for a particle [148];  $k_{e,n}$  is the effective thermal conductivity of non-touchable particles or skeletons;  $k_{e,mc}$  is the effective thermal conductivity of mixed chains of particles or skeletons with fluid;  $\beta$  is the ratio of thermal conductivity,  $\beta = k_s / k_l$ ;  $\varepsilon_c$  is the porosity within the microporous skeletons [148].

Overall, the above Equations formulate a theoretical foundation for the heat pipe heat transfer analysis.

### 4.2.2 Mathematical model for the MCLHP heat transfer limits

The operational MC-LHP is schematically presented in **Fig.4-3**. This novel MC-LHP is composed of the following main elements: the wicked micro-channels as the heat pipe

## CHAPTER 4: THEORETICAL ANALYSIS AND COMPUTING MODEL DEVELOPMENT

---

evaporator, the separate liquid and vapour transportation line for the condensate liquid return, the upper vapour gathering header and the liquid feeding header, co-axial triple-pipe heat exchanger as the condenser. It should be noted that within the liquid feeding header, four tiny holes are opened on the side wall of the micro-channel tubes, which allows the condensate liquid to penetrate the pipe wall, and thus formulate the downward liquid films; the micro-channel tubes are arranged side by side; the top sides of the tubes are integrated into the vapour and liquid headers which are arranged one another on the vapour transport line, while the bottom sides of the tubes are integrated into the liquid reservation header. The whole system, configured as an integrated loop, is charged with R134a instead of water as the working fluid. This is because water is incompatible to the material of micro-channel pipe (i.e., aluminium) while R134a does [149]. Particularly, this kind of MCLHP has a unique structure which, positioning the liquid and vapour headers on the top of the micro-channels array, can effectively collect the vapour from the array, and more importantly, make an even distribution of the liquid across the inner walls of the micro-channel pipes, via numerous tiny holes drilled on side walls of the pipes. This structure, originating from the authors' previous award-winning innovation titled 'liquid upper-fed loop heat pipe' [101], can achieve constant wetting condition of the heat pipes' wall, thus increasing its heat transport capacity which is justified by the limits of heat transfer.

In this section, the correlations between the heat transfer capacity of the MCLHP and a number of fractal parameters of the wick, e.g., sintered powder one, will be established by treating sintered powder wick of a MCLHP as a thin porous layer containing numerous metal skeletons and pores. There are five heat transfer limits governing the heat transport capacities of the LHP including boiling, capillary, viscous, entrainment, and sonic ones.

The minimum values of these limits are the actual governing limitation of the system heat transfer capacity. These problems will be discussed below.

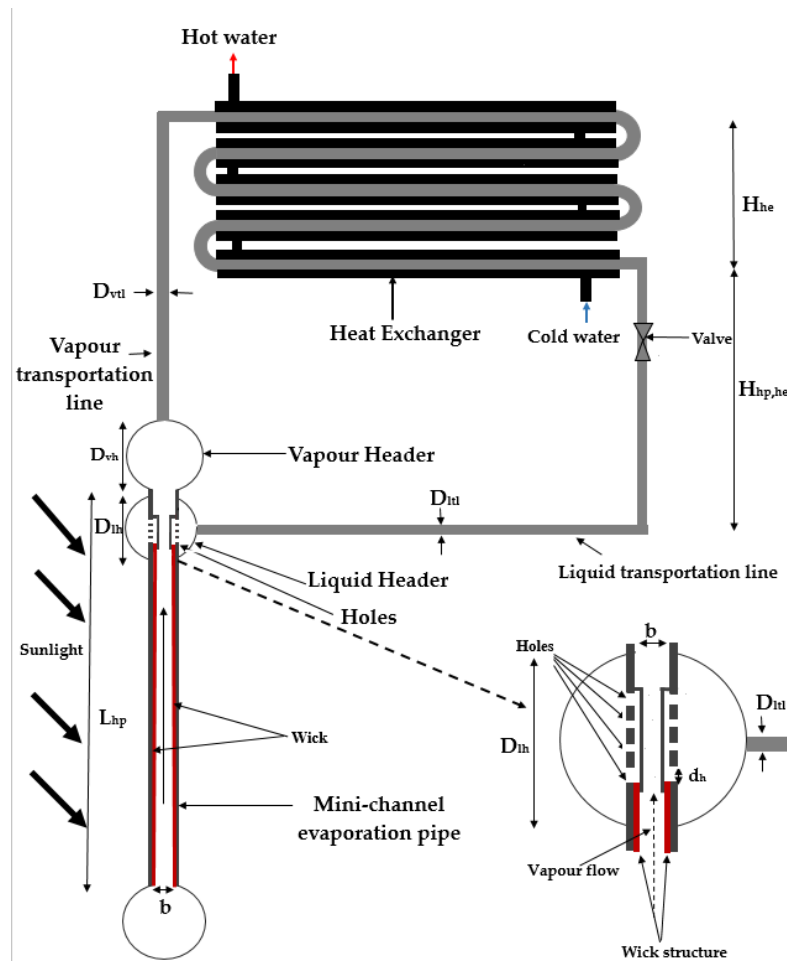


**Fig.4-3. Schematic of the novel solar loop-heat pipe, the refrigerant flow and evaporation in the micro-channel with porous wick**

**(1) Boiling limit ( $Q_{BL}$ )**

The boiling limit ( $Q_{BL}$ ) represents the maximum radial heat transfer rate within micro-channel tubes, which come together to become the limit of the evaporator of the MCLHP.

This limit generally occurs at an extremely high operational temperature, which can drive the liquid out of the porous wick and get the heat pipe wall dry, thus terminating the operation of the evaporator. Similarly, a certain level of the boiling limit will also exist in the condenser of the MCLHP. For the evaporator, the boiling limit can be expressed as

[70] [75]:

$$Q_{BL,e} = N_{ch} \frac{K_e L_e a}{\delta_w} \frac{T_v}{h_{fg} \rho_v} \left( \frac{2\sigma}{r_b} - P_c \right) \quad (4-20)$$

Where,  $D_{hp}$  is the hydraulic diameter of a single micro-channel tube;  $D_{v,e}$  is the equivalent diameter of the vapour section;  $N_{ch}$  is the number of the micro-channels (ports) of the solar panel;  $L_e$  is the length of micro-channel evaporator;  $r_b$  is the radius of the boiling bubbles, which could be assumed as  $2.54 \times 10^{-7}$  m for the general estimation of a normal heat pipe performance[150];  $P_c$  is the capillary pressure;  $K_e$  is the fractal effective thermal conductivity of the porous wick, which can be calculated by Eq. (4-19). Since the effective thermal conductivity  $K_e$  is the function of fractal dimensions, the boiling limit of the evaporator is the function of the fractal dimensions.

For the condenser, the boiling limit ( $Q_{BL,hx}$ ) can also be obtained from Eq. (4-20) by deleting  $N_{ch}$  and using the equivalent parameters of the heat exchanger tube. The minimum value among the evaporator and condenser boiling limits is the final boiling limit of the MCLHP, which can be expressed as:

$$Q_{BL} = \min(Q_{BL,e}, Q_{BL,hx}) \quad (4-21)$$

### **(2) Capillary limit ( $Q_{CL}$ )**

For this novel MCLHP, the capillary limit ( $Q_{CL}$ ) represents the capacity of the porous wick in distributing liquid across the inner surface of the micro-channel heat pipe, thus enabling necessary heat transfer across the heat pipe. The maximum heat transfer resulted from the capillary action of the wick is defined as capillary limit. A higher volume of liquid driven by the porous wick results in a higher heat transfer capacity of the MCLHP

## CHAPTER 4: THEORETICAL ANALYSIS AND COMPUTING MODEL DEVELOPMENT

---

[151][152]. Based on the calculation method developed by Zhang [70], the capillary limit for this novel MCLHP can be obtained by substituting the pressure drops in the MCLHP with the equivalent parameters of the new system, especially by replacing the conventional wick permeability with the new permeability obtained from Eqs. 4-15 to 4-18 based on fractal theory. The expressions used in estimating the pressure drops at different sections of the MCLHP system and within the wick are given in Refs. [139] and [152].

### (3) *Viscous limit ( $Q_{VL}$ )*

The viscous limit represents the level of vapour flow in carrying heat on its flow path. When the operating temperature is low, the viscous forces affect the performance of the vapor flow directly [152]. Using the methods presented in Dunn and Reay [153], Babin et al. [154], and Busse [155], the viscous limit  $Q_{VL,e}$  for the evaporator can be expressed as [75]:

$$Q_{VL,e} = \frac{N_{ch} A_v r_v h_{fg} \rho_v P_v}{16 \mu_v L_{hp}} \quad (4-22)$$

Where,  $N_{ch}$  is the micro-channel port number;  $A_v$  and  $r_v$  are the micro-channel port vapour equivalent area and equivalent radius of the vapour space;  $h_{fg}$  is the latent heat of vaporization;  $\rho_v$  is the vapour density;  $P_v$  is the vapour pressure;  $\mu_v$  is the vapour dynamic viscosity and  $L_e$  (m) is the evaporator length. Eq. (22) can be applied to the other components of the MCLHP, i.e. the vapour header  $Q_{VL,vh}$ , the vapor transportation line  $Q_{VL,vtl}$  and the condenser  $Q_{VL,c}$ . The minimum value of these limits would be the ultimate viscous limit of the MCLHP, which can be expressed as:

$$Q_{VL} = \min(Q_{VL,e}, Q_{VL,vh}, Q_{VL,vtl}, Q_{VL,c}) \quad (4-23)$$

**(4) Sonic limit ( $Q_{SL}$ )**

The sonic limit ( $Q_{SL}$ ) represents the constraint of the heat transfer of a heat pipe by its vapour flow velocity. Increasing the operational temperature of the heat pipe leads to the increased vapour flow velocity. When the vapour flow velocity is close to the sonic or reach the supersonic level, the Mach number of the vapour will be significantly high which will make the heat pipe to choke. In this circumstance, the heat transfer rate of the heat pipe will reach the maximum that is defined as the sonic limit [156]. This sonic limit may occur at a point where vapour flow is in existence, e.g., evaporator, vapour header, vapour transport line and the condenser (heat exchanger). For the evaporator, the sonic limit  $Q_{SL,e}$  can be expressed as [18] [101][149][157]:

$$Q_{SL,e} = N_{ch} A_v \rho_v h_{fg} \left[ \frac{(\gamma_v R_v T_v)}{2(\gamma_v + 1)} \right]^{\frac{1}{2}}. \quad (4-24)$$

Where,  $\gamma_v$  is the vapour's specific heat ratio whose magnitude is 4/3 for the polyatomic working liquid (R134a);  $T_v$  is the average vapour temperature in the micro-channel section; and  $R_v$  is the vapour constant, given by:

$$R_v = \frac{R_0}{M} \quad (4-25)$$

Where,  $R_0 = 8.314 \text{ kJ}/(\text{kmol} \cdot \text{K})$  is the universal gas constant,  $M$  is the molecular weight of the refrigerant R134a.

In this system, Eq. (24) can also be applied to the vapour header, thus yielding  $Q_{SL,vh}$ . It can also be applied to the vapor transportation line and the condenser, yielding  $Q_{SL,vtl}$

## CHAPTER 4: THEORETICAL ANALYSIS AND COMPUTING MODEL DEVELOPMENT

---

and  $Q_{SL,c}$ . Therefore, the minimum value among these limits would be the ultimate sonic limit of the MCLHP, which can be expressed as:

$$Q_{SL} = \min(Q_{SL,e}, Q_{SL,vh}, Q_{SL,vtl}, Q_{SL,c}) \quad (4-26)$$

### (5) *Entrainment limit ( $Q_{EL}$ )*

Owing to the counter flow layout between the liquid and vapour fluids with a heat pipe, a shear force will occur at the interface between the liquid and vapour phases. The entrainment limit represents a constraint of the heat transfer at which a very high shear force takes place between the liquid and vapour flows, leading to the separation of the liquid droplets from the liquid film attached to the heat pipe wall and the mixture of the liquid droplets into the vapour flow.

In this MCLHP system, the entrainment limit may only occur at the evaporator and the condenser, defined as  $Q_{EL,e}$  and  $Q_{EL,c}$  respectively [76][158]. As other parts of the system, i.e., headers and the liquid and vapour transporting lines, have only a single phase fluid, no entrainment would take place between the liquid and vapour flows. These limits can be expressed as:

For the evaporator

$$Q_{EL,e} = N_{ch} A_v h_{fg} \left( \frac{\sigma \rho_v}{\lambda} \right)^{0.5} \quad (4-27)$$

Where  $\lambda$  is the pore diameter.

For the condenser

$$Q_{EL,c} = \left( \frac{\pi(D_{c,i} - 2\delta_w)^2 h_{fg}}{4} \right) \left( \frac{\sigma \rho_v}{D_w} \right)^{0.5} \quad (4-28)$$

Where,  $\sigma$  is the surface tension coefficient of R134a;  $D_{c,i}$  is the internal diameter of the condenser;  $\delta_w$  is the liquid thickness and  $D_w$  is the condensed liquid hydraulic diameter. Thus, the smaller value between  $Q_{EL,e}$  and  $Q_{EL,c}$  is the ultimate entrainment limit of this system, which can be expressed as:

$$Q_{EL} = \min(Q_{EL,e}, Q_{EL,c}) \quad (4-29)$$

### 4.2.3 Algorithm of the Computer Model Set-up

A MATLAB-based analytical model is developed by bringing together the theoretical analysis of the heat pipe heat transfer limits and fractal theory based analysis on permeability, thermal conductivity of the heat pipe wall. The algorithm of the model set-up is: (1) to analyze various heat transfer limits by applying the classical heat transfer capacity equations, Newton-Raphson iteration method and fractal-theory-based analysis on a few key parameters (i.e., permeability, and effective thermal conductivity); (2) to compare these limits one another and sort out the minimum one by using the parallel comparison method; and (3) determination of the finalised heat transfer capacity of MLCHP under different operational conditions.

The model operational procedure can be outlined as follow; this is also indicated in **Fig.4-4**:

- 1) Entering the geometrical data the MCLHP system, which are shown in **Table 3-3**;
- 2) Entering the operational temperature of the MCLHP system, and then calculating the thermodynamic properties of the working fluid (R134a);

## CHAPTER 4: THEORETICAL ANALYSIS AND COMPUTING MODEL DEVELOPMENT

---

- 3) Entering the wick condition of the MCLHP, and then determining whether or not this wicked surface can be characterised by fractal theory, i.e., by using Equations (4-1) to (4-8);
- 4) Giving the initial value of the effective porosity  $\varepsilon$ . If  $\varepsilon \leq 1$ , the dimension  $d$  value in the Euclidean space will be determined (either 2 or 3), fractal dimensions  $D_f$  and  $D_t$  will then be calculated using equations (4-9) to (4-11). Otherwise, the program stops;
- 5) Calculating the fractal permeability and effective thermal conductivity of the porous wick by using Equations (4-12) to (4-19);
- 6) Calculating the boiling limits of the MCLHP evaporator and condenser by using Equations (4-20) and (4-21), and taking the smaller one as the boiling limit of the MCLHP system;
- 7) Working out the capillary limit  $Q_{CL}$  by using the Newton–Raphson method for iteration, described as follow:
  - a) Giving an initial value of capillary limit  $Q_{CL}$  based on the literature review;
  - b) Calculating the maximum capillary head  $\Delta P_c$ , gravity pressure  $\Delta P_g$ , vapor pressure drop  $\Delta P_v$  and liquid pressure drop  $\Delta P_l$  based on the data given in Table 1 and the new fractal permeability obtained from Equations (4-15) to (4-18);
  - c) Calculating the error by using the Equation as following:  
 $Error = ((\Delta P_c + \Delta P_g) - (\Delta P_v + \Delta P_l)) / (\Delta P_c + \Delta P_g)$ . If  $Error < -0.5\%$  (error allowance), reducing  $Q_{CL}$  by 1, and then returning to step (2) to re-calculate;
  - d) If  $Error > 0.5\%$  (error allowance), increasing  $Q_{CL}$  by 1, and then returning to step (2) for re-calculate;
  - e) If  $-0.5\% \leq Error \leq 0.5\%$  (error allowance), the heat balance is achieved, and thus the real capillary limit can be obtained.
- 8) Calculating the sonic limits relating to different parts of the MCLHP system, and taking the smallest one as the sonic limit of the system, by using Equations (4-24) to (4-26);
- 9) Calculating the entrainment limits in relation to the porously wicked absorbing micro-channel and heat exchanger, and taking the smaller one as the entrainment limit of the whole system by Equations (4-27) and (4-29);

## CHAPTER 4: THEORETICAL ANALYSIS AND COMPUTING MODEL DEVELOPMENT

---

- 10) Comparing the limits one another, and taking the minimum as the governing limit of the MCLHP system, based on the minimum value searching principle;
- 11) Increasing the value of the effective porosity  $\mathcal{E}$ , and return to the step (5) to re-calculate. If  $\mathcal{E} > 1$ , program stops.

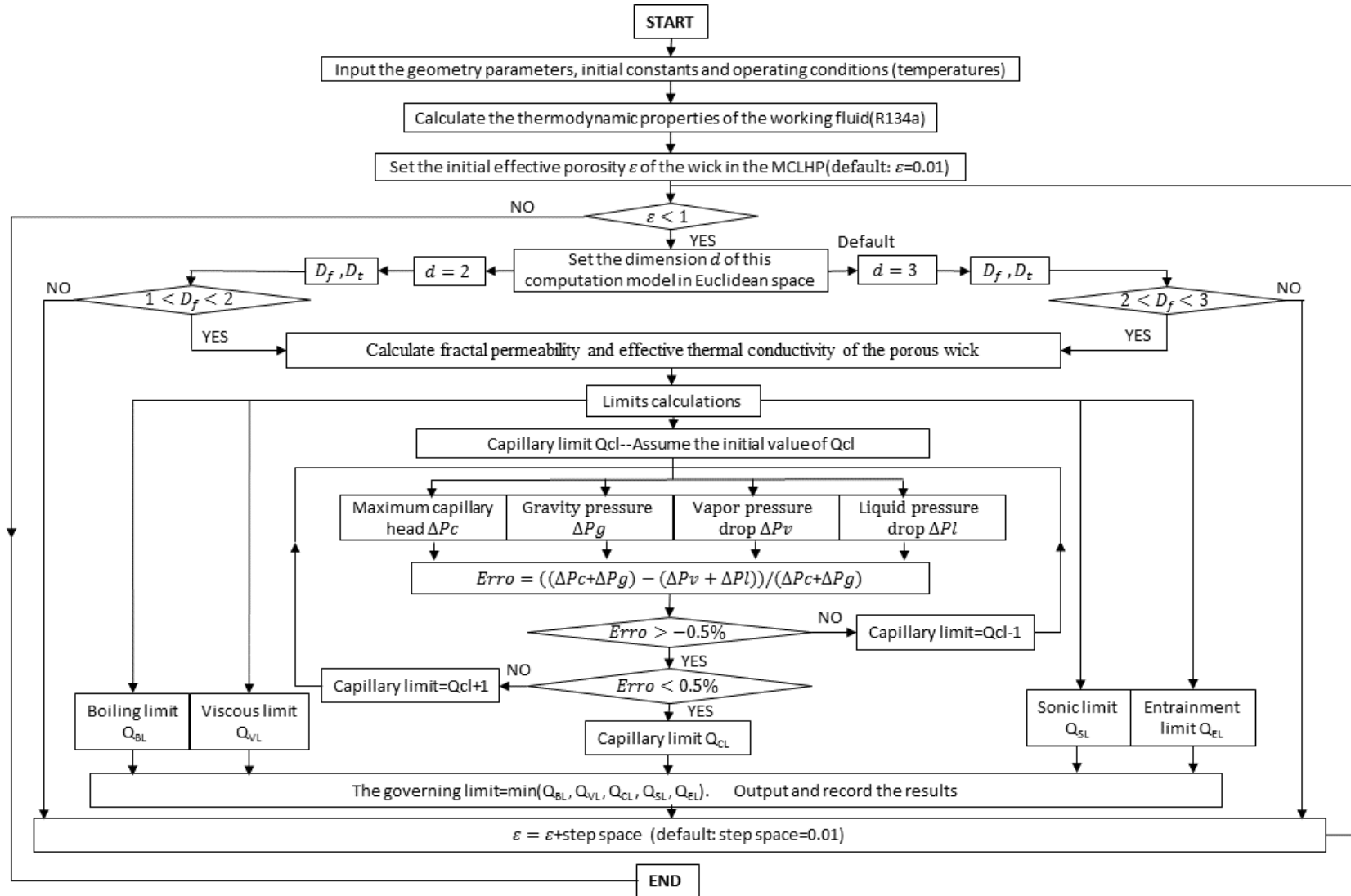


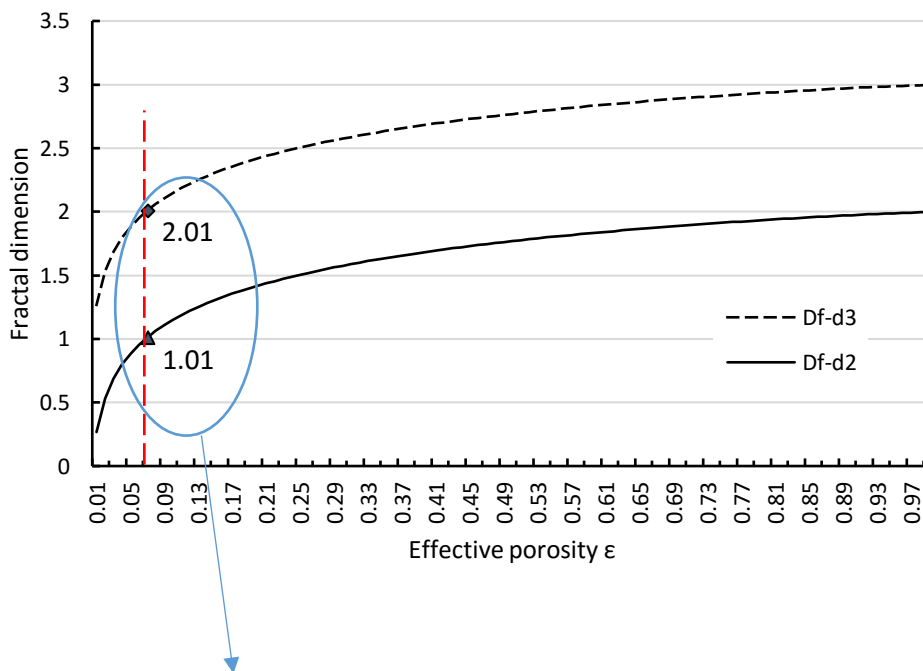
Fig.4- 4: Computation program flow chart

### 4.2.4 Case study - results and discussion

#### (1) Influence of the wick structure's fractal parameters to porosity

The correlation between the fractal dimensions ( $D_f$ ) and effective porosity ( $\epsilon$ ) is shown in Fig.4- 5. With the Euclidean dimension values of 2 and 3, the pores distribution fractal dimensions  $D_f$  of the porous wick increased with the increase of the effective porosity  $\epsilon$ . This can be easily understood with such a logic: increasing the effective porosity ( $\epsilon$ ) leads to the increased portion of pores, which consequently leads to a higher pore distribution fractal dimension ( $D_f$ ).

In terms of the limit, when the porosity figure approaches 1, the selected cell of the porous medium becomes a smooth plane. It is interesting to see that when porosity ( $\epsilon$ ) is less than 0.07 and Euclidean dimension ( $d$ ) is 2 and 3, the fractal dimension ( $D_f$ ) is always less than 1 and 2 respectively. This finding indicates that when porosity  $\epsilon$  is less than 0.07, the pores distribution in porous media is non-fractal.



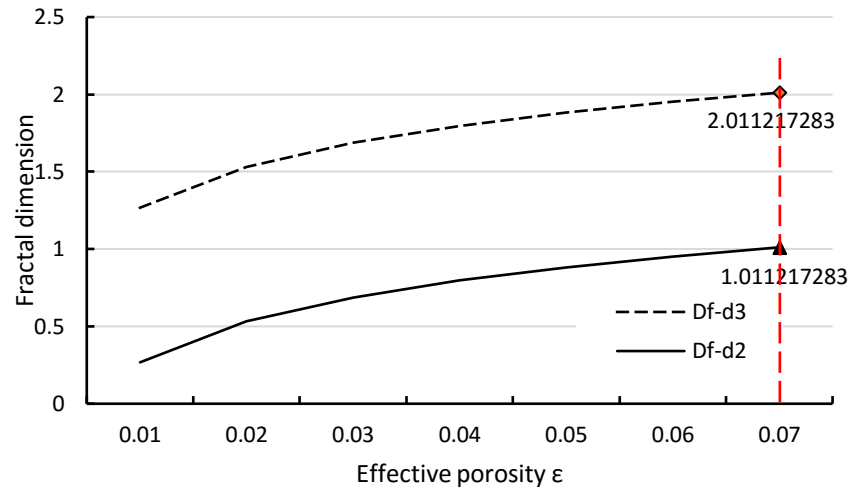


**Fig.4- 5: Fractal dimension Df vs. Effective porosity  $\epsilon$  (d=2, d=3)**

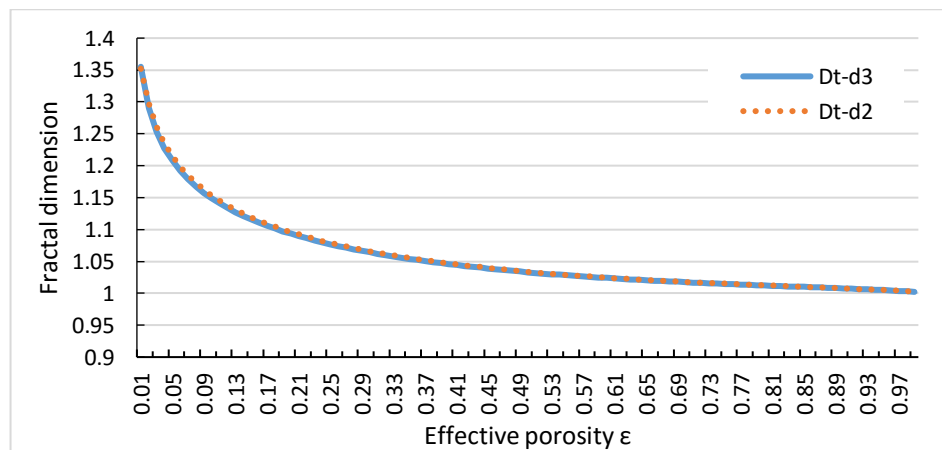


**Fig.4-6: Fractal dimensions Dt vs. effective porosity  $\epsilon$  (d=2, d=3)**

**Fig.4-6** indicates that for the Euclidean dimension of either 2 or 3, fractal dimensions for different cells in a porous media are almost the same. Furthermore, with the increase of porosity, the tortuosity fractal dimension initially falls sharply and then slowly approaches to 1. This is because an increased effective porosity ( $\epsilon$ ) leads to a lower tortuosity of capillaries, which gives a lower tortuosity fractal dimension. In this research, the dimension value of 3 is thought to be realistic figure applied.

CHAPTER 4: THEORETICAL ANALYSIS AND COMPUTING MODEL DEVELOPMENT

Correlation between permeability ( $K_p$ ) and effective porosity ( $\epsilon$ ) is shown in Fig.4-7.

Under the condition of Euclidean dimension of 3, permeability ( $K_p$ ) increases with the increase of effective porosity ( $\epsilon$ ). When effective porosity approaches to 1, the permeability  $K_p$  reaches its maximum possible value of  $7 \times 10^{-11} \text{ m}^2$  at the pore diameter of 200  $\mu\text{m}$ , and  $1 \times 10^{-12} \text{ m}^2$  at the pore diameter of 50  $\mu\text{m}$ .

It is also seen that permeability is directly affected by the pores' maximum diameter; a larger diameter results in a higher permeability. This could be explained as such: a larger pore diameter leads to a larger pore area, while a larger pore area causes a higher effective porosity and a higher fractal dimension. Permeability was found to grow sharply when effective porosity is less than 0.5 and then tend to slow down afterwards. When effective porosity is 0.5, the permeability  $K_p$  is about  $3.74 \times 10^{-12}$  at pore diameter of 100mm, approximately the same value as that for the experimental porous media sintered copper powder at porosity 0.52 [76] [158].

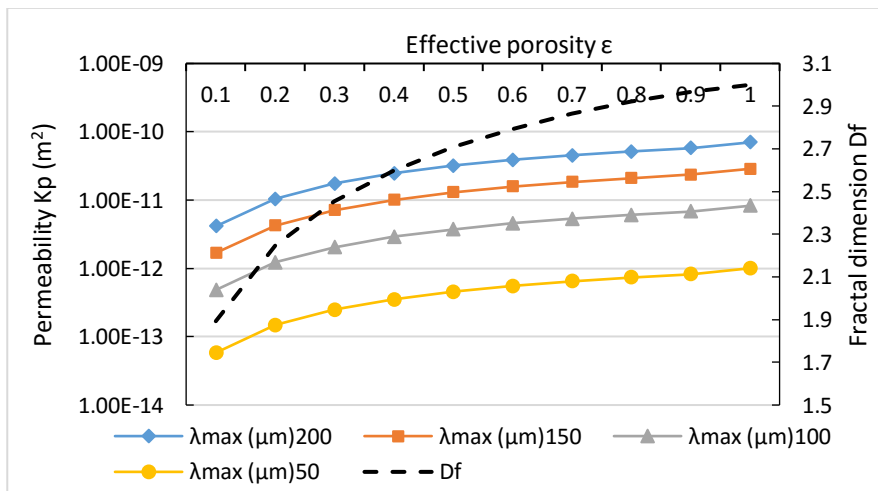


Fig.4-7. Permeability of different pores diameter vs. effective porosity  $\epsilon$  ( $d=3$ )

Correlation between effective thermal conductivity ( $K_e$ ) and effective porosity ( $\epsilon$ ) is shown in Fig.4-8. Under the condition of Euclidean dimension of 3, the effective thermal conductivity ( $K_e$ ) decreases with the increase of effective porosity ( $\epsilon$ ). This trend can be

## CHAPTER 4: THEORETICAL ANALYSIS AND COMPUTING MODEL DEVELOPMENT

---

explained by the fact when the porosity increases, the solid volume fraction decreases, which leads to the decrease of the thermal conductivity. When effective porosity approaches to 1, the effective thermal conductivity  $K_e$  reaches its minimum value of 0.066 W/m/K at the pore diameter of 50  $\mu\text{m}$ , and 0.12 W/m/K at the pore diameter of 200 $\mu\text{m}$ . It is also found that when the thermal conductivity is less than 0.5, the effective thermal conductivity decreases significantly and then tends to decrease slowly. It is seen that the effective thermal conductivity increases as the pore diameter increases.

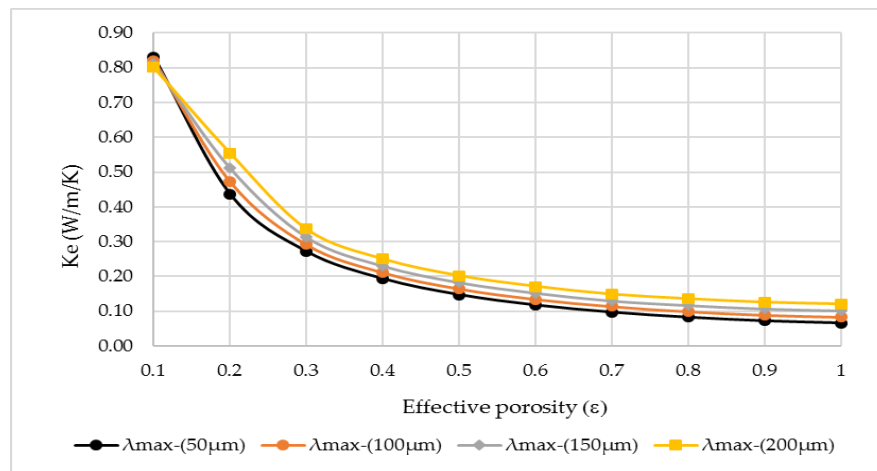


**Fig.4-8. Effective thermal conductivity of different pores diameter vs. effective porosity  $\epsilon$  ( $d=3$ )**

### *(2) The heat transfer limits of the MCLHP*

By bringing the fractal parametrical data for the sintered powder wick into the limits equations, the variation of the limits against these parameters was developed and analysed.

These are illustrated below:

**Table 4-1** presents the heat transfer limits of the MCLHP at Euclidian dimension of 3 and maximum pore diameter of 100 $\mu\text{m}$ . Comparison among these five potential limits indicates that governing limit of the MCLHP is the capillary limit that appears to be the

**CHAPTER 4: THEORETICAL ANALYSIS AND COMPUTING MODEL DEVELOPMENT**

---

lowest of the five limits. It is also found that the boiling limit ( $Q_{BL}$ ) and the capillary limit ( $Q_{CL}$ ) increase with the increase of the porosity, mainly owing to the fact that liquid flow rate is proportionally increasing with porosity. Entrainment limit ( $Q_{EL}$ ) remains constant as the porosity is not relevant to the pore diameter. Also, the viscous limit ( $Q_{VL}$ ) and the sonic limit ( $Q_{SL}$ ) remain constant because these two items are not affected by effective porosity.

**Table 4-1. Different heat transfer limits ( $d=3, \lambda_{max}=100 \mu m$ )**

Porosity	Boiling	Capillary	Viscous	Sonic limit	Entrainment
$\epsilon$	limit	limit	limit	$Q_{SL}(kW)$	Limit $Q_{EL}$
	$Q_{BL}(kW)$	$Q_{CL}(kW)$	$Q_{VL}(kW)$		(kW)
0.2	1490.83	<b>0.20</b>	698105.56	24503.70	172.69
0.3	920.41	<b>0.30</b>	698105.56	24503.70	172.69
0.4	666.14	<b>0.40</b>	698105.56	24503.70	172.69
0.5	518.82	<b>0.50</b>	698105.56	24503.70	172.69
0.6	423.72	<b>0.60</b>	698105.56	24503.70	172.69
0.7	358.46	<b>0.70</b>	698105.56	24503.70	172.69
0.8	312.31	<b>0.80</b>	698105.56	24503.70	172.69
0.9	279.87	<b>0.90</b>	698105.56	24503.70	172.69

**(3) Boiling limit ( $Q_{BL,e}$ ) against effective porosity ( $\epsilon$ ) and fractal dimensions ( $Df$ )**

**Fig.4-9** shows the variation of the boiling limit ( $Q_{BL,e}$ ) with effective porosity. Increasing effective porosity leads to the decreased boiling limit of the MLCHP. The reason for this is such explained: a higher relative porosity in a MCLHP wick reflects a lower solid volume fraction and thus a lower effective thermal conductivity. A lower thermal

conductivity increases the heat resistance of the wick. For an excessively higher heat resistance, the temperature of heat pipe wall is increased, which results in the boiling of the liquid in the wick. In this case, the vapour bubbles, due to the nucleation within the wick structure, cause hot spots and obstruct flow of the fluid within the heat pipe, thus leading to the dry-out of the wick.

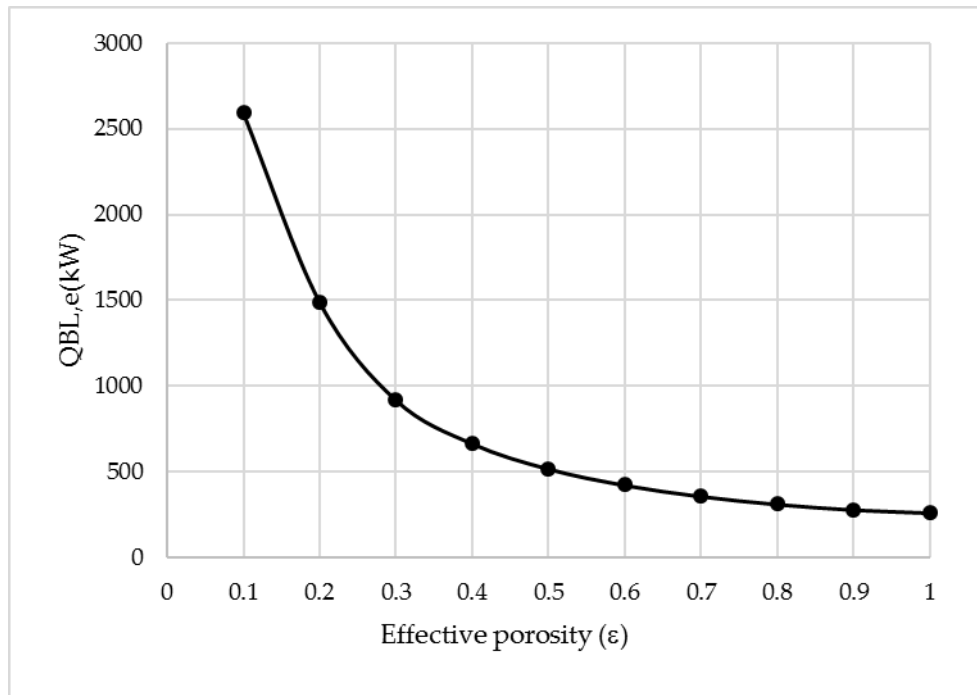


**Fig.4-9. Boiling limit ( $Q_{BL}$ ) vs. Effective porosity ( $\epsilon$ ) (Euclidean dimension  $d=3$ )**

**Fig.4-10** shows the variation of the boiling limit ( $Q_{BL}$ ) with fractal dimension ( $D_f$ ) of the pore wick area. The boiling limit decreases with the increase of the fractal dimension. The reason for this is such explained: a higher fractal dimension in a LHP wick surface represents a higher porosity, which means that a lower solid fraction in the wick leads to a lower wick effective thermal conductivity, and a lower level of the boiling limit of the MLCHP.

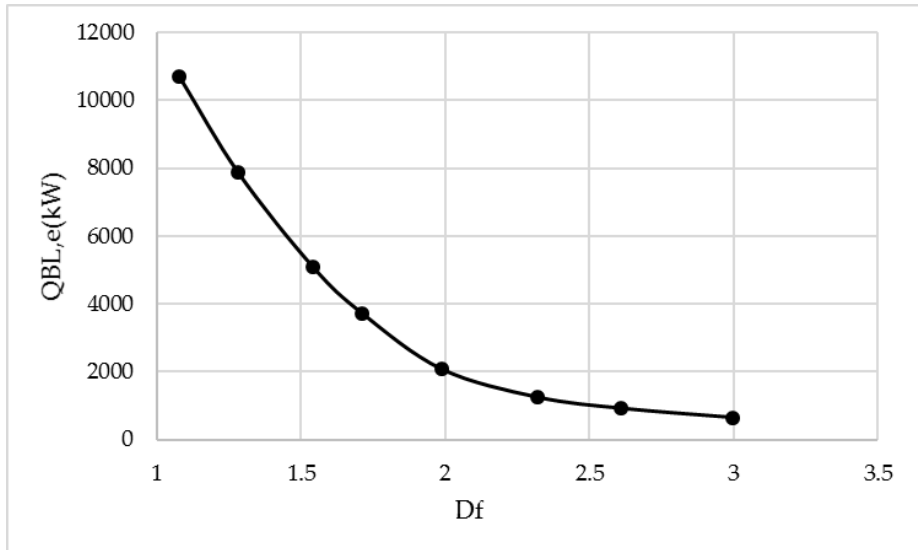


**Fig.4-10. Boiling limit (QBL) vs. Pore distribution fractal dimension (Df) (Euclidean dimension d=3)**

**Fig.4-11** shows the variation of the boiling limit ( $Q_{BL,e}$ ) with tortuosity fractal dimension ( $D_t$ ). Increasing fractal dimension ( $D_t$ ) led to the increase of the boiling limit ( $Q_{BL,e}$ ); This can be such explained: a higher tortuosity fractal dimension ( $D_t$ ) reflects a higher tortuosity of capillaries, while a higher tortuosity of capillaries can cause a lower thermal resistance that tends to increase the boiling limit of a MCLHP.

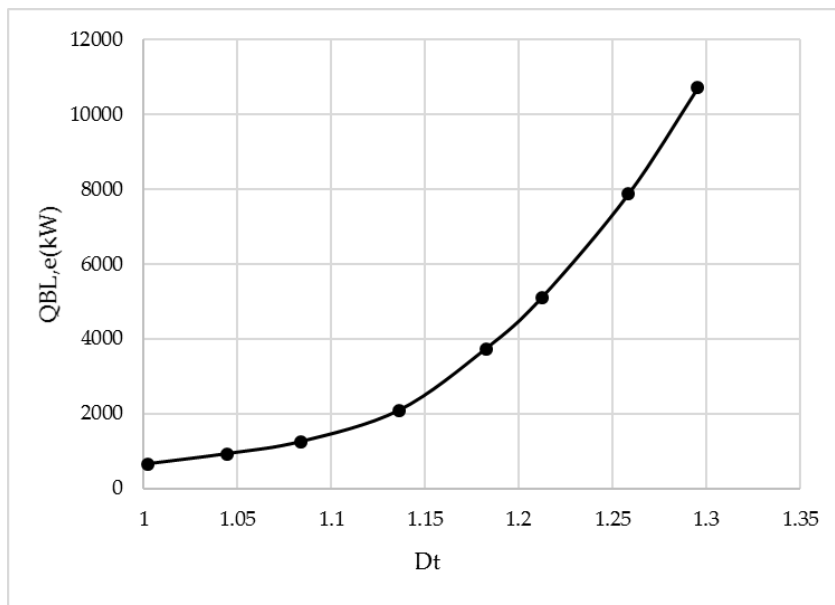
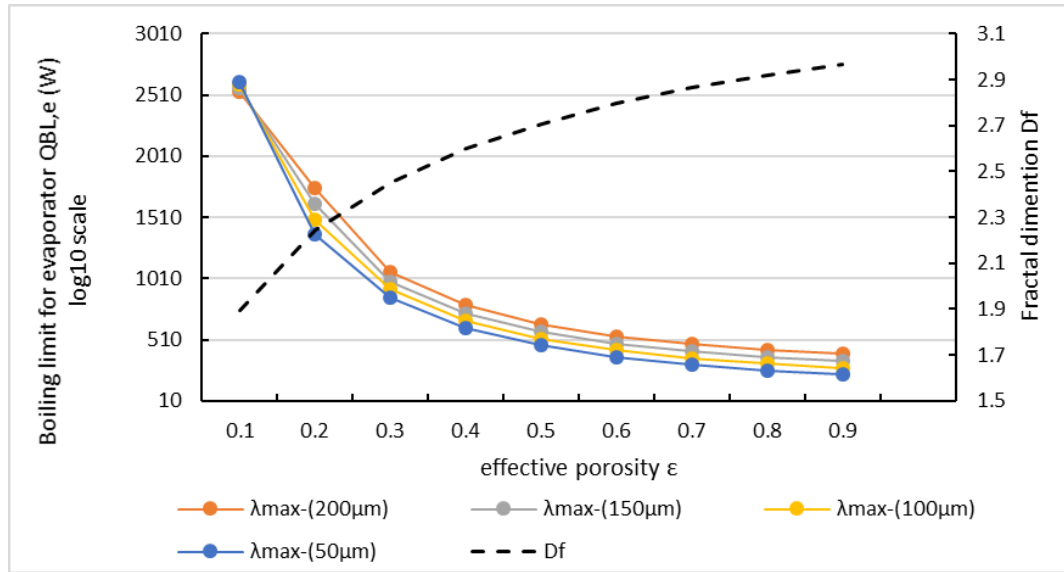
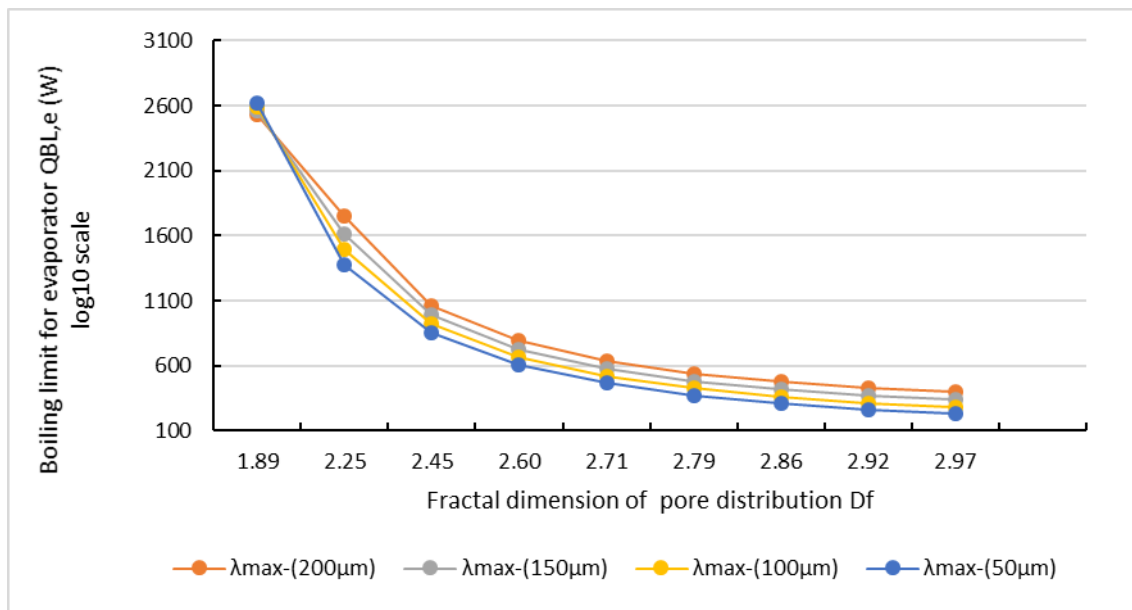


**Fig.4-11. Boiling limit (QBL) vs. the tortuosity fractal dimension  $D_t$ , d=3**



(a)



(b)

**Fig.4-12. Boiling limit for evaporator  $Q_{BL,\epsilon}$  vs. effective porosity  $\epsilon$  (a) and fractal dimension  $D_f$  (b) ( $d=3$ )**

**Fig.4-12** shows the variation of boiling limit with effective porosity and fractal dimension at different pore sizes (i.e., maximum pore diameter). Increasing effective porosity and

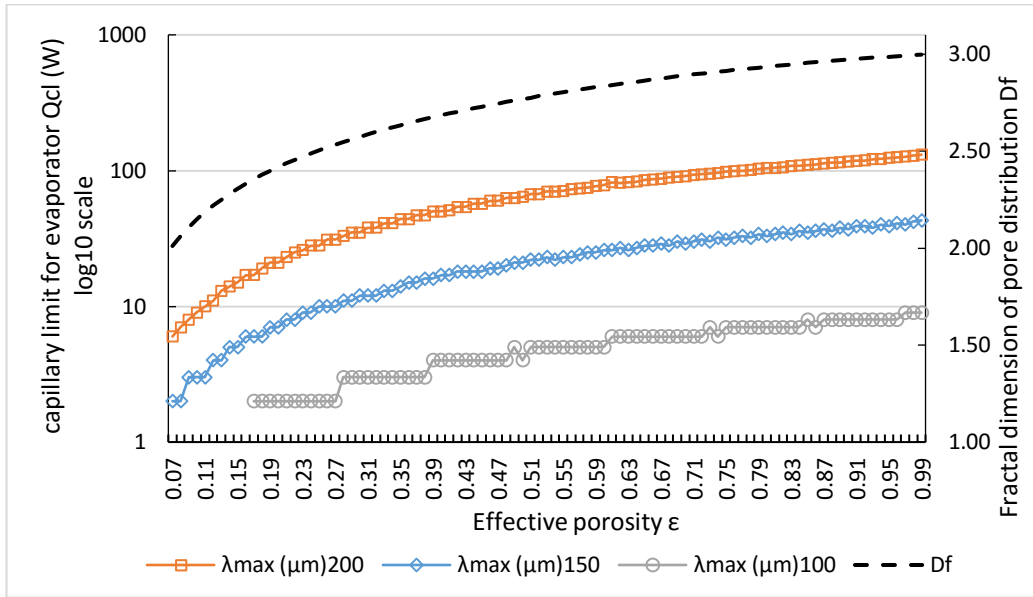
## CHAPTER 4: THEORETICAL ANALYSIS AND COMPUTING MODEL DEVELOPMENT

---

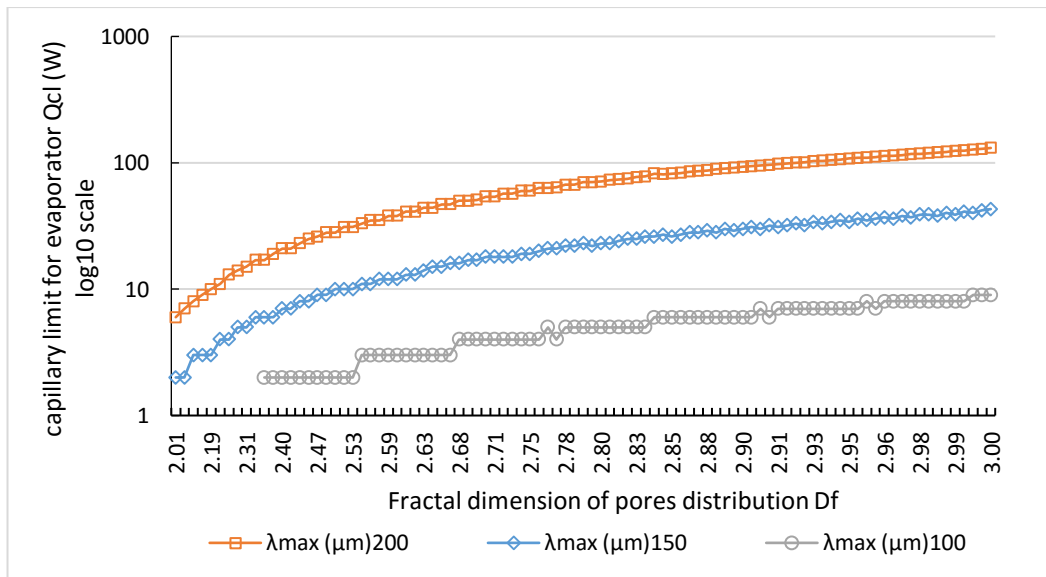
fractal dimension lead to the decreased boiling limit. This may be such explained: a higher porosity represents a larger pore area, while a higher fractal dimension refers to a larger quantity of pores. Both lead to a lower solid volume fraction in the wick and this leads to a lower thermal resistance of the wick that can increase the potential of liquid dry out, thus decreasing the boiling limit of the MCLHP. It is also found that boiling limit of the evaporator is closely related to the pores' size (i.e., maximum diameter). An increased maximum pore diameter means a decreased solid fraction of the wick and then thus this leads to the decrease of the wick effective thermal conductivity, which tends to decrease boiling limit of the MCLHP (referring to the evaporator).

### *(4) Capillary limit ( $Q_{cl}$ ) against effective porosity ( $\epsilon$ ) and fractal dimension ( $D_f$ )*

**Fig.4-13** shows the variation of capillary limit ( $Q_{cl}$ ) with effective porosity ( $\epsilon$ ) and fractal dimension ( $D_f$ ) at different pore sizes. Increasing the effective porosity and fractal dimension lead to the increased capillary limit. Reasons for these can be such explained: a higher effective porosity and a higher fractal dimension lead to a larger pores space that can hold more fluid within the wick. As the water will be distributed to the heat pipe surface through the capillary action of the wicks, and the increased water volume means a larger volume of water distribution, the heat transfer rate via the capillary action increases with the increase of the hold water within the wick. It is also found that the capillary limit increases with the increase of the pores' maximum diameter. This is because that a larger maximum pores diameter leads to a larger effective porosity which subsequently increase the capillary limit of the MCLHP.



(a)



(b)

**Fig.4-13. Capillary limit ( $Q_{cl}$ ) vs. Effective porosity  $\epsilon$  (a) and fractal dimension  $D_f$  (b), ( $d=3$ )**

**Fig.4-14** shows the variation of fractal dimension ( $D_f$ ) with porosity  $\epsilon_c$  of the skeleton within the wick. It is interesting to see that increasing the porosity ( $\epsilon_c$ ) leads to a slight fall of fractal the dimension ( $D_f$ ). This is because a larger porosity ( $\epsilon_c$ ), though leading to

a larger number of pores within the skeleton, may also cause a blockage in the pores. Increasing number of the blocked micro-pores leads to the decrease of effective porosity ( $\epsilon$ ) of the whole wick structure, which results in the reduced  $D_f$ . However, compared to the macro-pores of the wick structure, influence by the blocked micro-pores is relatively smaller, which explains why the fall of fractal dimension ( $D_f$ ) is a bit smaller.

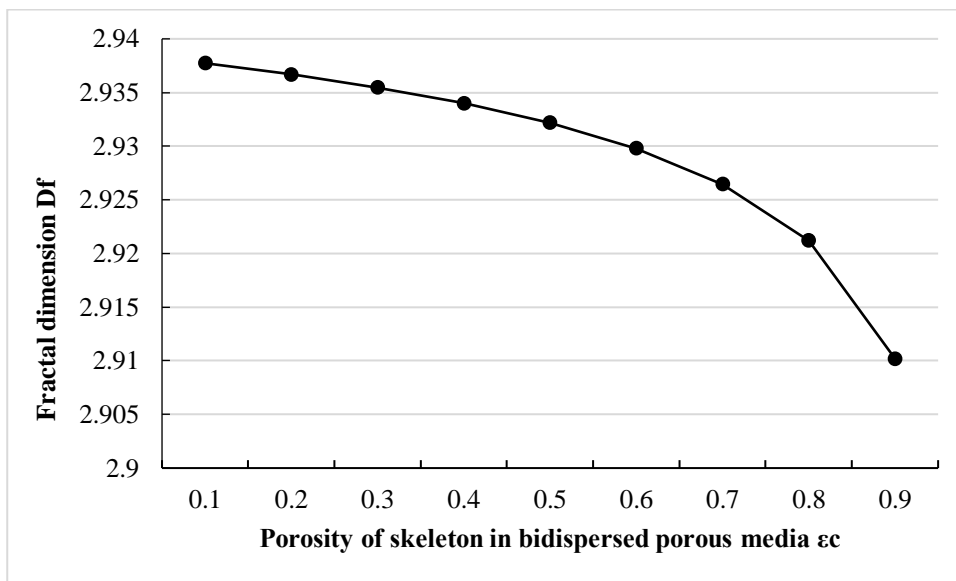
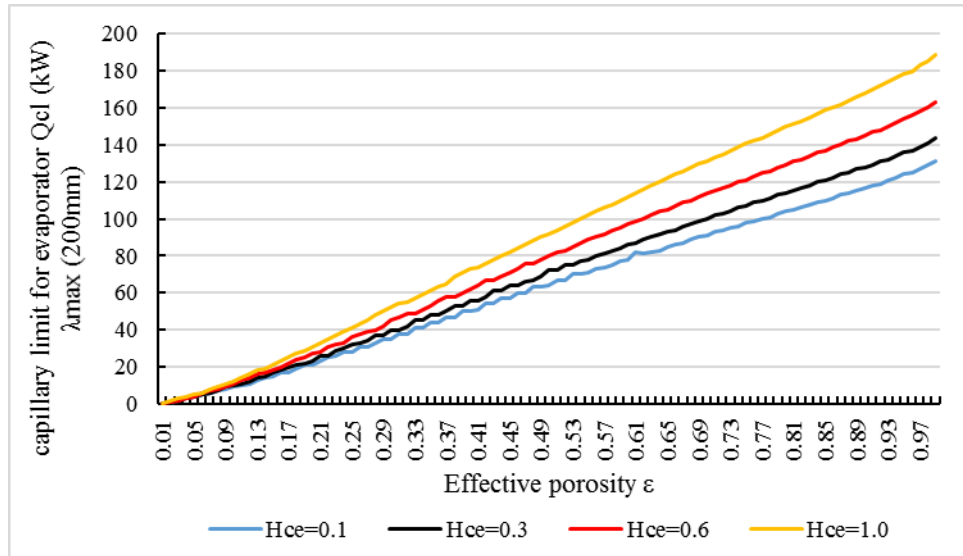
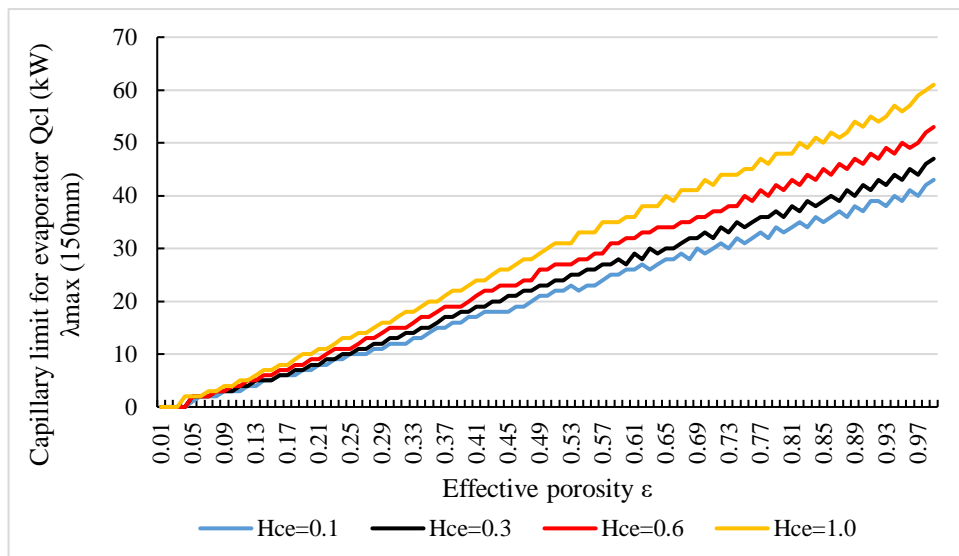


**Fig.4-14. Fractal dimension  $D_f$  vs. Porosity of skeleton (Effective porosity  $\epsilon=0.8$ ,  $d=3$ )**

**Fig.4-15** show the variation of capillary limit with effective porosity at several height differences between the evaporator and the condenser. Similar to **Fig.4-14a**, increasing effective porosity of the evaporator leads to a proportional increase of the capillary limit. A larger height difference between the evaporator and the condenser leads to a higher capillary limit. Reasons for this are such explained: as the micro-channel evaporator panel and the condenser are all vertically laid, which means that gravity is the driven force to the downward liquid flow, the impact of the height difference to capillary limit is positive. A higher height difference gives a higher driven force to the liquid flow which help increase the level of the capillary limit.



(a)



(b)

**Fig.4-15. Capillary limit vs. Porosity at different height differences (d=3)**

**(5) Impact of different parameters on the maximum heat transfer capacity (governing limit)**

By varying the investigated impactors separately while keeping the operational temperature, porosity at 0.8, maximum pore size at 200 $\mu$ m, fractal dimension Df=3, and other MCLHP parameters constant, a change of single parameter can impact the maximum heat transfer capacity of the MCLHP. **Fig.4-16** illustrated that increasing

## CHAPTER 4: THEORETICAL ANALYSIS AND COMPUTING MODEL DEVELOPMENT

evaporator inclination angle can lead a rising heat transfer capacity. And more micro-channel flat tubes applied could bring in increasing heat transfer capacity as shown in **Fig.4-17**, whilst the longer evaporator length caused declined heat transfer capacity as presented in **Fig.4-18**. The reasons may located in the specialization of this novel MC-LHP structure, and the governing limit is capillary limit, thus larger evaporator inclination angel up to vertical, more numbers of channels and declined evaporator length can lead higher capillary limit.

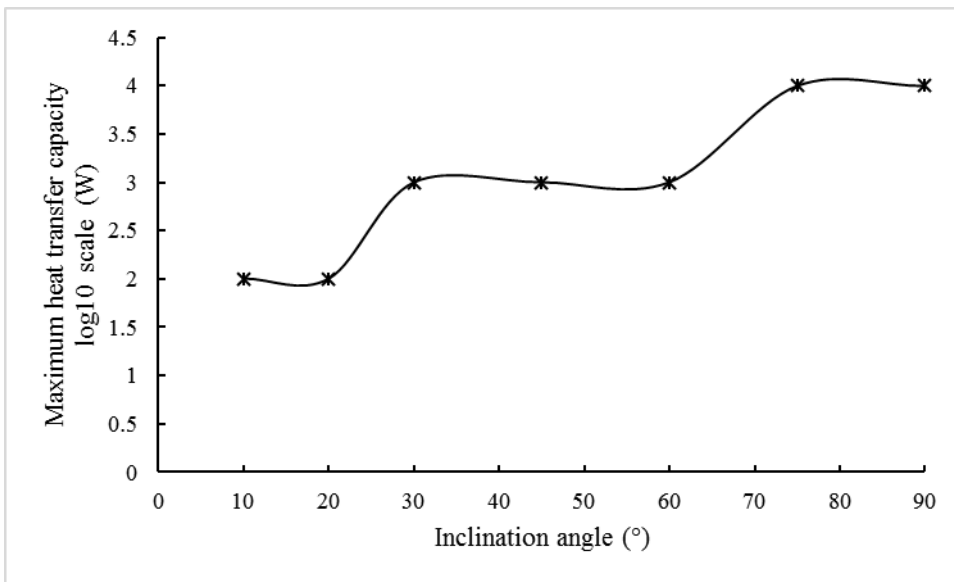


**Fig.4-16. Impact of evaporator inclination angle on the maximum heat transfer capacity**

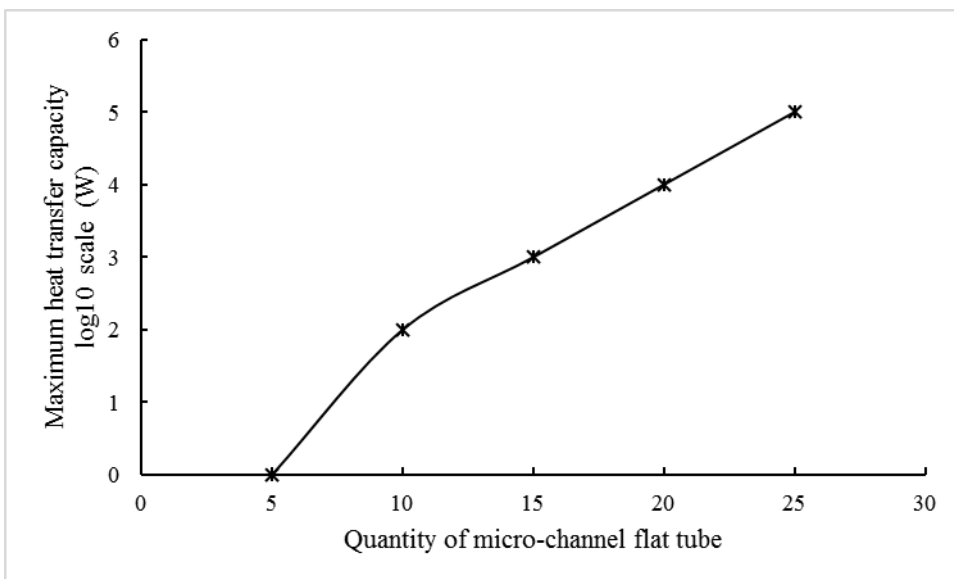


**Fig.4-17. Impact of quantity of MC-flat tube on max-heat transfer capacity**

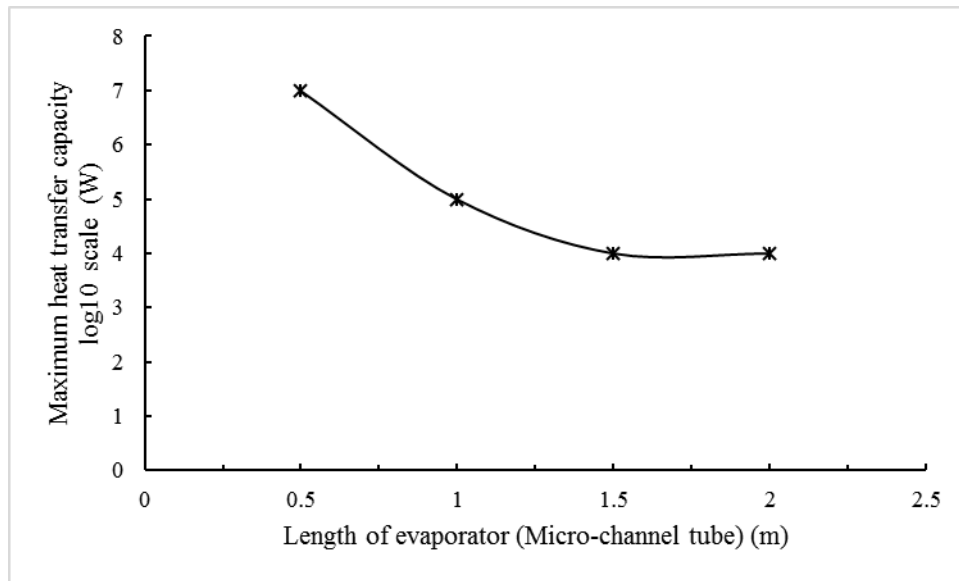


**Fig.4-18. Impact of evaporator length on max-heat transfer capacity**

In summary, comparison among these five limits was made using the minimum value searching approach, leading to the determination of the final heat transfer constraint of the MCLHP, which is identified as the capillary limit. A higher effective porosity and a larger pore diameter lead to an increased wick fractal dimension and thus a higher capillary limit. An increased height difference between the evaporator and the condenser also increases the heat transfer (i.e. capillary) limit of the MCLHP. Decreased effective porosity ( $\epsilon$ ), pores portion, and increased tortuosity of capillaries help enhance the heat transfer (boiling) limit of the MCLHP. Overall, fractal theory is thought to be an ideal method to address the impact of an irregular porous wick on the heat transfer performance of a MCLHP.

In addition, with the considered design of the MCLHP system and operational conditions, the system can achieve a higher heat transfer limit with larger evaporator inclination angel (vertical), more numbers of channels (21 MC-flat tube), evaporator length at 1.9m.

### **4.3 Steady state analytical model for the PV/MCLHP system**

This section aims to develop a steady-state analytical model to investigate the performance of this integrated PV/MCLHP heating and power generation system and its energy efficiencies under different controlled conditions. A parametric study will be performed to assess the influence of the key environmental and structure parameters on the energy efficiency of this novel system. In addition, the efficiency of the system will be compared with a conventional PVT-LHP. The theoretical model developed in this section will help to design and optimize such system for space heating, hot water and power supply.

#### **4.3.1 Theoretical and governing equations**

This computation model is based on the heat transfer process was developed to investigate the performance by establishing energy balance equations of the different section of this system, namely: (1) glazing cover; (2) PV layer; (3) Aluminium plate; (4) micro-channel loop heat pipe; (5) co-axial triple-pipe heat exchanger. In order to simplify the calculation, several assumptions were made as following:

- a. The temperature gradient across the glazing thickness was ignored.
- b. The ohm-electrical losses within the PV cells and layer were negligible.
- c. Heat capacities of the EVA filler were neglected, which enables assumption that the temperature distribution within the PV layer is uniform.
- d. Heat losses through the module insulation are negligible.
- e. Heat losses through the vapour and liquid transportation lines are ignored.

*(1) Heat balance of the glazing layer of PV lamination*

As shown in **Fig.4-19**, the energy balance of glazing layer includes solar radiation input, cover reflection, cover absorption, heat loss (conduction, convection, radiations). Since there is no glazing cover, then the solar energy received by the PV module which, is a function of three main components including (1) solar radiation striking on the panel, (2) the transmittance of glazing layer of PV lamination, and (3) the absorption of the PV layer and its baseboard, can be expressed as [159][160]:

$$Q_{abs} = \tau_{g,pv}[\alpha_{pv}\beta_p + \alpha_b(1 - \beta_p)]F_e I \quad (4-30)$$

Where,  $\tau_{g,pv}$  is the light transmittance of the glazing layer of PV lamination;  $\alpha_{pv}$  and  $\alpha_b$  are the absorption ratios of the PV layer and its baseboard;  $\beta_p$  is the packing factor of the PV layer;  $F_e$  is the effective collector area of the PV/T module ( $m^2$ ).

For a multi-glazing covered PV/T panel, the loss heat from the module will experience (1) heat transfer from the PV absorber surface to the inner glazing cover; (2) heat transfer from the inner cover to the outer cover; and (3) heat transfer from the outer glazing cover to the ambient air. The related model can be referenced to [99]Annex 2.

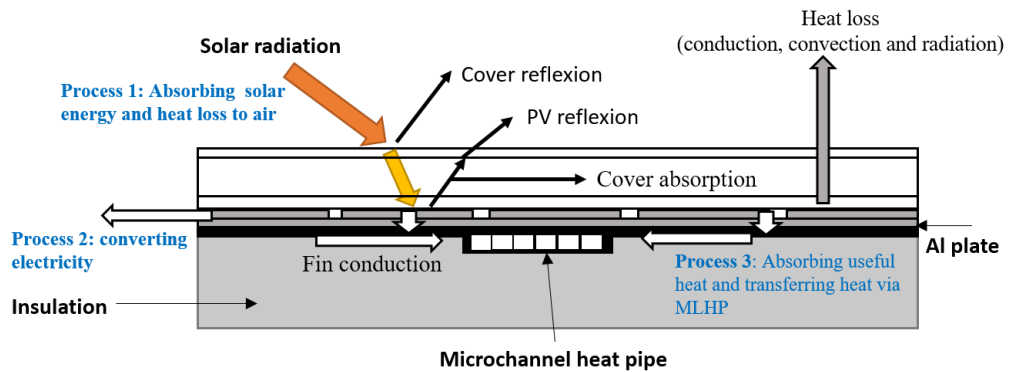


**Fig.4-19. Solar energy process model from the ambient air to the PV/MC-evaporator**

## CHAPTER 4: THEORETICAL ANALYSIS AND COMPUTING MODEL DEVELOPMENT

---

When the PV/evaporator receives the solar radiation striking on its upper surface, most of the solar radiation is absorbed by the PV/T panel, part of which is converted into electricity by PV cells to supply power and the rest is finally transformed into thermal energy. At the same time, a small percentage of the solar radiation energy will be dissipated into the sky resulted from the occurring directional/diffusive reflection and conductive/convective heat transfer. Under this relative specific steady-state operating condition, the useful energy obtained by the PV/T module is equal to the energy reaching to the PV surface minus the associate direct and indirect heat losses, which refers to the heat dissipation from the module surface to the sky through conduction, convection and infrared radiation. Thus the useful solar energy can be expressed as:

$$Q_U = Q_{abs} - Q_L \quad (4-31)$$

Where  $Q_L$  is the total heat loss (W) from the glazing of PV lamination to the surrounding air, experiencing (1) heat conducted through the adhesive layer from the PV surface to the glazing lamination and heat transfer from the outer surface of the glazing lamination layer to the surrounding air by convective and infrared radiation.

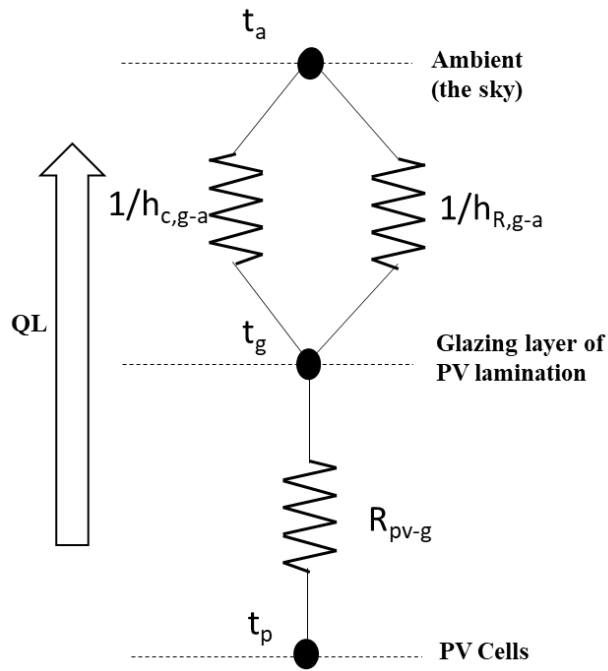


**Fig.4-20 Thermal circuit model**

As shown in **Fig.4-20**, the heat loss can be written as

$$Q_L = K_L F_e (T_p - T_a) \quad (4-32)$$

Where,  $T_p$  and  $T_a$  are the average temperature of PV layer and the surrounding air temperature (K);  $K_L$  is the heat loss coefficient (W/m<sup>2</sup>K) and can be expressed as

$$K_L = (R_{pv-g} + \frac{1}{h_{c,g-a} + h_{R,g-a}})^{-1} \quad (4-33)$$

Where,  $R_{pv-g}$  is the thermal resistance between the glazing layer and the PV (m<sup>2</sup>K/W), written as  $R_{pv-g} = \delta_{ad}/\lambda_{ad}$ ;  $h_{c,g-a}$  is the convective heat transfer coefficient from the glazing layer to the surrounding air (W/m<sup>2</sup>K), which can be expressed as

$$h_{c,g-a} = \frac{8.6v^{0.6}}{L^{0.4}} \quad (4-34)$$

$v$  is the wind velocity (m/s), and  $L$  is the characteristic length of the collector (m)

## CHAPTER 4: THEORETICAL ANALYSIS AND COMPUTING MODEL DEVELOPMENT

---

And  $h_{R,ga}$  is the radiation relevant coefficient which, converting the radiation heat transfer into equivalent convective heat transfer, can be calculated by:

$$h_{R,g-a} = \varepsilon_g \sigma (T_g^2 + T_e^2)(T_g + T_e) \quad (4-35)$$

$T_g$  and  $T_e$  are the average temperature of glazing layer and the sky (K) and  $T_e = 0.0552T_a^{1.5}$ ;  $\varepsilon_g$  is the emissivity of the glazing layer of PV lamination;  $\sigma$  is the Stefan-Boltzman constant ( $5.67 \times 10^{-8} W/(m^2 \cdot K^4)$ ).

### (2) Power generation ability

When the PV/evaporator receives the solar radiation striking on its upper surface, part of the absorbed solar energy is converted into electricity by PV cells to supply power. The PV cells' electrical efficiency is proven to be dependent upon the PV cells' surface temperature [26], which can be written as:

$$\eta_c = \eta_{rc} [1 - \beta_{pv}(T_{pv} - T_{rc})] \quad (4-36)$$

Where,  $\eta_{rc}$  is the initial electrical efficiency at reference temperature;  $\beta_{pv}$  is temperature coefficient;  $T_{pv}$  is PV cells temperature at operation;  $T_{rc}$  is reference temperature.

Then the overall electricity output is

$$Q_e = \eta_c \beta_p \alpha_{pv} \tau_{g,pv} F_e I \quad (4-37)$$

Therefore, the PV module's solar electrical efficiency can be obtained from

$$\eta_e = \frac{Q_e}{F_e I} \quad (4-38)$$

***(3) The remaining absorbed solar energy is transferred into MC-LHP refrigerant***

As described above, under the relative quasi-steady state condition, except the converting electricity part and the heat loss, the rest part of the absorbed solar energy is finally transformed into thermal energy. This part is the useful energy delivered by the PV/T module for heating, which thus can be calculated by the rate of absorbed solar energy minus the converted electricity and heat loss, expressed as

$$Q_{th} = Q_{abs} - Q_L - Q_e \quad (4-39)$$

Where,  $Q_{th}$ , the useful energy, will finally be converted into heat which, carried out by the refrigerant evaporating inside the micro-channel loop heat pipe, is denoted by  $Q_u$ . Subsequently as a result, the solar thermal efficiency of this PV/T module can be defined as

$$\eta_{th} = \frac{Q_{th}}{F_e I} = \frac{Q_u}{F_e I} \quad (4-40)$$

Furthermore, the PV/T module's overall solar efficiency denoted by  $\eta_o$  can be obtained by

$$\eta_o = \eta_e + \eta_{th} \quad (4-41)$$

At the LHP's evaporation section, i.e. micro-channel array, the useful energy ( $Q_{th}$ ), which is converted into the micro-channels, leads to the working fluid (Refrigerant R134a) evaporating inside the micro-channels. Then the vapour fluid which, is gathered into the upper vapour header and through the vapour transportation line, moves forward to the co-axil triple-pipe heat exchanger which works as the condenser where the vapour is condensed and releases the condensation heat into the adjacent water flow inside the middle annular tube, thus leading to hot water supply. The condensed refrigerant then

travels back to the upper liquid feeding header via the liquid transportation line. And finally, based on the pressure difference between the head liquid and the vapour in micro-channels, the backing liquid will penetrate the tiny holes opened on the side wall of micro-channels to formulate continuous downward wetting condition of the LHP's evaporation section to absorb heat and evaporate again, thus forming the complete heat transportation cycle, as shown in **Fig.4-3**. This heat transportation process which, involves a set of thermal resistances resulting in temperature variation of the refrigerant, is presented in **Fig.4-21** and detailed as the following section.

**(4) Thermal resistances**

Along the length direction of the Micro-channel heat pipe evaporation section, there would be no existing temperature gradient, owing to the even heat input. Then the total useful solar heat transferred into the water in the middle annulus tube of the co-axil triple-tube heat exchanger from absorbed Al plate can be calculated according to the Hottel-Whillier model[61][99] [161]:

$$Q_u = LWF_{th}[q_{abs} - K_L(T_w - T_a) - q_e] \tag{4-42}$$

Where,  $L$  and  $W$  are the length and width of the Al plate (m);  $q_{abs}$  is the absorbed heat per unit ( $W/m^2$ );  $q_e$  is the solar energy converted into electricity;  $T_w$  is the mean temperature of water in the middle annulus tube of the co-axil triple-pipe heat exchanger;  $F_{th}$  the thermal efficiency factor of the PV/T system which, representing the ratio of the actual useful heat gain by the system to the overall converted solar heat at a certain working fluid temperature, can be expressed as:

$$F_{th} = \frac{K_L^{-1}}{\frac{LW}{N_{MCT}} \left\{ \frac{1}{LK_L \left[ \left( \frac{W}{N_{MCT}} - D_{MCT} \right) F_f + \frac{D_{MCT}}{1+\tau_p - Al K_L} \right] + \sum_{i=1}^6 R_i} \right\}} \tag{4-43}$$

## CHAPTER 4: THEORETICAL ANALYSIS AND COMPUTING MODEL DEVELOPMENT

---

Where,  $N_{MCT}$  is the number of the micro-channel flat tube;  $\sum R_i$  is the overall thermal resistance of from the absorbed Al plate to the working fluid;  $F_f$  is the standard fin efficiency which can be defined as:

$$F_f = \frac{\tanh[m(W/N_{MCT}-D_{MCT})/2]}{m(W/N_{MCT}-D_{MCT})/2} \quad (4-44)$$

And where the variable  $m$  is given by

$$m = \sqrt{\frac{K_L}{\lambda_{Al}\delta_{Al}(1+r_{p-Al}K_L)}} \quad (4-45)$$

This thermal efficiency factor of this system which, is a constant figure under the fixed physical and operating condition, takes consideration of all the thermal resistances from the absorbed Al plate to the water in the middle annulus tube of the co-axil triple-pipe heat exchanger, including: (1) thermal resistances between the PV cells and absorbed Al plate ( $R_1 = R_{p-Al}$ ); (2) thermal resistance of the micro-channel heat pipe wall ( $R_2 = R_{MC}$ ); (3) equivalent radial thermal resistance of the flow ( $R_3 = R_{eq,v}$ ), which is composed of the resistance of the liquid film from holes on the side of the channel  $R_{lf,c}$  assumed parallel to the radial thermal resistance of the two phase flow on the other side of the channel  $R_{eq,v}$ ; (4) the resistance of the axial vapour flow ( $R_4 = R_{v,a}$ ); (5) the resistance of the condensation two phase flow ( $R_5 = R_{tp,c}$ ); (6) the thermal resistance of the central tube wall of the co-axial triple-pipe heat exchanger ( $R_6 = R_{HE1}$ ). These resistances will be analysed in the following sections. And before analysing, it should be noticed that the resistance of the silicon sealant and the heat capacity of the adhesive layer are neglected, resulting from their significantly smaller values compared to other factors [61][99] [65].

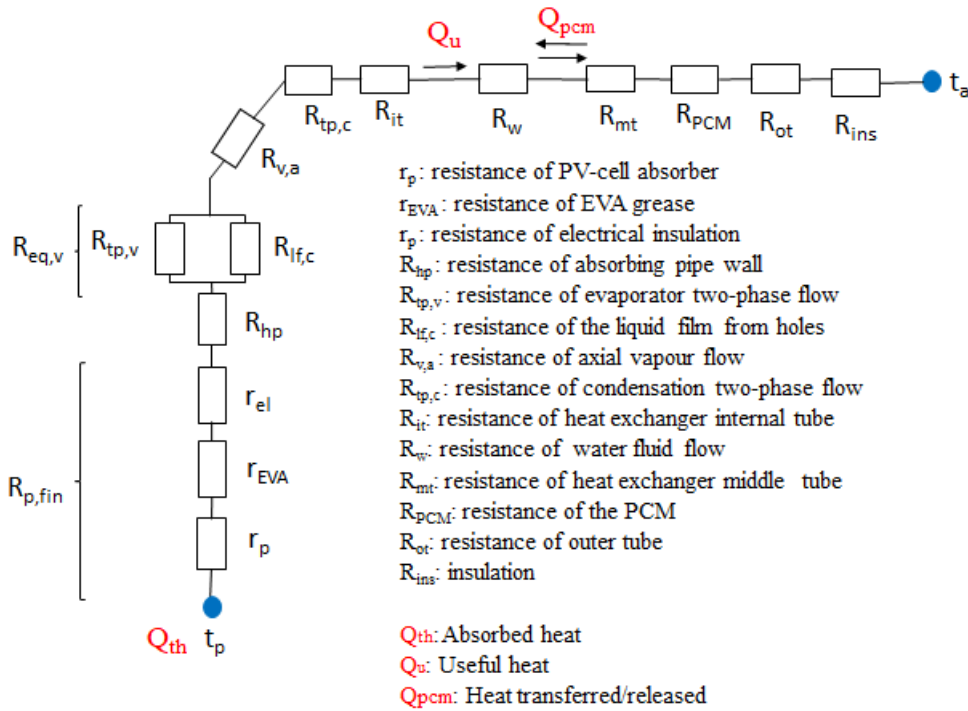


Fig.4-21 Schematic of heat transfer resistances along the PV/MC-LHP

(a) Thermal resistances between the PV cells and the Al plate

Heat transfer between the PV module and Al plate, which is working as the heat pipe fins, is a conventional one-dimensional multi-layer heat conduction process, thus the associate thermal resistance can be expressed as [99]:

$$R_{p-Al} = r_p + r_{EVA} + r_{ei} = \frac{\delta_p}{\lambda_p} + \frac{\delta_{EVA}}{\lambda_{EVA}} + \frac{\delta_{ei}}{\lambda_{ei}} \quad (4-46)$$

Where,  $R_{p-Al}$ ,  $r_p$ ,  $r_{EVA}$  and  $r_{ei}$  are the thermal resistances per unit area ( $m^2K/W$ ) of PV cells to absorbed Al plate, PV cells, EVA layer and electrical insulation respectively ;  $\lambda_p$  and  $\delta_p$ ,  $\lambda_{EVA}$  and  $\delta_{EVA}$ ,  $\lambda_{ei}$  and  $\delta_{ei}$  are the thermal conductivity ( $W/m^2 \cdot K$ ) and thickness (m) of PV layer, EVA layer and electrical insulation.

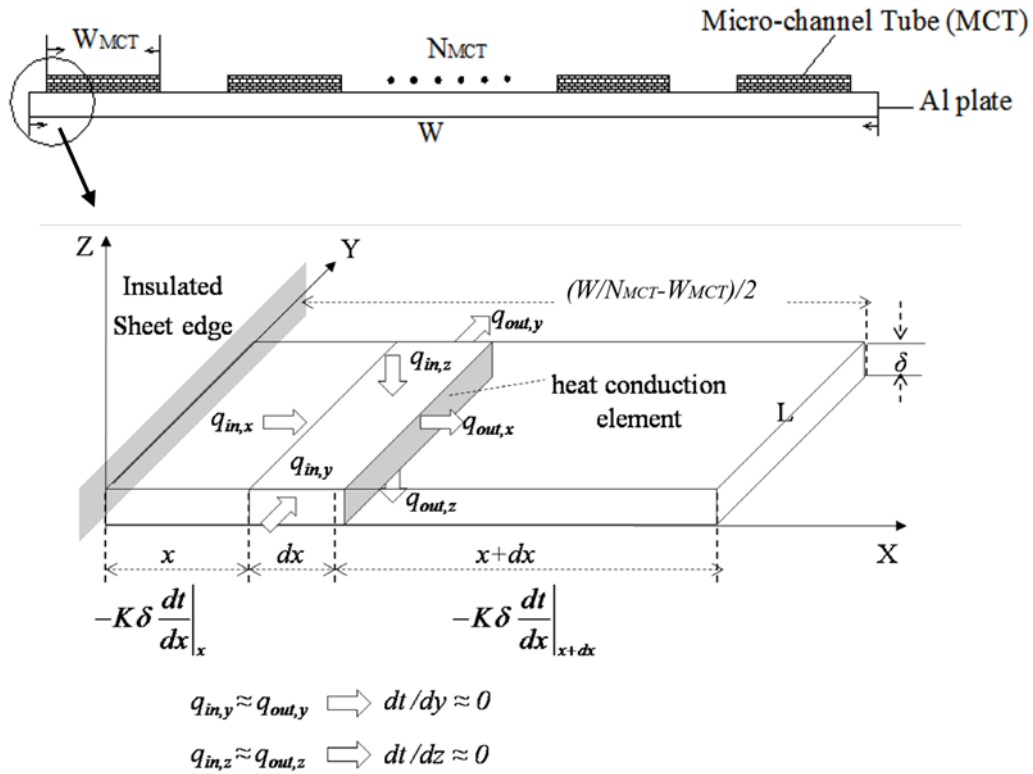


Fig.4-22 Heat flow pattern at the elemental length ‘dx’ on the Al plate[89]

(b) Thermal resistance across the Al plate length

The heat received by the Al plate is conducted to the micro-channel wall along its width direction, by leading the heat flow to travel across the cross sectional area of Al plate. This is considered a one-dimensional heat transfer process starting from the gap middle ( $x=0$ ) to the fin base [ $x = (W/N_{MCT} - W_{MCT})/2$ ][89]. Fig.4-22 indicates that the heat flow simulation process using finite element approach, where  $dx$  is taken as the step length of the numerical calculation. Therefore, for a controlled finite element per unit width, the energy conversation equation can be expressed as following:

$$\left[ \frac{q_{abs} - U_L(T - T_a) - q_e}{1 + r_{p-Al}U_L} \right] dx + \left( -\lambda_{Al}\delta_{Al} \frac{dt}{dx} \right)_x - \left( -\lambda_{Al}\delta_{Al} \frac{dt}{dx} \right)_{x+dx} = 0 \quad (4-47)$$

## CHAPTER 4: THEORETICAL ANALYSIS AND COMPUTING MODEL DEVELOPMENT

---

Where  $q_{abs}$  and  $q_e$  are the absorbed heat and energy converted into electricity per unit ( $W/m^2$ ) respectively;  $\lambda_{Al}$  and  $\delta_{Al}$  are the thermal conductivity and thickness of the Al plate.

### (c) Thermal resistance of the micro-channel heat pipe wall

Through the micro-channel heat pipe wall, heat transfer is a typical one dimensional steady-state conduction process, thus the thermal resistance of the micro-channel heat pipe wall can be expressed as:

$$R_{MC} = \frac{\delta_{MC}}{\lambda_{MC}(2 \times (a+b) \times L_{MC})N_{MCT}} \quad (4-48)$$

Where,  $\delta_{MC}$  is the thickness of the micro-channel heat pipe wall;  $a$  and  $b$  are the width and length of a single micro-channel respectively;  $L_{MC}$  is the length of the micro-channel heat pipe.

### (d) Equivalent radial thermal resistance of the flow

The equivalent radial thermal resistance of the flow is composed of the resistance of the liquid film from the holes on one side of the micro-channel wall and the resistance of the two-phase flow flowing along the other two sides of the channel port, where these two type of thermal resistance are assumed to be parallel. Thus the equivalent radial thermal resistance of the flow can be expressed as:

$$R_{eq,f} = \left( \frac{1}{R_{lf}} + \frac{1}{R_{tp,f}} \right) \quad (4-49)$$

Where,  $R_{lf}$  is the total thermal resistance of the condensate liquid film with thickness of  $\delta_{lf}$  at the two opposite micro-channel walls with holes, which can be calculated by:

CHAPTER 4: THEORETICAL ANALYSIS AND COMPUTING MODEL  
DEVELOPMENT

---

$$R_{lf} = \frac{\delta_{lf}}{\lambda_{lf}(2a \times L_{MC})N_{MCT}N_{ch}} \quad (4-50)$$

And  $R_{tp,f}$  is the thermal resistance of the two-phase flow flowing on the other two sides wall of the micro-channel expressed as:

$$R_{tp,f} = \frac{1}{2b\varepsilon_{of}L_{MC}h_{tp}N_{MCT}N_{ch}} \quad (4-51)$$

Where,  $h_{tp}$  calculated by considering the overall fin efficiency  $\varepsilon_{of}$  in the micro-channel heat pipe is the overall heat transfer coefficient of the two-phase flow in the micro-channel. The  $h_{tp}$  and  $\varepsilon_{of}$  can be obtained from the authors' previous paper[99].  $\delta_{lf}$  is the liquid film thickness which, assumed the same along the adjacent wall, is linked to the pressure difference between the outlets of the evaporator and condenser, where the height difference is denoted by  $H_{ce}$ . Based on this height difference, the condensed liquid penetrate the tiny holes on the side wall of the micro-channels to formulate this liquid film, which can be approximated as

$$\text{When } Re \leq 400, \quad \delta_{lf} = \left(\frac{3\mu_l^2}{\rho_l^2 g}\right)^{1/3} Re^{1/3} ;$$

$$\text{When } Re > 400, \quad \delta_{lf} = 0.369 \left(\frac{3\mu_l^2}{\rho_l^2 g}\right)^{1/2} Re^{1/2}$$

Where  $\mu_l$  is the liquid dynamic viscosity ( $Pa \cdot s$ );  $\rho_l$  is the liquid density ( $kg/m^3$ );  $Re$  is the Reynolds number given by

$$Re = \frac{\rho u_{lf}}{\mu_1} \delta_{lf} \quad (4-52)$$

## CHAPTER 4: THEORETICAL ANALYSIS AND COMPUTING MODEL DEVELOPMENT

---

$u_{lf}$  is the superficial velocity of the liquid film flow expressed as following, which depends on the pressure difference of the loop and is assumed to be the same for each tiny hole opened on the side wall of the micro-channel.

$$u_1 = A_h \frac{(2gH_{ev-co})^{1/2}}{A_{lf}(1-C_d^2(d_h/d_{lh}))} \quad (4-53)$$

Where,  $A_h$  is the cross-sectional area of the tiny hole;  $H_{ev-co}$  is the height difference between the top of the PV/micro-channel evaporator and the condenser working as the driving pressure head;  $d_h$  and  $d_{lh}$  are the diameter of the tiny hole and the liquid header respectively;  $A_{lf}$  is the liquid film cross-sectional area expressed as:

$$A_{lf} = \delta_{lf} a \quad (4-54)$$

And  $C_d$  is the discharge coefficient of the flow from the upper liquid header to the tiny holes, which can be calculated by [162][163]:

$$C_d = 0.611 \left[ 87 \left( \frac{4.5\mu_l}{\rho_l d_h \sqrt{gH_{ev-co}}} \right)^{1.43} + \left( \frac{4.5\mu_l}{\rho_l d_h \sqrt{gH_{ev-co}}} \right)^{-1.26} \right]^{-0.7} \quad (4-55)$$

(e) The resistance of the axial vapour flow ( $R_4 = R_{v,a}$ )

The vapour flow process from the PV/micro-channel evaporator to the condensing co-axial triple-pipe heat exchanger experiences certain pressure drop and consequently temperature decreasing, thus leading heat transfer resistance which can be expressed as[99][164]:

$$R_{v,a} = \frac{T_v^2 R_0 \Delta P_v N_{MCT} N_{ch}}{Q_u h_{fg} P_v} \quad (4-56)$$

## CHAPTER 4: THEORETICAL ANALYSIS AND COMPUTING MODEL DEVELOPMENT

---

Where  $\Delta P_v$  which, is the total pressure drop including (1) pressure drop in the PV/micro-channel evaporator section ( $\Delta P_e$ ); (2) vapour pressure drop in the upper vapour header ( $\Delta P_{vh,v}$ ); (3) pressure drop in the vapour transportation line ( $\Delta P_{vtl}$ ); (4) pressure drop in the condensing co-axial triple-pipe heat exchanger section ( $\Delta P_{cond}$ ), can be calculated by [61]:

$$\Delta P_v = \Delta P_e + \Delta P_{vh,v} + \Delta P_{vtl} + \Delta P_{cond} \quad (4-57)$$

These pressure drops have been calculated in the authors' previous publication [149].

(f) The resistance of the condensation flow ( $R_5 = R_{cond}$ )

According to Newton's law of cooling, the equivalent thermal resistance of the condensation flow in the central tube of the heat exchanger can be expressed as:

$$R_{cond} = \frac{1}{\pi D_1 L_{hx} h_{cond}} \quad (4-58)$$

Where,  $D_1$  is the diameter of the central tube of the heat exchanger (m);  $L_{hx}$  is the total length of the heat exchanger (m);  $h_{cond}$  is the condensation (convective) heat transfer coefficient ( $W/m^2K$ ), which can be calculated according to the Reynolds number of the vapour  $Re_v$ :

When  $Re_v < 3500$ ,

$$h_{cond} = 0.555 \left[ \frac{g \rho_l (\rho_l - \rho_v) \lambda_l^3 h_{fg}}{\mu d_1 (T_l - T_{wall})} \right]^{1/4}; \quad (4-59)$$

When  $Re_v \geq 3500$ ,

$$h_{cond} = \frac{k_l}{D} 0.23 Re_D^{0.8} Pr_l^{0.4} \left[ 1 + \frac{2.22}{X_{tt}^{0.89}} \right]$$

## CHAPTER 4: THEORETICAL ANALYSIS AND COMPUTING MODEL DEVELOPMENT

---

$$Re_D = 4 \dot{m}(1 - x) / (\pi D \mu_l)$$

$$X_{tt} = \left( \frac{1 - x}{x} \right)^{0.9} \left( \frac{\rho_v}{\rho_l} \right)^{0.5} \left( \frac{\mu_l}{\mu_v} \right)^{0.1}$$

Where  $g$ ,  $d_1$ ,  $\rho_l$ ,  $\rho_v$ ,  $\mu$ ,  $\lambda_l$  are the relevant acceleration of gravity, inner diameter of tube1, density of liquid(saturate), density of vapour(saturate), mean dynamic viscosity (kg/m-s), thermal conductivity of liquid respectively;  $T_l$ ,  $T_{wall}$  are the temperature of liquid film and inner tube wall respectively, which is assumed that  $T_l = T_v$ ,  $T_{wall} = T_w$ . Inner tube wall's temperature equals to the adjacent water temperature.

(g) The thermal resistance of the central tube wall of the co-axial triple-pipe heat exchanger  $R_6 = R_{HE1}$

Heat transfer through the central tube wall is a typical heat conduction process, thus the relevant thermal resistance can be expressed as

$$R_6 = R_{HE1} = \frac{1}{2\pi\lambda_1} \ln \frac{D_2}{D_1} \quad (4-60)$$

Where,  $D_2$  is the outer diameter of the central tube (m);  $\lambda_1$  is thermal conductivity of the central tube wall (W/mK).

(h) Heat transfer in the co-axial tubular triple-tube heat exchanger with PCM

The useful energy delivered by the PV/T module for heating  $Q_{th}$  leads to the evaporation of working fluid (R134a) in MCLHP. Then the vapour fluid, via the vapour transportation line, moves forward to the co-axial tubular triple-tube heat exchanger with PCM, where the evaporated fluid condenses and transfers the condensation heat into the adjacent cooling fluid (water) and PCM, thus heating the coolant water in the middle annulus tube, and leading to the fusion/melting of PCM in the outer channel of the heat exchanger to

## CHAPTER 4: THEORETICAL ANALYSIS AND COMPUTING MODEL DEVELOPMENT

storage excess heat. The condensed fluid in the heat pipe, via the liquid transportation line, then returns to the heat pipe evaporation section to regain heat, thus forming a complete heat transportation cycle. **Fig.4-23** shows the design of the heat exchanger.

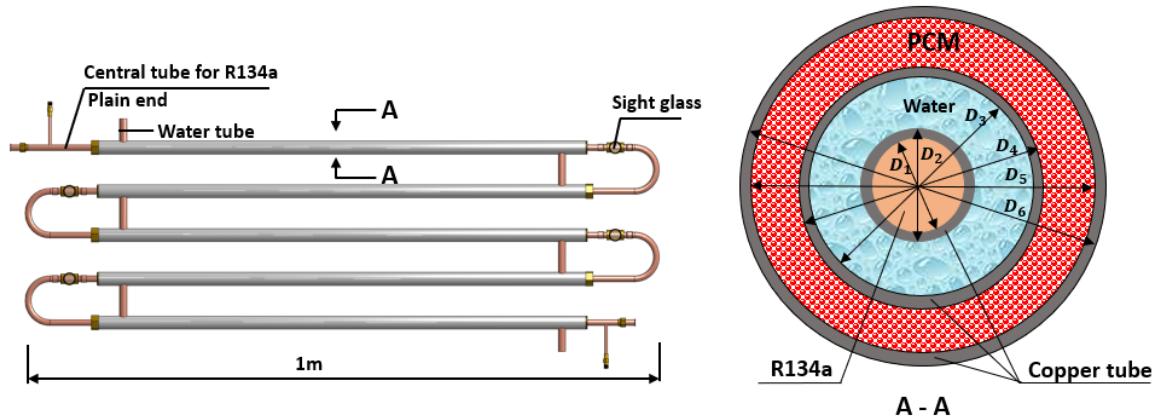


**Fig.4-23. The design of the heat exchanger**

Owing to the charge and discharge of the PCM in the outer tube, there are two heat transfer process of the coolant water in the middle annulus tube. The thermal resistance of the PCM considering the fraction of the melted PCM is expressed as the sum of the resistance of the PCM solid layer and the PCM liquid layer and is expressed as follows:

$$R_{PCM} = \log \left( \frac{(f(R_5^2 - R_4^2) + R_4^2)^{0.5}}{R_4} \right) \frac{1}{2\pi L_{he} k_{PCM,L}} + \log \left( \frac{R_5}{(f(R_5^2 - R_4^2) + R_4^2)^{0.5}} \right) \frac{1}{2\pi L_{he} k_{PCM,S}} \quad (4-61)$$

When charging the PCM, The heat transferred from water in the middle tube to the PCM is expressed as following:

$$Q_c = \varepsilon_c C_{min} (T_{c,out} - T_{c,in}) \quad (4-62)$$

With  $C_{min}$  (W/K) the minimum heat transfer capacity,  $\varepsilon_c$  is the average effectiveness of the melting process and is expressed as following [165]:

CHAPTER 4: THEORETICAL ANALYSIS AND COMPUTING MODEL DEVELOPMENT

---

$$\varepsilon_c = \int_0^1 (1 - \exp(-\frac{1}{R_T C_{\min}})) df \quad (4-63)$$

Where  $f$  is the fraction of melted PCM and varies from 0 (only solid) to 1 (only liquid),  $R_T$  is the total resistance from the water to the PCM material and is expressed as follows:

$$R_T = R_w + R_{mt} + R_{PCM} \quad (4-64)$$

Where  $R_w$  is the water resistance,  $R_{mt}$  is the resistance of the middle tube and  $R_{PCM}$  is the resistance of the PCM material. The different resistances are expressed as follows:

$$R_w = \frac{1}{h_w \pi D_2 L_{he}} \quad (4-65)$$

The convective heat transfer coefficient  $h_w$  of the water on the annulus side can be calculated by

$$h_w = \frac{Nu k_w}{D_{45}} \quad (4-66)$$

Thermal resistance of the middle tube  $R_{mt}$ , the conductive thermal resistance of the middle tube is expressed as follows:

$$R_{mt} = \frac{1}{2\pi k_{mt} L_{he}} \log\left(\frac{D_4}{D_3}\right) \quad (4-67)$$

When discharging the PCM, The heat transferred from water in the middle tube to the PCM is expressed as follows:

$$Q_{PCM,d} = \varepsilon_d C_{\min} (T_{PCM} - T_{c,in}) \quad (4-68)$$

## CHAPTER 4: THEORETICAL ANALYSIS AND COMPUTING MODEL DEVELOPMENT

---

With  $\varepsilon_d$  the average effectiveness of the solidification process. And the total heat transferred to the cold water is assumed equal to the sum of the heat released from the PCM material  $Q_{PCM,d}$  and the useful heat  $Q_u$ , so that the total heat transfer rate  $Q_w$  can be expressed as:

$$Q_w = Q_{PCM,d} + Q_u \quad (4-69)$$

### *(5) The coefficient of performance (COP) of the system*

The coefficient of performance (COP) of the system could be defined as the ratio of system's overall heat output (including the Power output converted to heat) and power consumption of the water pump as following [166]:

$$COP = \frac{Q_w + Q_e / 0.38}{P_{pump}} \quad (4-70)$$

The electricity consumption of the pump is expressed as follows:

$$P_{pump} = \frac{Q_v \rho_w g H}{\eta_{pump}} \quad (4-71)$$

Where  $Q_v$  is the water volume flow rate,  $\eta_{pump}$  the efficiency of the pump and  $H$  the total height  $H$  expressed as following:

$$H = f_{an} \frac{L_{he}}{D_3 - D_2} \left( \frac{u_w^2}{2g} \right) + \sum K \left( \frac{u_w^2}{2g} \right) \quad (4-72)$$

Where  $f_{an}$  is the friction factor for an annular tube given in ref.[99] and  $\sum K$  is the sum of loss coefficient for the four 180 returned bend, inlet and outlet fittings[167]

### 4.3.2 Programme algorithm development

When this PV/MCLHP system operates at a relative steady state condition after the beginning period, the heat transfer processes of this system will eventually achieve an energy balance and each component of the system will establish a certain dynamic steady temperature. Thus, in order to investigate the solar performance of this MC-LHP-PVT system based on different impactors, a computer model was established based on above analytical equations to simulate the performance.

This simulation model is resolved by applying the principle of heat balance at the PV/micro-channel evaporator and the co-axial triple-pipe heat exchanger with PCM. And the algorithm is summarized as following steps and the flow chart is presented in the **Fig.4-24**.

## CHAPTER 4: THEORETICAL ANALYSIS AND COMPUTING MODEL DEVELOPMENT

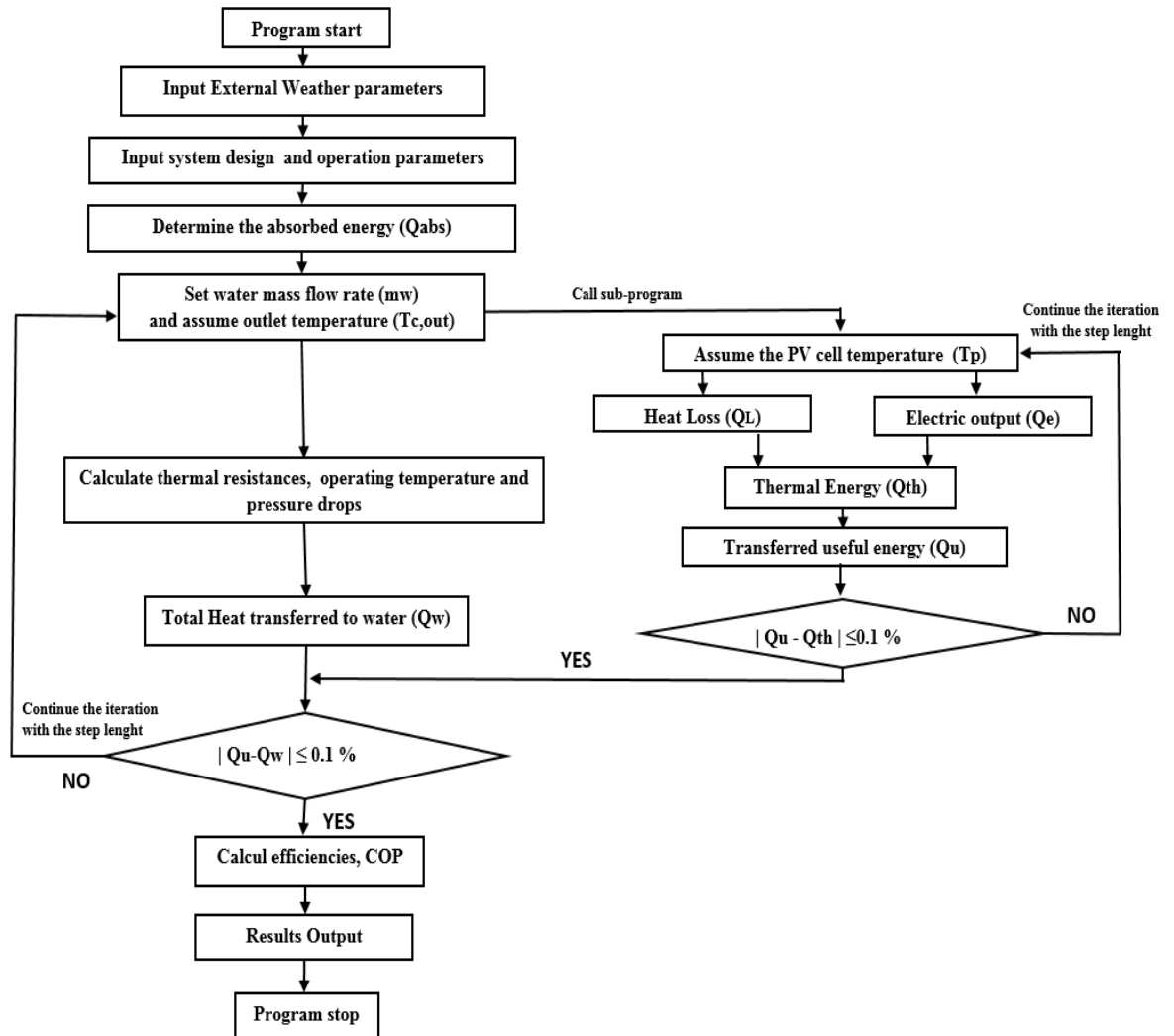


**Fig.4-24. PV/MCLHP system model simulation flow chart**

The algorithm is illustrated as following:

- (i) Input external weather variables, system design and operating parameters;
- (ii) Calculate the Absorbed heat equation (4-30);
- (iii) Set the cold water mass flow  $m_w$  rate and the water inlet temperature  $T_{c,int}$
- (iv) Assume the outlet temperature of the water  $T_{c,out}$ .
- (v) Assume the cell temperature  $T_p$ , and commence the following analysis:

## CHAPTER 4: THEORETICAL ANALYSIS AND COMPUTING MODEL DEVELOPMENT

---

- A. Heat balance of the glazing cover could be analysed using equations (4-30) to (4-35), which gives the heat loss,  $Q_L$ ;
- B. Heat balance of the PV cells gives of the converted solar electricity,  $Q_e$  and heat,  $Q_{th}$ ; (Eq. (4-37) and Eq. (4-39)).
- C. Heat transfer from the PV cells to the PCM heat exchanger could be analysed by equations (4-42) to (4-45), which gives the useful heat gain,  $Q_u$ ;
- D. If  $(Q_{th} - Q_u) / Q_{th} > 0.1\%$  (error allowance), then increase  $t_p$  by  $0.1\text{ }^\circ\text{C}$  and return to step (vi) for re-calculation;
- E. If  $(Q_{th} - Q_u) / Q_{th} < -0.1\%$  (error allowance), then decrease  $t_p$  by  $0.1\text{ }^\circ\text{C}$  and return to step (vi) for re-calculation;
- F. If  $-0.1\% \leq (Q_{th} - Q_u) / Q_{th} \leq 0.1\%$ , the system achieves heat balance;
- (vi) Calculate the total heat transfer rate to water  $Q_w$  equation (4-62) (Charge process) or (4-68) (Discharge process).
- (vii) If  $(Q_u - Q_w) / Q_u > 0.1\%$  (error allowance), then increase  $T_{c,out}$  by  $0.1\text{ }^\circ\text{C}$  and return to step (iii) for re-calculation;
- (viii) If  $(Q_u - Q_w) / Q_u < -0.1\%$  (error allowance), then decrease  $0.1\text{ }^\circ\text{C}$  and return to step (iii) for re-calculation;
- (ix) If  $-0.1\% \leq (Q_u - Q_w) / Q_u \leq 0.1\%$ , the system achieves heat balance;
- (x) Calculate the module's solar thermal, electrical and overall efficiencies

### 4.3.3 Modelling results and case studies

#### 4.3.3.1 Influence of the solar radiation

By varying the solar radiation from 200 W/m<sup>2</sup> to 800 W/ m<sup>2</sup> while keeping the other external variables constant, i.e. air temperature at 25°C, air velocity at 1 m/s, the energy performance of the is assessed. The PCM is assumed at the melting temperature of 44°C.

**Fig.4-25a** shows the influence of the solar radiation  $I$  on the thermal  $\eta_{th}$ , electrical  $\eta_e$  and overall  $\eta_o$  efficiencies. The increase of the solar radiation would lead to an increase of the thermal and overall efficiency and a decrease of the electrical efficiency. The thermal efficiency outweighs the electrical efficiency and then the overall efficiency follows the increasing trend. The increase is most significant for relatively lower solar radiations ( $I < 400$  W/m<sup>2</sup>) and is nearly linear. It can be found that the trend becomes rapid in 200-400 W/m<sup>2</sup>; however, it slows down above the solar radiation of 400 W/m<sup>2</sup>. For each 100 W/m<sup>2</sup> increase the overall efficiency increases by nearly by 7% and by 1.6 % for the slow trend. The slow trend is due to the increase of the water outlet temperature, therefore the heat loss from the panel to the ambient air while increasing the solar radiation. For a solar radiation of 800 W/m<sup>2</sup> the PVT module reaches an overall efficiency of 67.8 %. Otherwise, the increase of the solar radiation from 200 W/m<sup>2</sup> to 800 W/ m<sup>2</sup>, leads to a small decrease (0.28 %) of the electrical efficiency from 12.48 to 12.2 %. The higher solar radiation brings more instant heat to the PV layer, resulting in an increase of the PV cell temperature as shown in **Fig.4-25b** and the decrease of the electrical efficiency. For a solar radiation of 800 W/m<sup>2</sup> the PVT module reaches an overall efficiency of 67.8 %.

CHAPTER 4: THEORETICAL ANALYSIS AND COMPUTING MODEL DEVELOPMENT

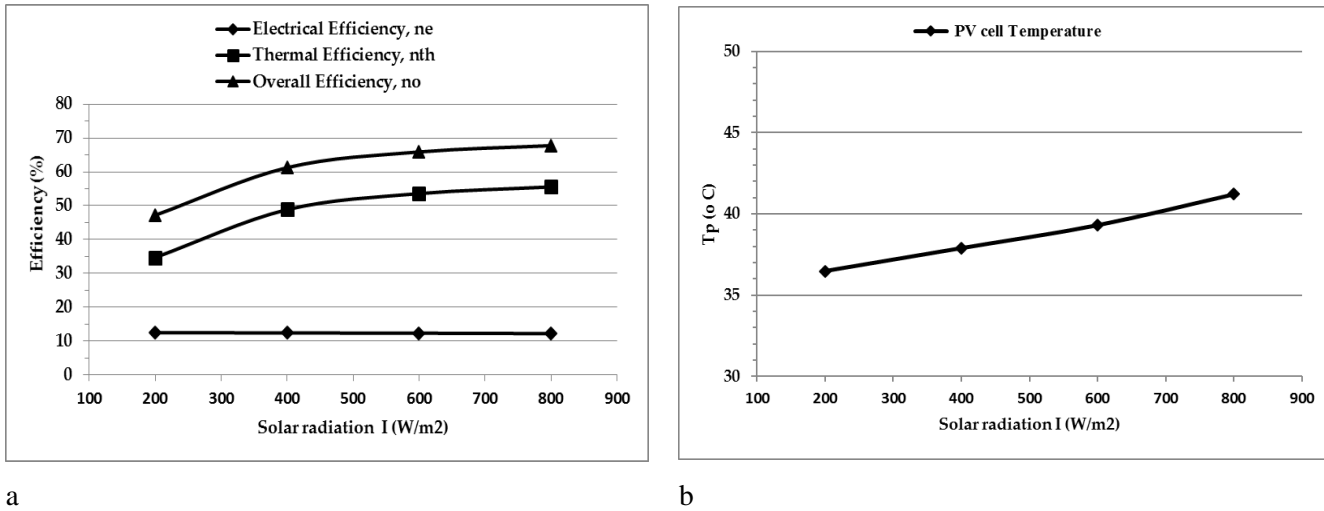


**Fig.4-25. Influence of solar radiation on: a) the thermal, electrical, overall efficiencies; b) PV cell temperature**

**Fig.4-26a** shows the influence of the solar radiation on the useful heat  $Q_u$  transferred to the circulating water temperature, the total heat transferred  $Q_w$  to the network/heat storage tank and  $Q_{pcm}$ . Increasing the solar radiation would increase the useful  $Q_u$  heat and therefore the total heat transferred to the circulating water the  $Q_w$ . The heat released (discharged) by the PCM  $Q_{pcm}$  and transferred to the water is constant as the calculation has been performed an assumed constant PCM temperature of 44°C (Equation 25). The amount of heat released by the PCM is 110 W. The contribution of the PCM release in the total heat transfer rate decreases with the solar radiation increases. For the solar radiation of 200 W/m<sup>2</sup>, the heat from the PCM  $Q_{pcm}$  represents 43% of the total heat transfer rate ( $Q_w=256$  W) and this percentage is 11 % ( $Q_w=987$  W) for higher solar radiation of  $I=800$  W/m<sup>2</sup>. It is seen that the presence of the PCM permits to increase the total heat transfer rate wick is more important for lower solar radiations. Increasing the solar radiation by 100 W/m<sup>2</sup> would increase the water output temperature by 1.33 °C (**Fig.4-26b**). For a solar radiation of 800 W/m<sup>2</sup>, the system delivers a water temperature of 45.8 °C.

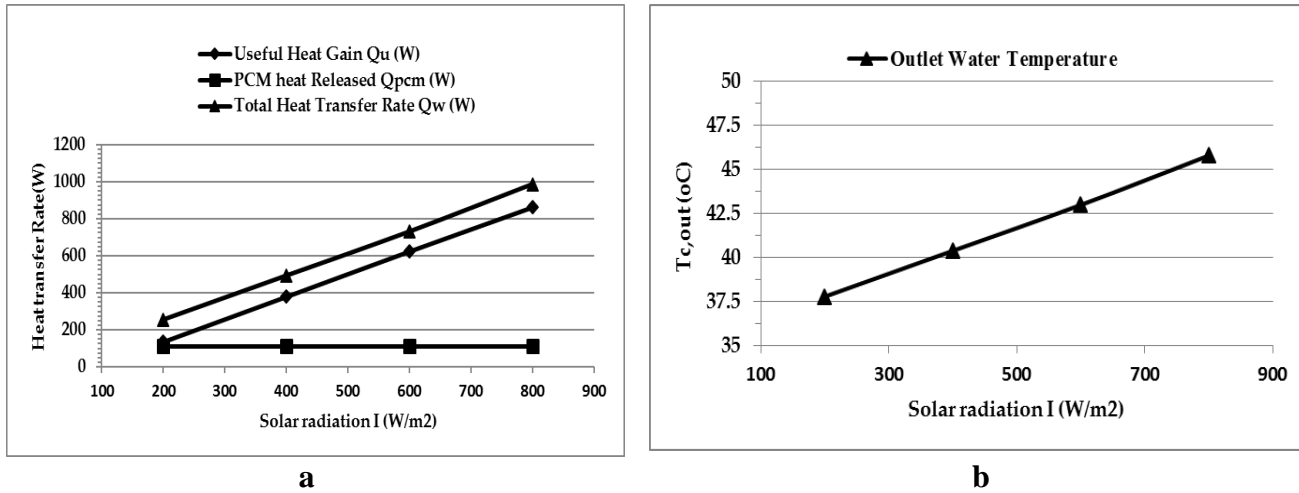


**Fig.4-26. Influence of solar radiation on: a) the heat outputs, and b) the water outlet temperature**

**Fig.4-27** presents the influence of the solar radiation the COP of the PVT system which considers both electrical and thermal outputs (Equation 28). The COP increases linearly with the solar radiation. The high COP value (2-3 order) reflects the small power consumption of the Pump. The increase of solar radiation significantly influences the COP which is multiplied by 4.3 when the solar radiation increases from 200 W/m<sup>2</sup> to 800 W/m<sup>2</sup>. The solar radiation increase is very beneficial to the PVT system.

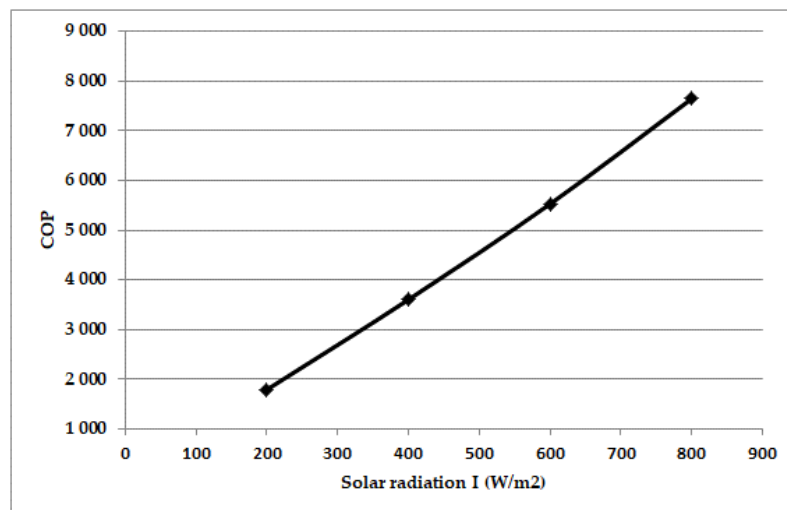
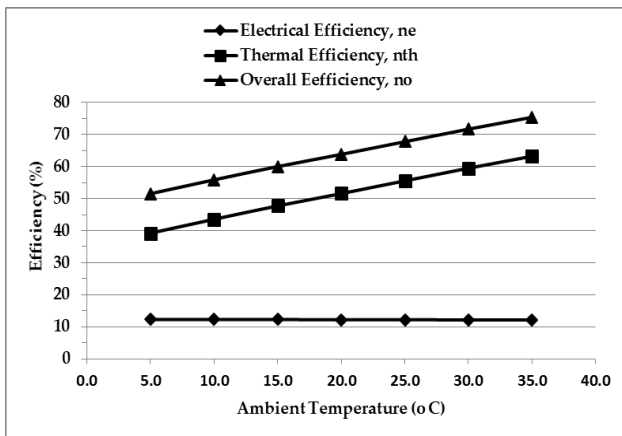


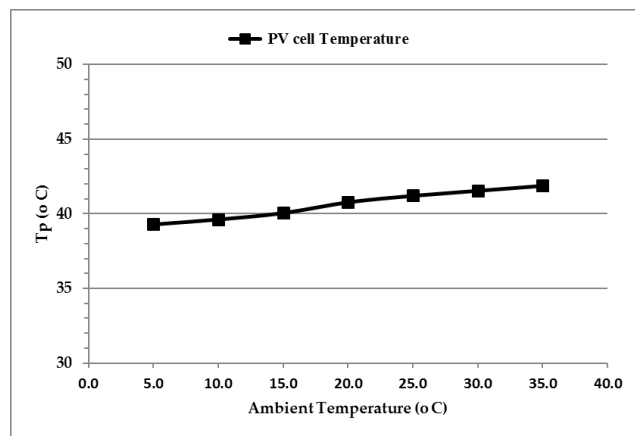
**Fig.4-27. Influence of solar radiation on the COP**

4.3.3.2 Influence of the Ambient Temperature

Varying the air temperature from 5°C to 35°C while keeping the other external variables constant, i.e. solar radiation at 800 W/m<sup>2</sup>, air velocity at 1 m/s, PCM melting temperature of 44°C, the energy performance of the system has been assessed. **Fig.4-28a** shows that increasing the ambient temperature would increase the thermal and the overall efficiency but decrease the electrical efficiency. As the thermal efficiency outweighs the electrical efficiency, the overall efficiency follows the thermal efficiency which increases linearly. For each 5°C ambient temperature increase the overall efficient increases by 4 %. From 5°C to 35°C ambient temperature, the electricity efficiency decreases slightly because of the the PV cell temperature rose of 2.58°C, from 39.3°C to 41.9°C as shown in **Fig.4-28b**. This little increase of the PV cell tell temperature can be explained by the high capacity of the micro-channel evaporator to absorb heat flux, the two phase heat transfer coefficient in the microchannel evaporator is in the order of  $4 \times 10^3$  W/m<sup>2</sup>/K and by the heat loss decrease when increasing the ambient temperature.



a



b

**Fig.4-28. Influence of the ambient air temperature on: a) the thermal, electrical, overall efficiencies, b) PV cell temperature**

**Fig.4-29a** presents the evolution the heat output rates and the circulation water outlet temperature at the PCM heat exchanger. Higher ambient temperature would lead to higher total

## CHAPTER 4: THEORETICAL ANALYSIS AND COMPUTING MODEL DEVELOPMENT

heat transfer rate  $Q_w$ . At 35°C, the system achieves a total heat transfer rate of 1096 W. **Fig.4-29b** shows that from 5 °C to 35°C ambient temperature, the water outlet temperature increases by 4°C, this means for each 7.5°C ambient temperature increase the water outlet temperature increases by 1°C.

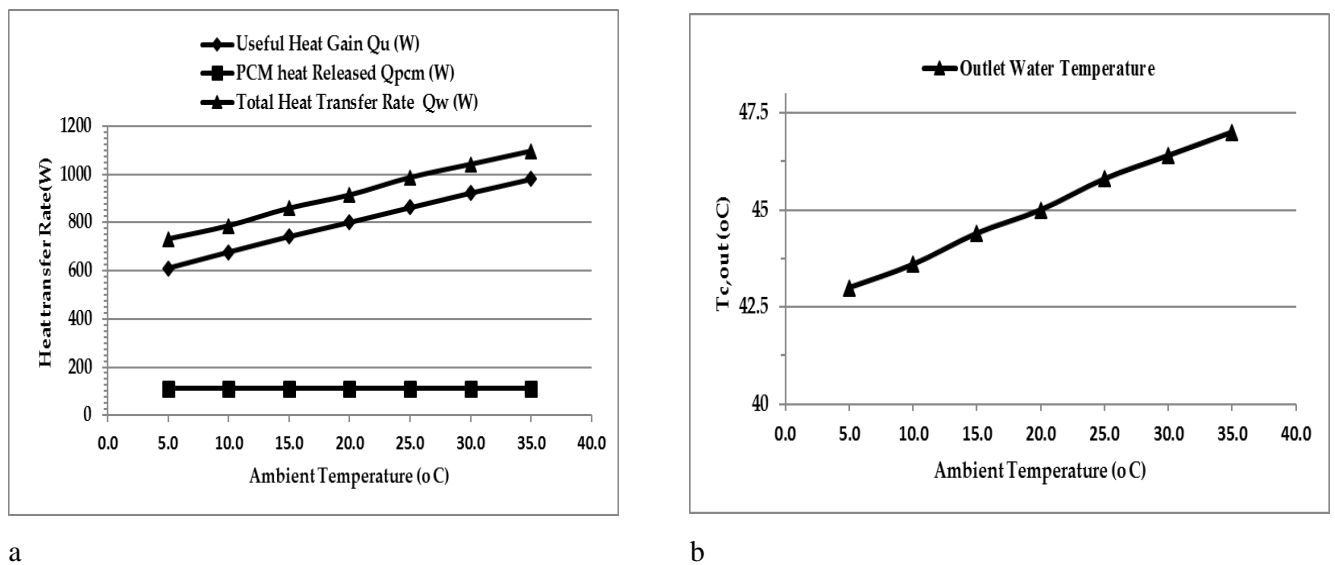


**Fig.4-29. Influence of the ambient temperature on a) the heat outputs and b) the water outlet temperature**

**Fig.4-30** presents the influence of the ambient temperature on the COP. The COP of the system increases linearly with the increase of the ambient temperature due the linear increase of the total heat transferred to the water  $Q_w$ . The temperature increase is a favourable factor on the COP that is multiplied by 1.34 when the ambient temperature increases from 5°C to 35°C. It can be seen that the influence of the solar radiation on the COP (**Fig.4-27**) is stronger than the influence of the ambient temperature (**Fig.4-30**).

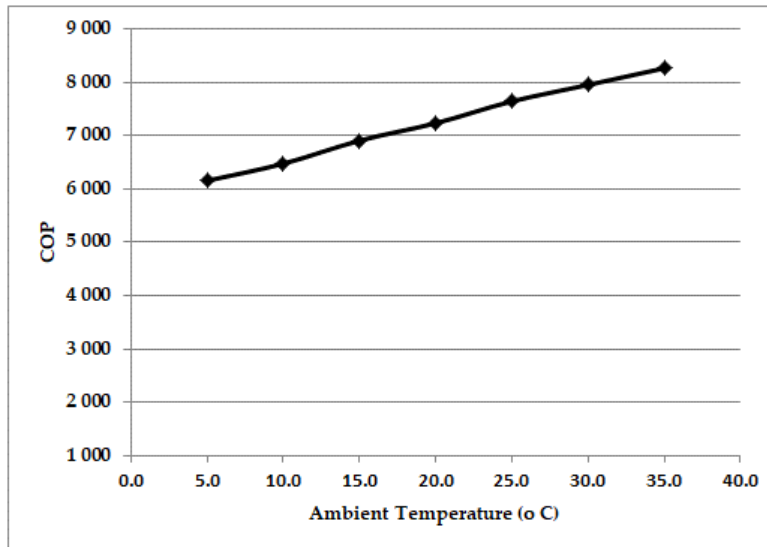


**Fig.4-30. Influence of ambient temperature on the COP**

#### 4.3.3.3 Influence of the Wind Velocity

Varying the wind velocity from 0.5 m/s to 5 m/s and holding the other external variables constant, i.e. solar radiation at 800 W/m<sup>2</sup>, air temperature at 25°C, the energy performance of the system has been assessed. It was found that increasing wind velocity would decrease slightly the overall efficiency and increase the electricity efficiency very slightly (**Fig.4-31a**). Increasing the wind velocity by 1 m/s decreases the overall efficiency by 0.3 % (from 67.9 - 66.5 %). This decrease is due to the little increase of the heat loss due to the increase of the convective heat transfer coefficient from the PV to the surroundings. However, this heat transfer coefficient is favourable for the electricity efficiency that increases very slightly (almost constant) from 12.2 to 12.2 %. As shown in **Fig.4-31b**, the wind velocity increase led to a very slight decrease in the temperature of the PV cells (40.6°C to 40.4°C). This PV cell temperature decrease is favourable to the system but weak. This phenomenon can be explained that: owing to one glazing layer, because higher wind velocity causes higher convective heat transfer coefficient. Therefore, it will enhance the heat loss due to the increase of the convective heat transfer coefficient from the PV to the surroundings, making slightly decrease of overall efficiency. While the increase

## CHAPTER 4: THEORETICAL ANALYSIS AND COMPUTING MODEL DEVELOPMENT

of the convective heat transfer coefficient can help to cool the PV cells, which would increase the electricity efficiency.

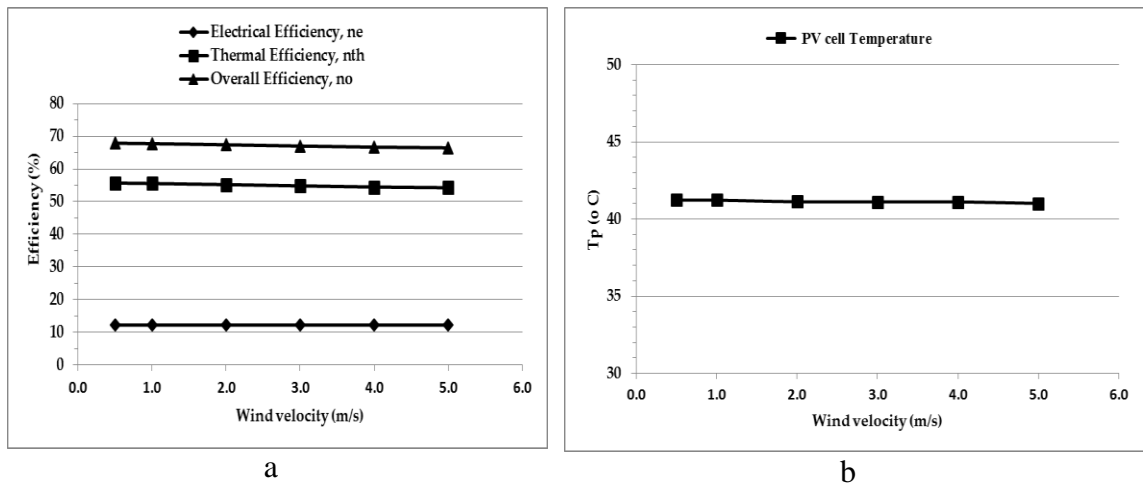


**Fig.4-31. Influence of the wind velocity on the a) the thermal, electrical, overall efficiencies, b) PV cell temperature**

**Fig.4-32** presents the influence of the wind velocity on the total heat transfer rate and the water outlet temperature. Increasing the wind velocity by 1 m/s slightly decreases the total heat transfer rate  $Q_w$  by 0.8 % (**Fig.4-32a**) and the water outlet temperature  $T_{c,out}$  by 0.08 $^{\circ}\text{C}$  (**Fig.4-32b**).

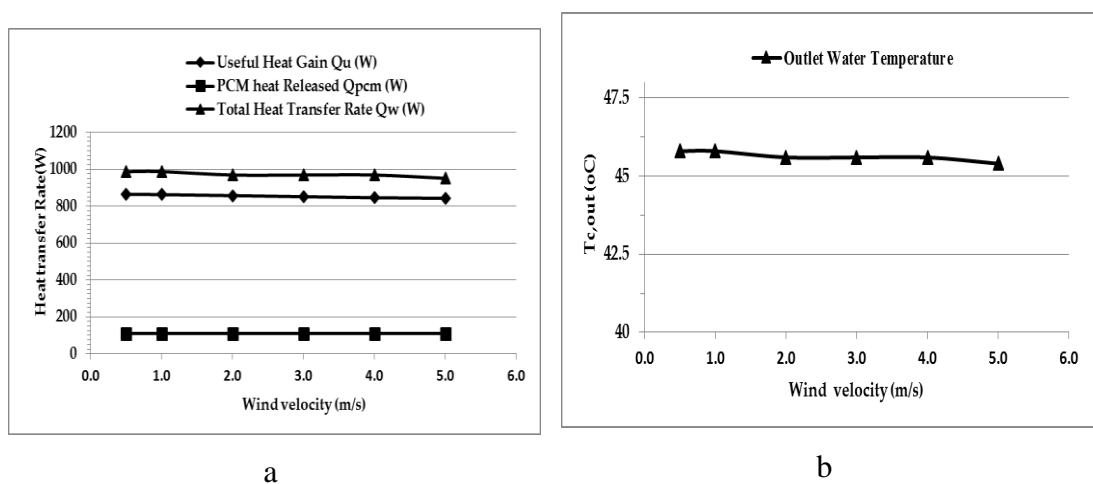


**Fig.4-32. Influence of wind velocity on: a) the heat outputs and b) the water outlet temperature**

**Fig.4-33** shows that COP decreases slightly with an increasing the velocity. Increasing the velocity from 0.5 m/s to 5 m/s decreases the COP by 4%. It can be seen that the influence the wind velocity on the COP of the system is very weak compared to the influences of the solar radiation (**Fig.4-27**) and the ambient temperature (**Fig.4-30**).

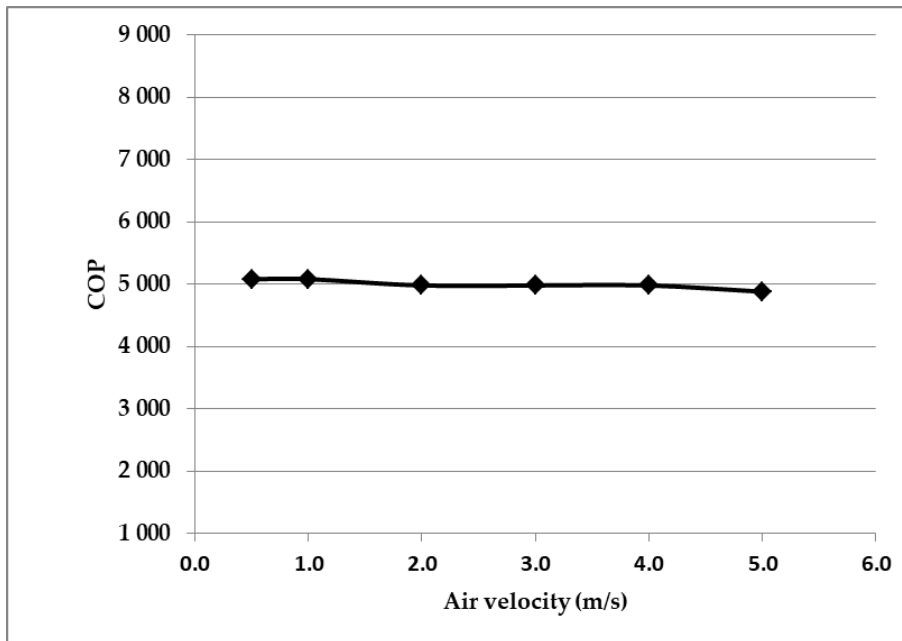


**Fig.4-33. Influence of wind velocity on the COP**

#### 4.3.3.4 Influence of Number of cover

By varying the number of top glazing covers from 0 to 2 while the other parameters remained constant, solar radiation at  $800 \text{ W/m}^2$ , air temperature at  $25^\circ\text{C}$ , velocity 1 m/s, it was found that increasing the number of glazing covers would increase the thermal and slightly decrease the electrical efficiency (**Fig.4-34a**). The thermal efficiency outweighs the electrical efficiency and the overall efficiency follows the thermal efficiency increase. The increases of the overall efficiency can be explained by the fact adding more glazing covers helps to reduce the overall heat losses and the amount of absorbed solar energy due to its reflection and reduced transmittance; therefore, the thermal efficiency and the

## CHAPTER 4: THEORETICAL ANALYSIS AND COMPUTING MODEL DEVELOPMENT

PV cell temperature rises slightly from 39.2 to 40.9°C (**Fig.4-34b**), and then the electrical efficiency falls slightly (12.19 % to 12.17 %). The increase of the cover number is favourable for thermal efficiency and unfavourable for electrical efficiency.

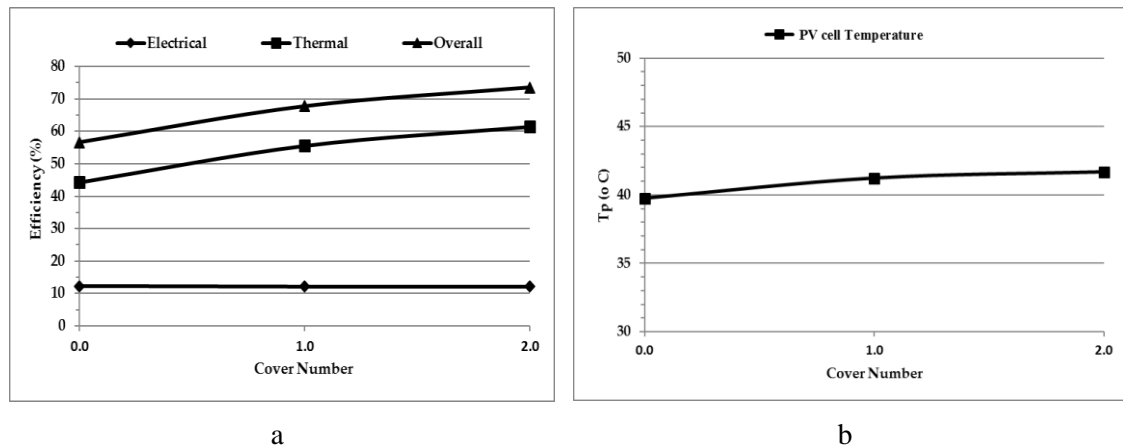


**Fig.4-34. Influence of the cover number on the efficiency**

**Fig.4-35** shows that increasing the number of cover from 1 to 2 increases the heat transfer rate by 7.3 % (**Fig.4-35a**) and water outlet temperature by 0.8°C (**Fig.4-35b**). **Fig.4-36** shows that the cover number is a favourable factor for the performance of the system. From 1 to 2 number of cover the COP increases only by 5.4% (Figure 4-31), this means using 2 covers does not significantly increase the COP. To minimize heat loss and maximize solar energy input, the single-glazing cover was considered to be the most appropriate option.

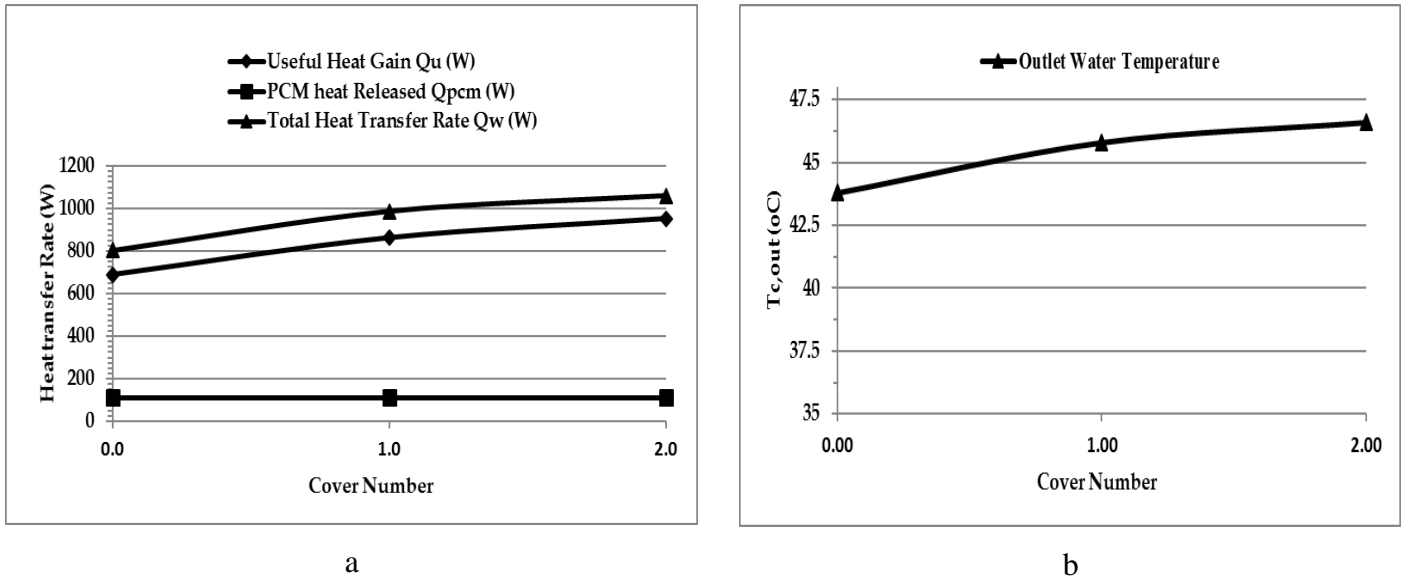


Fig.4-35. Influence of the cover number on heat transfer rates and the outlet water temperature

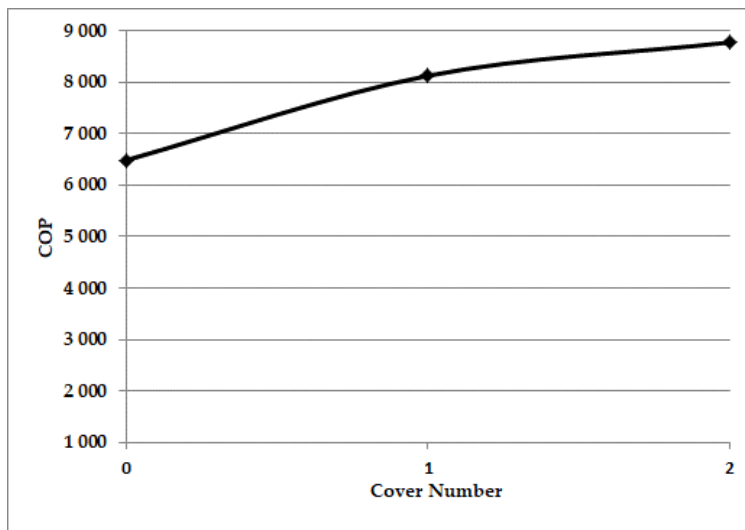


Fig.4-36. Influence of the cover on the COP

#### 4.3.3.5 Influence of the packing factor

The influence of the packing factor on the energy performance of the system has been investigated for a constant solar radiation at  $800 \text{ W/m}^2$ , air temperature at  $25^\circ\text{C}$ , velocity  $1 \text{ m/s}$ . The packing factor has been varied by changing the number of PV cells. It was found that increasing the packing factor from 0.1 to 0.9 increases the overall efficiency

## CHAPTER 4: THEORETICAL ANALYSIS AND COMPUTING MODEL DEVELOPMENT

from 60.4 % to 67.7% (**Fig.4-37a**). This increase is in majority due to the significant increase of the electricity efficiency (1.5 % to 12.2 %), the thermal efficiency decreases less (58.9 % to 55.5 %). **Fig.4-37b** shows that the increase of the packing factor slightly influences the PV cell temperature. The packing is significantly favourable to the electricity efficiency and unfavourable to the thermal efficiency.

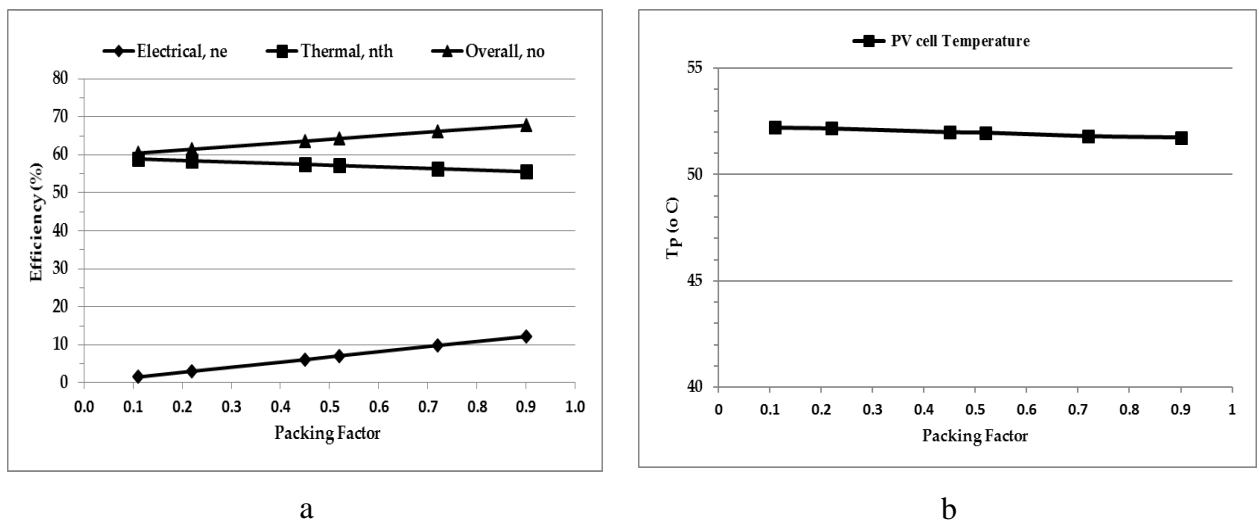


**Fig.4-37. Influence of the packing on the efficiency**

**Fig.4-38** shows that total heat transferred to the water  $Q_w$  and the outlet water temperature decreases slightly with the packing factor. As a result, from a packing factor of 0.1 to 0.9 the COP decreases slightly by 36.5 % (**Fig.4-39**). In fact, this increase of the COP is due to the increase of the electrical output that compensates the small decrease of the total heat output. Finally, it was found that higher packing factor is beneficial for the overall system performance.

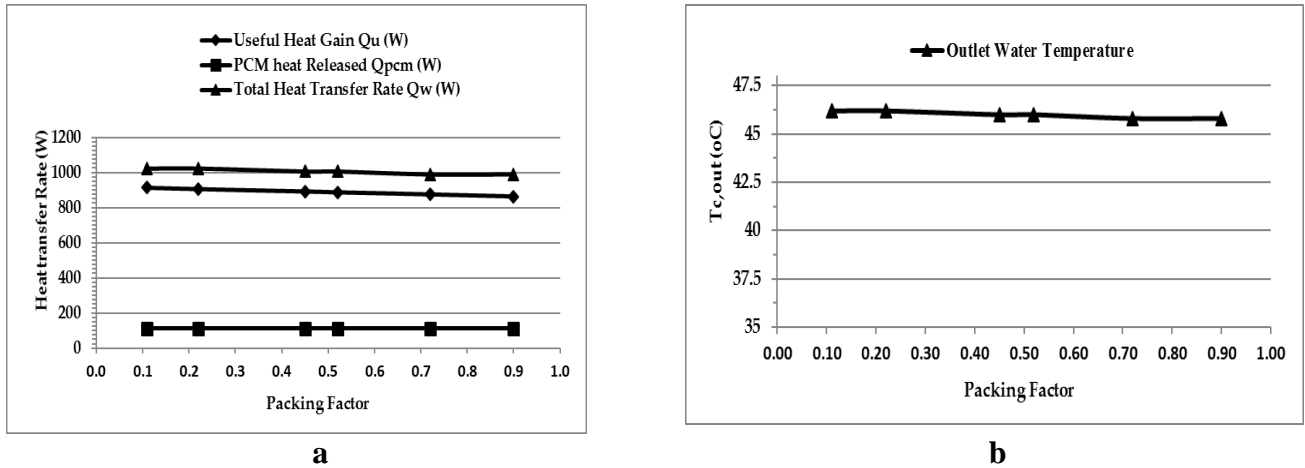


Fig.4-38. Influence of the packing factor on heat transfer rates and the outlet water

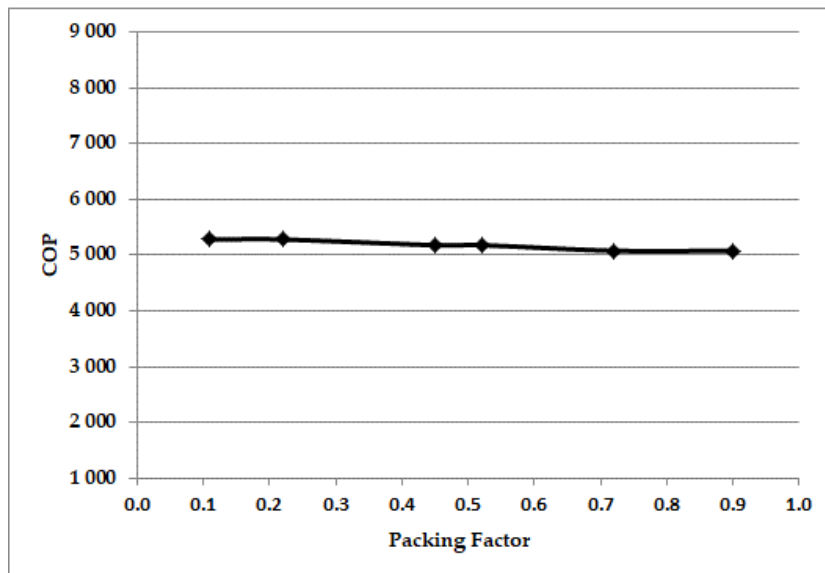


Fig.4-39. Influence of the packing factor on the COP

#### 4.3.3.6 Influence of Number of heat pipe

By varying the number of heat pipes from 5 to 10 while the other parameters remained constant, solar radiation at  $800 \text{ W/m}^2$ , air temperature at  $25^\circ\text{C}$ , velocity  $1 \text{ m/s}$ . It was found that increasing the number of microchannel heat pipes increases the overall efficiency of the system from  $64.9\%$  to  $67.85\%$  (Fig.4-40a) and the effect is most evident for of heat pipe quantities less than 10. It is found that for the microchannel heat pipe number ( $N_{hp}$ ) superior to 20 the overall heat transfer coefficient is approximately constant.

## CHAPTER 4: THEORETICAL ANALYSIS AND COMPUTING MODEL DEVELOPMENT

The total heat transfer rate tends also to be constant. **Fig.4-41** shows also that for  $N_{hp} > 20$ , the PV cell and the outlet water temperatures,  $40.48^{\circ}\text{C}$   ~~$5^{\circ}\text{C}$~~  and  $45.8^{\circ}\text{C}$  respectively, are constant. The COP of system follows also this behaviour (**Fig.4-42**) and is constant for a  $N_{hp}$  superior to 20. This means that 20 microchannel heat pipes represent an optimal microchannel number.

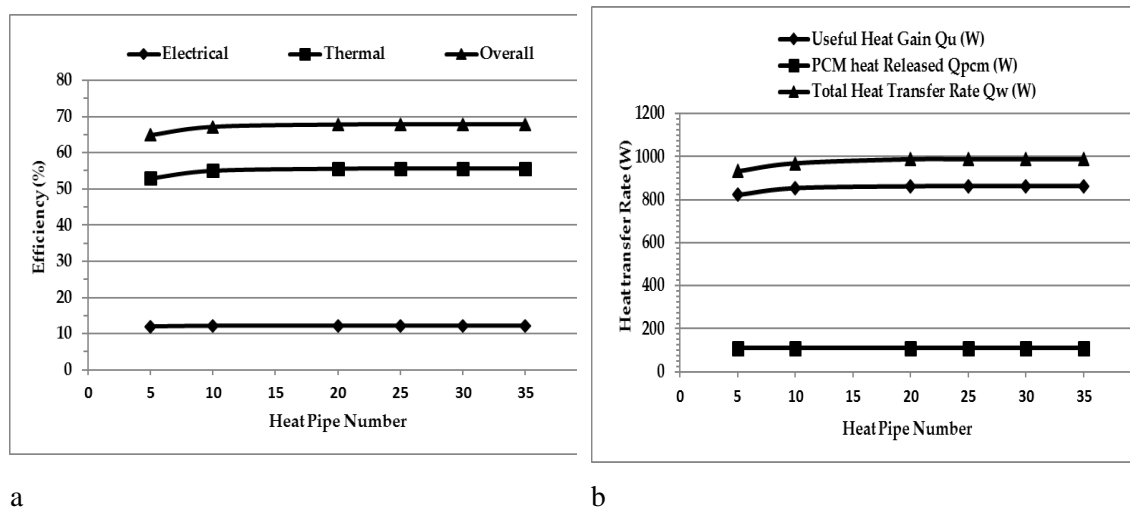


**Fig.4-40 Influence of the microchannel heat pipe number on the efficiency**

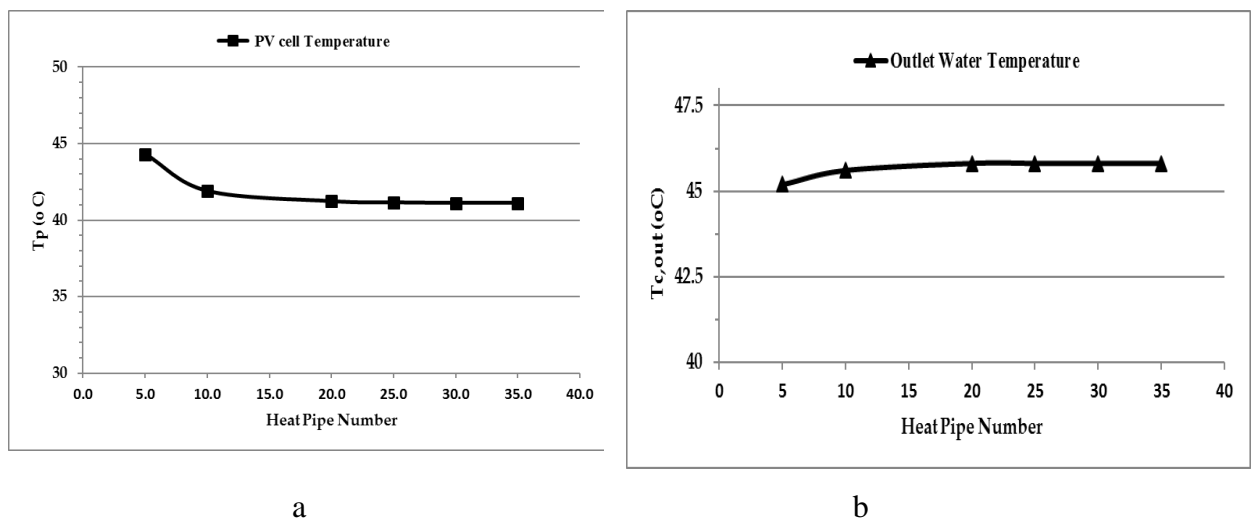


**Fig.4-41. Influence of microchannel the heat pipe number on the PV cell temperature and the outlet water temperature**

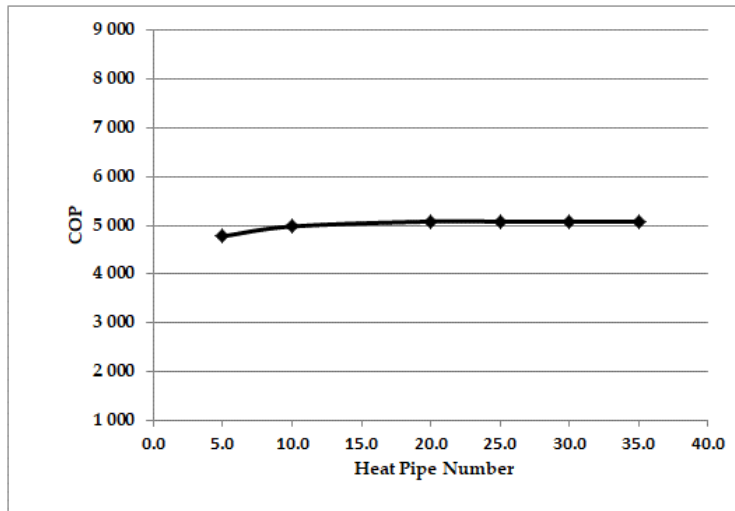
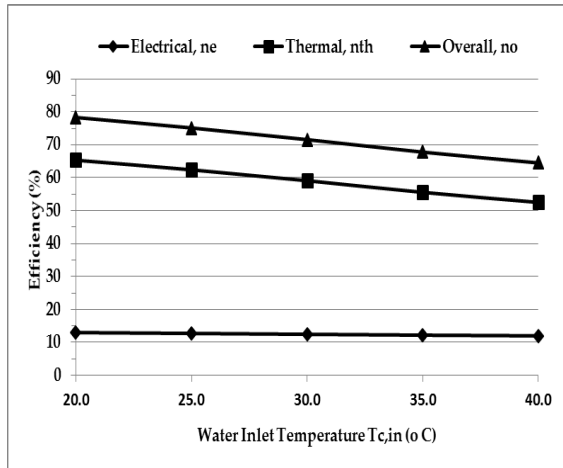


**Fig.4-42. Influence of microchannel heat pipe number on the COP**

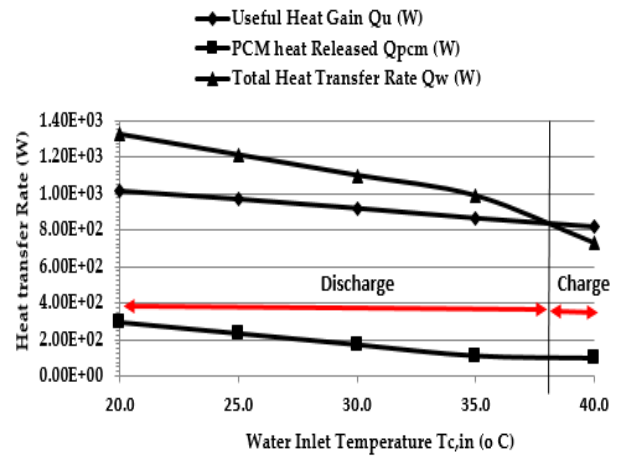
#### 4.3.3.7 Influence of water inlet temperature

By varying the cold water inlet temperature at the heat exchanger from 20°C to 40°C. While the other parameters remained constant solar radiation at 800 W/m<sup>2</sup>, air temperature at 25°C, velocity 1 m/s. It was seen that increasing the water inlet temperature would significantly decrease the overall efficiency of the system (**Fig.4-43a**). This decrease is due to the increase of the water outlet temperature (**Fig.4-44b**) that increases the heat loss in the loop system. Figure 4-38a shows that the increase of the water inlet temperature significantly decreases the total heat transfer rate. This significant decrease is due to the decrease of the useful heat  $Q_u$  because of the heat loss incises and the decrease of the total heat released the PCM  $Q_{cm}$ . It can be seen that for water inlet temperature near 48°C the useful heat  $Q_u$  is superior to the total heat transfer rate  $Q_w$  (**Fig.4-3939b**). This means there is excess heat is charged in the PCM material.

## CHAPTER 4: THEORETICAL ANALYSIS AND COMPUTING MODEL DEVELOPMENT

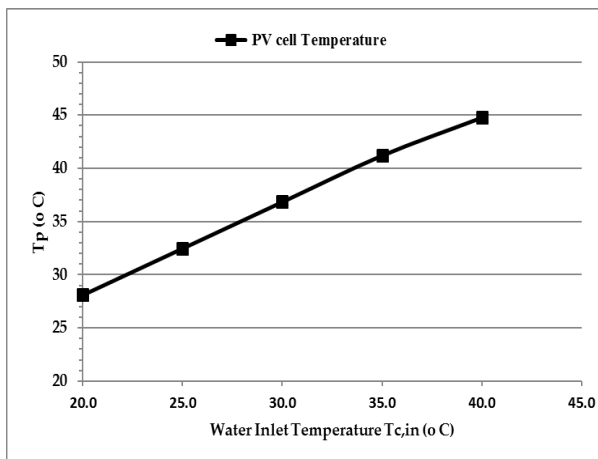


a

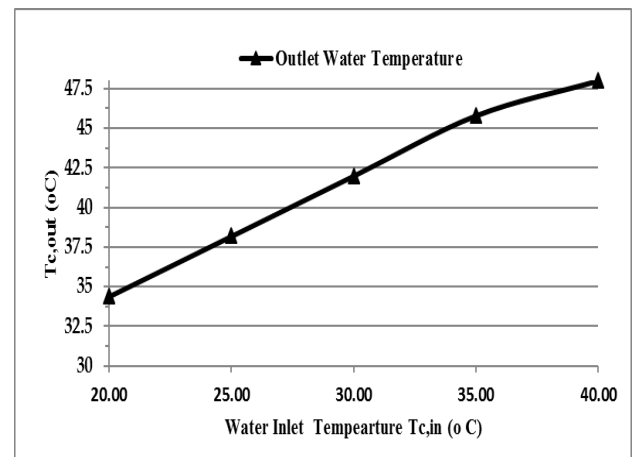


b

**Fig.4-43. Influence of the water inlet temperature on the efficiency**



a



b

**Fig.4-44. Influence of the water inlet temperature on heat transfer rates and the outlet water**

**Fig.4-45** shows that the COP evolution presents a maximum value where the heat excess is beginning to be charged in the PCM material and the COP falls.

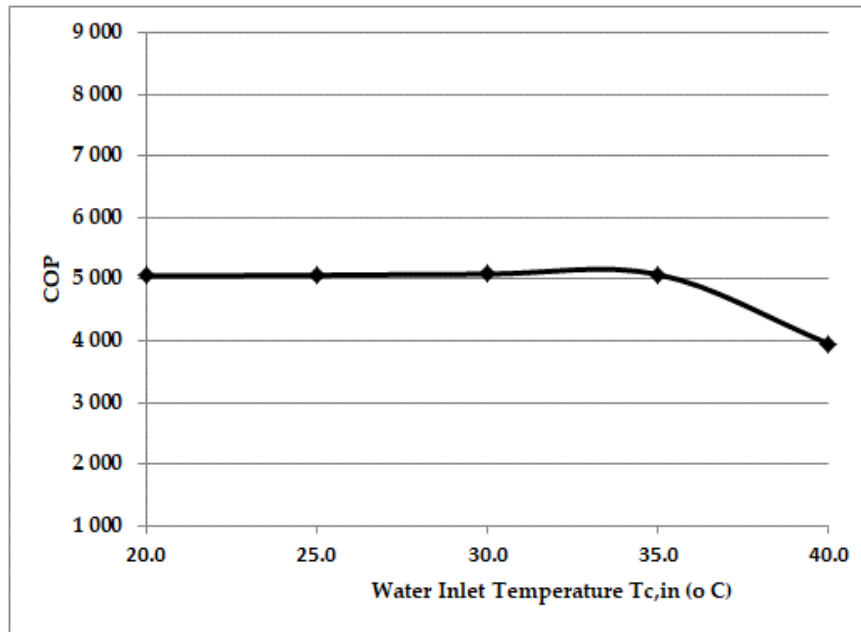


**Fig.4-45 Influence of the water inlet temperature on the COP**

#### 4.3.3.8 Influence of the water mass flow

By varying the water mass flow rate from 0.01 to 0.087 kg/s, while the other parameters remained constant, the influence this variation on the system performance has been assessed. For lower mass flow rates  $m_w < 0.04$  m/s, the overall efficiency of the module increases with the flow rate, after this point the efficiency tends to be constant (**Fig.4-46a**). This can be explained by the fact that increasing the mass flow rate decreases the mean temperature of the water in the annular tube and then decreases of the heat losses in the system. Consequently, the useful heat gain increases (**Fig.4-47b**) and the thermal efficiency increases. The electrical efficiency also increases because of the PV cell temperature decreases (**Fig.4-46**). Otherwise the increase of the mass flow rate decreases the heat released by the PCM for flow rate inferior to 0.02 kg/s and above this tends to be constant. **Fig.4-48** shows that the increase of the mass flow rate significantly influences the COP of the system, because of the supplementary electricity consumption of the system. It is seen that the flow rate of 0.0125 kg/s would be an optimal value for high COP and high heat output simultaneously.

## CHAPTER 4: THEORETICAL ANALYSIS AND COMPUTING MODEL DEVELOPMENT

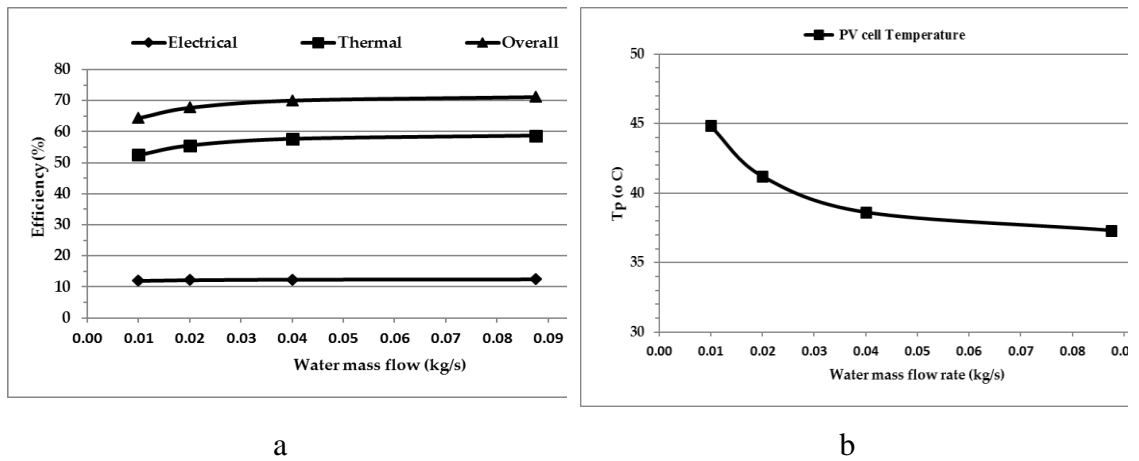


**Fig.4-46. Influence of the water mass flow rate on heat transfer rates and the outlet water**

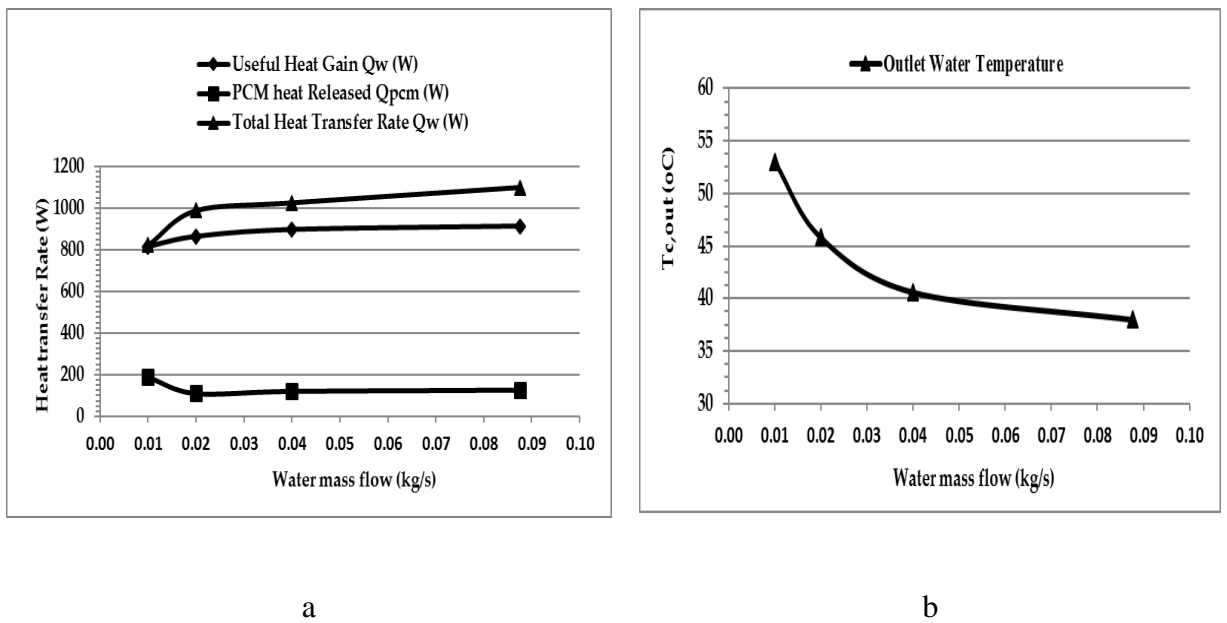


**Fig.4-47. Influence of the water mass flow rate on the efficiency**

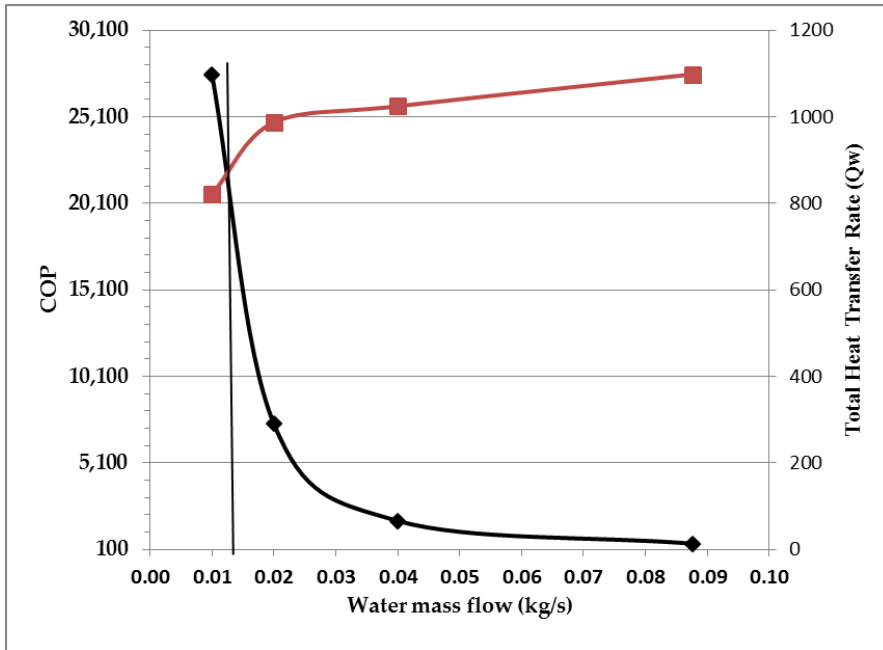


**Fig.4-48. Influence of the water mass flow rate on the COP**

#### 4.3.4 Comparison of the novel system with the conventional system

In this section the novel PVT system has been compared with a conventional system as shown in **Fig.4-49**. The conventional system has a hydraulic diameter of 12 mm (vs 1.2 mm for the novel system) and the loop heat pipe has a plate flat heat exchanger for the condensation. The model of the plate heat exchanger is described in [25]. For the conventional system, the liquid return enters by the bottom of the system. For each system the same number (20) of heat pipe collectors has been supposed. For the two systems the same PV and glazing cover optical and thermal properties were used. The efficiency of these systems was assessed for an ambient temperature of 25°C and wind velocity of 1 m/s.

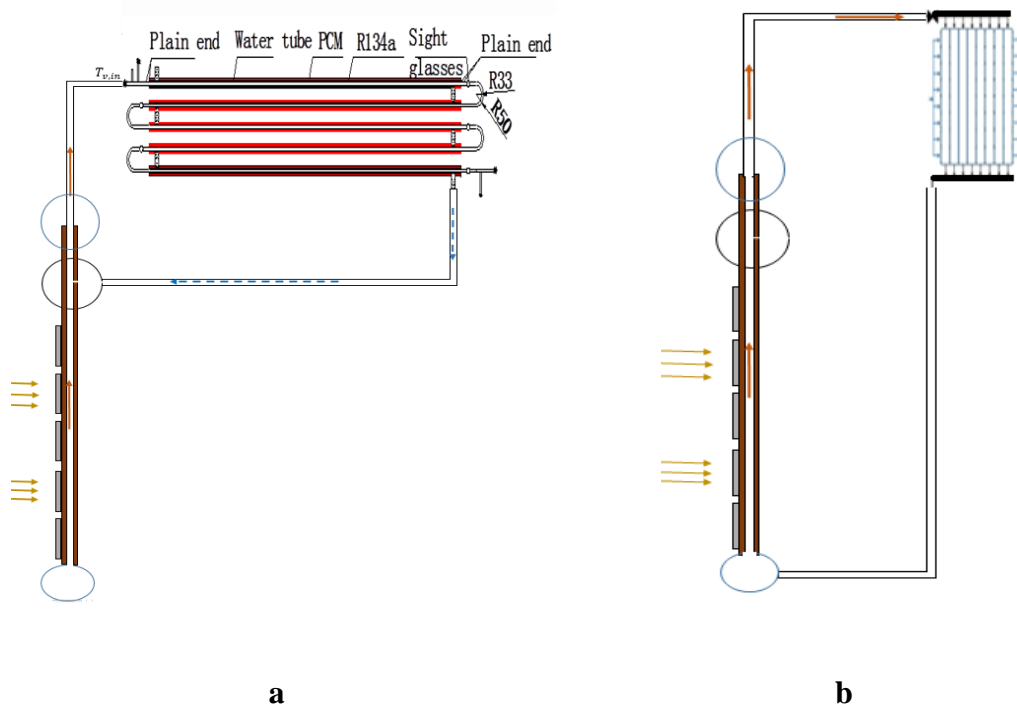
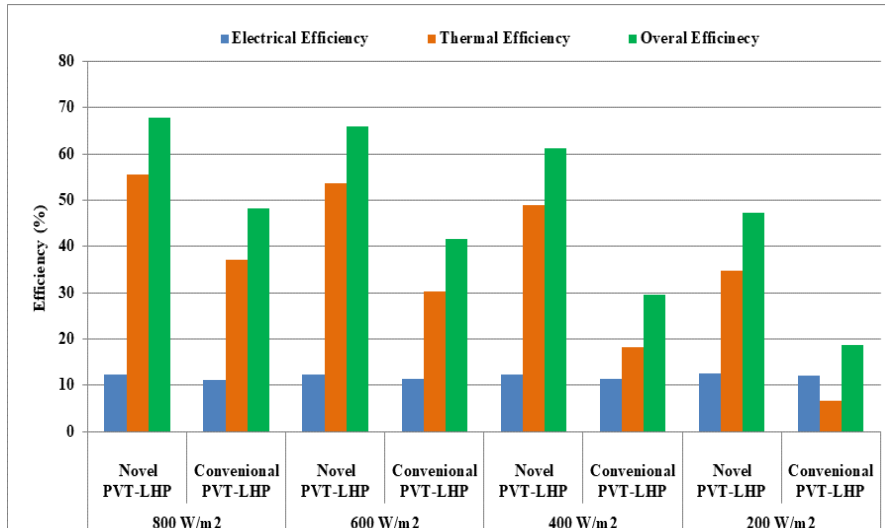


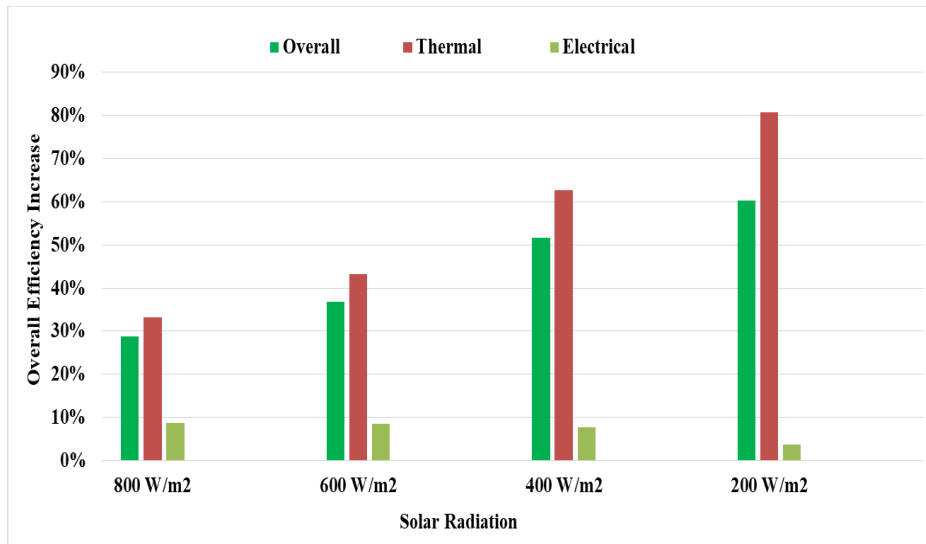
**Fig.4-49 Comparison between, a) the novel PVT system b) the conventional PVT system**

**Fig.4-50** shows the efficiency of the system for different solar radiation intensities and the resulting efficiency increase. Compared to the novel system, the system efficiency increases at least by 33% for the thermal efficiency, 8.7% for the electrical efficiency and 28.8% for the overall efficiency. The efficiency increase is more important at lower solar radiations. This performance is due to three main factors: Firstly, the higher heat transfer rate in the micro-channel evaporator that absorbs more heat ( $4340 \text{ W/m}^2/\text{K}$  against  $1500 \text{ W/m}^2/\text{K}$ ), secondly the significantly decrease of the PV cell temperature (e.g. decrease of  $12.31^\circ\text{C}$  at  $800 \text{ W/m}^2$ ) and finally because of the heat released by the PCM heat exchanger.

CHAPTER 4: THEORETICAL ANALYSIS AND COMPUTING MODEL DEVELOPMENT



a



b

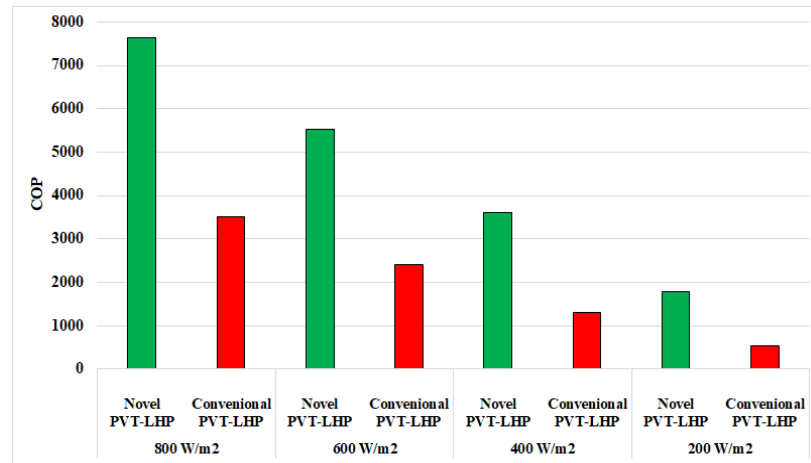
**Fig.4-50. Comparison between the new PVT system and the conventional PVT system a) evolution of thermal, electrical, overall efficiencies b) overall efficiency increase**

**Fig.4-51** shows the COP of the system for different solar radiation intensities and the COP ratio of the novel system to the conventional system. It was found that the overall COP of the system was at least 2.2 times higher when compared to the conventional

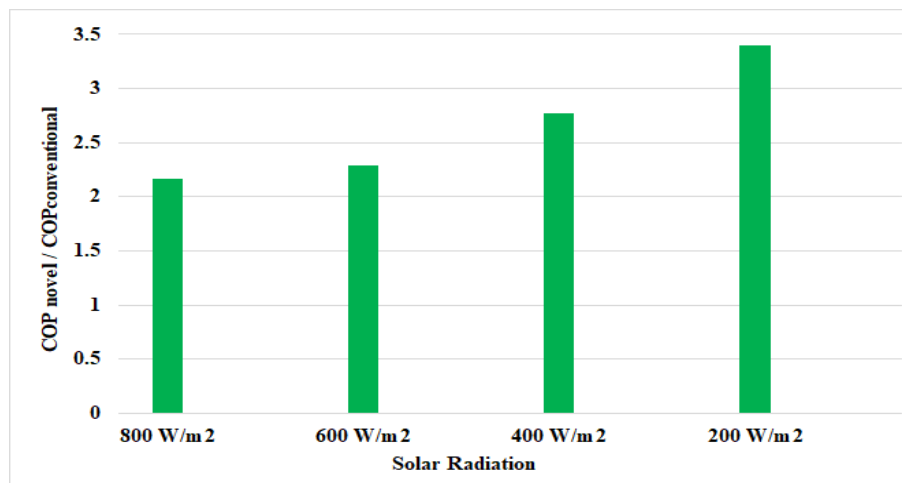
## CHAPTER 4: THEORETICAL ANALYSIS AND COMPUTING MODEL DEVELOPMENT

---

system. This higher COP is due to the higher heat output of the novel system and the lower power consumption of the water pump (0.18 W against 0.12 W).



**a**



**b**

**Fig.4-51. Comparison between the new PVT system and the conventional PVT system a) evolution of the COP<sub>PVT</sub> and b) the ration of COP novel by COP conventional**

### 4.3.5 Conclusion

This section presented a novel solar PVT Loop Heat Pipe (PVT-LHP) system using a Micro-channel evaporator and a PCM triple heat exchanger. A computer model was developed to assess the performance of the PVT-LHP system on the basis of a heat

## CHAPTER 4: THEORETICAL ANALYSIS AND COMPUTING MODEL DEVELOPMENT

---

balance mechanism, which gave the predicted PV modules' solar thermal, electrical and overall efficiencies, and the system's overall performance coefficient ( $COP_{PV/T}$ ) at the specified operational conditions. The influence of the environmental parameters (i.e. solar radiation, air temperature, wind velocity), structural parameters (i.e. glazing covers, number of the absorbing heat pipes, PC cell packing factor), the variable inputs (i.e. water inlet temperature, mass flow rate) on the energy performance of the system was investigated individually. The novel PVT-LHP has been compared with a conventional Solar PVT-LHP system. It was found that:

- (1) Increasing the solar radiation led to an increase in thermal efficiency and a decrease in the electrical efficiency, resulting in an increase the system's overall performance coefficient ( $COP_{PV/T}$ );
- (2) Increasing the ambient air temperature led to an increase in the thermal efficiency, a decrease in the electrical efficiency and an increase in the system's overall performance coefficient ( $COP_{PV/T}$ );
- (3) Increasing the wind speed led to a slight decrease in the thermal efficiency, slight increase decrease in the electrical efficiency and slight decrease in the system's overall performance coefficient ( $COP_{PV/T}$ );
- (4) Increasing number of the glazing covers led to increase in the module's thermal efficiency but a decrease in the module's electrical efficiency and in the system's overall performance coefficient ( $COP_{PV/T}$ );
- (5) Increasing the packing factor led to decrease in the module's thermal efficiency but an increase in the module's electrical efficiency and in the system's overall performance coefficient ( $COP_{PV/T}$ );

## CHAPTER 4: THEORETICAL ANALYSIS AND COMPUTING MODEL DEVELOPMENT

---

(6) Increasing number of the heat absorbing pipes led to increase in the fin's efficiency and in the system's overall performance coefficient.

(7) Increasing the cold water inlet temperature led to decrease in the module's thermal efficiency, the module's electrical efficiency and the system's overall performance coefficient ( $COP_{PV/T}$ ).

(8) Increasing the water mass flow rate led to an increase in the module's thermal efficiency and the module's electrical efficiency and in a decrease the system's overall performance coefficient ( $COP_{PV/T}$ ) because of the increase of the pump electricity consumption. The results show that a flow rate of 0.0125 kg/s would be an optimal flow for a high Heat output and high COP simultaneously.

Furthermore, on the whole, the increase of solar radiation, ambient temperature, cover number, heat pipe number, packing factor have seen as the favourable factors for the  $COP_{PV/T}$  (Coefficient Of Performance) of the system, whereas higher wind velocity and cold water mass flow rate have seen to be unfavourable. Under the given design conditions, a number of micro-channel heat pipes of 20 and one glazing cover was found optimal. The electrical, thermal and overall efficiency of the PVT-LHP module were found 12.2%, 55.6 % and 67.8 % respectively and can achieve 28% higher overall energy efficiency, 2.2 times higher overall coefficient of performance  $COP_{PV/T}$  compared to the conventional system. The model developed in this study can be used to design and optimize the energy performance of a novel PVT-LHP system.

### 4.4 Chapter summary

This chapter presents the investigation of the heat transport capacity of a specific micro-channel loop heat pipe (MC-LHP) by applying the latest fractal theory and heat transfer

## CHAPTER 4: THEORETICAL ANALYSIS AND COMPUTING MODEL DEVELOPMENT

---

limits calculation method. In the MC-LHP analytical model, fractal theory was applied to analyse the equivalent heat conductivity of the LHP wicks and a set of operational heat transfer limits including viscous, sonic, entrainment, capillary, boiling and liquid filling mass limit were calculated using the heat pipe heat transfer analytical theories. The results show that the capillary limit is the governing limit of this ML-CHP system. This study helps the assessment of the heat transfer capacity and determination of the optimum geometrical sizes (e.g. diameter, length, and number) of the LHP, thus assisting in the design of the PV/MCLHP system.

Further, this chapter also presents an analytical study of a specifically designed PV/MCLHP system using a dedicated energy balance simulation model. A number of factors, including solar radiation, air temperature, air velocity, heat pump evaporation temperature, and the number of heat-absorbing pipes, were found to impact on the operational performance of the PV/MCLHP system. It is found that under the given design conditions, 20 sets of MC-LHP with a single glazing cover is able to achieve the highest heat and power outputs. The electrical, thermal and overall efficiency of the PV/MCLHP module were 12.2%, 55.6 % and 67.8 % respectively and had 28% higher overall energy efficiency, 2.2 times higher overall coefficient of performance (COP) compared to the conventional system. The model developed in this study can be used for design and optimization of the PV/MCLHP system and prediction of its energy performance under various operational conditions.

# CHAPTER 5: PROTOTYPE CONSTRUCTION AND EXPERIMENTAL TESTING, AND MODEL VALIDATION

## 5.1 Chapter introduction

This chapter presents the fabrication and experimental testing of a prototype PV/MCLHP system, as well as associated computer model validation/refinement. The major works involved include:

- (1) The fabrication of the major PV/MCLHP system components, i.e. the PV/MCLHP-evaporator, the co-axial trip-pipe heat exchanger, and the integrated PV/MCLHP module.
- (2) Experimental testing of 1.2kW rated PV/MCLHP system with a water tank under the controlled laboratory and real weather conditions
- (3) Investigation of the impact of the operational parameters to the performance of the PV/MCLHP system. These parameters include solar radiation, coolant water flow rate, coolant water inlet temperature, ambient temperature, as well as the height difference between the condenser and the evaporator.
- (4) Validation/refinement of the computer analytical model established in Chapter 4, by using the experimental data obtained from the experiment.

## 5.2 Fabrication of the prototype system

### 5.2.1 PV/micro-channel evaporator with headers

Structure of the PV/micro-channel-evaporator is shown schematically in **Fig.5-1**, while a photograph of such an experimental PV/T evaporator prototype is shown in **Fig.5-2**. The

## CHAPTER 5: PROTOTYPE CONSTRUCTION AND EXPERIMENTAL TESTING, AND MODEL VALIDATION

parametrical data of PV panel were shown in **Table 5-1**. The micro-channel tubes, comprising numerous mini holes with equivalent hydraulic diameter of around 0.75mm, were used to make the evaporator of the loop heat pipe. These tubes were then adhered to an aluminium plate and grouped by the lower end liquid header and upper end vapour and liquid headers. This formed a fully integrated micro-channel tubes array which acted as the evaporator of the LHP. This evaporator was then combined with a PV module by including: (1) back tedlar polyester tedlar (TPT), (2) ethylene-vinyl-acetate (EVA), (3) PV cells, (4) ethylene-vinyl acetate (EVA), and glazing cover which is directly pressed on without air gap, thus formulating an integrated PV/micro-channel evaporator. This PV/ micro-channel evaporator was then accommodated into an insulated house and thus became a modular PV/evaporator unit.

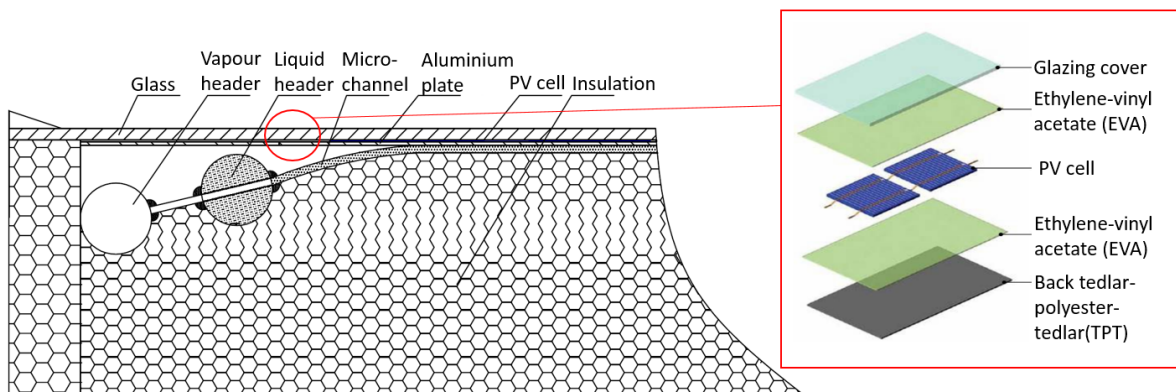


**Fig.5-1. PV/micro-channel-evaporator module**

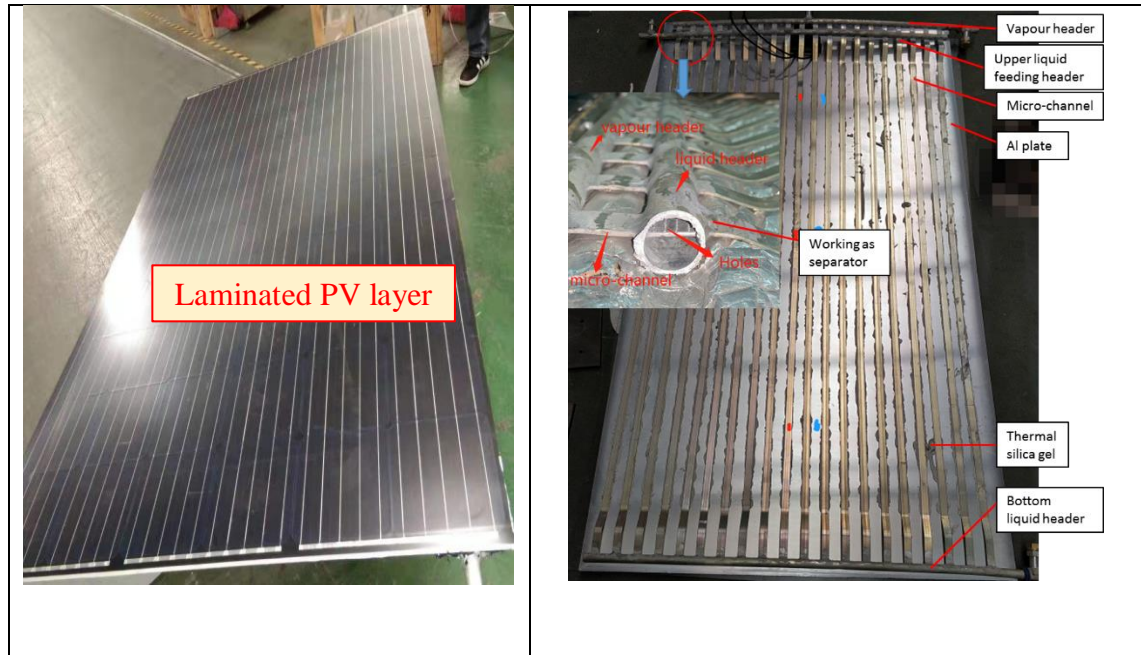


Fig.5-2. The photographic image of Micro-channel evaporator

Table 5-1. Parametrical data of the PV panels

Item	Parameter
Technology (PV cell)	Multi-c-Si
Packing factor (%)	85.4
PV area $A_{pv}$ (m <sup>2</sup> )	1.769
Electrical Efficiency under standard condition $\eta_{rc}$ (%)	18.6
Temperature attenuation coefficient $B_{pv}$ (1/°C)	-0.45
Isc (A)	7.637
Voc (V)	44.894
Pm (W)	292.792
Ipm (A)	7.534
Vpm (V)	38.869

Both the upper end vapour header and lower end liquid header were simply the aluminium cylinders with a diameter of 22 mm each. These, being welded with the micro-channel tubes, served as the containers to collect liquid and vapour from the micro-channel tubes. Unlike in the upper end vapour header and lower end liquid header, the micro-channel in the upper end liquid header was drilled with numerous tiny holes which are dedicated to

deliver liquid across the inner wall of the micro-channel evaporator, thus creating a uniformly distributed liquid film across the inner surface of the evaporator. It should be noted that pressure difference of the liquid prior and after the holes was controllable by adjusting the height of the liquid level within the header, thus matching the heat input through the micro-channel surface and keeping a balance between the liquid supply and evaporation.

## **5.2.2 Co-axial tubular triple-pipe heat exchanger with PCM (as the condenser)**

### *(1) Structure of the co-axial tubular heat exchanger*

Structure of the co-axial tubular heat exchanger is shown in **Fig. 3-5**, while its parametrical data are presented in **Table 3-3**. This heat exchanger, laid with a serpentine form with a total length of 5m, is composed of three co-axially laid copper pipes. The inner pipe is the refrigerant flow path in which the refrigerant is gradually condensed. The middle annulus pipe is the water flow path in which the water absorbs the heat released from the refrigerant during its condensation process and thus is heated to the required temperature. The outer annulus pipe is for accommodation of an organic PCM which absorbs the heat from the water if its temperature is higher and releases heat when the water temperature is lower. In order to observe the phase state of the refrigerant inside the central pipe, four sight glasses were installed on the turning corners of the central pipe. At the both ends of the pipe, two vertical copper pipes were assembled, with one for refrigerant charging and the other for pressure sensor installation. A photograph of the co-axial tubular heat exchanger is shown in **Fig.5-3**. The design drawings of the co-axial tubular heat exchanger is shown in **Fig.5-4**. The item description of the co-axial tubular heat exchanger is presented in **Table 5-2**.



**Fig.5-3.** A photograph of such a co-axial condensation heat exchanger

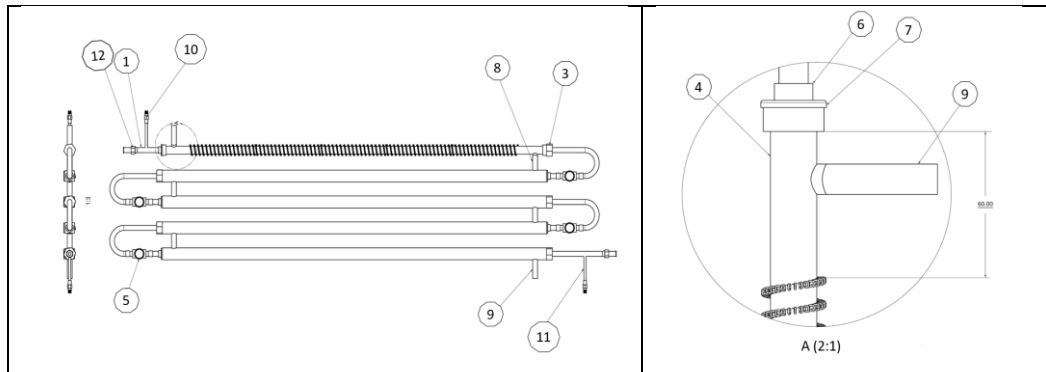


**Fig.5-4.** Co-axial condensation heat exchanger

**Table 5-2.** Item description of the heat exchanger configuration

Item No.	QTY	Description
1	1	Ref. (R134a) Tube
2	4	PCM External Tube
3	5	Screw End Cap
4	5	Water Tube
5	1	Sight Glass
6	10	End Caps
7	5	Threaded
8	4	Water Spacer
9	2	In/Out Pipe
10	2	R134a Connector Purge
11	2	R134a In/Out Pipe
12	2	Connecting Nut

**(2) Selection of phase change material (PCM)**

PCM material within the outer tube was produced by Phase Change Material Products Ltd. In order to find the proper PCM for the heat exchanger of this system, the Differential Scanning Calorimeter (DSC) technique was applied to investigate the thermal

## CHAPTER 5: PROTOTYPE CONSTRUCTION AND EXPERIMENTAL TESTING, AND MODEL VALIDATION

performance of a range of PCMs with phase change temperatures varying from 28°C to 58°C. Work was largely focused on PCMs with phase change temperature in the region of 45°C. Through the experiments conducted by PCM Ltd., A44 is found to be the candidate PCM which, as shown in **Fig.5-5**, has a narrow freezing/melting range, and a latent heat of 242kJ/kg. The thermal physical properties of A44 are presented in **Table 5-3**.

This PCM is shaped into a thin layer and fitted into the outer tube of the heat exchanger to serve as the heat storage body with a relatively high thermal conductivity. This forms a lower cost and small-sized heat storage/exchanger.

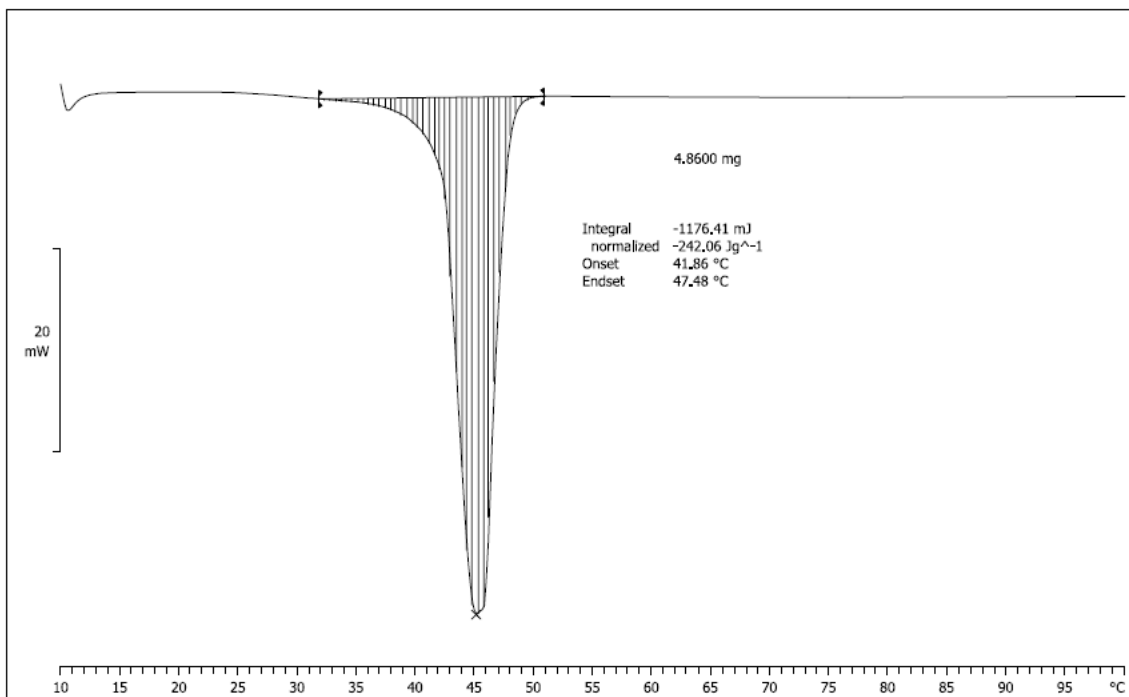


**Fig.5-5 DSC of A44**

**Table 5-3. Thermal physical properties of PCM (A44)**

PCM type	A44
Phase change temperature (°C)	44
Latent heat capacity (kJ/kg)	242
Specific heat capacity (kJ/kg/K)	2.15
Thermal conductivity (W/m·K)	0.18

### 5.2.3 The integrated PV/MCLHP Module

In order to reduce the thermal resistance between the PV cells and the Al plate, PV cells covered with textured tempered glass is directly pressed on the aluminium (Al) plate by applying a thermal grease, which has thermal conductivity of  $2.68\text{W/m}\cdot\text{K}$  owing to the addition of silver. The MC-LHP evaporator was pressed and attached on the aluminium plate, which works as heat conductor fin sheet adhering to the back surface of the PV layer, by applying thermal-conductive silica gel with relatively high thermal conductivity. Before grouping all the components, a leakage test of the MC-LHP evaporator was undertaken in order to avoid any potential refrigerant leakage. The MC-LHP evaporator was then connected to the water line to test the heat transfer performance between the refrigerant and water flow, as shown in **Fig.5-6**. Further, the PV panels were tested to ensure their electrical output at the normal standard.

After completing the preliminary tests of the major system components, the PV/MCLHP module, as illustrated in **Fig.5-7**, was fabricated. This is simply made by integrating all the system components including the single glass covering, PV layer, aluminium plate, MC-LHP evaporator into an AL-alloy casing, which is filled with fiber glass wool to provide excellent thermal insulation.

The co-axial tubular heat exchanger (i.e. condenser) and the PV/MCLHP evaporator were then connected using the long flexible hoses, thus formulating a complete PV/MCLHP heat and power system. The flexible hoses, acting as the vapour and liquid transportation lines, enable the refrigerant to circulate between the PV/MCLHP evaporator and the co-axial tubular heat exchanger. The integrated PV/MCLHP system was fixed to a vertical frame to make both the evaporator and condenser in vertical position, which helps the liquid working fluid to flow from the condenser to the evaporator and also favours the

## CHAPTER 5: PROTOTYPE CONSTRUCTION AND EXPERIMENTAL TESTING, AND MODEL VALIDATION

formation of the uniform liquid film on the inner wall of the evaporator to assist the evaporation of the refrigerant.

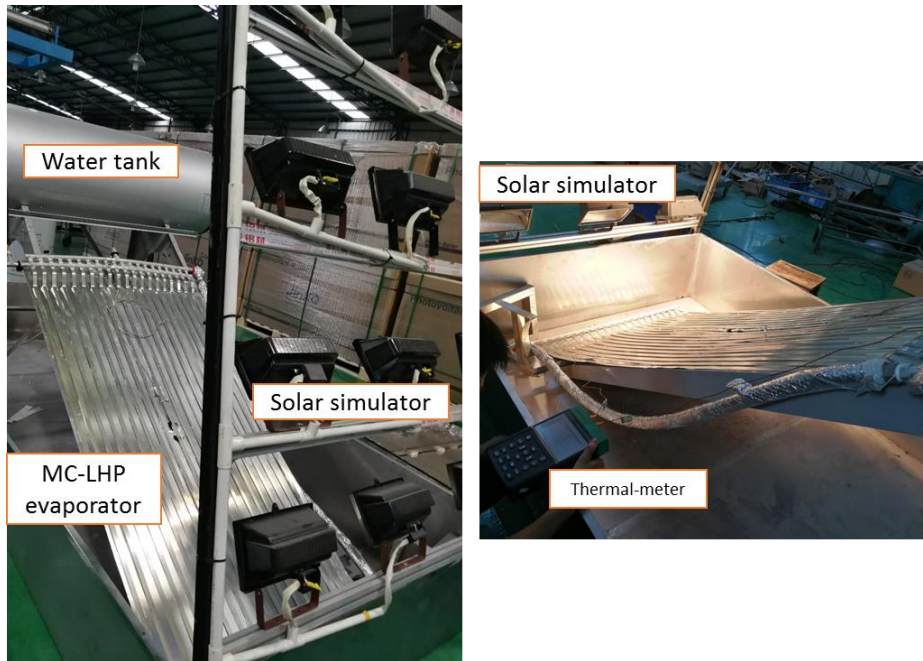


**Fig.5-6. MC-LHP evaporator pre-assembling testing**

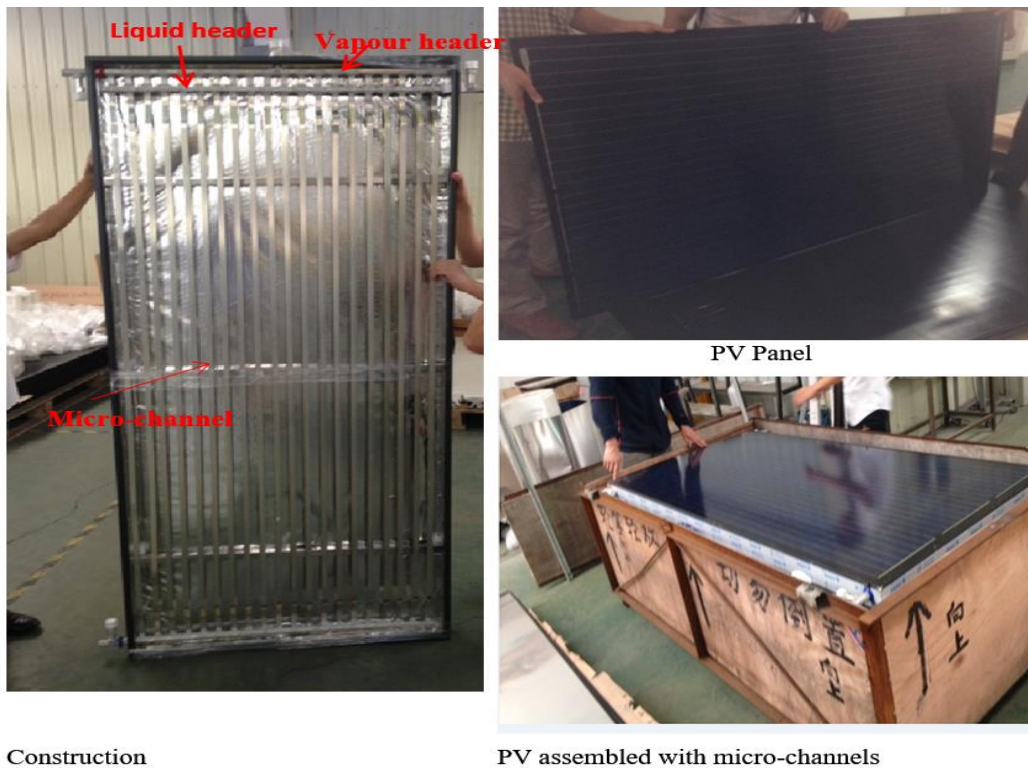


**Fig.5-7. The photographic image of the PV/MCLHP module**

## 5.3 Experimentation set-up

### 5.3.1 Experimental system

A single experimental PV/MCLHP system with a 45-litre water tank was designed and constructed to test the performance of the system. The coolant water is designed to take the heat away from the condenser of the LHP and discharge the collected heat to an external source (e.g. water tank). The water loop consists of (1) a water circulation pump which is used to drive water through the loop by overcoming the relevant flow resistances within the loop; (2) an axial fan to discharge the heat from the coolant water to the atmosphere; (3) flow meter, pressure meter, and water pipelines that, being connected to the co-axial heat exchanger, forms the circulation route for the coolant water. The technical specifications of the loop components are presented in **Table 5-4**.

**Table 5-4. List of the testing and monitoring components**

Item	Specification
Temperature sensor	T-type
Power sensor	Solar Power controllerMPPT
Pressure sensor	Diffused silicon pressure transmitter sensor (4-20mA, 0.1~2.5Mpa, G1/4)
Pyranometer	HQTBQY (Wuhan Hanqin System Science & Technology Co., Ltd. China)
Data logger	Aglient 34972A, TR230X temperature recorder
Water pump	BJZ037-B (Head 20m)
Fan coil	1.5p*4D300/380 (1380r/min, max 1450m3/h, Boyoung Co., Ltd. China )
Solar simulator	PD1-ZNK1 (600-1200W/m <sup>2</sup> , 280-3000nm ±5%, Sunshine Technology Co., Ltd. China)

As shown in **Fig.5-8**, a MPPT solar power controller, installed with Maximum Power Point Tracking (MPPT) algorithm, can maximize the amount of current charged into the battery. This controller acts as both an electrical recorder and a converter, which accepts the DC input from the PV/T module, converts it into AC, and then deliver the AC into

the battery bank to reserve. A separate DC/AC inverter was used to convert DC from the battery bank into AC which is used to driven the fan and pump in this system. Such a system can keep a balance between the electrical supply and demand.

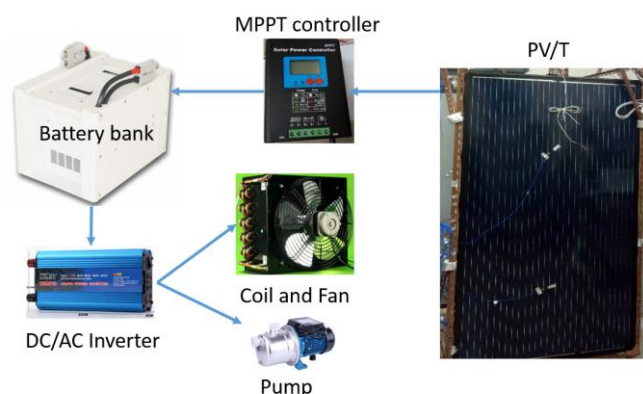


**Fig.5-8. Solar power process from the PVs to the User (Coils and Fan)**

The electrical efficiency of the PVs is proven to be dependent upon the PV cells' temperature[26]. In line with this unique feature and considering the light spectrum characteristics of the solar simulator which, falling into a range between 280 and 3000 nm, is only suitable for the use in solar thermal simulation, we decided to measure the solar electrical and thermal efficiencies separately. The electrical efficiency of the PV/MCLHP system was measured under real weather condition which aimed to determine the one-to-one relationship between the solar electrical efficiency and PV cells' temperature. The photograph of the outdoor experimental system is shown in **Fig.5-9**.

Solar thermal efficiency of the system was a bit more complex and varied with numerous operational parameters, e.g., solar radiation, coolant water flow rate, coolant water inlet temperature, ambient temperature, as well as the height difference between the condenser and the evaporator. In order to evaluate the operational performance of the PV/MCLHP system, a range of tests were carried out at an indoor (laboratory, as shown in **Fig.5-10**)

## CHAPTER 5: PROTOTYPE CONSTRUCTION AND EXPERIMENTAL TESTING, AND MODEL VALIDATION

---

space at GDUT in which the relatively steady state operational conditions can be maintained. These tests were dedicate designed to investigate the impact of a range of operational conditions to solar thermal efficiencies of the system. This will be achieved by remaining other parametrical data unchanged but letting only one parametrical data change.

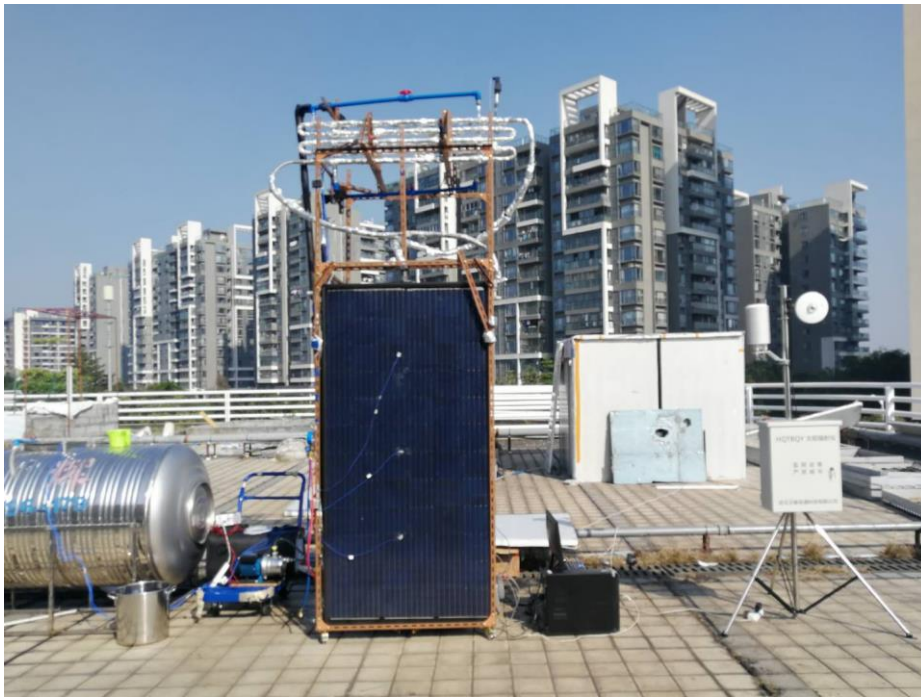


**Fig.5-9. Outdoor experimental system**

The fully established experimental system was equipped with various measurement instruments and sensors, including a pyranometer, a rotameter, thermocouples/temperature probes, and pressure sensors, which were installed at appropriate positions to measure solar radiation, flow rate, temperature and pressure, respectively. A Solar Power Controller (MPPT) was used to test the output electricity of the PV/MCLHP module. **Table 5-4** presents the technical information of the measurement instruments/sensors used in the testing process. **Fig.5-11** shows the installation profile of the measurement instruments and sensors in the experimental system.

# CHAPTER 5: PROTOTYPE CONSTRUCTION AND EXPERIMENTAL TESTING, AND MODEL VALIDATION

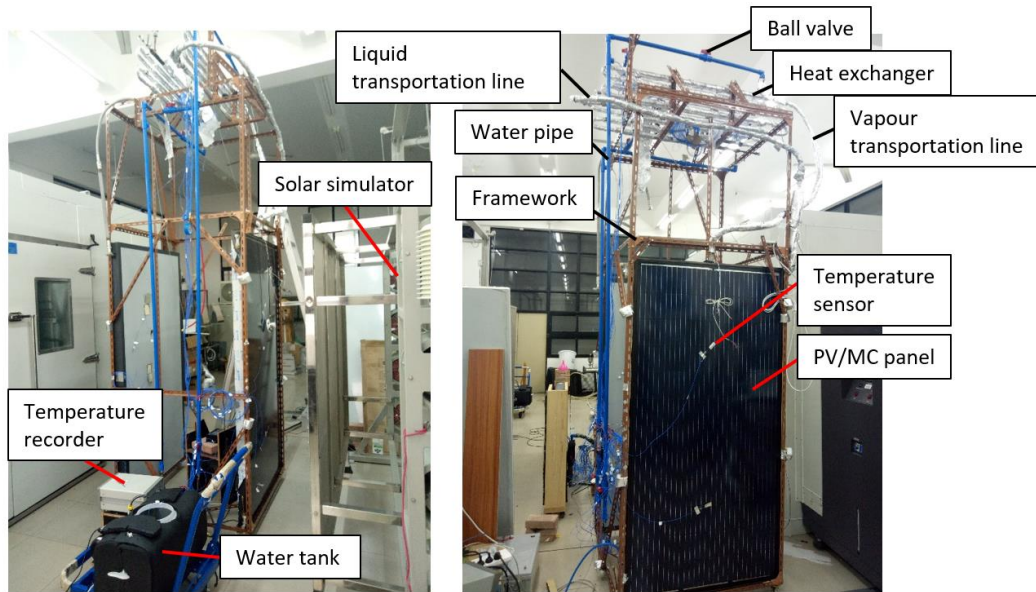
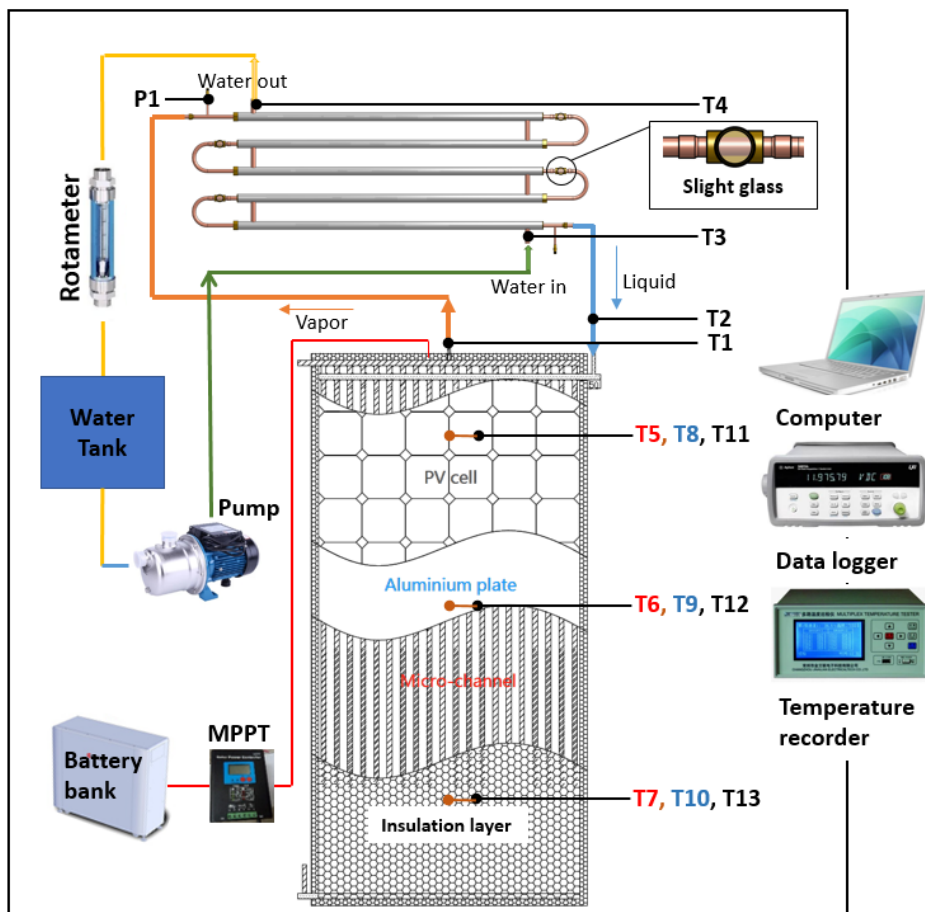


**Fig.5-10 Experimental PV/MCLHP heating system view in the lab**



P1-pressure of the LHP; T5, T6, T7-Surface temperature of PV panel

T8,T9,T10-Surface temperature of Al plate; T11,T12,T13-Temperature of micro-channel

**Fig.5-11. Schematic of the experimental set up and instrumentation**

### 5.3.2 Experimental procedure

The measurement data was recorded at 30s interval and logged into the computer to enable the follow-on analysis to be made. The analyses of the experimental data took into account the potential uncertainties of the measurement instruments, e.g. tolerance of the solar radiation ( $\pm 10\text{W}$ ), measurement discrepancy of the temperature sensors ( $\pm 0.1^\circ\text{C}$ ), etc. Furthermore, some potential random errors, caused by personal mal-operation, random electronic data fluctuation, and fluid friction etc, were also taken into consideration.

### 5.3.3 Performance evaluation indicators

A number of key indicators, including the output power, solar electrical and thermal efficiencies, and overall solar efficiency, were applied to evaluate the performance of the PV/MCLHP system. These are defined as below:

Output power of PV/T ( $P_{PVT}$ ) can be expressed as:

$$P_{PVT} = U_{PVT} I_{PVT} \quad (5-1)$$

Where;  $U_{PVT}$  is the output voltage of the PV/MCLHP panel and  $I_{PVT}$  is the current of the PV/MCLHP panel.

Solar electrical efficiency ( $\eta_e$ ) can be expressed as:

$$\eta_e = \frac{P_{PVT}}{G \cdot A_{PV}} = \frac{U_{PVT} I_{PVT}}{G \cdot A_{PV}} \quad (5-2)$$

## CHAPTER 5: PROTOTYPE CONSTRUCTION AND EXPERIMENTAL TESTING, AND MODEL VALIDATION

---

Where  $\eta_e$  is the electrical efficiency of PV/T panel,  $P_{PVT}$  is the output power of PV/T panel,  $U_{PVT}$  is the output voltage of PV/T panel,  $I_{PVT}$  is the current of the PV/T panel, and  $G$  is the solar radiation,  $A_{PV}$  is the PV area of base panel. Alternatively, Electrical efficiency ( $\eta_e$ ) can be written as:

$$\eta_e = \eta_{rc}[1 - \beta_{PV}(T_{PV} - T_{rc})] \quad (5-3)$$

Where,  $\eta_{rc}$  is the initial electrical efficiency at reference temperature;  $\beta_{PV}$  is temperature coefficient;  $T_{PV}$  is PV cells temperature at operation;  $T_{rc}$  is reference temperature.

Solar thermal efficiency ( $\eta_t$ ) can be expressed as:

$$\eta_t = \frac{q_{th}}{G \cdot A_{PV}} = \frac{c_w m_w (T_{wout} - T_{win})}{G \cdot A_{PV}} \quad (5-4)$$

Overall solar efficiency can be expressed as:

$$\eta_{overall} = \eta_e + \eta_t \quad (5-5)$$

### 5.3.4 Uncertainties analysis

The uncertainties of this experiment were analysed based on to the theory of error propagation, i.e. the experimental error of the independent variables, such as temperature, output power and solar radiation, is determined by the accuracy of the specific measurement instrument; while the error of dependent variables, such as solar efficiencies,

## CHAPTER 5: PROTOTYPE CONSTRUCTION AND EXPERIMENTAL TESTING, AND MODEL VALIDATION

---

can be calculated on the error of the independent variables. For a given dependent variable  $y$ , the following equation can apply:

$$y = f(x_1, x_2, \dots, x_n) \quad (5-6)$$

The relative error (RE) can be expressed as [44, 45]:

$$RE = \frac{dy}{y} = \frac{\partial f}{\partial x_1} \frac{dx_1}{y} + \frac{\partial f}{\partial x_2} \frac{dx_2}{y} + \dots + \frac{\partial f}{\partial x_n} \frac{dx_n}{y} \quad (5-7)$$

Where  $x_i$  ( $i = 1, 2, \dots, n$ ) is the variable of the dependent variable  $y$ ; and  $\partial f / \partial x$  is the error transfer coefficient of the variables.

The experimental relative mean error (RME) during the test period can be expressed as:

$$RME = \frac{\sum_1^N |RE|}{N} \quad (5-8)$$

Based on the Eqs. (6) to (8), the REMs of all the variables were calculated and the results were listed in **Table 5-5**.

**Table 5-5. The experimental RMEs of the variables**

Variable	T (%)	G (%)	$\eta_e$ (%)	$\eta_t$ (%)
RME	0.067	2.0	4.2	21.4

### 5.4 Results and discussion

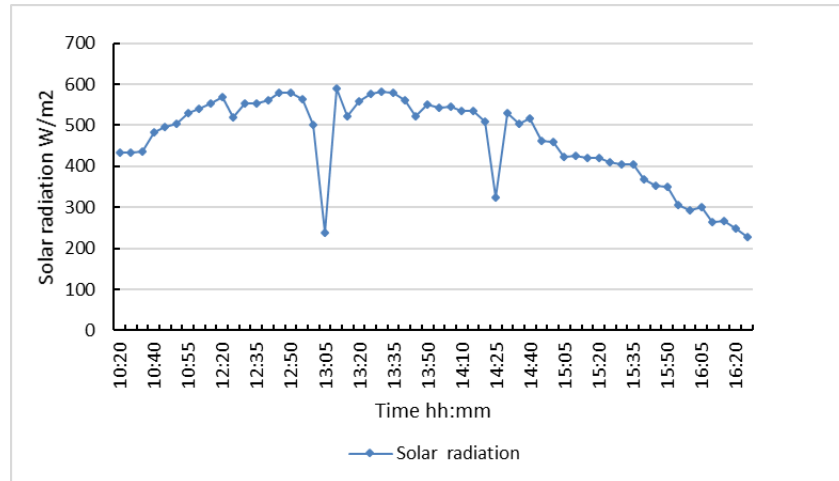
The key performance indicators of the novel PV/MCLHP system, including temperature distribution across the PV/MCLHP evaporator panel surface and along the LHP components, solar thermal, electrical efficiency and overall efficiency were obtained from

dedicated experimental testing. These indicators are found to be largely dependent upon the operational condition of the system, including solar radiation, coolant water flow rate, coolant water inlet temperature, ambient temperature, and height difference between the condenser and evaporator. The impacts of each parameter to the performance of the system were presented and discussed below.

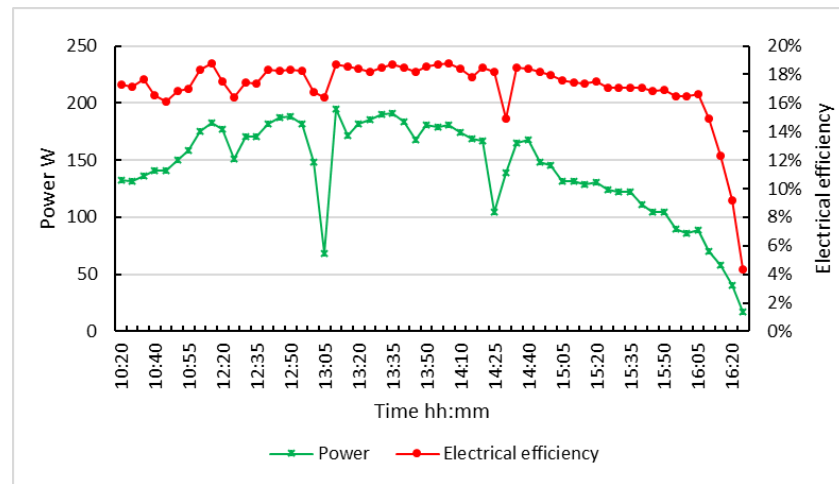
#### **5.4.1 Solar electrical efficiency of the novel PV/MCLHP system**

Solar electrical efficiency of the PV/MCLHP was measured under the real weather condition running from 21<sup>st</sup> to 27<sup>th</sup> Dec. 2018. **Fig.5-12** shows the variation of solar radiation, output power and cell temperature during a single day operation from 10:00 to 16:30. Based on these measurement data, correlation between the solar electrical efficiency and cell temperature was established and this is shown in **Fig.5-13**. Meanwhile, theoretical correlation between the solar electrical efficiency and PV cells' temperature was obtained from the manufacturer testing, as shown in **Table 5-1**, with the intersection efficiency ( $\eta_0$ ) of 18.6% and slope factor of 0.45. The statistic curve for the experimental solar electrical efficiency shows that when the temperature of the PV cells changed from 19 to 60°C, the solar electrical efficiency changed from 18.3% to 15.6%. In addition, it is seen that both the experimental and theoretical correlations show a reasonably good agreement, with discrepancy of -4.18%-1.48%. The reasons for the difference were multiple, including insufficient measurement data, errors in the measurement, as well as sensors' discrepancy etc.

## CHAPTER 5: PROTOTYPE CONSTRUCTION AND EXPERIMENTAL TESTING, AND MODEL VALIDATION



(a)



(b)

**Fig.5-12. (a) Solar radiation, (b) electrical efficiency, and power output**

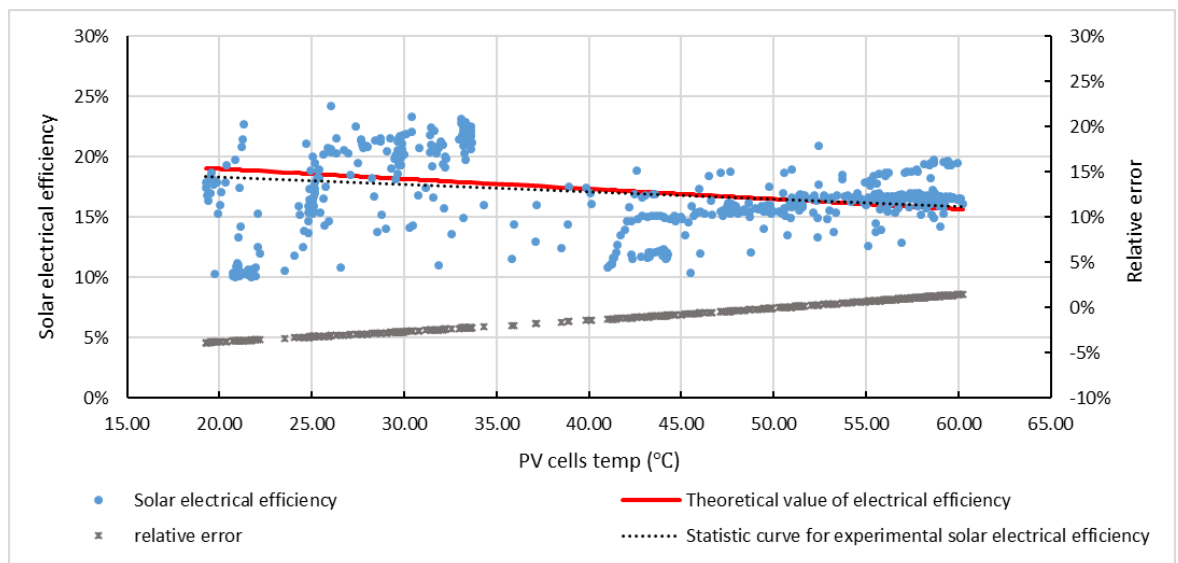


**Fig.5-13. Solar electrical efficiency against PV cells temperature**

### 5.4.2 Impact of the solar radiation

Keeping other parameters unchanged (i.e., height difference at 1.3m, ambient air temperature at  $30\pm 0.5^\circ\text{C}$ , inlet coolant water temperature at  $25\pm 1^\circ\text{C}$ , coolant water flow rate at  $0.17\text{ m}^3/\text{h}$ ), and varying solar radiation from  $489\text{ W}/\text{m}^2$ ,  $561\text{ W}/\text{m}^2$ , and  $667\text{ W}/\text{m}^2$  respectively, impact of the solar radiation on the performance of the PV/MCLHP system was experimentally investigated. **Fig.5-14** shows the variation of the PV/T evaporator surface temperature against solar radiation. It is found that the mid-level of panel had a higher temperature than the lower and higher levels of the panel, indicating that solar radiation distribution across the panel is non-uniform and mid-level of the panel received a higher radiation compared to the lower and upper parts. In view of different layers of the panel, it is surprised to see that the aluminium plate in the mid-layer achieved a little higher temperature compared to the PV surface and micro-channel evaporator which were above and below the aluminium plate respectively. This indicates that the heat transfer across the panel was two-directional: one part of the heat is transferred from the aluminium plate to ambient through the glazing cover, and the other part is conducted directly into the refrigerant within the LHP evaporator. This phenomenon can be explained by the energy transaction processes according to section 3 of the authors' previous published paper[99].

CHAPTER 5: PROTOTYPE CONSTRUCTION AND EXPERIMENTAL TESTING, AND MODEL VALIDATION

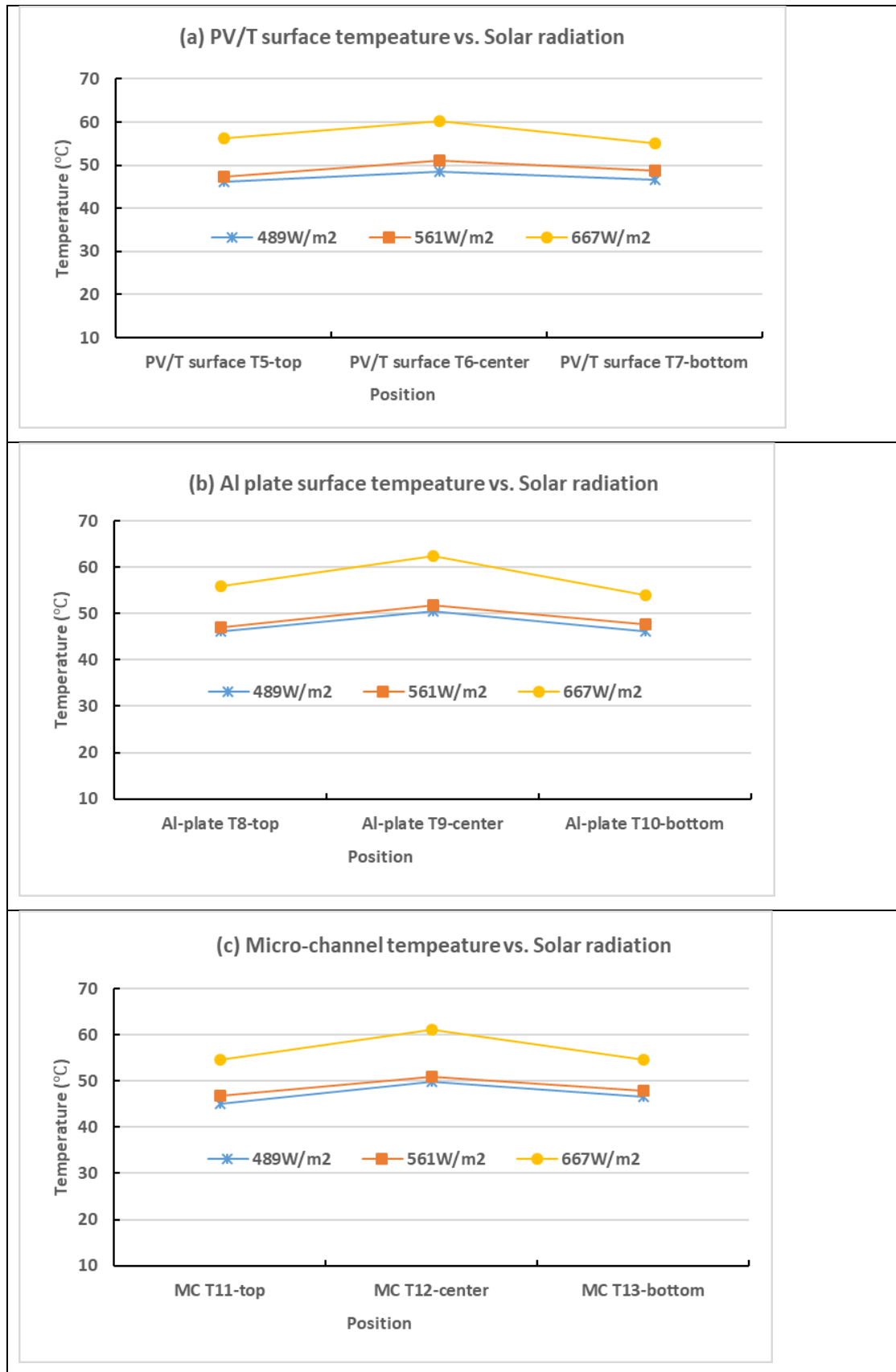
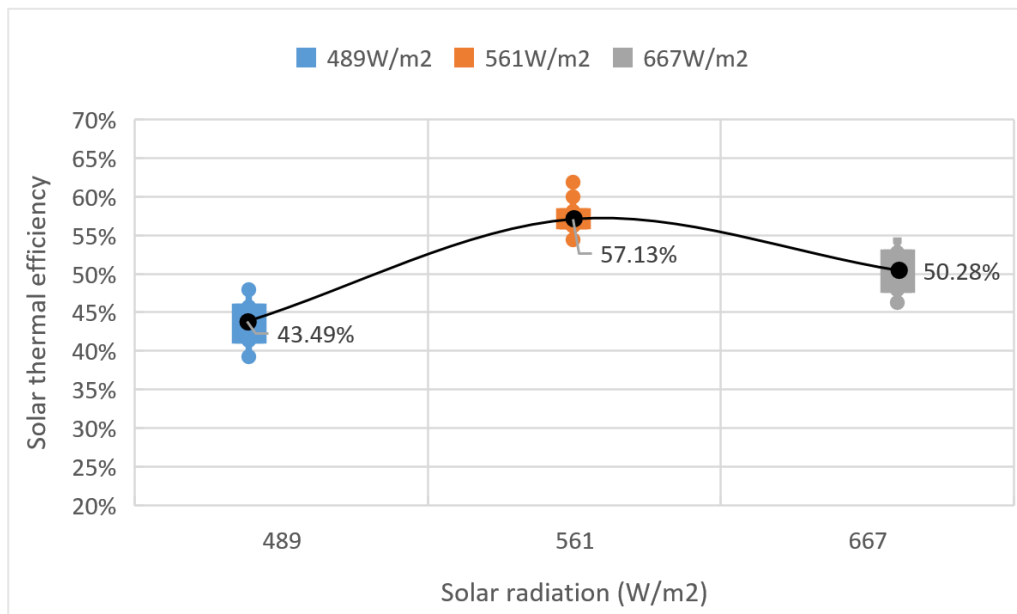


Fig.5-14 Temperature distribution on different parts the PV/T panel under three solar radiation levels

A higher radiation led to a higher panel surface temperature, thus creating the enhanced heat transfer between the panel surface and fluid across the evaporator. However, solar thermal performance of the system may not follow the same variation trend. Under the three different radiation levels (i.e., 489W/m<sup>2</sup>, 561 W/m<sup>2</sup> and 667 W/m<sup>2</sup>), the average solar thermal efficiency of the panels varied from 43.49%, 57.13% and 50.28%, as shown in **Fig.5-15**, indicating that 561W/m<sup>2</sup> is the most appropriate radiation level under this specific operational condition.



**Fig.5-15. Variation of the average solar thermal efficiency against solar radiation**

### 5.4.3 Impact of the coolant water inlet temperature

By varying the coolant water inlet temperature from 18°C to 37°C and keeping other parametrical data unchanged (i.e., solar radiation at 561 W/m<sup>2</sup>, coolant water flow rate at 0.17m<sup>3</sup>/h, ambient air temperature at 30°C), impact of the coolant water inlet temperature on the performance of the PV/MCLHP system was experimentally investigated. **Fig.5-16** shows the variation of the solar thermal efficiency of the panel against the coolant water inlet temperature. It is clear to see that under this testing condition, (1) when the inlet coolant water temperature is 18 °C , the system achieved a peak solar thermal efficiency

of 71.67%; (2) the solar thermal efficiency decreased with the increase of the coolant water inlet temperature, which complied well with the common knowledge of the solar thermal collector. When the coolant water temperature is increased, the heat transfer between the refrigerant within the interior channel of the co-axial tubular exchanger and the coolant water through the mid-channel of the exchanger is decreased. The reduced heat transfer directly affected the performance of the MC-LHP, leading to either the reduced cycling refrigerant flow rate or increased refrigerant temperature. As a result, the heat loss of the PV/evaporator panel to the ambient was increased and solar thermal efficiency of the system was reduced.

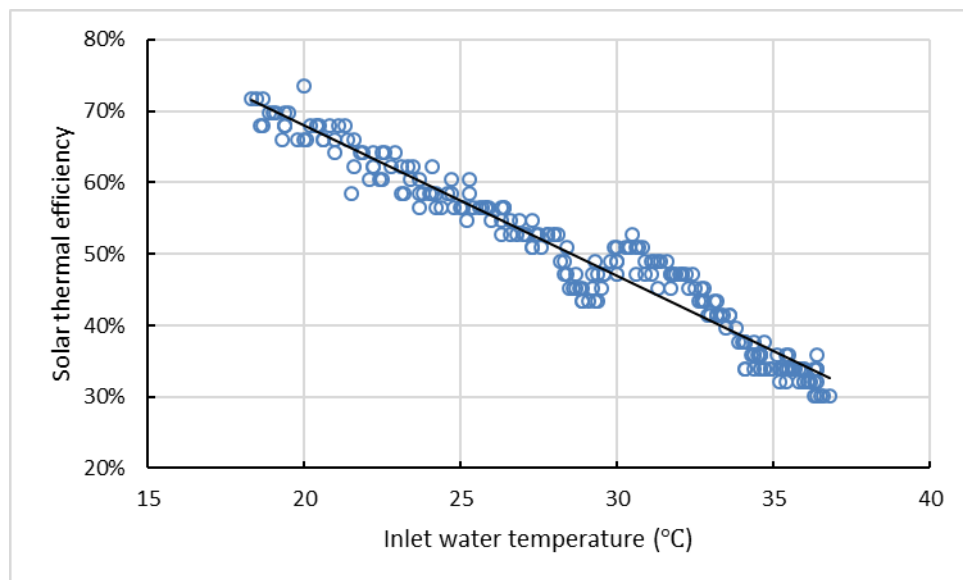


**Fig.5-16. Solar thermal efficiency against the coolant water inlet temperature**

#### **5.4.4 Impact of the coolant water flow rate**

By varying the coolant water flow rate from 0.05, 0.13, to 0.17m<sup>3</sup>/h and keeping other parametrical data unchanged (i.e., solar radiation at 560±5W/m<sup>2</sup>, height difference at 1.3m, ambient air temperature at around 30 °C, inlet water temperature at 20±1°C), impact of the coolant water flow rate to the performance of the PV/MCLHP system was experimentally investigated. **Fig.5-17** shows variation of the solar thermal efficiency of

## CHAPTER 5: PROTOTYPE CONSTRUCTION AND EXPERIMENTAL TESTING, AND MODEL VALIDATION

the panel against the coolant water flow rate. It is clear to see that the thermal efficiency of the PV/evaporator panel increased with the increase of the coolant water flow rate firstly and then lightly decreased.

It is clear to see that the thermal efficiency of the PV/evaporator panel increased with the increase of the coolant water flow rate, which complied well with the common knowledge of the solar collector. When the coolant water flow rate was increased, heat transfer rate between the refrigerant within the interior channel of the co-axial tubular exchanger and the coolant water within the mid-channel of the exchanger was increased. This led to the increased heat transfer rate of the MC-LHP, represented by an increased refrigerant flow rate. As a result, the heat loss of the PV/evaporator panel to ambient was decreased and solar thermal efficiency of the system was increased. Under this specific operational condition, the solar thermal efficiency increased from 42.83% to 49.70% while the coolant water flow rate increased from 0.05m<sup>3</sup>/h to 0.17 m<sup>3</sup>/h.

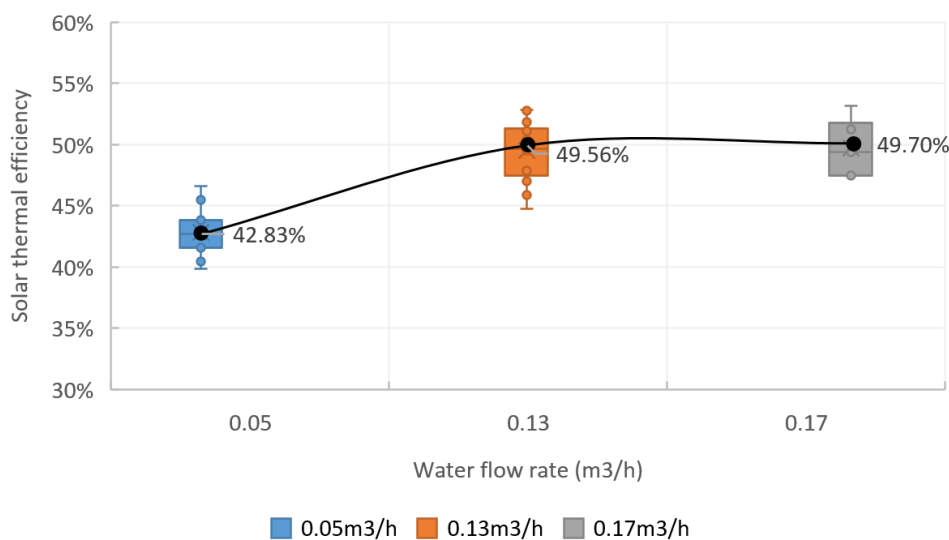


**Fig.5-17. Solar thermal efficiency against coolant water flow rate**

### 5.4.5 Impact of the ambient temperature

By varying the ambient temperature from 24.1, 26.3, to 30 °C while keeping other parameters unchanged (i.e., solar radiation at  $560\pm 5\text{W/m}^2$ , coolant water flow rate at 0.17, height difference at 1.3m, inlet water temperature at  $25\pm 1^\circ\text{C}$ ), impact of the ambient temperature on the performance of the PV/MCLHP system was experimentally investigated. **Fig.5-18** shows variation of the solar thermal efficiency of the panel against the ambient temperature. It is clearly seen that the thermal efficiency of the PV/evaporator panel increased with the increase of the ambient temperature, which complied well with the common knowledge of the solar collector performance. When the ambient temperature is increased, the heat transfer between the PV/evaporator panel surface and surrounding is decreased. As a result, the heat loss of the PV/evaporator panel to ambient was decreased and solar thermal efficiency of the system was increased. Under the specific operational condition, the average solar thermal efficiency increased from 47.05% to 57.13% while the ambient temperature of the fluid increased from  $24.1^\circ\text{C}$  to  $30^\circ\text{C}$ .

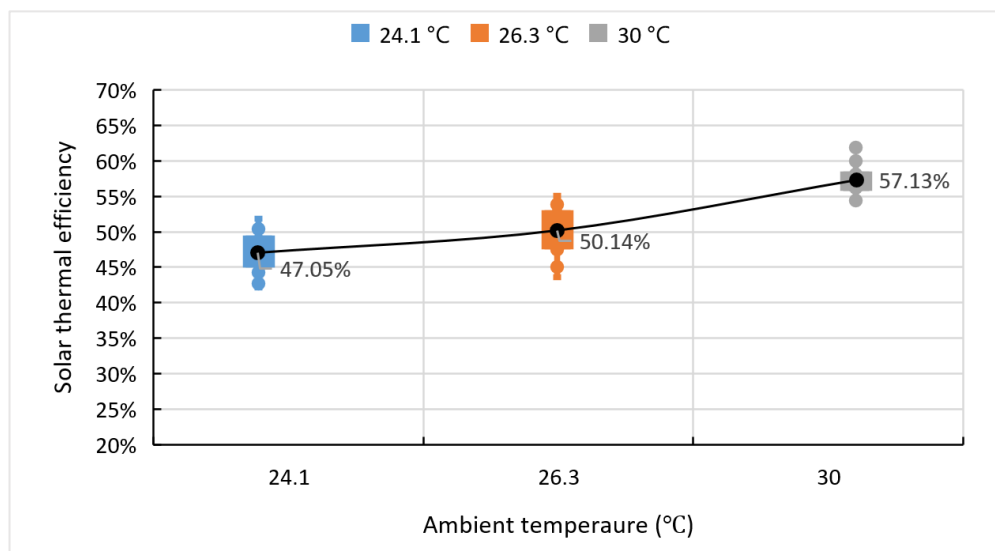


**Fig.5-18. Average heat efficiency vs ambient air temperature**

#### **5.4.6 Impact of the height difference between the condenser and the evaporator**

By varying the height difference from 0.7, 0.9, 1.1, to 1.3m and keeping other parametrical data unchanged (i.e., solar radiation at  $560\pm 5\text{W/m}^2$ , coolant water flow rate at 0.17, ambient air temperature at  $30\pm 1^\circ\text{C}$ , inlet water temperature at  $25\pm 1^\circ\text{C}$ ), impact of the condenser-evaporator height difference to the performance of the PV/MCLHP system was experimentally investigated. **Fig.5-19** shows the variation of the solar thermal efficiency of the PV/MCLHP system against the height difference between the heat exchanger and the evaporator. Increased height difference led to the increased solar thermal efficiency of the PV/MCLHP system, which complied well with the common knowledge of the solar thermal collector. When the height difference is increased, the heat transfer capacity of the LHP is increased owing to the enhanced thermo-siphon effect caused by the density difference between the refrigerant vapour and liquid. This led to the increased heat transfer rate from the evaporator to condenser. As a result, the solar thermal efficiency of the system was increased. Under this specific operational condition, solar thermal efficiency of the system increased from 48.85% to 57.13% while the height difference increased from 0.7 m to 1.3m. In addition, it is obvious that there is not much difference between the average solar thermal efficiency when the height difference is 1.1m and 1.3m, so 1.1m is taken as an optimal value of height difference between heat exchanger and evaporator.

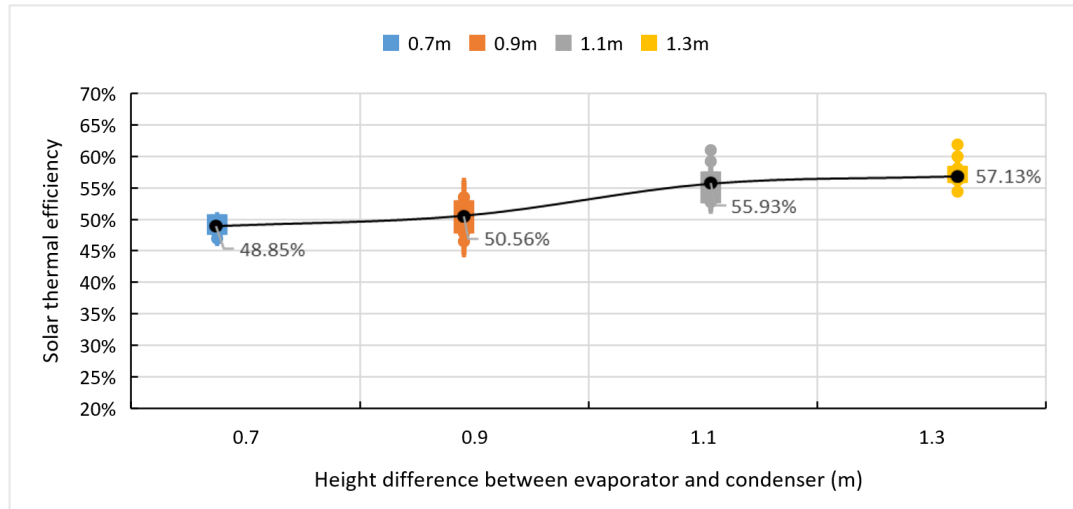


**Fig.5-19. Solar thermal efficiency changing with height difference between heat exchanger (condenser) and evaporator**

#### 5.4.7 Overall efficiency of the PV/MCLHP system

Based on the above tests, the most favourite operational condition of the PV/MCLHP system was identified. This is outlined as: coolant water flow rate at  $0.17\text{m}^3/\text{h}$ , height difference at 1.1m, and initial coolant water temperature at  $18^\circ\text{C}$ . Taking this as the testing condition, a full range of tests against the PV/MCLHP system were undertaken under the real weather condition dated in 18<sup>th</sup> Dec. 2018 in Guangzhou, China. The measurement data of the solar radiation, ambient temperature, panel temperature, coolant water temperatures and flow rate are presented in **Table 5-6** and **Fig.5-20**. The solar thermal, electrical and overall efficiencies of the PV/MCLHP system were calculated and presented in **Fig.5-21**. Correlations between the efficiencies and the indicative parameter,  $(T_{in}-T_a)/G$ , were further developed and these are shown graphically in **Figure 5-22**. It is found that all efficiencies decreased with the increase of the indicative parameter,  $(T_{in}-T_a)/G$ , with both the thermal and overall efficiencies varying sharply but the electrical efficiency varying slightly. In addition, under these specific operational condition and the real weather solar radiation, the solar thermal efficiency of the system was in the range

## CHAPTER 5: PROTOTYPE CONSTRUCTION AND EXPERIMENTAL TESTING, AND MODEL VALIDATION

25.2% to 62.2%, and the average thermal, electrical and overall efficiencies are 38.36%, 16.54% and 54.90%, respectively.

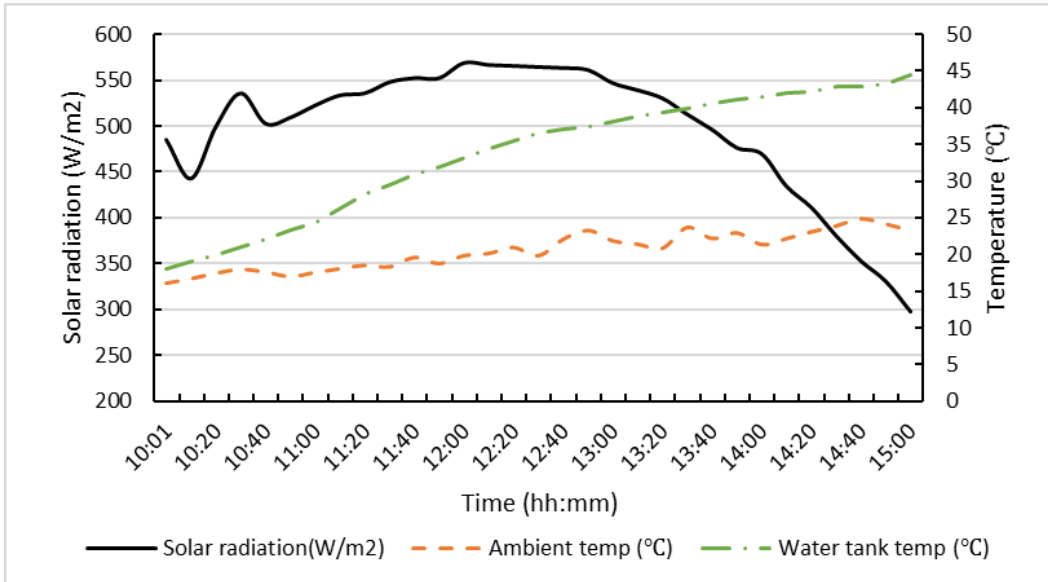


**Fig.5-20. Water tank temperature under real weather**

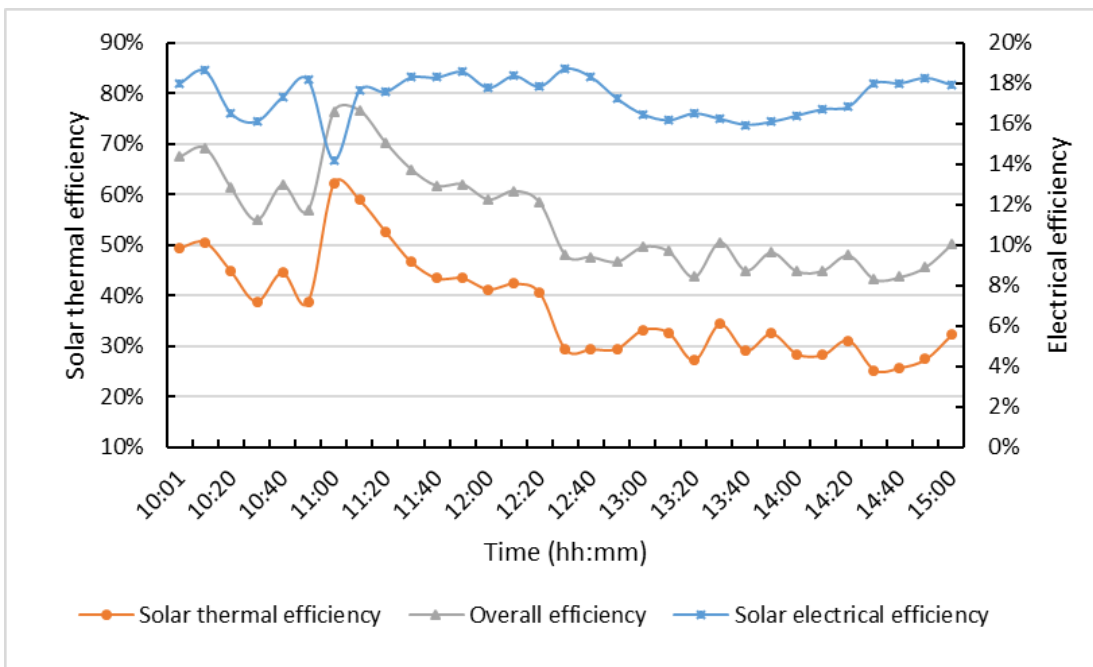


**Fig.5-21. Solar thermal and electrical performance under real weather**

**CHAPTER 5: PROTOTYPE CONSTRUCTION AND EXPERIMENTAL TESTING, AND MODEL VALIDATION**

---

**Table 5-6: The test data of the PV/MCLHP system under real weather condition**

Time	Solar radiation (W/m <sup>2</sup> )	Ambient temp (°C)	panel surface temp (°C)	Micro-channel temp (°C)	Water tank temp (°C)	Water flow rate m <sup>3</sup> /h	Power (W)
10:01	485.1	16.15	50.55	47.95	18	0.17	154.39
10:10	443	16.75	51.85	48.95	19.05	0.17	145.95
10:20	499.4	17.5	53.8	51.65	20.05	0.17	145.95
10:30	535.7	18	53.85	51.95	21.1	0.17	152.6
10:40	502.7	17.65	55.6	53.4	22.1	0.17	154
10:50	509.3	17.05	55.35	53.85	23.25	0.17	163.8
11:00	522.5	17.6	56.75	54.15	24.45	0.17	131.1
11:10	533.5	18.1	52.95	55.55	26.35	0.17	166.6
11:20	535.7	18.55	49.25	54.9	28.25	0.17	166.6
11:30	547.8	18.35	50.15	54.25	29.55	0.17	177.32
11:40	552.2	19.6	52	55.4	30.9	0.17	178.75
11:50	552.2	18.8	55.15	56.9	31.95	0.17	181.44
12:00	568.7	19.85	55.1	58.4	33.25	0.17	178.92
12:10	566.5	20.15	56.35	59.1	34.45	0.17	184.15
12:20	565.4	20.95	57.3	59.15	35.45	0.17	178.55
12:30	564.3	19.85	55.65	57.7	36.45	0.17	187.03
12:40	563.2	22.05	56.4	57.6	37.1	0.17	182.46
12:50	561	23.25	58.35	58.55	37.5	0.17	171.12
13:00	546.7	21.85	59.85	59.2	38.1	0.17	159.25
13:10	539	21.4	60.45	60.25	38.75	0.17	154.18
13:20	530.2	20.85	59.75	59.6	39.3	0.17	154.85
13:30	512.6	23.65	60.3	60.3	39.9	0.17	147.24
13:40	496.1	22.15	60.9	60.6	40.55	0.17	139.94
13:50	476.3	22.9	60.6	60.65	41.05	0.17	135.56
14:00	469.7	21.35	59.95	60.3	41.5	0.17	136.29
14:10	434.5	22.15	59.3	59.05	42	0.17	128.53
14:20	411.4	23.05	59.05	59	42.15	0.17	122.61
14:30	380.6	23.85	56.75	58.1	42.8	0.17	121.26
14:40	353.1	24.8	56.75	57.1	42.9	0.17	112.50
14:50	331.1	24.1	56.25	56.7	43.25	0.17	107.07
15:00	298.1	23.25	56.9	56.35	44.45	0.17	94.52

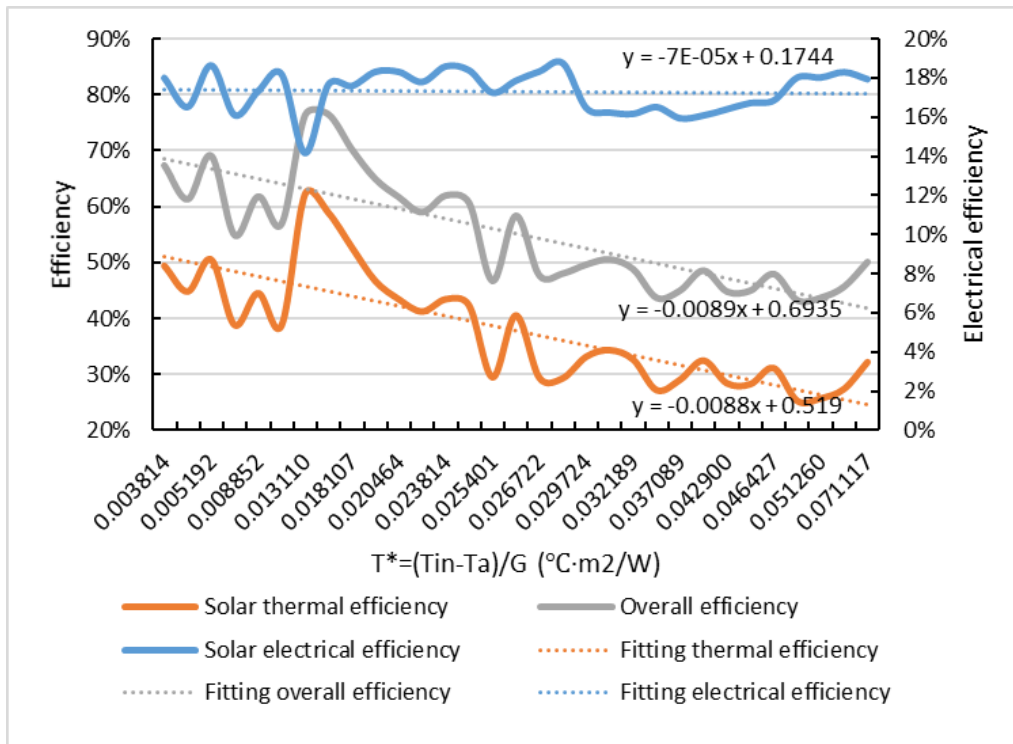


**Fig.5- 22. Correlations between the efficiencies and the indicative parameter,  $(t_{in}-t_a)/G$**

### 5.4.8 Comparison between the PV/MCLHP system and the existing PV/T system and BIPV/T system

Comparison between the PV/MC-LHP- and the existing PV/T and BIPV/T system was undertaken and the results are shown in **Table 5-8**. This derived the experimental correlations between the overall solar efficiency and indicative operational parameter (i.e.,  $T_{in} - T_a/G$  or  $(T_{in} - T_a)/H$ ) for the three systems.

Under the a specific operational condition (i.e., Solar radiation of  $16.14MJ/m^2/day$  ( $560.41W/m^2$ ), water inlet temperature of  $35^{\circ}C$ , ambient temperature of  $36.7^{\circ}C$ , and 8 hours per day in operation, the new PV/MC-LHP-T system had the average thermal efficiency of 51.9% and average electrical efficiency of 16.54%, while the existing PV/T system had the average thermal efficiency of 41.34% and average electrical efficiency of 10% [168]. Compared to the existing PV/T system, the new PV/MCLHP system obtained 33.31% higher overall solar efficiency.

## CHAPTER 5: PROTOTYPE CONSTRUCTION AND EXPERIMENTAL TESTING, AND MODEL VALIDATION

Under the a specific operational condition (i.e., solar radiation of 850W/m<sup>2</sup>, water inlet temperature of 20°C, and ambient temperature of 25°C), the new PV/MCLHP system had the average thermal efficiency of 51.91% and average electrical efficiency of 16.54%, while the existing PV/T system had the average thermal efficiency of 44.3% and average electrical efficiency of 14.1%[169]. Compared to the existing BIPV/T system, the new PV/MC-LHP- system obtained 17.20% higher overall solar efficiency.

**Table 5-7: The novel PV/MCLHP system vs. other PV/T systems**

System	MC-LHP-PV/T	Conventional PV/T	BIPV/T
Solar thermal equation ( $\eta_{th}=\eta_0 - \alpha_0 T^*$ , $T^*=(T_{in} - T_a)/G$ or $T^*=(T_{in} - T_a)/H$ )	$\eta_{th}=0.519-0.0088T^*$ , $T^*=(T_{in} - T_a)/G$	$\eta_{th}=0.400-0.195T^*$ , $T^*=(T_{in} - T_a)/H$	-
Solar thermal efficiency under specific operational condition 1 (Solar radiation: H=16.14MJ/m <sup>2</sup> /day or G=560.41W/m <sup>2</sup> ; T <sub>in</sub> =35°C; T <sub>a</sub> =36.7°C; operational time: 8h/day)	51.90%	41.34%	-
Solar thermal efficiency under specific operational condition 2 (Solar radiation: 850W/m <sup>2</sup> ; T <sub>in</sub> =20°C; T <sub>a</sub> =25°C)	51.91%	-	44.30%
Daily average electrical efficiency	16.54%	10%	14.10%
Overall efficiency under condition 1	68.44%	51.34%	-
Overall efficiency under condition 2	68.45%	-	58.40%
Ref.	Present study	[168]	[169]
Overall efficiency improving ratio to Ref.[168]	33.31%	-	-
Overall efficiency improving ratio to Ref. [169]	17.20%	-	-

### 5.5 Comparison between the experimental and modelling results - model validation

To evaluate the degree of agreement between the experimental and simulation results, the relative errors (RE) are calculated by:

$$RE = \frac{Y_{exp} - Y_{sim}}{Y_{exp}} \times 100\% \quad (5-9)$$

Where the  $Y_{exp}$  and  $Y_{sim}$  are the values of the experimental and simulation results respectively.

### 5.5.1 Influence of the ambient air temperature

The average solar radiation from the solar simulator to the surface of the PV/MCLHP collector was  $561\text{W/m}^2$  and the circulating water flow rate was set as a constant value of  $0.17\text{m}^3/\text{h}$  with a fixed inlet water temperature at around  $25^\circ\text{C}$ . Further, the height difference between the evaporator and the condenser was kept at  $1.3\text{m}$ , while the air temperature varied from  $24.1, 26.3, 30,$  to  $32.2^\circ\text{C}$  during the experiment time.

The experimental and simulation results of the outlet water temperature under different ambient air temperature are presented in **Fig.5-23**, indicating that the outlet water temperature of coolant loop of the PV/MCLHP system slightly increases with the ambient air temperature when keep other parameters constant. The relative errors between the experimental and simulation the outlet water temperatures are less than 5%, which shows that the simulated results are in good agreement with the experimental ones.

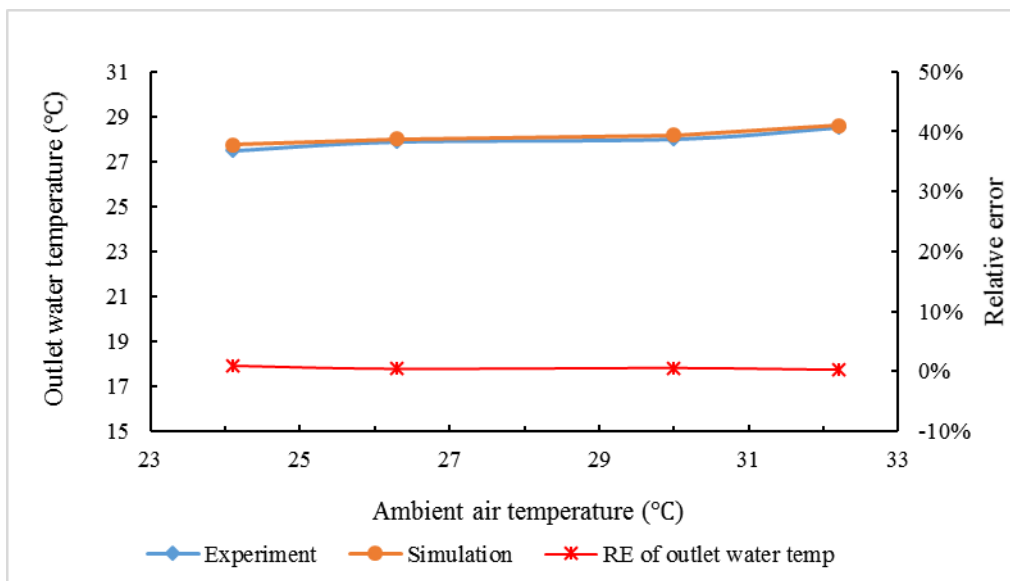


**Fig.5-23. Experimental and simulation results of outlet water temperature under different ambient air temperature**

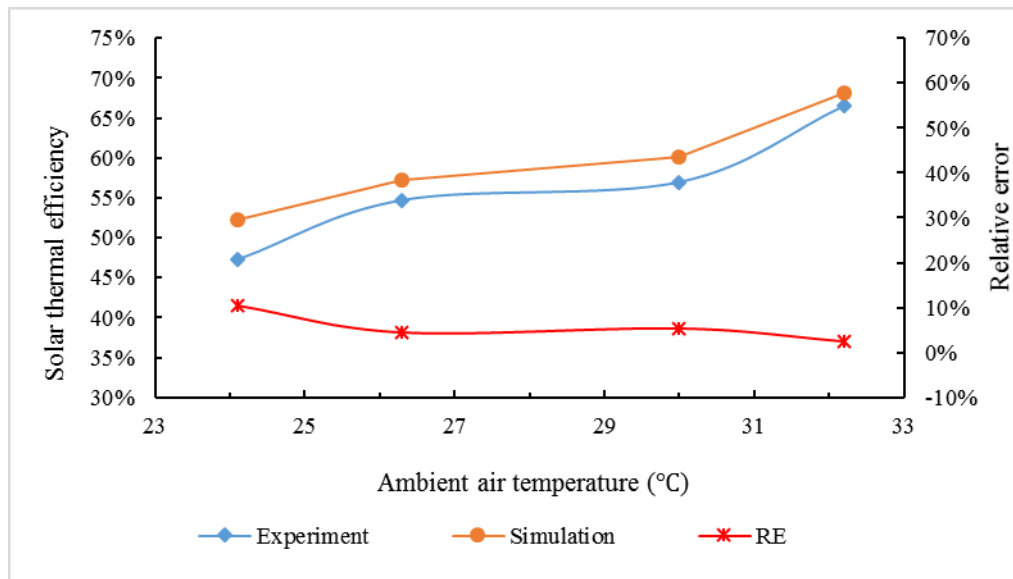


**Fig.5-24. Experimental and simulation results of the solar thermal efficiency with different ambient air temperature**

**Fig.5-24** shows the experimental and simulation results of solar thermal efficiencies under different ambient air temperature. Both results show that the trend of the solar thermal efficiencies are increasing with the ambient air temperature. When the ambient air temperature were 24.1, 26.3, 30, and 32.2 °C, the simulation results of the solar thermal efficiencies were 52.3%, 57.2%, 60.1%, and 68.1%, whilst the experimental results were 47.3%, 54.7%, 56.9%, and 66.4%, respectively. This phenomenon complied well with the common knowledge of the solar collector performance that when the ambient temperature is increased, the heat transfer between the PV/evaporator panel surface and surrounding is decreased. As a result, the heat loss of the PV/evaporator panel to ambient was decreased and solar thermal efficiency of the system was increased.

### 5.5.2 Influence of solar radiation

The average ambient air temperature was around 30 °C and the circulating water flow rate was set as a constant value of 0.17m<sup>3</sup>/h with a fixed inlet water temperature at around 25°C. As well as, the height difference between the evaporator and the condenser was

## CHAPTER 5: PROTOTYPE CONSTRUCTION AND EXPERIMENTAL TESTING, AND MODEL VALIDATION

kept at 1.3m, while the average solar radiation from the solar simulator striking on the surface of the PC/MC-LHP collector were set varied from 489, 561, to 667 W/m<sup>2</sup> during the experiment time.

The experimental and simulation results of the outlet water temperature under different solar radiation are presented in **Fig.5-25**, indicating that the outlet water temperature of coolant loop of the PV/MCLHP system slightly increases with the solar radiation when keep other parameters constant. The relative errors between the experimental and simulation the outlet water temperatures are less than 5%, which shows that the simulated results are in good agreement with the experimental ones.

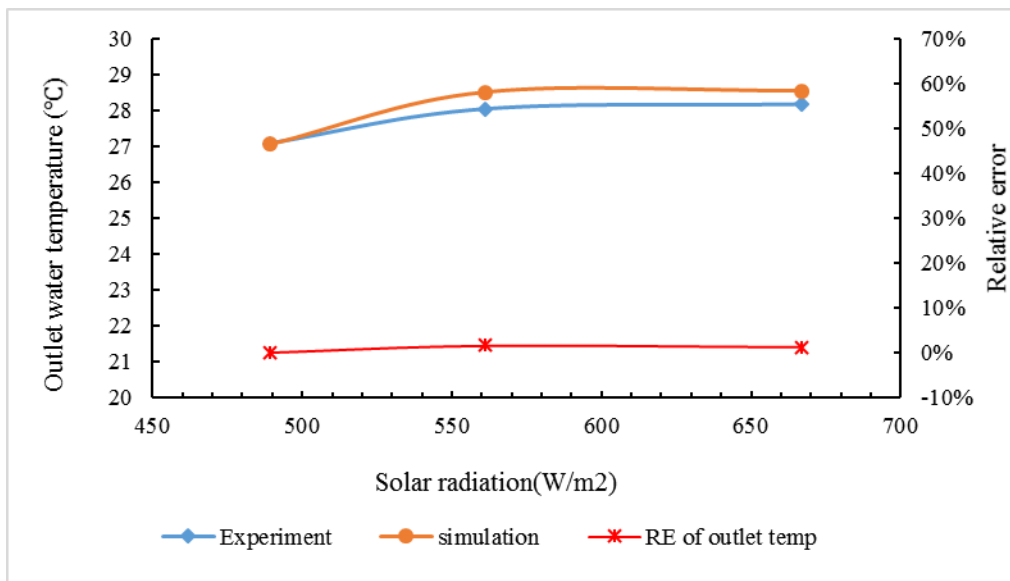


**Fig.5-25. Influence of the solar radiation on the outlet water temperature of the PV/MCLHP system (exp. vs sim.)**

Then the modelling results of the solar thermal efficiencies were compared with the test results obtained under the same operational conditions, which yielded the comparison diagram displayed as **Fig.5-26**. Good agreement between the experimentation and simulation was observed with relative errors in the range of -0.75% ~ 15.16%. It was found that the increasing solar radiation didn't lead to an increase in the solar thermal efficiency of this system, whilst the solar thermal efficiency performed a highest value at

66.67% when the average solar radiation was  $561\text{W/m}^2$ , indicating that  $561\text{W/m}^2$  is the most appropriate radiation level under this specific operational condition.

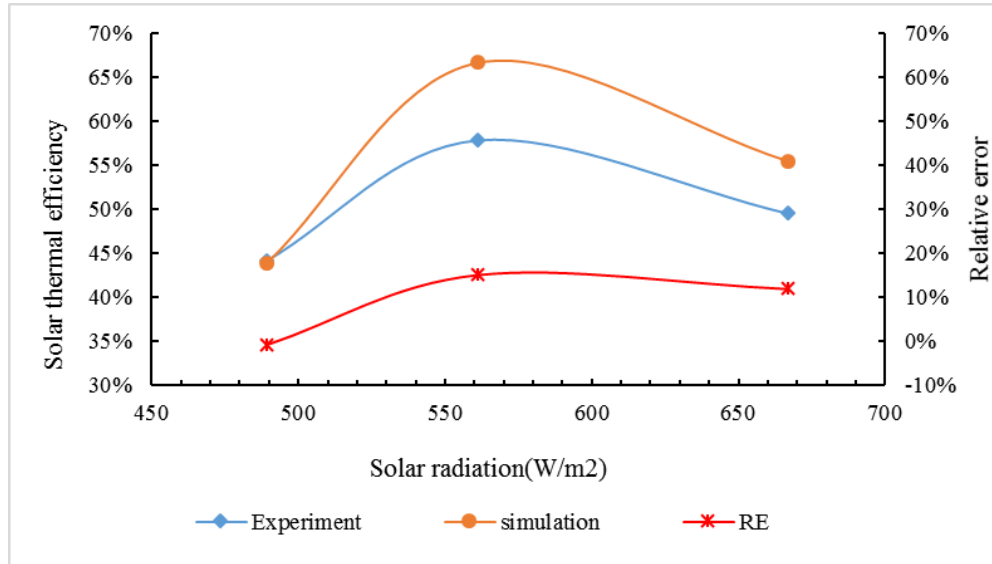


**Fig.5-26. Influence of the solar radiation on the solar thermal efficiency of the PV/MCLHP system (exp. vs sim.)**

### 5.5.3 Influence of different height difference between evaporator and condenser

By varying the height difference between the evaporator and condenser from 0.7m, 0.9m, 1.1m to 1.3m while the other parameters keeping constant as that the average ambient air temperature was around  $30\text{ }^\circ\text{C}$  and the circulating water flow rate was set as a constant value of  $0.17\text{m}^3/\text{h}$  with a fixed inlet water temperature at around  $25\text{ }^\circ\text{C}$ , as well as that the average solar radiation was set around  $561\text{W/m}^2$ . A simulation was completed by using the established computation model. And the simulation results were evaluated in parallel vs the experimentation results, thus giving the comparison illustrations in **Fig.5-27** and **Fig.5-28**. Good agreements were found in these two sets of comparison, giving relative errors in the range of  $-1.31\% \sim 0.32\%$  and  $-10.00\% \sim 3.65\%$  for outlet water temperatures and solar thermal efficiencies respectively. It was found that increasing height difference led to rising solar thermal efficiency of the PV/MCLHP system. When the height

## CHAPTER 5: PROTOTYPE CONSTRUCTION AND EXPERIMENTAL TESTING, AND MODEL VALIDATION

---

difference is increased, the heat transfer capacity of the LHP is increased owing to the enhanced thermo-siphon effect caused by the density difference between the refrigerant vapour and liquid. This led to the increased heat transfer rate from the evaporator to condenser. As a result, the solar thermal efficiency of the system was increased. In addition, it is obvious that there is not much difference between the average solar thermal efficiency when the height difference is 1.1m and 1.3m, so 1.1m is taken as an optimal value of height difference between heat exchanger and evaporator as described as before.

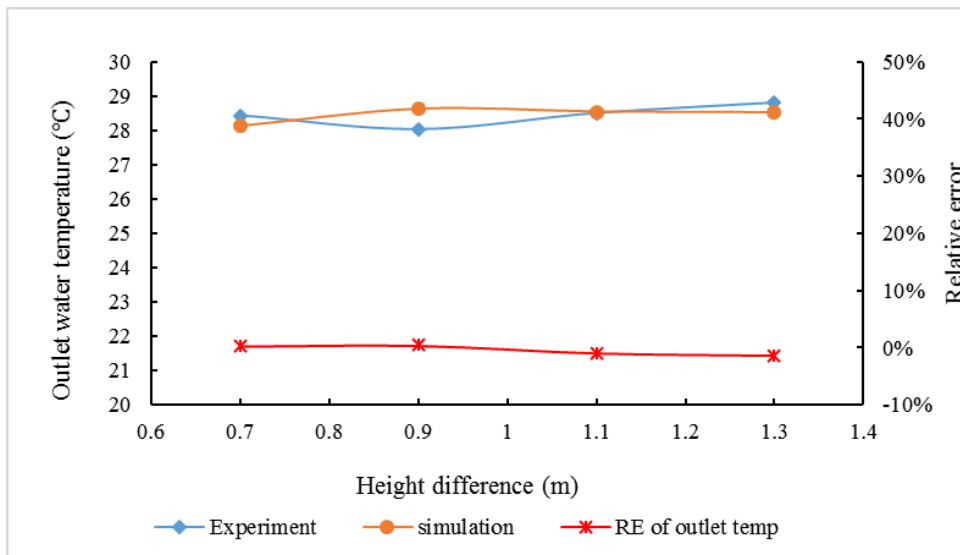


**Fig.5-27 Influence of height difference on the outlet water temperature (exp. vs sim.)**

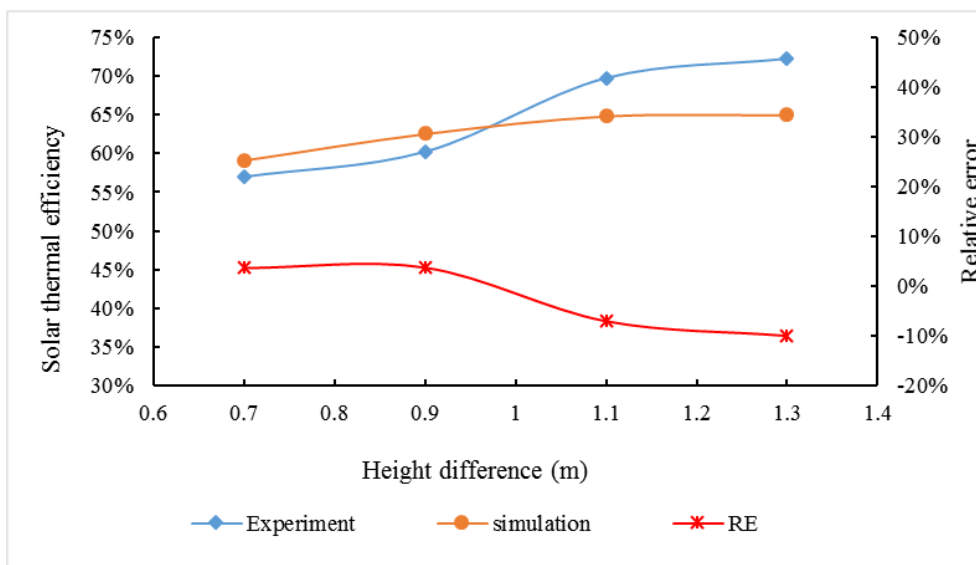


**Fig.5-28 Influence of height difference on solar thermal efficiency (exp. vs sim.)**

#### **5.5.4 Error analysis**

It was found that the certain relative errors existed between the modelling and test results for all sets of comparison were no greater than 16%, which are acceptable in terms of general engineering applications and indicate that the established model can predict system performance at a reasonable level of accuracy. The minor differences in existence may be due to simplified assumptions, the utilisation of empirical formulas, and measurement errors.

### **5.6 Chapter summary**

This chapter addressed a dedicated experimental investigation into a novel solar micro-channel loop-heat-pipe PV/T (PV/ MCLHP) system in order to evaluate its operational performance and assess the impact of a number of operational parameters to its performance, as well as the steady-state simulation model validation with the experimentation results.

The system made use of the co-axial tubular heat exchanger as the condenser, PV integrated multiple micro-channel-tubes-array as the PV/evaporator, the upper end liquid header with tiny holes as the liquid feeder and liquid/vapour separator, and the upper end vapour header as the vapour collector and distributor. The combination of these innovations was proved to be able to create the improved condensation and evaporation effects within the LHP, and thus, lead to the 17.20% to 33.31% higher overall efficiency compared to the existing solar PV/T and BIPV/T systems.

Solar thermal and electrical efficiencies were considered as the key performance indicators of the PV/MCLHP system. The electrical efficiency was found to be dependent upon the temperature of PV cells. A higher cell temperature led to a reduced PV electricity,

## CHAPTER 5: PROTOTYPE CONSTRUCTION AND EXPERIMENTAL TESTING, AND MODEL VALIDATION

---

with the intersection efficiency ( $\eta_0$ ) of 18.6% and slope factor of 0.45. The experimental relationship shows a good agreement with the theoretical one, with the discrepancy between -4.18% and 1.48%.

Solar thermal efficiency of the PV/MCLHP system varied with the inlet temperature and flow rate of coolant water, ambient temperature, as well as height difference between the condensation and the evaporator. A lower inlet water temperature, a higher water flow rate, a higher ambient temperature, and a larger height difference between the condenser and evaporator can help increase the solar thermal efficiency of the system. Under the refrigerant charge ratio of 30%, solar radiation of 561W/m<sup>2</sup>, initial inlet water temperature of 18°C, water flow rate of 0.17 m<sup>3</sup>/h, ambient temperature of 30°C, and height difference of 1.3m, the system achieved a peak solar thermal efficiency of 71.67%. These operational parametrical data in combination are therefore regarded as most favourite operational condition of the PV/MCLHP system. Under these specific operational condition and the real weather solar radiation, the solar thermal efficiency of the system was in the range 25.2% to 62.2%.

The solar simulator generated a certain level of non-uniformity in radiation distribution across the surface of the PV/evaporator panel, leading to a higher temperature at the mid-part of the panel and lower temperature at the lower and higher parts of the panel. This may cause certain level of inaccuracy in the efficiency calculation.

A higher solar radiation created a larger heat transfer rate within the PV/MCLHP system. However, the solar thermal and electrical efficiency of the system may not follow the same variation trend. Under the three different radiation levels (i.e., 489, 561, and 667W/m<sup>2</sup>), the thermal efficiency of the panels varied from 43.49%, 57.13% and 50.28%, indicating that 561W/m<sup>2</sup> is the most appropriate radiation level.

## CHAPTER 5: PROTOTYPE CONSTRUCTION AND EXPERIMENTAL TESTING, AND MODEL VALIDATION

---

The certain relative errors existed between the modelling and test results for all sets of comparison were no greater than 16%, which are acceptable in terms of general engineering applications and indicate that the established model can predict system performance at a reasonable level of accuracy. The minor differences in existence may be due to simplified assumptions, the utilisation of empirical formulas, and measurement errors.

# CHAPTER 6: ENERGY SAVING, ECONOMIC, ENVIRONMENTAL AND REGIONAL ACCEPTANCE ANALYSIS

## 6.1 Chapter introduction

In this chapter, the computation model developed in chapter 4 is applied to predict the annual operational performance of the proposed novel PV/MCLHP system. Further the system life cycle, carbon dioxide emission reduction, and power and heat output will be theoretical analysed to evaluate the relevant socio-economic and environmental impacts.

## 6.2 Annual operational performance

Based on the good agreement between the simulation model and the experimental results being achieved in previous chapters. The established model is applicable for prediction of the annual operational performance of the PV/MCLHP heat and power system.

### 6.2.1 Weather conditions as the input parameters

Weather data by region can be download from EnergyPlus[170], such as London ‘GBR\_London.Gatwick. 037760\_IWEC’, and ‘450070\_City UHK’ for Hong Kong. The monthly averages for solar radiation and ambient air temperature in London and Hong Kong are presented in **Fig.6-1** and **Fig.6-2** respectively.

**Table 6-1** presents the monthly average wind speed for these two places. It can be found that (1) the monthly solar radiation of London is on a lower level, while in Hong Kong it is on a relative higher level; (2) London is warm in summer and cold in winter, whilst Hong Kong is hot in summer and warm in winter; (3) the monthly average wind speed in Hong Kong is larger than in London.

CHAPTER 6: ENERGY SAVING, ECONOMIC, ENVIRONMENTAL ANALYSIS

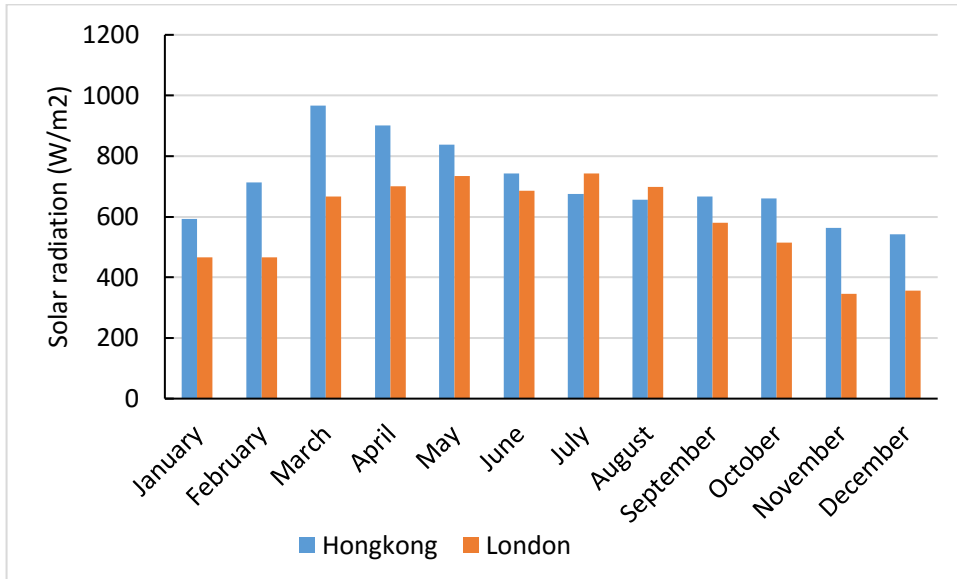


Fig.6-1. Monthly average solar radiation in London and Honking

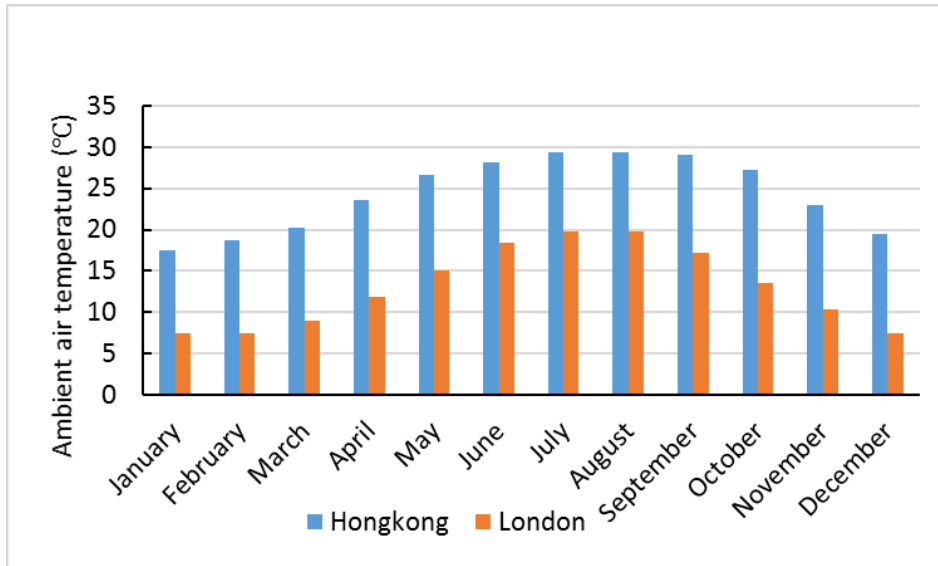


Fig.6-2. Monthly average ambient air temp London and Hong Kong

Table 6-1 Monthly average wind speed in London and Hong Kong (m/s)

Location	Jan	Feb	Mar	Apr	May	Jun	Jul	Aug	Sep	Oct	Nov	Dec
London	3	2.6	2.7	2.2	2.4	2.1	2.3	1.9	2	2.2	2.2	2.4
Hong Kong	5.4	5.6	5.8	5.8	5.3	5.4	5.5	5.1	5.2	5.3	5.4	5.3

In terms of the annual performance simulation, it was supposed that the prototype system starts work from 9:00 to 17:00 as the end. The monthly average weather data were applied to be the instant input parameter to calculate the monthly average performance indicators.

### 6.2.2 Monthly performance predictions of the PV/MCLHP system in London and Hong Kong

This section studies the annual operational performances of the PV/MCLHP prototype system in London and Hong Kong. Fig.6-3 shows the monthly average PV temperature and air temperature in these two regions. It is easy to find that the PV temperature had a similar variation trend to the ambient air temperature and the solar radiation, where Hong Kong reached to a maximum temperature in March and a minimum temperature in winter while London in July and winter respectively. In London, the monthly temperature of PV was in the range from 36.4°C (in December) to 45.3°C (in July).

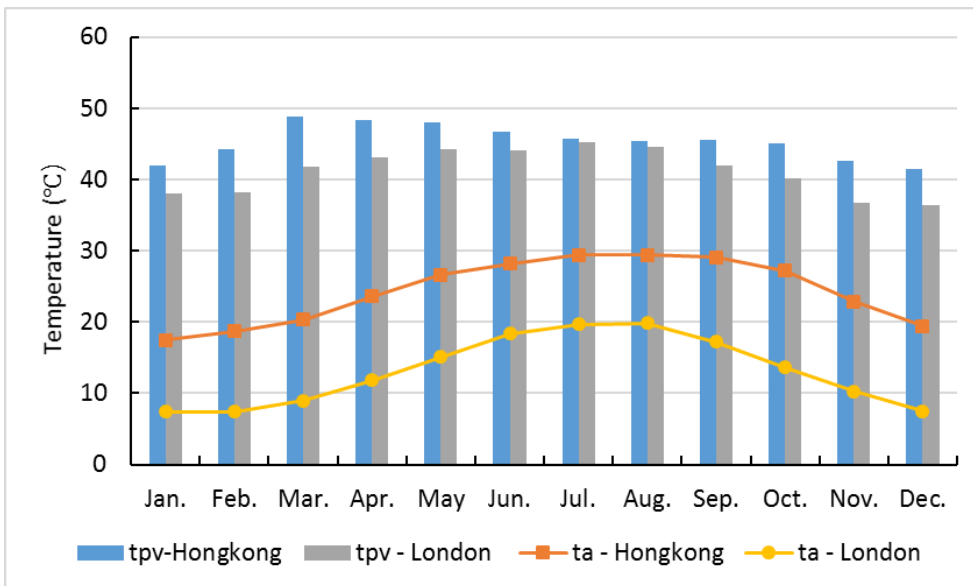


**Fig.6-3. Monthly average PV temperature and air temperature in London and Hong Kong**

In Hong Kong, the monthly temperature of PV was in the range from 41.5°C (in December) to 48.9°C (in March) owing to the highest monthly average solar radiation occurring in March. PV temperature in London is lower than in Hong Kong throughout

## CHAPTER 6: ENERGY SAVING, ECONOMIC, ENVIRONMENTAL ANALYSIS

the whole year. The predicted year average PV temperatures in London and Hong Kong were 41.2°C and 45.3°C respectively.

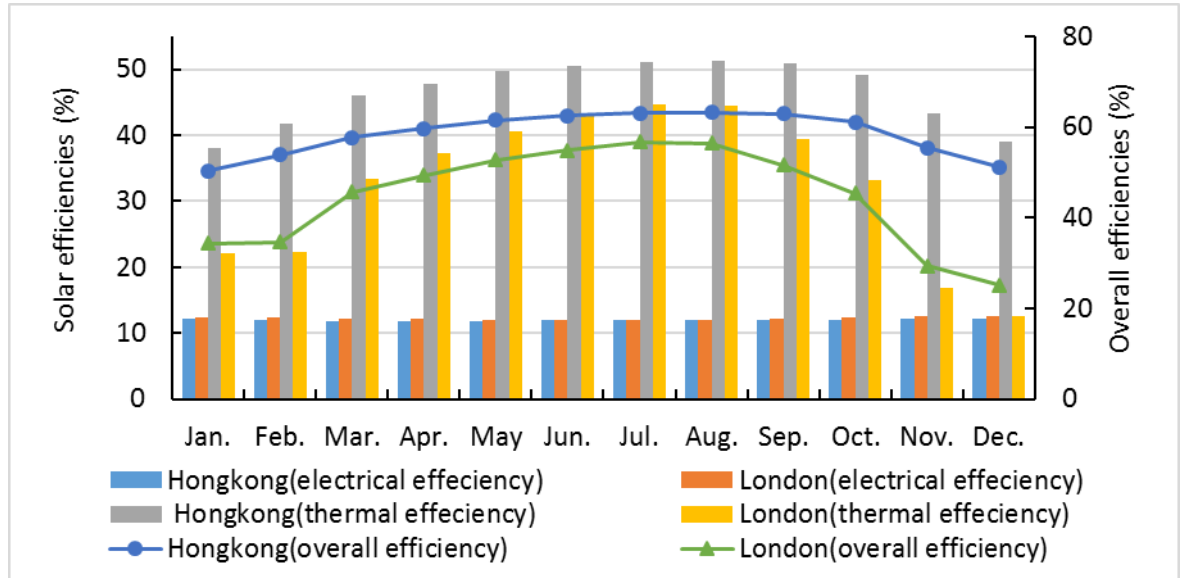


**Fig.6-4. Solar energy efficiencies of the PV/MCLHP system in London and Hong Kong**

**Fig.6-4** gives the monthly solar energy efficiencies of the PV/MCLHP module showing that the monthly solar electrical efficiencies of the module varies in the opposite of the PV temperature presented by the value of it in the range from 11.9% (July) to 12.5% (December) in London and from 11.7% (March) to 12.2%(December) in Hong Kong. It was found that the monthly solar electrical efficiencies in London are relatively higher than in Hong Kong throughout the year, owing to that monthly PV temperature in London is lower than in Hong Kong throughout the whole year as mentioned before. However, the monthly solar thermal efficiencies of the module varies at the same trend as its PV temperature while inversely to the solar electrical efficiency, indicated by the value of solar thermal efficiency in the range from 12.6%(December) to 44.7%(July) in London and from 38.1%(January) to 51.3%(August) in Hong Kong. In addition, the monthly solar thermal efficiencies in London are relatively lower than in Hong Kong in the year round which presents a larger difference between solar thermal efficiencies than the difference

## CHAPTER 6: ENERGY SAVING, ECONOMIC, ENVIRONMENTAL ANALYSIS

between in solar electrical efficiencies. Furthermore, there is clear trend that the operation of the PV/MCLHP system in Hong Kong is more stable than in London owing to the warmer temperature and higher solar radiation in Hong Kong, generating a much higher annual average thermal efficiency at around 46.7%. From aspect of the overall efficiency, there is a tendency that overall efficiencies of the PV/MCLHP prototype system which, varies in a same way as the solar thermal efficiency, have annual averages at around 58.5% in Hong Kong and around 44.6% in London.

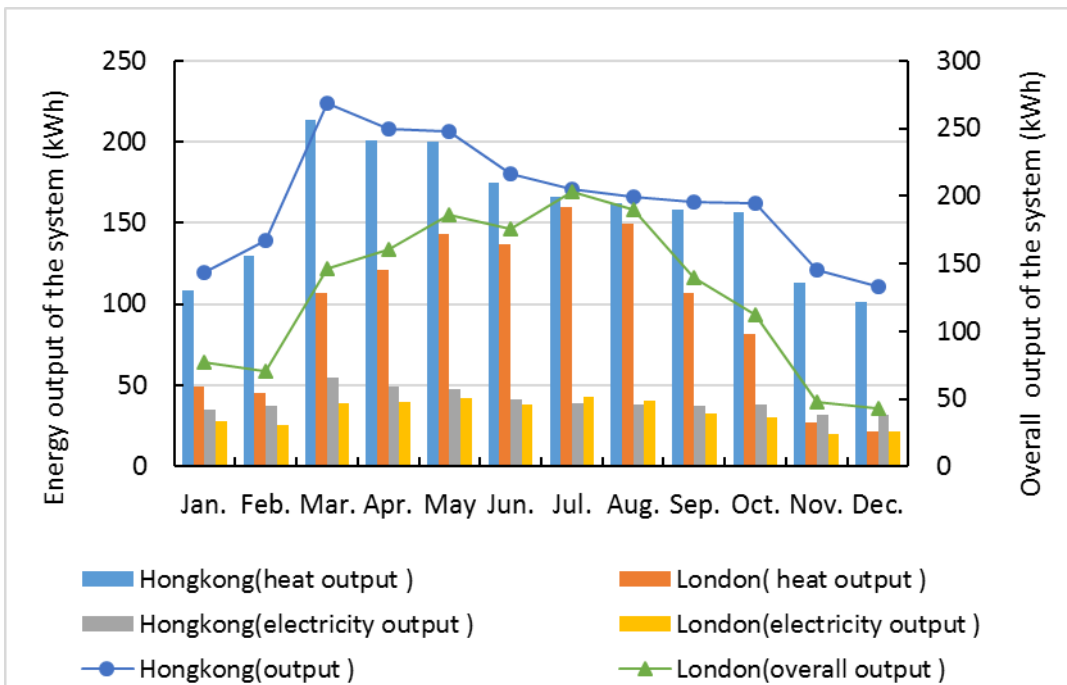


**Fig.6-5. Overall energy output of the PV/MCLHP system in London and Hong Kong**

The overall energy outputs are illustrated in **Fig.6-5**, showing that the amount of energy outputs is positively correlated with the magnitude of solar radiation and influenced by the ambient air temperature of the region. The electricity generated by the prototype system in London varied from 20.12kWh (November) to 42.80kWh (July) with the average value of 33.34kWh, while in Hong Kong it varied from 31.78kWh (November) to 54.66kWh (March) with the average value of 40.00kWh. The solar thermal output ranges of the prototype system were from 21.60kWh (December) to 160kWh (July) with

the average value of 95.84kWh in London, whilst from 101.65kWh (December) to 213.90kWh (March) with the average value of 157.67kWh in Hong Kong. Apparently, operating this system in Hong Kong could have much more energy output than in London which can also be proved by the overall output figure as shown in **Fig.6-5** and the total annual energy output listed in **Table 6-2**, owing to the rich solar resources and warm climate in Hong Kong.

**Table 6-2 Total annual energy output of the prototype system in Hong Kong and London**

Location	Hong Kong	London
Solar radiation (kWh/m <sup>2</sup> - yr)	2044.41	1669.94
Solar electricity output of this prototype system (kWh/m <sup>2</sup> - yr)	259.15	216.02
Solar thermal output of this prototype system (kWh/m <sup>2</sup> - yr)	1018.10	620.86

### 6.3 Life-cycle economic analysis

#### 6.3.1 Capital cost of the PV/MCLHP systems

##### *(1) Capital cost*

Based on the prototype system and demonstration system constructions and testing results, the capital cost of a 1.2kW related PV/MCLHP system has been estimated and the results are presented in **Table 6-3**. The capital cost of the overall PV/MCLHP system is calculated by adding all the individual prices of the different components in the whole system, including appropriate commercial profits (20%). It is found that the initial cost of this type of PV/MCLHP system is GBP 941.10. In addition, the PV/MCLHP module was the most expensive of this system components, which accounts for around 53% of the total system cost.

CHAPTER 6: ENERGY SAVING, ECONOMIC, ENVIRONMENTAL  
ANALYSIS

**Table 6-3: 1.2kW related PV/MCLHP capital cost summary**

No.	Component	Type	Quantity/Size	Unit Price (¥)	Cost (¥)
<b><i>PV/MCLHP Model ( 3746 53.07% )</i></b>					
1	PV/T module	2000*1000	1	1550	1550
2	Heat exchanger (condenser)	Triple pipe heat exchanger	1	2000	2000
3	Transportation Lines	TS2732412	2	98	196
<b><i>Other components ( 1842 26.10% )</i></b>					
3	water pump for the system	BJZ037-B (Head 20m)	1	338	338
5	Refrigerant	R134a (kg)	1.2	150	150
6	Eelectrical wire	(coil)	1	80	80
7	Hot water storage tank (closed)	45L	1	200	200
8	DC/AC inverter	2kW	1	150	150
9	Temperature Sensor	Pt	2	53	106
10	Pressure sensor	4-20mA	1	468	468
11	Solar Power Controller	MPPT	1	350	350
<b><i>Other accessories ( 1470 20.83% )</i></b>					
12	Waterproof insulation materials	cover the water tank and transportation lines	5	29	145
13	PV/T system Module bracket	Aluminum alloy	1	800	800
14	Thermal silicon seal	K-5205 (bottle)	35	15	525
<b><i>Subtotal</i></b>					
Total system fabrication cost (¥)					7058
Additional profit (20% of total fabrication cost)(¥)					1411.6
Capital cost(¥)					8469.6
Capital cost(GBP)					941.1

## CHAPTER 6: ENERGY SAVING, ECONOMIC, ENVIRONMENTAL ANALYSIS

---

### (2) *Renewable Earning (RE)*

To install a new solar PV or solar heating system, it might be possible to get grants through the government's renewable policy, such as the Renewable Heat Incentive (RHI) scheme in London to encourage the uptake of renewable heating technologies within households, businesses and communities through the provision of financial incentives. The financial support available for installing such a solar thermal system are ‘‘P20.06/kWh yr heat (7 years)’’ for UK[171], and ‘HKD5/kWh-yr-power (from 2018 to 2023)’ for Hong Kong[172] in China. Then the ultimate initial cost of installing such a PV/MCLHP heating system equals the value obtained by subtracting the local incentive amounts for renewable projects from the capital cost.

**Table 6-4: Renewables tariffs for the installation of a solar system in London and Hong Kong**

location	London	Hong Kong
Tariff	£ 0.2006/kWh-yr-heat	HK\$ 5/kWh-yr-power
Years	7	15
Total earning(£)	1743.62	3416.88

### 6.3.2 Annual operational cost and saving of the PV/MCLHP systems

The annual operational cost and saving calculation is based on the 1.2 kW prototype PV/MCLHP system with a 45-litre water tank taken into consideration for the economic analysis. The initial water temperature in the water tank was assumed to be equal to the local ground water temperature [32] [70]. The final hot water temperature was set to be 45°C. Therefore the annual hot water heat demand,  $Q_{h,w}$  (W), can be obtained by

$$Q_{h,w} = M_w c_w \Delta T_w N_d \quad (6-1)$$

**CHAPTER 6: ENERGY SAVING, ECONOMIC, ENVIRONMENTAL ANALYSIS**

---

Where  $Q_{h,w}$  is the thermal energy for hot water;  $M_w$  is the quality of hot water per day[173] (150L/p/d for Hong Kong[174], and 100L/p/d for London [175] water consumption was taken into calculation for hypothesis.);  $\Delta T_w$  is the temperature difference of the initial and final water temperature (K);  $N_d$  is the annual number of days for hot water, which is assumed to be 365 day/yr.

**Table 6-5 Annual operational costs of different systems**

<b>location</b>	<b>Hong Kong</b>	<b>London</b>
<i>Energy price and demand</i>		
Gas price(GBP/kWh) [176]	0.15	0.05
Electricity price(GBP/kWh)	0.12	0.14
Feed-in Tariff (GBP/kWh)[172]	0.5	0.20
Total heat demand (kWh/yr)	1405.25	1149.75
<b>PV/MCLHP heat pump system operational performance</b>		
Installation fee (GBP)	75.29	94.11
Heat produced from system (kWh/yr)	2036.20	1241.72
Energy required from auxiliary heater (kWh/yr)	-630.95	-91.97
Total electricity output from module (kWh/yr)	518.30	432.04
Electricity consumed by water pump (kWh/yr)	1065.60	1065.60
Net electricity output (kWh/yr)	1093.98	477.40
Operational cost(GBP/yr)	65.68	62.52
Maintenance fee(GBP/yr)	18.82	18.82
<b>Electric water heater (efficiency 90%)</b>		
capital cost (GBP)	150.00	150.00
Installation fee (GBP)	30.00	30.00
Electricity consumed by electric heater(kWh/yr)	1561.39	1277.50
Operational cost(GBP/yr)	187.37	178.85
Maintenance fee(GBP/yr)	9.00	15.00
<b>Gas Boiler (efficiency 80%)</b>		
capital cost (GBP)	200.00	200.00
installation fee (GBP)	12.00	20.00
Required gas energy (kWh/yr)	1756.56	1437.19
Operational cost(GBP/yr)	263.48	71.86
Maintenance fee(GBP/yr)	12.00	12.00
Annual saving by replacing a gas boiler (GBP/yr)	190.99	26.39
Annual saving by replacing a electric heater (GBP/yr)	111.87	112.51

In terms of some terrible weather that the proposed system may operate unsatisfactorily, an auxiliary heater is needed to heat the water up to the expected 45°C. A power heater and gas boiler are taken into consideration as the auxiliary heater of the prototype PV/MCLHP system, respectively, when comparing to a conventional gas boiler with efficiency of 80% and a typical electric heater with efficiency of 90% [70]. These systems' annual operational cost can be calculated and the results are presented in **Table 6-5**. It is found that operating the proposed PV/MCLHP system can save nearly GBP 191/112, GBP 26/113 per year in Hong Kong and London respectively by replacing a conventional gas boiler/electric heater.

### 6.3.3 Annual maintenance cost

Normally, the annual maintenance cost of a solar heating and power system is around 1.75%-3% of the capital cost[32][177]. Therefore, the maintenance fee of this PV/MCLHP system is assumed to be 2% in this research for the economic analysis as calculated in **Table 6-5**.

### 6.3.4 Cost payback time and life-cycle net cost savings

Replacing the conventional heating system, gas boiler and electric heater, by the proposed PV/MCLHP system, the cost payback period ( $PP_{PV/MC-LHP}$ ) can be estimated by

$$\begin{aligned}
 PP_{PV/MCLHP} &= \frac{\text{Capital Cost} - \text{Incentives}}{\text{Annual (Operational \& maintenance) Cost Saving}} \\
 &= \frac{CC_{PV/MCLHP} - C_{RE} - CC_{CH}}{(C_{O,CH} + C_{M,CH}) - (C_{O,PV/MCLHP} + C_{M,PV/MCLHP})} \quad (6-2)
 \end{aligned}$$

CHAPTER 6: ENERGY SAVING, ECONOMIC, ENVIRONMENTAL  
ANALYSIS

---

Where  $PP_{PV/MCLHP}$  is the payback period of PV/MCLHP system (year);  $CC_{PV/MCLHP}$  and  $CC_{CH}$  are the capital cost of the proposed PV/MCLHP system and the conventional heating system respectively (GBP);  $C_{RE}$  is the renewable earnings according to the local RHI (GBP);  $C_{O,CH}$  and  $C_{M,CH}$  are the operational and maintenance cost of the conventional heating system;  $C_{O,PV/MCLHP}$  and  $C_{M,PV/MCLHP}$  are the annual operational cost and maintenance cost of the novel PV/MCLHP heating and power system (GBP).

As one of solar photovoltaic and thermal system, this novel hybrid solar PV/MCLHP system is assumed to have a life span of 25 years [70]. Thus the life-cycle net cost saving,  $CS_{PV/MC-LHP}$  of this system in energy bills can be calculated by

$$CS_{PV/MCLHP} = (Lifetime - paybacktime) \times Annual(Operational \& maintenance)CostSaving$$

$$CS_{PV/MCLHP} = (25 - PP_{PV/MCLHP})[(C_{O,CH} + C_{M,CH}) - (C_{O,PV/MCLHP} + C_{M,PV/MCLHP})] \tag{6-3}$$

As shown in **Table 6-6**, the payback period and life-cycle net cost saving of the novel solar PV/MCLHP system were estimated compared to the conventional heat system.

**Table 6-6 Cost payback period and life-cycle net cost saving**

location	Hong Kong	London
<b><i>Replacing a gas boiler</i></b>		
Payback period $PP_{PV/MCLHP}$ (yr)	4.21	27.60
Life-cycle cost saving $CS_{PV/MCLHP}$ (GBP)	3970.32	-
<b><i>Replacing a electric heater</i></b>		
Payback period $PP_{PV/MCLHP}$ (yr)	5.16	6.83
Life-cycle cost saving $CS_{PV/MCLHP}$ (GBP)	2219.53	2044.03

When compared to a conventional gas boiler, this PV/MCLHP system has the shortest cost payback period of less than 5 years and the highest life-cycle net cost saving of nearly GBP 3970 in Hong Kong. While in London, the cost payback period would be around 28 years, which exceeds life span of the system. In terms of 28 years payback period in London, it is essential to reclaim the initial investment owing to the current lowest gas charging tariff, which shows that it would be uneconomical to replace a gas boiler by the proposed PV/MCLHP system in this area at this moment. When replacing a conventional electric water heater, the payback periods of this proposed system were estimated at nearly 5.6 and 7 years in Hong Kong and London, respectively, due to the different governmental support policies and electricity feed-in tariffs. The net cost saving would be around GBP 2220 and GBP2044 in Hong Kong and London respectively, throughout the system life span.

#### **6.4 Life-cycle environmental benefits based on CO<sub>2</sub> emission**

The carbon emissions are mostly contributed by fossil fuel combustion and cement production where raw coal was the primary source of CO<sub>2</sub> emissions, accounting for 52.58% in 2015. Further, it was recognized that the energy production and heavy manufacturing industries were the primary contributors. Consequently, the development of cleaner and sustainable energy production has become a major focus. In this section, we will analyse the environmental impacts of our PV/MCLHP system in relation to CO<sub>2</sub> emissions.

Annual carbon emission performance is one of the main indicator to evaluate the environmental benefits when operating a renewable system. Therefore, when running this proposed PV/MCLHP system to replace a traditional gas boiler or a conventional electric water heater. The carbon reduction can be calculated by [70]

**CHAPTER 6: ENERGY SAVING, ECONOMIC, ENVIRONMENTAL ANALYSIS**

---

$$CR_{PV/MCLHP} = f'_{CH} Q_{CH} - f'_{ele} Q_{PV/MCLHP} \quad (6-4)$$

Where  $CR_{PV/MCLHP}$  is the quality of CO<sub>2</sub> emission reduction (kg);  $f'_{CH}$  represents the CO<sub>2</sub> emission factor of burning gas ( $f'_{gas}$ ) or electricity consumption ( $f'_{ele}$ ), (kg CO<sub>2</sub>/kWh);  $Q_{CH}$  and  $Q_{PV/MCLHP}$  are the energy produced by the conventional heater and the proposed PV/MCLHP system (kWh/yr).

**Table 6-7 Annual CO<sub>2</sub> emission reduction of the proposed PV/MCLHP system**

location	Hongkong	London
<b>CO<sub>2</sub> emission factor (kg/kWh)</b>		
Electric consumption[178]	0.740	0.545
Gas burning[179]	0.26	0.26
<b>CO<sub>2</sub> emission reduction (kg/yr)</b>		
Annual CO <sub>2</sub> emission reduction saving by replacing a gas boiler	456.71	373.67
Annual CO <sub>2</sub> emission reduction saving by replacing a electric heater	1299.86	783.27

**Table 6-7** presents the comparison of the annual CO<sub>2</sub> emission among the proposed PV/MCLHP system and the conventional gas boiler and electric heater. It is estimated that the proposed PV/MCLHP system can reduce annual CO<sub>2</sub> emission 456.71kg and 373.67kg in Hong Kong and London when compared to gas boiler, while compared to the traditional electrical water heater, the annual CO<sub>2</sub> emission reduction is 1299.86kg and 783.27kg in Hong Kong and London, respectively.

## **6.5 Chapter summary**

In this chapter, the computation model developed in chapter 4 is applied to predict the annual operational performance of the proposed novel PV/MC-LHPT system; and the system life cycle, carbon dioxide emission saving, power and heat output will be theoretical analyzed to evaluate the relevant socio-economic and environmental impacts.

## CHAPTER 6: ENERGY SAVING, ECONOMIC, ENVIRONMENTAL ANALYSIS

---

The system monthly performance indicators were predicted in the London and Hong Kong. The results indicate that the system obtained the highest heat output of 1018 kWh/m<sup>2</sup>-yr in Hong Kong, which allowed the system to provide sufficiently high water temperatures (above 45 °C) throughout the year. In London, the system provided a lower volume of electricity and heat than in Hong Kong, owing to its low solar radiation and air temperature. As a result, the system, if operated in London, would consume a higher volume of additional energy provided by the backup heaters. The simulation results indicate that the prototype PV/MCLHP heat pump system would be best suited for use in a subtropical climatic region, such as Hong Kong.

Compared to a conventional gas boiler, this PV/MCLHP system has the shortest cost payback period of less than 5 years and the highest life-cycle net cost saving of nearly GBP 3970 in Hong Kong. While in London, the cost payback period would be around 28 years, which exceeds life span of the system. When replacing a conventional electric water heater, the payback periods of this proposed system were estimated at nearly 5.6 and 7 years in Hong Kong and London, respectively, due to the different governmental support policies and electricity feed-in tariffs. The net cost saving would be around GBP 2220 and GBP2044 in Hong Kong and London respectively, throughout the system life span. the proposed PV/MCLHP system can reduce annual CO<sub>2</sub> emission 456.71kg and 373.67kg in Hong Kong and London when compared to gas boiler, while compared to the traditional electrical water heater, the annual CO<sub>2</sub> emission reduction is 1299.86kg and 783.27kg in Hong Kong and London, respectively.

Nevertheless, as the solar panels are installed on roofs, no extra land usage is required and the extra energy can be supplied to the grid. Thus we can confidently conclude that the PV/T system is an effective means for the sustained development in regions using

## CHAPTER 6: ENERGY SAVING, ECONOMIC, ENVIRONMENTAL ANALYSIS

---

solar energy (a renewable energy resource) for cleaner air, greener energy supply, and minimal environmental impact. For maintenance, it only requires some washing of the panels and replacement of the faulted panels, which are relatively easy to recycle.

## CHAPTER 7: CONCLUSIONS AND FUTURE WORKS

### 7.1 Conclusions

This research has investigated a novel solar PV/MCLHP heat and power system through a critical literature review, preliminary design, theoretical analysis, computation modelling, prototype design and construction, indoor (laboratory-controlled) and outdoor (real weather conditions) testing, simulation models validation, and energy saving and socio-economic performance analysis.

The major achievements include: (1) a novel micro-channel loop heat pipe (MC-LHP) with an upper liquid feeding header; (2) an integrated PV/MCLHP heat and power system; (3) a MC-LHP analytical model based on fractal theory to evaluate its heat transfer capacity; (4) a steady state simulation model for the integrated PV/MCLHP system to investigate its heat and power generation performances; (6) a prototype PV/MCLHP heat and power system; (7) a socio-economic performance model for predicting the system's annual performance, concerning the energy saving and associated economic/environmental benefits for the use of the novel PV/MCLHP system in London and Hong Kong. The key conclusions derived from this PhD research are given as below.

#### **7.1.1 Micro-channel loop heat pipe with a unique upper liquid feeding header**

An innovative micro-channel loop heat pipe (MC-LHP) with an upper liquid feeding header was developed and investigated. Compared to the conventional LHP system in which the condensed liquid returns from the bottom of the system, the novel MC-LHP can prevent the dry-out phenomena occurring in the upper part of the LHP evaporator and incur a clear separation between the vapour and liquid, thus providing a higher heat transfer rate compared to the conventional LHP (4340 W/m<sup>2</sup>/K against 1500 W/m<sup>2</sup>/K).

In terms of the wick structure in the LHP, a fractal theory based analytical model was developed to study the impact of the wick's fractal parameters on the heat transfer capacity of the LHP. By treating the wick of the MCLHP as a thin porous layer, i.e. a combination of random/tortuous pores and water-containing skeletons, the impact of the fractal geometrical parameters of the wick on the heat transport capacity of the MCLHP was investigated. Based on the classical heat transfer limits and fractal equations, a dedicated computerised analytical model was developed by using the Newton-Raphson method; this model was then applied to analyze a few macro parameters of the wick (i.e., effective thermal conductivity and permeability) and heat transfer limits of the MCLHP, including capillary, viscous, entrainment, sonic and boiling ones. Comparison among these five limits was made using the minimum value searching approach, leading to the determination of the final heat transfer constraint of the MCLHP, which is identified as the capillary limit. A higher effective porosity and a larger pore diameter lead to an increased wick fractal dimension and thus a higher capillary limit. An increased height difference between the evaporator and the condenser also increases the heat transfer (i.e. capillary) limit of the MC-LHP. Decreased effective porosity ( $\epsilon$ ), pores portion, and increased tortuosity of capillaries help enhance the heat transfer (boiling) limit of the MC-LHP. Overall, fractal theory is thought to be an ideal method to address the impact of an irregular porous wick on the heat transfer performance of a MC-LHP.

### **7.1.2 An integrated PV/MCLHP heat and power system**

An integrated PV/MCLHP heat and power system was investigated. This system makes use of a novel micro-channel loop heat pipe (MCLHP) as the evaporator and a co-axial triple-pipe heat exchanger with PCM as the condenser. A computer simulation model was established to assess the performance of this novel PV/MCLHP system on the basis of a heat balance mechanism, which gave the PV modules' solar thermal, electrical and

overall efficiencies, and the system's overall performance of coefficient (COP-PV/T) at the specified operational conditions. The influence of the environmental parameters (i.e. solar radiation, air temperature, and wind velocity), structural parameters (i.e. glazing covers, number of the absorbing heat pipes, PC cell packing factor), the variable inputs (i.e. water inlet temperature, mass flow rate) on the energy performance of the system was investigated individually. It is found that (1) increasing the solar radiation led to an increase in thermal efficiency but a decrease in the electrical efficiency, resulting in an increase the system's overall coefficient of performance (COPPV/T); (2) increasing the ambient temperature led to an increase in the thermal efficiency, a decrease in the electrical efficiency and an increase in the system's overall coefficient of performance (COP-PV/T); (3) increasing the wind speed led to a slight decrease in the thermal efficiency, slight increase in the electrical efficiency and slight decrease in the system's overall performance coefficient (COPPV/T); (4) increasing the number of the glazing covers led to an increase in the module's thermal efficiency but a decrease in the module's electrical efficiency and in the system's overall performance coefficient (COP-PV/T); (5) increasing the packing factor led to a decrease in the module's thermal efficiency but an increase in the module's electrical efficiency and in the system's overall coefficient of performance (COP-PV/T); (6) increasing the number of the heat absorbing pipes led to an increase in the fin's efficiency and in the system's overall performance coefficient; (7) increasing the cold water inlet temperature led to a decrease in the module's thermal and electrical efficiency, and the system's overall coefficient of performance (COP-PV/T); (8) increasing the water mass flow rate led to an increase in the module's thermal efficiency and the module's electrical efficiency, and in a decrease the system's overall coefficient of performance (COP-PV/T) because of the increase of the pump electricity consumption. The results show that a flow rate of 0.0125 kg/s would be an optimal value enabling the maximum heat output and highest COP simultaneously.

Compared to the conventional PV/LHP system, the new PV/MCLHP system achieves 33% higher thermal efficiency, 8.7% higher electrical efficiency and 28.8% higher overall efficiency. Its overall COP is 2.2 times that of the conventional PV/LHP system.

### **7.1.3 A prototype PV/MCLHP system for testing and model validation**

A prototype PV/MCLHP heat and power system employing R134a as the working fluid was designed, constructed and tested. The testing results were used to evaluate its operational performance including solar thermal and electrical efficiencies and their relevant impact factors. It is found that solar thermal efficiency of the PV/MCLHP system varied with the inlet temperature and flow rate of coolant water, ambient temperature, as well as height difference between the condenser and evaporator. A lower inlet water temperature, a higher water flow rate, a higher ambient temperature, and a larger height difference between the condenser and the evaporator can help increase the solar thermal efficiency of the system. Under a range of testing conditions with the refrigerant charge ratio of 30%, a peak solar thermal efficiency (i.e., 71.67%) happened at solar radiation of 561W/m<sup>2</sup>, inlet water temperature of 18°C, water flow rate of 0.17m<sup>3</sup>/h, ambient temperature of 30°C, and height difference of 1.3m. This set of parametrical data is therefore regarded as the optimal operational condition of the PV/MCLHP system. Under these specific operational conditions and the real weather solar radiation, the solar thermal efficiency of the system was in the range 25.2% to 62.2%, while the solar electrical efficiency varied from 15.59% to 18.34%. Compared to the existing PV/T and BIPV/T systems, the new PV/MCLHP system achieved 17.20% and 33.31% higher overall solar efficiency.

### **7.1.4 Energy saving and socio-economic analysis**

A dedicated environmental and socio-economic performance study of this novel PV/MCLHP heat and power system was carried out. The simulation is conducted based

on real weather conditions of London in UK and Hong Kong in China. The system's monthly performance indicators were predicted in the London and Hong Kong. The results indicate that the system obtained the highest heat output of 1,018 kWh/m<sup>2</sup>-yr in Hong Kong, which allowed the system to provide sufficiently high water temperatures (above 45°C) throughout the year. In London, the system provided a lower amount of electricity and heat than in Hong Kong, owing to its low solar radiation and air temperature. As a result, the system, if operated in London, would consume a higher volume of additional energy provided by the backup heaters. The simulation results indicate that the prototype PV/MCLHP heat and power system would be best suited for the use in a subtropical climatic region, such as Hong Kong. This system has a cost payback period of around 5 years and the life-cycle net cost saving of nearly GBP 3970 in China compared to a conventional gas boiler, while compared to a conventional electric water heater, the cost payback period of around 5 years and the life-cycle net cost saving of this proposed system are 5.6 years and GBP 2220 respectively. Further, the relevant CO<sub>2</sub> emissions reduction are 456.7kg and 1751.3kg in Hong Kong.

## **7.2 Further opportunities and Challenges**

### **7.2.1 System demonstration**

Based on the theoretical modelling and lab testing, the parameters of the PV/MCLHP system has been characterized. The on-site demonstration of this kind of PV/MCLHP system should be undertaken in order to evaluate its real life operational performance and compatibility to different weather conditions.

### **7.2.2 PV/MCLHP stakeholders**

Aiming to conduct widespread application of such a PV/MCLHP technology, the explicit advantages and challenges for the PV/MCLHP stakeholders should be investigated.

Based on the challenges/barriers existing for the PV/MCLHP technologies, more study and collaboration among the stakeholders need to be carried out in the coming years. It is essential to develop an interdisciplinary working package in PV/MCLHP technology and the information includes R&D, specifications of design, fabrication challenges, investigation theory, experimentation methods, practical installation challenges, market exploitation analysis, policy improvement, etc. Therefore, this interdisciplinary cooperation could bring in a better understanding about the various barriers which may occur throughout the PV/MCLHP development.

### **7.2.3 Research Development**

Although the performance of such a PV/MCLHP system has been investigated, further study is still needed in order to improve its performance. These include: (1) enabling durable thermal interaction between heat storage tank and PV/MCLHP panel; (2) evaluating the solar energy performance under different control and operational conditions, such as cloudy or rainy date and an overnight preheating mode under a low-price electricity tariff; (3) designing an auxiliary heat source (e.g. air source heat pump) (4) applying better thermal greases with higher thermal conductivity into the integration of heat pipe and the PV module; (5) utilising more effective technology to produce better wick structure for the micro-channel heat pipes for better heat transfer; (6) improving manufacturing standards; (7) developing a high performance PCM applicable to the condenser of the PV/MCLHP system.

### **7.2.4 Evaluation Standards**

To date, there is no legal standard applied to such a PV/MCLHP system owing to its initial stage status. As soon as the system is converted into a commercial technology, the legal technical and manufacturing standards are required. Further, assessment standard for the PV/MCLHP system should be specified. Current approaches are not suitable for comparing such a PV/MCLHP with other energy systems equally, as the results are

various from different operational conditions e.g. climate region, PV cell types. It is therefore essential to develop relevant suitable testing procedures or standards based on the existing standards of stand-alone PV panels and solar thermal collectors.

### **7.2.5 Market analysis**

#### ***Global photovoltaic (PV) market and outlook***

According to the Bloomberg NEF(2019), the global newly installed PV capacity reached 109 GW in 2018, which was the second time it surpassed the combination of fossil fuels and nuclear since 2017. The global total solar power capacity has now reached 511 GW, exceeding the previous capacity of 402 GW in 2017, 300 GW in 2016 and 200 GW in 2015 (Solar Power Europe, 2018). IHS Markit predicts that the global new PV installed capacity will increase to 123 GW in 2019 (IHS Markit, 2019).

The prospective of the Top 20 global solar market until 2022 is positive, even though the manufacturers might suffer from the continual price drop of the PV panels, the increased affordability of PV and PV/T systems will definitely contribute to further market expansion over the next five years. According to Solar Power Europe, the estimated global PV capacity is expected to reach approximately 1,270 GW in 2022. The optimistic perspective of the Solar PV market will benefit the development of PV/T systems, encouraging innovation and adoption.

#### ***Global thermal market and outlook***

The solar heating & cooling systems used for both commercial and household purposes continues to draw global interest. In 2016, the newly installed solar heat capacity was 457 GW corresponding to 653 million square metres operated in a record breaking 66 countries (AEE-Institute for Sustainable Technologies, 2018).

## CHAPTER 7: CONCLUSIONS AND FUTURE WORKS

---

According to the report of the solar heating & cooling programme, the optimistic growth was in the markets of India (26%), Mexico (7%) and Turkey (4%). It is worth noting that approximately 90% of the solar water heating systems were installed in residential properties, such as houses and flats. However, the market for the system is also under pressure from competition of heat pumps and PV systems (AEE-Institute for Sustainable Technologies, 2018).

There is great potential for the developed system in Southern Europe and the near East, where solar irradiance is much greater meaning that the end user will see even greater savings each year. Access the European market would be very valuable, but the various accreditations and certifications will pose a significant challenge to overcome in order to access the market properly.

### ***Global PV/MCLHP market analysis***

Although markets for PV and solar thermal have been investigated on annual base, the market perspectives of the PV/T, including this new PV/MC-LHP, have yet been studied. The market analysis will be undertaken by both top-down and bottom-up approaches. Top-down approach includes survey and interview solar industry experts about industry potential of this new system within three years and Delphi process with experts' solar manufacturer & distributor to forecast industry potential of this new system in terms of sales volume and revenue. Bottom-up approach includes survey with households and facility managers in various climate regions in the UK to forecast the market penetration of this new system and Delphi process with marketing experts to forecast the market potential of this new system in terms of sales revenue. The market analysis results need to take into account the influence of global warming and climate changes, Ofgem's electricity decarbonisation action plan, and the possible new innovation of the PV/MCLHP system.

## REFERENCE

- [1] UN Sustainable Development Goals (13-Climate Change) <<https://www.un.org/sustainabledevelopment/climate-change/>> [accessed on 04th November, 2019.], (n.d.).
- [2] United Nations Climate Change Conference (Katowice, 2018) <<https://www.un.org/en/climatechange/cop24.shtml>> [accessed on 04th November, 2019.], (n.d.).
- [3] United Nations Sustainable Development Goals (7-Energy) <<https://www.un.org/sustainabledevelopment/energy/>> [accessed on 04th November, 2019.], (n.d.).
- [4] Ahead of Climate Action Summit <<https://www.un.org/sustainabledevelopment/blog/2019/09/un-secretariat-climate-action-plan/>> [accessed on 05th November, 2019.], (n.d.).
- [5] Directive (EU) 2018/844 of the European Parliament and of the Council of 30 May 2018 amending Directive 2010/31/EU on the energy performance of buildings and Directive 2012/27/EU on energy efficiency <<https://eur-lex.europa.eu/legal-content/EN/TXT/?uri=ur>, (n.d.).
- [6] Building performance factsheet. European Commission <<https://ec.europa.eu/energy/en/content/factsheet-energy-performance-buildings-directive>> [accessed on 12th November, 2019.], (n.d.).
- [7] Y. Jiang, China Energy Consumption Research Report (2020), China Architecture & Building Press, ISBN : 9787112249015., (n.d.).

## REFERENCE

---

- [8] BP statistical review of world energy <  
<https://www.webwire.com/ViewPressRel.asp?aId=242217>> [accessed on 10th August, 2020.], (n.d.).
- [9] M. Thirugnanasambandam, S. Iniyan, R. Goic, A review of solar thermal technologies, *Renew. Sustain. Energy Rev.* 14 (2010) 312–322.  
<https://doi.org/10.1016/j.rser.2009.07.014>.
- [10] B.N. Anderson, *Solar energy: fundamentals in building design*, Mgh. (1977).
- [11] A. Ummadisingu, M.S. Soni, Concentrating solar power – Technology, potential and policy in India, *Renew. Sustain. Energy Rev.* 15 (2011) 5169–5175.  
<https://doi.org/https://doi.org/10.1016/j.rser.2011.07.040>.
- [12] Y.W. Jinshun Wu, Xingxing Zhang, Jingchun Shen, A review of thermal absorbers and their integration methods for the combined solar photovoltaic/thermal (PV/T) modules, *Renew. Sustain. Energy Rev.* 75 (2017) 839–854.  
<https://doi.org/10.1016/j.rser.2016.11.063>.
- [13] J.J. Michael, I. S, R. Goic, Flat plate solar photovoltaic–thermal (PV/T) systems: A reference guide, *Renew. Sustain. Energy Rev.* 51 (2015) 62–88.  
<https://doi.org/https://doi.org/10.1016/j.rser.2015.06.022>.
- [14] Solar energy, International Renewable Energy Agency.  
<https://www.irena.org/solar> [accessed on 10th August, 2020.], (n.d.).
- [15] H.A. Zondag, W.G.J. Van Helden, M. Bakker, A roadmap for the development and market introduction of PVT technology, *Proceeding 15th symposium thermische solarenergie*, Bad Staffelstein Germany, 27-29 April, (2005).

## REFERENCE

---

- [16] J.J. Michael, I. S, R. Goic, Flat plate solar photovoltaic-thermal (PV/T) systems: A reference guide, *Renew. Sustain. Energy Rev.* 51 (2015) 62–88. <https://doi.org/10.1016/j.rser.2015.06.022>.
- [17] W. He, X. Hong, X. Zhao, X. Zhang, J. Shen, J. Ji, Operational performance of a novel heat pump assisted solar façade loop-heat-pipe water heating system, *Appl. Energy.* 146 (2015) 371–382. <https://doi.org/10.1016/j.apenergy.2015.01.096>.
- [18] A. Faghri, *Heat pipe science and technology*, Global Digital Press, 1995.
- [19] J. Zhao, Z. Li, T. Ma, Performance analysis of a photovoltaic panel integrated with phase change material, *Energy Procedia.* 158 (2019) 1093–1098. <https://doi.org/10.1016/j.egypro.2019.01.264>.
- [20] J. Nelson, *The Physics of Solar Cells*, PUBLISHED BY IMPERIAL COLLEGE PRESS AND DISTRIBUTED BY WORLD SCIENTIFIC PUBLISHING CO., 2003. <https://doi.org/10.1142/p276>.
- [21] J.N. Shive, *Semiconductor Devices*, in: Van Nostrand, New Jersey, 1959.
- [22] M.A. Green, *Photovoltaics: coming of age*, in: *IEEE Photovolt. Spec. Conf.*, 2002.
- [23] M. Tao, L. Zhenpeng, Z. Jiaxin, Photovoltaic panel integrated with phase change materials (PV-PCM): technology overview and materials selection, *Renew. Sustain. Energy Rev.* 116 (2019) 109406. <https://doi.org/10.1016/j.rser.2019.109406>.
- [24] *Test Method for Photovoltaic Module Power Rating*, January 2010, FSEC Stand. 202-10. (n.d.).
- [25] K. Lynn, *Test method for photovoltaic module ratings*, FSEC-GP-68-01. (2001)

## REFERENCE

---

1–15.

- [26] T.T. Chow, A review on photovoltaic/thermal hybrid solar technology, *Appl. Energy*. 87 (2010) 365–379. <https://doi.org/10.1016/j.apenergy.2009.06.037>.
- [27] A. Luque, S. Hegedus, Handbook of photovoltaic science and engineering, in: 2003.
- [28] S.A. Kalogirou, Y. Tripanagnostopoulos, Industrial application of PV/T solar energy systems, *Appl. Therm. Eng.* 27 (2007) 1259–1270. <https://doi.org/10.1016/j.applthermaleng.2006.11.003>.
- [29] A. Zarei, M. Liravi, M. Babaie Rabiee, M. Ghodrat, A Novel, eco-friendly combined solar cooling and heating system, powered by hybrid Photovoltaic thermal (PVT) collector for domestic application, *Energy Convers. Manag.* 222 (2020) 113198. <https://doi.org/https://doi.org/10.1016/j.enconman.2020.113198>.
- [30] J. Edward C. Kern, M.I. es C.R. I, Hybrid photovoltaic-thermal solar energy systems, (n.d.).
- [31] E.C. Kern, M.C. Russell, Combined photovoltaic and thermal hybrid collector systems, 13th IEEE Photovolt. Spec. Conf. (1978).
- [32] J. Zhou, Investigation of Novel Micro-Channel, Mini-Channel PV/T And Thermal Modules Based Solar Heat Pump Systems, 2018.
- [33] M. Buker, S. Riffat, Building integrated solar thermal collectors – A review, *Renew. Sustain. Energy Rev.* 51 (2015) 327–346. <https://doi.org/10.1016/j.rser.2015.06.009>.
- [34] T.K. Ghosh, M.A. Prelas, *Energy Resources and Systems*, Springer Netherlands,

## REFERENCE

---

- 2011.
- [35] E. Skoplaki, J.A. Palyvos, Operating temperature of photovoltaic modules: A survey of pertinent correlations, *Renew. Energy*. 34 (2009) 23–29. <https://doi.org/10.1016/j.renene.2008.04.009>.
- [36] H.P. Garg, R.S. Adhikari, Conventional hybrid photovoltaic/thermal (PV/T) air heating collectors: Steady-state simulation, *Renew. Energy*. 11 (1997) 363–385. [https://doi.org/10.1016/S0960-1481\(97\)00007-4](https://doi.org/10.1016/S0960-1481(97)00007-4).
- [37] N. Aste, G. Chiesa, F. Verri, Design, development and performance monitoring of a photovoltaic-thermal (PVT) air collector, *Renew. Energy*. 33 (2008) 914–927. <https://doi.org/https://doi.org/10.1016/j.renene.2007.06.022>.
- [38] F. Sarhaddi, S. Farahat, H. Ajam, A. Behzadmehr, M. Mahdavi Adeli, An improved thermal and electrical model for a solar photovoltaic thermal (PV/T) air collector, *Appl. Energy*. 87 (2010) 2328–2339. <https://doi.org/https://doi.org/10.1016/j.apenergy.2010.01.001>.
- [39] S.C. Solanki, S. Dubey, A. Tiwari, Indoor simulation and testing of photovoltaic thermal (PV/T) air collectors, *Appl. Energy*. 86 (2009) 2421–2428. <https://doi.org/10.1016/j.apenergy.2009.03.013>.
- [40] Y. Sukamongkol, S. Chungpaibulpatana, B. Limmeechokchai, P. Sripadungtham, Condenser heat recovery with a PV/T air heating collector to regenerate desiccant for reducing energy use of an air conditioning room, *Energy Build*. 42 (2010) 315–325. <https://doi.org/https://doi.org/10.1016/j.enbuild.2009.09.009>.
- [41] F. Hussain, M.Y.H. Othman, K. Sopian, B. Yatim, H. Ruslan, H. Othman, Design development and performance evaluation of photovoltaic/thermal (PV/T) air base

## REFERENCE

---

- solar collector, *Renew. Sustain. Energy Rev.* 25 (2013) 431–441.  
<https://doi.org/https://doi.org/10.1016/j.rser.2013.04.014>.
- [42] W. Fan, G. Kokogiannakis, Z. Ma, A multi-objective design optimisation strategy for hybrid photovoltaic thermal collector (PVT)-solar air heater (SAH) systems with fins, *Sol. Energy.* 163 (2018) 315–328.  
<https://doi.org/https://doi.org/10.1016/j.solener.2018.02.014>.
- [43] J.K. Tonui, Y. Tripanagnostopoulos, Improved PV/T solar collectors with heat extraction by forced or natural air circulation, *Renew. Energy.* 32 (2007) 623–637.  
<https://doi.org/10.1016/j.renene.2006.03.006>.
- [44] A. Fudholi, M. Zohri, N.S.B. Rukman, N.S. Nazri, M. Mustapha, C.H. Yen, M. Mohammad, K. Sopian, Exergy and sustainability index of photovoltaic thermal (PVT) air collector: A theoretical and experimental study, *Renew. Sustain. Energy Rev.* 100 (2019) 44–51. <https://doi.org/https://doi.org/10.1016/j.rser.2018.10.019>.
- [45] G. Barone, A. Buonomano, C. Forzano, A. Palombo, O. Panagopoulos, Experimentation, modelling and applications of a novel low-cost air-based photovoltaic thermal collector prototype, *Energy Convers. Manag.* 195 (2019) 1079–1097. <https://doi.org/https://doi.org/10.1016/j.enconman.2019.04.082>.
- [46] A. Herez, H. El Hage, T. Lemenand, M. Ramadan, M. Khaled, Review on photovoltaic/thermal hybrid solar collectors: Classifications, applications and new systems, *Sol. Energy.* 207 (2020) 1321–1347.  
<https://doi.org/10.1016/j.solener.2020.07.062>.
- [47] B.J. Huang, T.H. Lin, W.C. Hung, F.S. Sun, Performance evaluation of solar photovoltaic/thermal systems, *Sol. Energy.* 70 (2001) 443–448.

## REFERENCE

---

- [https://doi.org/https://doi.org/10.1016/S0038-092X\(00\)00153-5](https://doi.org/https://doi.org/10.1016/S0038-092X(00)00153-5).
- [48] G. Fraisse, C. Ménézo, K. Johannes, Energy performance of water hybrid PV/T collectors applied to combisystems of Direct Solar Floor type, *Sol. Energy.* 81 (2007) 1426–1438. <https://doi.org/https://doi.org/10.1016/j.solener.2006.11.017>.
- [49] N. Aste, C. del Pero, F. Leonforte, Water flat plate PV–thermal collectors: A review, *Sol. Energy.* 102 (2014) 98–115. <https://doi.org/https://doi.org/10.1016/j.solener.2014.01.025>.
- [50] M. Herrando, C.N. Markides, K. Hellgardt, A UK-based assessment of hybrid PV and solar-thermal systems for domestic heating and power: System performance, *Appl. Energy.* 122 (2014) 288–309. <https://doi.org/https://doi.org/10.1016/j.apenergy.2014.01.061>.
- [51] J. Yazdanpanahi, F. Sarhaddi, M. Mahdavi Adeli, Experimental investigation of exergy efficiency of a solar photovoltaic thermal (PVT) water collector based on exergy losses, *Sol. Energy.* 118 (2015) 197–208. <https://doi.org/https://doi.org/10.1016/j.solener.2015.04.038>.
- [52] N. Aste, F. Leonforte, C. Del Pero, Design, modeling and performance monitoring of a photovoltaic–thermal (PVT) water collector, *Sol. Energy.* 112 (2015) 85–99. <https://doi.org/https://doi.org/10.1016/j.solener.2014.11.025>.
- [53] S. Senthilraja, R. Gangadevi, R. Marimuthu, M. Baskaran, Performance evaluation of water and air based PVT solar collector for hydrogen production application, *Int. J. Hydrogen Energy.* 45 (2020) 7498–7507. <https://doi.org/https://doi.org/10.1016/j.ijhydene.2019.02.223>.
- [54] X. Zhang, X. Zhao, S. Smith, J. Xu, X. Yu, Review of R&D progress and practical

## REFERENCE

---

- application of the solar photovoltaic/thermal (PV/T) technologies, *Renew. Sustain. Energy Rev.* 16 (2012) 599–617. <https://doi.org/10.1016/j.rser.2011.08.026>.
- [55] J. Ji, K. Liu, T. Chow, G. Pei, W. He, H. He, Performance analysis of a photovoltaic heat pump, *Appl. Energy.* 85 (2008) 680–693. <https://doi.org/https://doi.org/10.1016/j.apenergy.2008.01.003>.
- [56] M. Hammad, Experimental study of the performance of a solar collector cooled by heat pipes, *Renew. Energy.* 6 (1995) 11–15. [https://doi.org/https://doi.org/10.1016/0960-1481\(94\)00063-C](https://doi.org/https://doi.org/10.1016/0960-1481(94)00063-C).
- [57] P. Gang, F. Huide, Z. Tao, J. Jie, A numerical and experimental study on a heat pipe PV/T system, *Sol. Energy.* 85 (2011) 911–921. <https://doi.org/10.1016/j.solener.2011.02.006>.
- [58] S.Y. Wu, Q.L. Zhang, L. Xiao, F.H. Guo, A heat pipe photovoltaic/thermal (PV/T) hybrid system and its performance evaluation, *Energy Build.* 43 (2011) 3558–3567. <https://doi.org/10.1016/j.enbuild.2011.09.017>.
- [59] P. Gang, F. Huide, J. Jie, C. Tin-tai, Z. Tao, Annual analysis of heat pipe PV/T systems for domestic hot water and electricity production, *Energy Convers. Manag.* 56 (2012) 8–21. <https://doi.org/https://doi.org/10.1016/j.enconman.2011.11.011>.
- [60] P. Gang, F. Huide, Z. Huijuan, J. Jie, Performance study and parametric analysis of a novel heat pipe PV/T system, *Energy.* 37 (2012) 384–395. <https://doi.org/10.1016/j.energy.2011.11.017>.
- [61] X. Zhang, X. Zhao, J. Xu, X. Yu, Characterization of a solar photovoltaic/loop-heat-pipe heat pump water heating system, *Appl. Energy.* 102 (2013) 1229–1245. <https://doi.org/10.1016/j.apenergy.2012.06.039>.

## REFERENCE

---

- [62] J. Zhou, X. Zhao, X. Ma, Z. Qiu, J. Ji, Z. Du, M. Yu, Experimental investigation of a solar driven direct-expansion heat pump system employing the novel PV/micro-channels-evaporator modules, *Appl. Energy*. 178 (2016). <https://doi.org/10.1016/j.apenergy.2016.06.063>.
- [63] X. Zhao, Z. Wang, Q. Tang, Theoretical investigation of the performance of a novel loop heat pipe solar water heating system for use in Beijing, China, *Appl. Therm. Eng.* 30 (2010) 2526–2536.
- [64] H. Li, Y. Sun, Operational performance study on a photovoltaic loop heat pipe/solar assisted heat pump water heating system, *Energy Build.* 158 (2018) 861–872. <https://doi.org/10.1016/j.enbuild.2017.10.075>.
- [65] X. Ren, M. Yu, X. Zhao, J. Li, S. Zheng, F. Chen, Z. Wang, J. Zhou, G. Pei, J. Ji, Assessment of the cost reduction potential of a novel loop-heat-pipe solar photovoltaic/thermal system by employing the distributed parameter model, *Energy*. 190 (2020) 116338. <https://doi.org/10.1016/j.energy.2019.116338>.
- [66] J. Zhou, X. Zhao, X. Ma, Z. Qiu, J. Ji, Z. Du, M. Yu, Experimental investigation of a solar driven direct-expansion heat pump system employing the novel PV/micro-channels-evaporator modules, *Appl. Energy*. 178 (2016) 484–495. <https://doi.org/10.1016/j.apenergy.2016.06.063>.
- [67] H. Li, Y. Sun, Performance optimization and benefit analyses of a photovoltaic loop heat pipe/solar assisted heat pump water heating system, *Renew. Energy*. 134 (2019) 1240–1247. <https://doi.org/10.1016/j.renene.2018.09.055>.
- [68] Y.F. Maydanik, Loop heat pipes, *Appl. Therm. Eng.* 25 (2005) 635–657. <https://doi.org/10.1016/j.applthermaleng.2004.07.010>.

## REFERENCE

---

- [69] X. Zhang, X. Zhao, J. Shen, X. Hu, X. Liu, J. Xu, Design, fabrication and experimental study of a solar photovoltaic/loop-heat-pipe based heat pump system, *Sol. Energy*. 97 (2013) 551–568. <https://doi.org/10.1016/j.solener.2013.09.022>.
- [70] X. Zhang, Investigation of a novel solar PV/loop-heat-pipe heat pump transfer. PhD thesis. University of Hull, Hull, UK., (2014).
- [71] J. Ku, Introduction to Heat Pipes GSFC· 2015 • Heat Pipe Design and Selection, (2015).
- [72] H. Alizadeh, R. Ghasempour, M.B. Shafii, M.H. Ahmadi, W.M. Yan, M.A. Nazari, Numerical simulation of PV cooling by using single turn pulsating heat pipe, *Int. J. Heat Mass Transf.* 127 (2018) 203–208. <https://doi.org/10.1016/j.ijheatmasstransfer.2018.06.108>.
- [73] A. Gandomkar, M.H. Saidi, M.B. Shafii, M. Vandadi, K. Kalan, Visualization and comparative investigations of pulsating ferro-fluid heat pipe, *Appl. Therm. Eng.* 116 (2017) 56–65. <https://doi.org/10.1016/j.applthermaleng.2017.01.068>.
- [74] M. Ebrahimi, M.B. Shafii, M.A. Bijarchi, Experimental investigation of the thermal management of flat-plate closed-loop pulsating heat pipes with interconnecting channels, *Appl. Therm. Eng.* 90 (2015) 838–847. <https://doi.org/10.1016/j.applthermaleng.2015.07.040>.
- [75] S.W. Chi, Heat pipe theory and practice, Washington, DC, Hemisph. Publ. Corp.; New York, McGraw-Hill B. Co., 1976. 256 P. (1976).
- [76] D.A. Reay, P.A. Kew, R.J. McGlen, Chapter 3 - Heat pipe components and materials, in: D.A. Reay, P.A. Kew, R.J. McGlen (Eds.), *Heat Pipes (Sixth Ed., Sixth Edit, Butterworth-Heinemann, Oxford, 2014: pp. 65–94.*

## REFERENCE

---

- <https://doi.org/https://doi.org/10.1016/B978-0-08-098266-3.00003-0>.
- [77] D.A. Reay, P.A. Kew, R.J. McGlen, eds., Appendix 1 - Working fluid properties, in: Heat Pipes (Sixth Ed., Sixth Edit, Butterworth-Heinemann, Oxford, 2014: pp. 227–237. <https://doi.org/https://doi.org/10.1016/B978-0-08-098266-3.00017-0>.
- [78] D.A. Reay, P.A. Kew, R.J. McGlen, Chapter 2 - Heat transfer and fluid flow theory, in: D.A. Reay, P.A. Kew, R.J. McGlen (Eds.), Heat Pipes (Sixth Ed., Sixth Edit, Butterworth-Heinemann, Oxford, 2014: pp. 15–64. <https://doi.org/https://doi.org/10.1016/B978-0-08-098266-3.00002-9>.
- [79] J. Ku, Introduction to Heat Pipes, 1994. <https://doi.org/10.1016/j.lpm.2014.03.015>.
- [80] D.A. Reay, P.A. Kew, R.J. McGlen, Chapter 4 - Design guide, in: D.A. Reay, P.A. Kew, R.J. McGlen (Eds.), Heat Pipes (Sixth Ed., Sixth Edit, Butterworth-Heinemann, Oxford, 2014: pp. 95–104. <https://doi.org/https://doi.org/10.1016/B978-0-08-098266-3.00004-2>.
- [81] L. Ling, Q. Zhang, Y. Yu, S. Liao, Z. Sha, Experimental study on the thermal characteristics of micro channel separate heat pipe respect to different filling ratio, Appl. Therm. Eng. 102 (2016) 375–382. <https://doi.org/10.1016/j.applthermaleng.2016.03.016>.
- [82] E.R. Babu, H.N. Reddappa, G. V. Gnanendra Reddy, Effect of Filling Ratio on Thermal Performance of Closed Loop Pulsating Heat Pipe, Mater. Today Proc. 5 (2018) 22229–22236. <https://doi.org/10.1016/j.matpr.2018.06.588>.
- [83] M. Li, L. Li, D. Xu, Effect of filling ratio and orientation on the performance of a multiple turns helium pulsating heat pipe, Cryogenics (Guildf). 100 (2019) 62–68. <https://doi.org/10.1016/j.cryogenics.2019.04.006>.

## REFERENCE

---

- [84] T. Ding, H. wen Cao, Z. guang He, Z. Li, Experiment research on influence factors of the separated heat pipe system, especially the filling ratio and Freon types, *Appl. Therm. Eng.* 118 (2017) 357–364. <https://doi.org/10.1016/j.applthermaleng.2017.02.085>.
- [85] W. Ling, W. Zhou, W. Yu, R. Liu, K.S. Hui, Thermal performance of loop heat pipes with smooth and rough porous copper fiber sintered sheets, *Energy Convers. Manag.* 153 (2017) 323–334. <https://doi.org/10.1016/j.enconman.2017.10.009>.
- [86] C. Yue, Q. Zhang, Z. Zhai, L. Ling, CFD simulation on the heat transfer and flow characteristics of a microchannel separate heat pipe under different filling ratios, *Appl. Therm. Eng.* 139 (2018) 25–34. <https://doi.org/10.1016/j.applthermaleng.2018.01.011>.
- [87] L. Hong, H. Pingwei, S. Yue, Photoelectricity and photothermal performance experiment on solar photovoltaic/loop-heat-pipe water heating system, *Trans. Chinese Soc. Agric. Eng.* (2018) 30.
- [88] A. Samba, H. Louahlia-Gualous, S. Le Masson, D. Nörterhäuser, Two-phase thermosyphon loop for cooling outdoor telecommunication equipments, *Appl. Therm. Eng.* 50 (2013) 1351–1360. <https://doi.org/10.1016/j.applthermaleng.2012.05.023>.
- [89] X. Zhang, INVESTIGATION OF A NOVEL SOLAR PHOTOVOLTAIC/LOOP-HEAT-PIPE HEAT PUMP SYSTEM, 2014.
- [90] D. Liu, G.F. Tang, F.Y. Zhao, H.Q. Wang, Modeling and experimental investigation of looped separate heat pipe as waste heat recovery facility, *Appl. Therm. Eng.* 26 (2006) 2433–2441.

## REFERENCE

---

- <https://doi.org/10.1016/j.applthermaleng.2006.02.012>.
- [91] X. Zhang, X. Zhao, J. Shen, J. Xu, X. Yu, Dynamic performance of a novel solar photovoltaic/loop-heat-pipe heat pump system, *Appl. Energy*. 114 (2014) 335–352. <https://doi.org/10.1016/j.apenergy.2013.09.063>.
- [92] G. Zhou, J. Li, L. Lv, An ultra-thin miniature loop heat pipe cooler for mobile electronics, *Appl. Therm. Eng.* 109 (2016) 514–523. <https://doi.org/10.1016/j.applthermaleng.2016.08.138>.
- [93] D.A. Reay, *Heat Pipes*, 6th Edition, (1985).
- [94] Patel, K. Vivek, An efficient optimization and comparative analysis of ammonia and methanol heat pipe for satellite application, *Energy Convers. Manag.* 165 (2018) 382–395.
- [95] J. Li, D. Wang, G.P. Peterson, Experimental studies on a high performance compact loop heat pipe with a square flat evaporator, *Appl. Therm. Eng.* 30 (2010) 741–752.
- [96] X.Y. Lu, T.C. Hua, M.J. Liu, Y.X. Cheng, Thermal analysis of loop heat pipe used for high-power LED, *Thermochim. Acta*. 493 (2009) 25–29.
- [97] A.M. Alkhalabi, Evaluating the possible configurations of incorporating the loop heat pipe into the air-conditioning systems, *Int. J. Refrig.* 31 (2008) 807–815.
- [98] N. Michael, H. Alexander, P. Babak, D. Marius, K. Juergen, Experimental evaluation of a heat pipe cooled structured reactor as part of a two-stage catalytic methanation process in power-to-gas applications, *Appl. Energy*. 229 (2018) 289–298.

## REFERENCE

---

- [99] T.M.O. Diallo, M. Yu, J. Zhou, X. Zhao, S. Shittu, G. Li, J. Ji, D. Hardy, Energy performance analysis of a novel solar PVT loop heat pipe employing a microchannel heat pipe evaporator and a PCM triple heat exchanger, *Energy*. 167 (2019) 866–888. <https://doi.org/10.1016/j.energy.2018.10.192>.
- [100] M. Yu, T.M.O. Diallo, X. Zhao, J. Zhou, Z. Du, J. Ji, Y. Cheng, Analytical study of impact of the wick's fractal parameters on the heat transfer capacity of a novel micro-channel loop heat pipe, *Energy*. 158 (2018) 746–759. <https://doi.org/10.1016/j.energy.2018.06.075>.
- [101] X. Zhang, X. Zhao, J. Xu, X. Yu, Study of the heat transport capacity of a novel gravitational loop heat pipe, *Int. J. Low-Carbon Technol.* 8 (2013) 210–223. <https://doi.org/10.1093/ijlct/cts028>.
- [102] He, Wei, Tan, Junyi, Zhang, Xingxing, Xu, Peng, Zhao, Xudong, Comparative study of a novel liquid-vapour separator incorporated gravitational loop heat pipe against the conventional gravitational straight and loop heat pipes - Part I: Conceptual development and theoretical analyses, *Energy Convers. Manag.* (2015).
- [103] I.W. Eames, K.T. Adref, Freezing and melting of water in spherical enclosures of the type used in thermal (ice) storage systems, *Appl. Therm. Eng.* 22 (2002) 733–745. [https://doi.org/https://doi.org/10.1016/S1359-4311\(02\)00026-1](https://doi.org/https://doi.org/10.1016/S1359-4311(02)00026-1).
- [104] Z.U.R.E.& A. DICKEN, Initial Investigation of Phase Change Materials for Innovate with China, Report. (n.d.).
- [105] B. Zalba, J.M. Marín, L.F. Cabeza, H. Mehling, Review on thermal energy storage with phase change: materials, heat transfer analysis and applications, *Appl. Therm. Eng.* 23 (2003) 251–283. <https://doi.org/https://doi.org/10.1016/S1359->

## REFERENCE

---

4311(02)00192-8.

- [106] M.K. Rathod, J. Banerjee, Thermal stability of phase change materials used in latent heat energy storage systems: A review, *Renew. Sustain. Energy Rev.* 18 (2013) 246–258. [https://doi.org/https://doi.org/10.1016/j.rser.2012.10.022](https://doi.org/10.1016/j.rser.2012.10.022).
- [107] D. Zhou, C.Y. Zhao, Y. Tian, Review on thermal energy storage with phase change materials (PCMs) in building applications, *Appl. Energy.* 92 (2012) 593–605. [https://doi.org/https://doi.org/10.1016/j.apenergy.2011.08.025](https://doi.org/10.1016/j.apenergy.2011.08.025).
- [108] N. Fuxin, N. Long, Q. Minglu, Y. Yang, D. Shiming, A novel triple-sleeve energy storage exchanger and its application in an environmental control system, *Appl. Therm. Eng.* 54 (2013) 1–6. <https://doi.org/10.1016/j.applthermaleng.2012.11.022>.
- [109] A. García, R. Herrero-Martin, J.P. Solano, J. Pérez-García, The role of insert devices on enhancing heat transfer in a flat-plate solar water collector, *Appl. Therm. Eng.* 132 (2018) 479–489. [https://doi.org/https://doi.org/10.1016/j.applthermaleng.2017.12.090](https://doi.org/10.1016/j.applthermaleng.2017.12.090).
- [110] D. Qin, Z.J. Yu, T. Yang, S. Li, G. Zhang, Thermal performance evaluation of a new structure hot water tank integrated with phase change materials, *Energy Procedia.* 158 (2019) 5034–5040.
- [111] M. Ibáñez, L.F. Cabeza, C. Solé, J. Roca, M. Nogués, Modelization of a water tank including a PCM module, *Appl. Therm. Eng.* 26 (2006) 1328–1333. [https://doi.org/https://doi.org/10.1016/j.applthermaleng.2005.10.022](https://doi.org/10.1016/j.applthermaleng.2005.10.022).
- [112] L.F. Cabeza, M. Ibáñez, C. Solé, J. Roca, M. Nogués, Experimentation with a water tank including a PCM module, *Sol. Energy Mater. Sol. Cells.* 90 (2006) 1273–1282. [https://doi.org/https://doi.org/10.1016/j.solmat.2005.08.002](https://doi.org/10.1016/j.solmat.2005.08.002).

## REFERENCE

---

- [113] M. Dzikevics, A. Ansonė, I. Veidenbergs, Experimental investigation of flow rate impact on thermal accumulation system with PCM, *Energy Procedia*. 128 (2017) 386–392. <https://doi.org/https://doi.org/10.1016/j.egypro.2017.09.043>.
- [114] A. López-Navarro, J. Biosca-Taronger, J.M. Corberán, C. Peñalosa, A. Lázaro, P. Dolado, J. Payá, Performance characterization of a PCM storage tank, *Appl. Energy*. 119 (2014) 151–162. <https://doi.org/https://doi.org/10.1016/j.apenergy.2013.12.041>.
- [115] A. Castell, M. Belusko, F. Bruno, L.F. Cabeza, Maximisation of heat transfer in a coil in tank PCM cold storage system, *Appl. Energy*. 88 (2011) 4120–4127.
- [116] D. Lafri, D. Semmar, A. Hamid, M. Ouzzane, Experimental investigation on combined sensible and latent heat storage in two different configurations of tank filled with PCM, *Appl. Therm. Eng.* (2018).
- [117] [ Nan Zhang, Y. Yuan, Y. Du, X. Cao, Y. Yuan], Preparation and properties of palmitic-stearic acid eutectic mixture/expanded graphite composite as phase change material for energy storage, *Energy*. (2014).
- [118] Mandelbrot, B. Benoit, *The Fractal Geometry of Nature*, *Am. J. Phys.* 51 (1998) 468 p.
- [119] P.M. Adler, Transports in fractal porous media, *J. Hydrol.* 187 (1996) 195–213.
- [120] P.M. Adler, J.F. Thovert, *Real Porous Media: Local Geometry and Macroscopic Properties*, *Appl. Mech. Rev.* 51 (1998) 537–585.
- [121] J. Feder, *Fractals*, Plenum Press, 1988.
- [122] B. Yu, P. Cheng, A fractal permeability model for bi-dispersed porous media, *Int.*

## REFERENCE

---

- J. Heat Mass Transf. 45 (2002) 2983–2993. [https://doi.org/10.1016/S0017-9310\(02\)00014-5](https://doi.org/10.1016/S0017-9310(02)00014-5).
- [123] B. Yu, Fractal Analysis of Permeabilities, *AIChE J.* 50 (2004).
- [124] B. Yu, J. Li, Fractal dimensions for unsaturated porous media, *Fractals*. 12 (2004) 17–22. <https://doi.org/10.1142/S0218348X04002409>.
- [125] X. Huai, W. Wang, Z. Li, Analysis of the effective thermal conductivity of fractal porous media, *Appl. Therm. Eng.* 27 (2007) 2815–2821. <https://doi.org/10.1016/j.applthermaleng.2007.01.031>.
- [126] S. Spagnol, B. Lartigue, A. Trombe, V. Gibiat, Thermal modeling of two-dimensional periodic fractal patterns, an application to nanoporous media, *Epl*. 78 (2007) 1–6. <https://doi.org/10.1209/0295-5075/78/46005>.
- [127] J. Wu, B. Yu, A fractal resistance model for flow through porous media, *Int. J. Heat Mass Transf.* 50 (2007) 3925–3932. <https://doi.org/10.1016/j.ijheatmasstransfer.2007.02.009>.
- [128] F. Zhu, S. Cui, B. Gu, Fractal analysis for effective thermal conductivity of random fibrous porous materials, *Phys. Lett. Sect. A Gen. At. Solid State Phys.* 374 (2010) 4411–4414. <https://doi.org/10.1016/j.physleta.2010.08.075>.
- [129] L. Li, B. Yu, Fractal analysis of the effective thermal conductivity of biological media embedded with randomly distributed vascular trees, *Int. J. Heat Mass Transf.* 67 (2013) 74–80. <https://doi.org/10.1016/j.ijheatmasstransfer.2013.08.003>.
- [130] T. Miao, Z. Long, A. Chen, B. Yu, Analysis of permeabilities for slug flow in fractal porous media, *Int. Commun. Heat Mass Transf.* 88 (2017) 194–202.

## REFERENCE

---

<https://doi.org/10.1016/j.icheatmasstransfer.2017.09.002>.

- [131] P.E. Phelan, An introduction to heat pipes: : Modelling, Testing, and Applications. Wiley-Interscience Press. New York, 12 (1996) 105.  
[https://doi.org/https://doi.org/10.1016/S0894-1777\(96\)90020-5](https://doi.org/https://doi.org/10.1016/S0894-1777(96)90020-5).
- [132] M. Kuroda, J.Y. Chang, P. Gwin, R. Mongia, M. Mochizuki, DEVELOPMENT OF ALUMINUM-WATER HEAT PIPES, Heat Pipe Sci. Technol. An Int. J. 5 (2014) 129–136.
- [133] S. Launay, V. Sartre, J. Bonjour, Parametric analysis of loop heat pipe operation: a literature review, Int. J. Therm. Sci. 46 (2007) 621–636.  
<https://doi.org/10.1016/j.ijthermalsci.2006.11.007>.
- [134] Heat Pipes: Theory, design, and Applications. Fifth Edition., Mech. Eng. (2007).
- [135] N.J. Gernert, G.J. Baldassarre, J.M. Gottschlich, Fine Pore Loop Heat Pipe Wick Structure Development, in: Aersp. Atl. Conf. Expo., 1996.
- [136] F. Wang, S. Li, Determination of the Surface Fractal Dimension for Porous Media by Capillary Condensation, Ind. Eng. Chem. Res. 36 (1997) 1598–1602.
- [137] C. ?zge. Karacan, P.M. Halleck, A fractal model for predicting permeability around perforation tunnels using size distribution of fragmented grains, J. Pet. Sci. Eng. (2003).
- [138] J. Cai, B. Yu, M. Zou, L. Luo, Fractal Characterization of Spontaneous Co-current Imbibition in Porous Media, Energy & Fuels. 24 (2010) 1860–1867.
- [139] Z. Chen, X. Tong, H. Liu, C. Guo, F. Qu, H. Cong, A design of the Micro-Plate Loop Heat Pipe and development of the porous nickel capillary wick, Procedia

## REFERENCE

---

- Eng. 205 (2017) 3931–3937. <https://doi.org/10.1016/j.proeng.2017.10.031>.
- [140] J. Xu, X. Ji, W. Yang, Z. Zhao, Modulated porous wick evaporator for loop heat pipes: Experiment, *Int. J. Heat Mass Transf.* 72 (2014) 163–176. <https://doi.org/10.1016/j.ijheatmasstransfer.2014.01.005>.
- [141] F.C. Lin, B.H. Liu, C.T. Huang, Y.M. Chen, Evaporative heat transfer model of a loop heat pipe with bidisperse wick structure, *Int. J. Heat Mass Transf.* 54 (2011) 4621–4629. <https://doi.org/10.1016/j.ijheatmasstransfer.2011.06.015>.
- [142] P., B., Qiao, X., Qiu, S., Jiang, Z., Radial permeability of fractured porous media by Monte Carlo simulations, *Int. J. Heat Mass Transf.* 57 (2013) 369–374.
- [143] L.I. Jianhua, Y.U. Boming, SOME FRACTAL CHARACTERS OF POROUS MEDIA, *Fractals*. (2001).
- [144] Y. Bo-Ming, Fractal Character for Tortuous Streamtubes in Porous Media, *Chinese Phys. Lett.* 22 (2004) 158.
- [145] X. Chen, G. Yao, An improved model for permeability estimation in low permeable porous media based on fractal geometry and modified Hagen-Poiseuille flow, *Fuel*. 210 (2017) 748–757. <https://doi.org/10.1016/j.fuel.2017.08.101>.
- [146] B. Yu, W. Liu, Fractal analysis of permeabilities for porous media, *Aiche J.* 50 (2010) 46–57.
- [147] H. ~J. Su, Heat transfer in porous media with fluid phase changes, California Univ., Berkeley. Lawrence Berkeley Lab, 1981.
- [148] B. Yu, P. Cheng, Fractal Models for the Effective Thermal Conductivity of Bidispersed Porous Media, *J. Thermophys. Heat Transf.* 16 (2002) p.22-29.

## REFERENCE

---

- [149] T.M.O. Diallo, M. Yu, J. Zhou, X. Zhao, J. Ji, D. Hardy, Analytical investigation of the heat-transfer limits of a novel solar loop-heat pipe employing a mini-channel evaporator, *Energies*. 11 (2018). <https://doi.org/10.3390/en11010148>.
- [150] Zhuang J, Zhang H. Heat Pipe Technology and Engineering Application, 1st edn. The Press of Chemistry Industry, 2000., n.d.
- [151] Reay D, Kew P. Heat Pipes (5th edn). Elsevier: Amsterdam, 2006; 48–52, 93–96, 122 and 234–236, n.d.
- [152] Z. Xiaobao, Analysis and Amendment of Design Factors about Heat Pipe of Screen Wicks, J. Nanjing Norm. Univ. Technol. (2004).
- [153] Dunn P.D, Reay D.A. Heat Pipes, third ed., Pergamon Press, New York, 1982., (n.d.).
- [154] B.R. Babin, G.P. Peterson, D. Wu, Steady-State Modeling and Testing of a Micro Heat Pipe, *Asme Trans. J. Heat Transf.* 112 (1990) 595–601.
- [155] C.A. Busse, Theory of the ultimate heat transfer limit of cylindrical heat pipes, *Int. J. Heat Mass Transf.* 16 (1973) 169–186. [https://doi.org/10.1016/0017-9310\(73\)90260-3](https://doi.org/10.1016/0017-9310(73)90260-3).
- [156] X. Zhao, Investigation of a novel heat pipe solar collector/CHP system, Test. (2003). <http://theses.nottingham.ac.uk/1255/>.
- [157] S.B. Riffat, X. Zhao, P.S. Doherty, Analytical and numerical simulation of the thermal performance of “mini” gravitational and “micro” gravitational heat pipes, *Appl. Therm. Eng.* 22 (2002) 1047–1068. [https://doi.org/10.1016/S1359-4311\(02\)00029-7](https://doi.org/10.1016/S1359-4311(02)00029-7).

## REFERENCE

---

- [158] Freggens R.A. Experimental determination of wick properties for heat pipe applications. Fourth Intersociety Energy Conference Engineering Conference, Washington Dc 1969., (n.d.).
- [159] J.A. Duffie, W.A. Beckman, W.M. Worek, Solar Engineering of Thermal Processes, 2nd ed., Wiley, 1991.
- [160] S.A. Kalogirou, Solar Energy Engineering: Processes and Systems: Second Edition, Sol. Energy Eng. Process. Syst. Second Ed. (2014) 1–819. <https://doi.org/10.1016/C2011-0-07038-2>.
- [161] Hottel HC, Willier A. Evaluation of flat-plate solar collector performance. Transactions of the conference on the use of solar energy, vol. 2. Tucson, Arizona: University of Arizona Press; 1958., n.d.
- [162] P.K. Swamee, N. Swamee, Discharge equation of a circular sharp-crested orifice, J. Hydraul. Res. 48 (2010) 106–107.
- [163] Shabanlou, Saeid, Improvement of Extreme Learning Machine Using Self-Adaptive Evolutionary Algorithm for Estimating Discharge Capacity of Sharp-Crested Weirs Located on the end of Circular Channels, Flow Meas. Instrum. (2017) S0955598617301942.
- [164] D. Reay, R. Mcglen, P. Kew, Heat Pipes (Sixth Edition), 2014.
- [165] N.H.S. Tay, M. Belusko, F. Bruno, An effectiveness-NTU technique for characterising tube-in-tank phase change thermal energy storage systems, Appl. Energy. 91 (2012) 309–319.
- [166] W. He, X. Hong, X. Zhao, X. Zhang, J. Shen, J. Ji, Theoretical investigation of the

## REFERENCE

---

thermal performance of a novel solar loop-heat-pipe façade-based heat pump water heating system, *Energy Build.* 77 (2014) 180–191. <https://doi.org/10.1016/j.enbuild.2014.03.053>.

[167] F.M. White, *Fluid Mechanics*, 7th Edition, McGraw-Hill, New York, 2011., in: n.d.

[168] W. He, Y. Zhang, J. Ji, Comparative experiment study on photovoltaic and thermal solar system under natural circulation of water, *Appl. Therm. Eng.* 31 (2011) 3369–3376. <https://doi.org/https://doi.org/10.1016/j.applthermaleng.2011.06.021>.

[169] H.M. Yin, D.J. Yang, G. Kelly, J. Garant, Design and performance of a novel building integrated PV/thermal system for energy efficiency of buildings, *Sol. Energy.* 87 (2013) 184–195. <https://doi.org/10.1016/j.solener.2012.10.022>.

[170] <https://energyplus.net/weather> weather data [accessed on 10th August 2020], (n.d.).

[171] Renewable Heat Incentive (RHI). <http://www.energysavingtrust.org.uk/scotland/grants-loans/renewables/renewable-heat-incentive> [accessed on 10th August 2020], (n.d.).

[172] RE Hongkong  
<<https://www.gov.hk/en/residents/environment/renewable/feedintariff.htm>>  
[accessed on 25th January, 2021], (n.d.).

[173] Domestic Hot Water Service Systems - Design Procedure, (n.d.). [https://www.engineeringtoolbox.com/design-hot-water-system-d\\_92.html](https://www.engineeringtoolbox.com/design-hot-water-system-d_92.html).

[174] Water Supplies Department, The Government of the Hongkong Special Administrative Region <<https://www.wsd.gov.hk/>> [accessed on 25th January, 2021], (n.d.).

## REFERENCE

---

- [175] H. Abu-Bakar, L. Williams, S.H. Hallett, A review of household water demand management and consumption measurement, *J. Clean. Prod.* (2021) 125872. <https://doi.org/10.1016/j.jclepro.2021.125872>.
- [176] Global petrol prices <[https://www.globalpetrolprices.com/Hong-Kong/gasoline\\_prices/](https://www.globalpetrolprices.com/Hong-Kong/gasoline_prices/)> [accessed on 25th January, 2021], (n.d.).
- [177] N.I. Ibrahim, F.A. Al-Sulaiman, S. Rehman, A. Saat, F.N. Ani, Economic analysis of a novel solar-assisted air conditioning system with integral absorption energy storage, *J. Clean. Prod.* 291 (2021) 125918. <https://doi.org/10.1016/j.jclepro.2021.125918>.
- [178] Global Energy & CO2 Status Report 2017, International Energy Agency, March 2018., (n.d.).
- [179] Energy <[www.greenspec.co.uk](http://www.greenspec.co.uk)> [accessed on 25th January, 2021], (n.d.).